



HAL
open science

Condensation of exciton polaritons

Jacek Kasprzak

► **To cite this version:**

Jacek Kasprzak. Condensation of exciton polaritons. Condensed Matter [cond-mat]. Université Joseph-Fourier - Grenoble I, 2006. English. NNT: . tel-00118316

HAL Id: tel-00118316

<https://theses.hal.science/tel-00118316>

Submitted on 4 Dec 2006

HAL is a multi-disciplinary open access archive for the deposit and dissemination of scientific research documents, whether they are published or not. The documents may come from teaching and research institutions in France or abroad, or from public or private research centers.

L'archive ouverte pluridisciplinaire **HAL**, est destinée au dépôt et à la diffusion de documents scientifiques de niveau recherche, publiés ou non, émanant des établissements d'enseignement et de recherche français ou étrangers, des laboratoires publics ou privés.

THÈSE

pour obtenir le grade de

Docteur de l'Université Joseph Fourier – Grenoble 1
Spécialité : physique

présentée et soutenue publiquement par

Jacek KASPRZAK

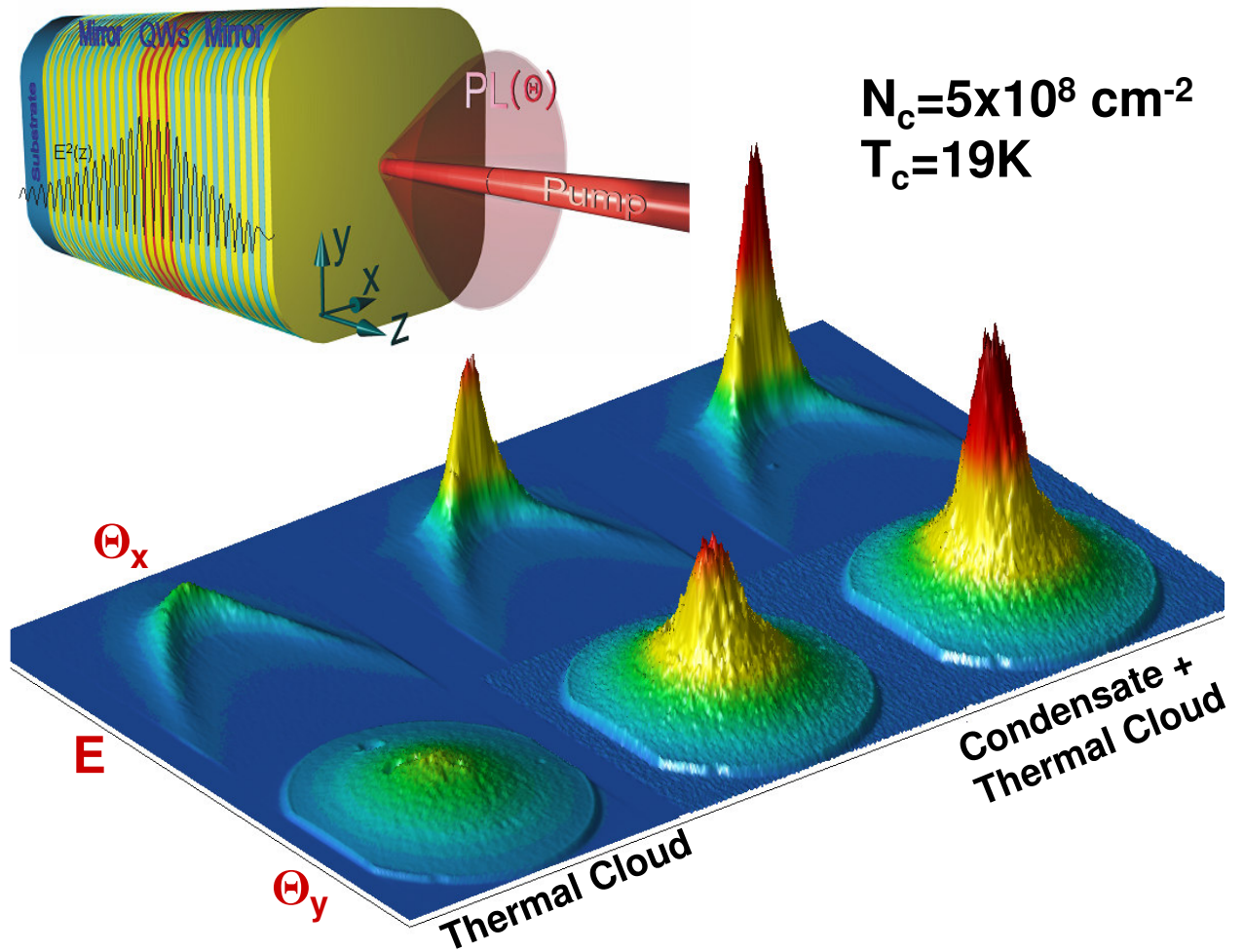
le 23 Octobre 2006

Condensation of exciton polaritons

Composition du jury

<i>Président :</i>	B. Boulanger
<i>Rapporteurs :</i>	M. S. Skolnick J. Y. Marzin
<i>Examineurs :</i>	B. Deveaud-Plédran A. V. Kavokin
<i>Directeur de thèse :</i>	Le Si Dang

Mis en page avec la classe thloria.



A separation is effected; one part condenses, the rest remains a saturated ideal gas

A. Einstein, 1925

Beauty is created by nature, sometimes we succeed in making it visible

W. Ketterle, 2001

Background motivation and main statements of this work

Surprisingly, a large number of fundamental concepts of modern physics have their origins in Einstein's works. Among them there is an intriguing phenomenon called Bose-Einstein condensation (BEC). This phase transition occurs upon increasing the phase space density of bosons - particles with integer spin, and is a consequence of their statistical properties. Nowadays the accepted definition of the BEC describes the transition in which a large fraction of massive bosons spontaneously occupy the same quantum state, leading to the formation of a long-range phase coherence.

From the very beginning, the idea of the BEC was a subject of animated debate and strong criticism ([Woo80], p.524). Even Einstein himself had doubts about his discovery, when he referred to the BEC in the following words:

"The theory is pretty, but is there also some truth to it?"

after "Current Science", vol.82, no.1, p.10, 2002

The proposal of Bose and Einstein had remained a hypothetical peculiarity of the Bose gas until 1938, when London noticed that the temperature of the λ -point is close to the BEC critical temperature, when applied to liquid helium [Lon38]. The connection between BEC and superfluidity was settled and developed in the following years by Landau, Tischa and Bogoliubov. It is interesting to note that the convincing evidence for BEC in a liquid helium below the λ -point was provided only in the 80's (see Sokol in [Gri95]).

Further developments in condensed matter physics established the description of BEC in terms of a macroscopic wave function and pointed out the onset of spontaneous long-range coherence as an important criterion for the BEC [Pen56]. The idea of long-range coherence unified the understanding of the BEC, superfluidity, superconductivity and lasing. However, this last one remains very distinct from BEC since it describes coherence of a pure photon field.

The first unambiguous proof for a BEC in weakly interacting systems came from atomic physics in the 90's, when massive occupation of the ground state [And95] and long-range coherence [Andr97] of cold, trapped alkali atoms were demonstrated. Yet, much effort had previously been put into observing this phase transition in the solid state. Here the natural candidate is an exciton [Bla62, Mos62]: a composite boson arising owing to the Coulomb attraction between an electron and a hole in a semiconductor. Its major advantage is a light effective mass, four orders of

magnitude lighter than the atom's. This could enable excitonic BEC at temperatures available by standard cryogenic means. On the other hand, due to its small binding energy, the bosonic nature of an exciton is rather "fragile". Thus, increasing the exciton density could lead to ionization towards the electron-hole plasma before BEC could take place.

The principal aim of this work is to demonstrate experimentally the condensation phenomenon in a solid state system. Our efforts to reach this goal are focalized on the exciton's cousin called the exciton polariton [Wei92]. This bosonic quasi-particle is the result of the strong coupling between a quantum well exciton and the photon mode of a Fabry-Perot like microcavity. Its effective mass is 4-5 orders of magnitude smaller than the exciton's, hence allowing bosonic degeneracy significantly below the exciton saturation density at temperature as high as 50K. This last condition is secured in our case by choosing CdTe as a basis of the microcavity; in this material system the bosonic character of excitons is preserved up to densities ten times higher than for GaAs.

The first indications suggesting polariton condensation in CdTe-based microcavities have already been found before this thesis work [Dan98, Max05, Blo05, Mul00]. Here we detail a comprehensive set of experiments giving compelling evidence for BEC of polaritons. Our experimental techniques are based on near- and far-field optical spectroscopy, first and second order interferometry measurements and basic polarization studies. The results were obtained in the range of temperature from 4K up to the room temperature.

Above a critical density, we observe a massive occupation of the polariton ground state, developing from a thermalized and saturated distribution of the polariton population at (16-20)K. We study polariton thermalization in detail and we show that it strongly depends on the exciton fraction in the polariton. We demonstrate as well the existence of a critical temperature for this transition and we find an upper temperature limit for polariton condensation in CdTe microcavities to be around 50K.

The spontaneous onset of a coherent state is manifested by an increase of temporal coherence, a build-up of long-range spatial coherence and a reduction of the thermal noise observed in intensity correlation experiments. The marked degree of linear polarization of the emission from the condensate is also measured.

All of these findings indicate the spontaneous onset of a macroscopic quantum phase.

At the same time we emphasize that polariton condensation differs in many ways from Einstein's proposal: the polariton gas is far from the ideal Bose gas and interactions play an important role. Moreover, we deal here with an open system: polaritons leak out of the microcavity within their very short radiative lifetime ($\sim 10^{-12}$ s), hence continuous pumping is needed to compensate radiative losses. We are also faced with further complications resulting from the reduced dimensionality, the finite size and the intrinsic structural disorder.

Contents

Background motivation and main statements of this work	iii
List of Figures	vi
List of Tables	vii
Chapter 1 Introduction	1
<hr/>	
1.1 Origin of the BEC	1
1.2 Realization of a BEC in cold atom vapors	6
1.3 Related phenomena	8
1.4 Towards condensation in solids	9
1.4.1 The exciton as a boson	9
1.4.2 Systems studied	12
Chapter 2 Why polariton condensation?	15
<hr/>	
2.1 From exciton to microcavity polariton	16
2.1.1 Weak versus strong exciton-photon coupling	16
2.1.2 Cavity effect: Purcell effect or Rabi oscillations?	17
2.2 Polariton dispersion: the key for condensation	21
2.2.1 Polariton trap in momentum space	21
2.2.2 Momentum space mapping	23
2.2.3 Peculiar polariton relaxation	25
Chapter 3 Polariton condensation - state of the art	28
<hr/>	
3.1 GaAs	28

3.2 CdTe	31
Chapter 4 Experimental methods	37
<hr/>	
4.1 Cryostat	37
4.2 Excitation	38
4.2.1 Laser	38
4.2.2 Acousto-optic modulator	39
4.2.3 Formation of the excitation spot	39
4.2.4 White light	40
4.3 Detection	41
4.3.1 Real and k-space imaging	41
4.3.2 Monochromator and CCD camera	43
4.3.3 Michelson interferometer	43
4.3.4 Photon correlator	44
Chapter 5 Sample description and evidence for strong coupling	46
<hr/>	
5.1 Microcavity sample	46
5.2 Evidence for strong coupling	48
5.3 Polaritons at room temperature	50
Chapter 6 Polariton condensation in momentum space	54
<hr/>	
6.1 Peculiarities of the condensation in the solid state	55
6.2 Polariton condensation in internal equilibrium - positive detuning	57
6.3 Non-equilibrium polariton condensation - negative detuning	72
6.4 The nature of the polariton condensation - theoretical remarks	76
Chapter 7 Temperature dependence studies	83
<hr/>	
7.1 Temperature dependent polariton condensation	83
7.2 Polariton condensation at high temperature - towards the phase diagram	89
Chapter 8 Transition into the weak coupling regime	95
<hr/>	

8.1	T=5.3K	95
8.2	T=106K	96
Chapter 9 Polaritons in real space		98
<hr/>		
9.1	Spatial localization of the polariton condensate	98
9.2	Characterization of localization	100
Chapter 10 Polarization		105
<hr/>		
10.1	Experimental procedure	105
10.2	Build-up of linear polarization	106
10.2.1	Detuning $\delta = +5$ meV	106
10.2.2	Detuning $\delta = 0$ meV	108
10.3	Origin of the linear polarization	110
10.3.1	Linear polarization as a signature of symmetry breaking	110
10.3.2	Ground state splitting	110
Chapter 11 Coherence		112
<hr/>		
11.1	Field correlation	113
11.1.1	First order correlation function $g^1(\mathbf{r}_1, \mathbf{r}_2, t)$	113
11.1.2	First order temporal coherence $g^1(\mathbf{r}_1 = \mathbf{r}_2, \tau)$	113
11.1.3	First order spatial coherence $g^1(\mathbf{r}_1, \mathbf{r}_2, \delta\tau = 0)$	114
11.1.4	Spatial correlation mapping $g^1(\mathbf{r}_1, -\mathbf{r}_1, \delta\tau = 0)$	116
11.2	Intensity correlations	119
11.2.1	Second order coherence function $g^2(\tau)$	119
11.2.2	CW excitation	121
11.2.3	Pulsed excitation	124
Chapter 12 Conclusions and outlook		133
Appendix A "Polariton laser" versus photon laser		137
Bibliography		142
Remerciements		157

List of Figures

1.1	a: A. Einstein and S. N. Bose, b: energy distribution for bosons. . . .	4
1.2	The BEC in the trapped 3D system.	5
1.3	Atomic condensation.	7
1.4	Spatial coherence of atomic condensates: a) [Andr97], b)[Blo00]. . . .	8
2.1	Free QW versus strong coupling microcavity emission.	18
2.2	A Bragg mirror and a microcavity: schematic structure and optical response.	19
2.3	In-plane dispersion of the exciton polariton.	22
2.4	The conceptual difference between 3D and 2D polaritons.	23
2.5	Conservation laws enable probing of the polariton states by angle resolved measurements.	24
2.6	The far field imaging as a tool for the momentum and dispersion space mapping.	25
2.7	Evolution of the polariton distribution as a function of detuning. . . .	27
3.1	Geometry of a parametric scattering experiment.	30
3.2	Situation of a non-resonant experiment.	31
3.3	Condensation on a degenerate ring of excited states.	33
3.4	The light diffused from the bottleneck emission giving the effect of "non-dispersive bar".	34
3.5	Spot-size dependence of the energy of the stimulated states.	35
4.1	Schema of the excitation part of the optical setup.	38
4.2	Formation of the excitation spot.	40
4.3	Schema of the detection part of the optical setup.	41
4.4	Real and k-space imaging.	42
4.5	Polariton dispersion measured with the Fourier plane imaging technique and with the optical fiber technique.	42
4.6	Schema of the interferometry setup.	43
4.7	Photon correlator.	45
5.1	Sample structure.	47
5.2	Reflectivity spectrum.	48
5.3	Sample characterization. Position of the polariton peaks vs. cavity energy.	49

5.4	Sample characterization. Temperature tuning.	50
5.5	Polariton dispersion in reflectivity experiment.	51
5.6	Strong coupling at room temperature.	52
5.7	Polariton dispersion at T=300K.	52
6.1	Polariton condensation in real space, $\delta = +5.4$ meV.	58
6.2	Polariton condensation in momentum space, $\delta = +7.7$ meV.	59
6.3	Polariton condensation in momentum space, $\delta = +7.2$ meV and $\delta =$ $+5.4$ meV.	60
6.4	Polariton occupancy, T=5.4K, $\delta = +7.7$ meV.	62
6.5	Polariton state occupancy, T=4.9K, $\delta = +5.4$ meV.	63
6.6	Saturation of the polariton excited states around threshold, $\delta = +5.4$ meV.	64
6.7	Threshold pump power for condensation as a function of detuning, T=5.2K	65
6.8	Acceleration of the polariton dynamics - linewidth analysis.	66
6.9	Evolution of the dispersion curve with increasing power.	69
6.10	Upper polariton red-shift with increasing power, T=28K.	70
6.11	The condensate fraction.	71
6.12	Non-equilibrium polariton condensation in momentum space.	73
6.13	Characteristics of the polariton ground state emission vs. pump power under negative detuning.	74
6.14	Polariton distribution along the dispersion curve for $\delta = -1$ meV, T=5.2K.	75
6.15	Lower polariton blue-shift as a function of the pump power.	80
7.1	Lower polariton energy for $\delta = +6.8$ meV as a function of the tem- perature.	85
7.2	Polariton condensation induced by lowering the cryostat temperature. Detuning fixed.	86
7.3	Polariton condensation induced by lowering the cryostat temperature. Transition characteristics and statistics.	87
7.4	Polariton condensation induced by lowering the cryostat temperature. The position on the sample fixed.	88
7.5	Polariton condensation induced by changing the temperature. The position on the sample is fixed. The characteristics of the data pre- sented in figure 7.4.	89
7.6	Threshold power for the ground state nonlinear emission as a function of the cryostat temperature.	90
7.7	Polariton condensation at high temperatures.	91
7.8	The characteristics of the ground state polariton emission as a func- tion of the pump power at high temperatures.	92
7.9	Polariton distribution at high cryostat temperature.	93
8.1	The transition towards the weak coupling regime, T=5.3K.	96

8.2	Photon lasing in the microcavity, T=106K. Dispersion characteristic.	97
8.3	Photon lasing in the microcavity, T=106K. PL spectra at $k_{ } = 0$.	97
9.1	Real space polariton emission versus excitation power, T=5.4K.	99
9.2	Spatial selection of the emitting area within the excitation spot.	101
9.3	Spectrally and spatially resolved polariton condensate emission.	102
9.4	Spectrally resolved near-field image of the polariton emission in the weak excitation regime.	102
9.5	Number of localized spot as a function of the detuning.	103
9.6	Effect of the photonic disorder on the lower polariton branch as a function of detuning.	104
10.1	Linear polarization degree of the polariton ground state as a function of the pump power.	106
10.2	Linear polarization buildup, $\delta = +5$ meV.	107
10.3	Linear polarization buildup, $\delta = 0$ meV.	108
10.4	Polarization properties of the polariton emission, $\delta = 0$ meV.	109
10.5	Real space polarization properties, $\delta = 0$ meV.	109
10.6	Polarization splitting.	111
11.1	The first order temporal coherence.	114
11.2	Spatial correlation measurements by analyzing the interference pattern produced by overlapping the images from both arms of the interferometer.	115
11.3	Spatial correlations measured between two points separated by $8 \mu m$.	115
11.4	The principle of spatial correlation mapping.	116
11.5	Mapping of the contrast of the spatial correlations.	117
11.6	Mapping of time-resolved spatial correlations.	118
11.7	$g^2(\tau)$ function for thermal and coherent light.	120
11.8	The correlation signal measured on the Ti:Sapphire laser.	121
11.9	$g^2(\tau)$ for the CW-Ti:Sapphire laser light.	122
11.10	Polariton transition from thermal towards coherent state in $g^2(\tau)$ experiment.	123
11.11	The reduction of the thermal fluctuations in polariton transition towards condensed state.	123
11.12	The reduction of the photon noise with increasing number of coincidences.	124
11.13	Dynamic polariton condensation.	124
11.14	The correlation peaks in pulsed experiments.	126
11.15	The correction of the "pile-up" effect and $g^2(\tau)$ for the laser in the pulsed experiment.	127
11.16	$g^2(\tau)$ for the polariton emission in the pulsed experiment.	127
11.17	Non-corrected $g^2(\tau)$ and linewidths as a function of the power.	128
11.18	Fine structure of the zero delay correlation peak below threshold.	129
11.19	The acceleration of the polariton dynamics.	129

11.20	The narrowing of the correlation peaks.	130
11.21	The comparison of the unnormalized $g^2(\tau = 0)(P/P_{thr})$ obtained in this work and in [Den02].	131
A.1	Strong versus weak coupling regime in microcavities.	140
A.2	The line broadening and the blueshift as a function of detuning.	141
A.3	The asymmetric line broadening above the condensation threshold.	141

List of Tables

1.1	The difference between the statistics of classical, distinguishable particles and bosons.	2
1.2	The differences between atom and exciton as concerns the BEC.	12
2.1	Distinction between emission in a weak and strong coupling regimes.	17
2.2	The difference between atom and polariton considering BEC.	23
6.1	The impact of the dimensionality, interactions and size on the possibilities of the phase transitions.	78
11.1	Statistical properties of thermal and coherent light.	120
11.2	The corrected $g^2(\tau)$ values in the pulsed experiment.	130
A.1	The differences between "polariton lasing" and photon lasing - summary.	140

Chapter 1

Introduction

In this introductory part the origin of Bose-Einstein Condensation (BEC) is explained. First, we show how bosonic attraction and the Bose-Einstein distribution arise from the indistinguishability principle. The modern definition of the BEC is given. Next, we briefly recall the famous realization of the BEC in cold atom vapors. Finally, we place the BEC in the broader context of spontaneous coherence. In the next section the excitonic molecule is introduced in the context of the search for a BEC in the solid state. In order to obtain the BEC in a solid, at the very beginning one has to be sure that the particle that is under consideration can be treated as a boson. The limits of the bosonic approximation for the exciton are discussed. The systems in which the BEC is being searched for are briefly presented.

Contents

1.1	Origin of the BEC	1
1.2	Realization of a BEC in cold atom vapors	6
1.3	Related phenomena	8
1.4	Towards condensation in solids	9
1.4.1	The exciton as a boson	9
1.4.2	Systems studied	12

1.1 Origin of the BEC

Consequences of the indistinguishability principle We are used to the length scales given by the classical world. This loads us with habits and reasoning that we take for granted. We believe that we can distinguish between objects by naming them, for instance by giving them different numbers. Yet, intuitions inherited from the macroscopic world may be misleading as soon as we enter the microscopic world, where the length scales are comparable to the size of the wave functions describing

particles. The fundamental postulate of quantum mechanics is the indistinguishability principle: we are not able to detect any feature distinguishing quantum objects of the same species, like electrons with the same spin.

This has deep consequences and leads to the fundamental division of the quantum particles into two kinds:

- **bosons** described by a symmetric wave function and possessing integer spin
- **fermions** described by an antisymmetric wave function and having half-integer spin

These two types of particles show radically different statistical behavior. On the one hand the antisymmetric properties of fermions (destructive quantum interference), gives rise to the Pauli exclusion principle, while on the other hand the bosonic symmetry (constructive quantum interference) is the origin of the bosonic attraction, of stimulation phenomena and finally of Bose-Einstein condensation.

The tendency of bosons to cluster into the same state is revealed already by the following, trivial example. Let us consider two particles that can be disposed between two states. We can ask what is the probability (P) of obtaining double occupancy of a state? In the case of classical particles the answer is 50%, whereas in the case of bosons this probability is higher and is equal to 66% (see table 1.1). In the case of three particles and three states the probability to get triple occupancy of the state is already 2.7 times higher for bosons compared to classical particles. It should be pointed that this bosonic agglomeration is uniquely due to symmetry properties and does not require interactions.

N°	Classical particles		Bosons
1	1	2	
2	2	1	• •
3	12		••
4		12	••
P	50%		66%

Table 1.1: *The difference between the statistics of classical, distinguishable particles and bosons. The agglomeration of bosons into the single state is seen already for the system of two particles. The probability of observing double occupancy of the boson state is 1.32 times bigger compared to classical particles.*

The symmetry leads also to the bosonic commutation rules:

$$[b_j, b_k^\dagger] = \delta_{jk} \quad [b_j, b_k] = 0 \quad (1.1)$$

Starting from these equations it can be shown easily that the scattering rate towards a bosonic state is enhanced by the presence of other bosons in that state. Namely, if the occupancy is of order N , the scattering rate is proportional to $(N+1)$ [Mie98]. Thus we deal with an avalanche like process: the higher the occupancy of the state,

the faster its occupancy increases¹. This phenomenon, known as the **bosonic final state stimulation**, can be considered as the origin and basis of the BEC.

Bose-Einstein distribution and condensation as a solution for the divergence The ideal Bose gas is usually treated in the frame of the grand canonical ensemble [Pit03, Coh03]. This classical calculation leads to the Bose-Einstein distribution (see figure 1.1): a distribution of the gas particles among the accessible states N_l depending on the temperature and density.

$$n_l = \frac{1}{\exp\left(\frac{E_l - \mu}{k_B T}\right) - 1} \quad (1.2)$$

T is the temperature and μ is the chemical potential, which is fixed by the total number of particles in the system $N = \sum_l n_l$. Let us assume an energy of the ground state $E_0 = 0$. Thus μ has negative values and is an increasing function of the density. The striking feature of distribution (1.2) is its divergence as soon as $\mu \rightarrow 0$: The ground state occupancy $n_0 \simeq \frac{k_B T}{E_0 - \mu}$ becomes large without limit. At the same time, (in the three dimensional case) the number of particles that can be acquired into the excited states is limited even if $\mu = 0$ (thermodynamic limit). Two situations are possible. If N is smaller than the critical density defined as $N_{cr} = N_{E \neq 0}(T, \mu = 0)$ (where $N_{E \neq 0}$ stands for total number of particles in the excited states), the ground state occupancy is of the same order as excited states. On the other hand, as soon as $N > N_{cr}$ the decision has to be made where to put the additional $N - N_{cr}$ bosons? Inspired by the work of Bose [Bos24], Einstein proposed the solution in [Ein25]². Taking into account saturation of the excited states, additional particles start to massively occupy the ground state i.e. the number of the particles in the ground state becomes comparable with the total number of particles in the system, or equivalently a non-negligible condensate fraction n_0/N appears. **This saturation of the excited states and macroscopic occupation of the ground state is the phase transition called the Bose-Einstein condensation.**

Even though the BEC is a purely statistical phenomenon and does not require interactions, it is difficult to argue in the above picture why condensation should occur into the single quantum state, and not, for instance, into several nearly degenerate states around the ground state? As was pointed out by P. Nozières (p.15 in [Gri95]), only by introducing interactions and by considering the energetic cost of exchange terms for an interacting Bose gas one can understand why occupation of the single state is favored.

Another way of deriving the BEC is to compare the average distance between particles and their thermal de Broglie wavelength $\lambda_{dB} = \sqrt{\frac{2\pi\hbar^2}{mk_B T}}$. In the diluted

¹Introducing interactions may change this picture.

²It is interesting to note that the BEC was predicted before division of the particles into fermions and bosons was cleared up (1927). Bose's work was based on photons. It was Einstein who applied Bose's idea for massive particles, justifying it by saying that if particles were waves, they should obey the same statistics as photons. This was the first time that anyone referred to de Broglie's idea of matter waves [Gri99].

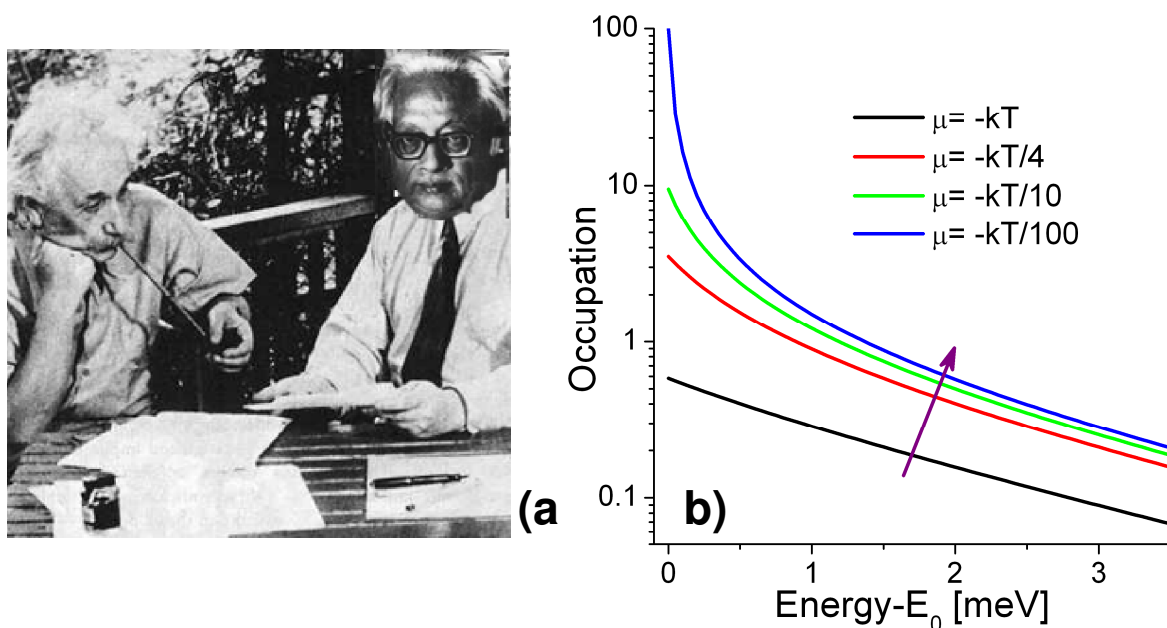


Figure 1.1: (a): *A. Einstein and S. N. Bose: the fathers of the concept of bosonic condensation.* b): *Bose-Einstein distribution for constant temperature and increasing particle density: saturation of the excited states and agglomeration in the ground state are clearly visible.*

limit, i.e. when the average distance between particles d is much larger than λ_{dB} , the particle gas can be treated classically (see figure 1.2). But with increasing phase space density³, the quantum degeneracy situation is finally reached when $d \sim \lambda_{dB}$. At this point the gas becomes degenerate and the quantum Bose-Einstein distribution should be used, opening the possibility of a BEC. In particular, one can see that **the lower the mass and the temperature, the faster a quantum degeneracy is revealed with increasing particle density.**

The language of phase transitions is usually applied in the thermodynamic limit and hence for infinite systems. One can ask about the possibility and criterion for a BEC in a finite size and/or interacting system. It can be shown that massive occupation of the ground state can occur in a finite (trapped) 3D system. However the more precise condition for condensation is given by the "modern" definition of the BEC [Pit03, Leg01], discussed in the next paragraph.

Macroscopic phase coherence and order parameter The crucial point in the "modern" concept of the BEC is the spontaneous appearance of **long range phase coherence in the condensed state** [Pit03]. The coherence between particles separated by $s = |\mathbf{r}_1 - \mathbf{r}_2|$ is described by the density matrix:

$$n(\mathbf{r}_1, \mathbf{r}_2) = \langle \psi(\mathbf{r}_1)^\dagger \psi(\mathbf{r}_2) \rangle \quad (1.3)$$

³i.e. the number of particles contained within the volume λ_{dB}^3 [Pet02]

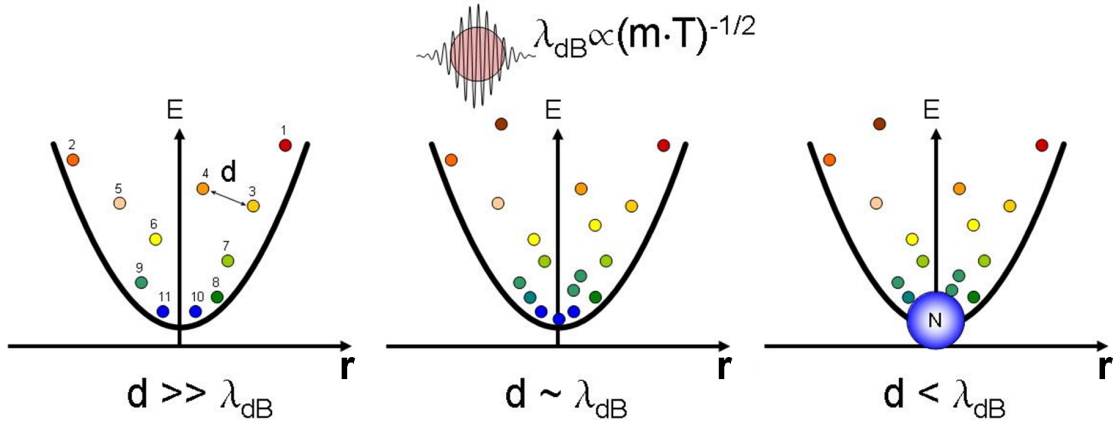


Figure 1.2: *The BEC in the trapped 3D system. In the dilute limit, particles are distinguishable and the classical Boltzmann distribution could be used to describe the system. With increasing phase space density, λ_{dB} becomes comparable with the interparticle separation d . Quantum degeneracy is reached when, for bosons, the Bose-Einstein distribution should be used to describe the particle gas. With further increase of phase space density, a BEC occurs: "one part condenses, the rest remains a saturated thermal cloud".*

, where $\psi(\mathbf{r})$ is the field operator associated with the particle.

The important property of the density matrix is its connection with the momentum distribution of the particle density through the Fourier transform [Pit03]. It appears that, in the normal state, the density matrix has significant values only for $s < \lambda_{dB}$, whereas for $s \gg \lambda_{dB}$ it goes smoothly to zero. This shows that quantum correlations are limited by the thermal de Broglie wavelength.

In the condensed state the situation is different. Now the momentum distribution has a δ -like term in the ground state corresponding to the presence of the condensate, and consequently the density matrix (1.3) has a nonvanishing value in the limit $s \rightarrow \infty$. This property, named **off-diagonal long range order**, is nowadays considered as the most important token of a BEC.

Thus, practically, the long range coherence means that there exists a phase relation between points separated by distances much larger than λ_{dB} . The amount of correlation for $s \gg \lambda_{dB}$ appears at the condensation threshold and increases with condensate fraction (see figure 1.4). Experimentally studied systems are always finite, thus a formal check (measurement of correlations for $s \rightarrow \infty$) of this criterion is not possible. A more adequate question is whether phase coherence is spread over the entire size of the system or does it disappear at the smaller length scales? So macroscopic phase coherence can be experimentally confirmed by measuring a high spatial correlation over distances much larger than λ_{dB} and comparable with the sample size.

A more detailed discussion of the signatures of the BEC in "real life" systems is given in chapter 6.4.

In the Bogoliubov approximation, the condensate can be treated as a classical

object [Dal99, Leg01, Pit03], characterized by a single macroscopic wave function that can be written in the following way:

$$\Psi(r) = \sqrt{n_0}|\psi(r)| \cdot e^{i\phi(r)} \quad (1.4)$$

Here, n_0 is the number of condensed particles, $\psi(r)$ is the single particle wave function of the ground state and $\phi(r)$ is the phase characterizing coherence and superfluid phenomena [Pit03]. This macroscopic wave function of the condensate $\Psi(r)$ can be considered as an order parameter for the BEC: a macroscopic quantity that emerges at the transition point. Making an explicit choice of the phase of the order parameter formally corresponds to the symmetry breaking in the system: in fact, any physical properties stays unchanged when varying the phase. The concept of an order parameter is an important issue in the theory of phase transitions, characterizing a given transition. For instance, in the paramagnetic-ferromagnetic transition the order parameter is the macroscopic, spontaneous magnetization developed at the transition point.

1.2 Realization of a BEC in cold atom vapors

The Bose condensation was considered for a long time as some unrealistic peculiarity of the Bose gas. For many years the only example of a Bose condensed system was superfluid helium He_4 . However, due to strong interactions in He_4 the condensate features are masked: for instance the condensate fraction does not exceed 10%. The first unambiguous proof for a BEC in a weakly interacting system came from atomic physics in 1995 [And95]. This achievement was honored by the Nobel prize in 2001 [Ket02, Cor02]⁴.

Why alkalis? At first sight, atomic condensation seems to be an easy task: take the dense atomic cloud and lower its temperature until the degeneracy condition is reached. The problem is that usually a transition into the solid state would appear well before a BEC could take place. Thus, in order to achieve an atomic BEC, one is forced to work with an extremely diluted sample ($n \simeq 10^8 \text{cm}^{-3}$), where three body collisions leading to the formation of molecules are not active. This, combined with the atom's mass ($10^4 m_e$), leads to extremely low critical temperatures of order $T_c \simeq 10^{-6} - 10^{-7} \text{K}$. The ability to obtain such impressively low temperatures was a key to success in atomic physics. **In particular the last step towards a BEC: evaporative cooling, works particularly well for the alkali atoms** [Ket02, Cor02]. Moreover, the optical detection techniques for those atoms are relatively simple, since atomic transitions occur in the visible wavelengths.

⁴W. Ketterle, Eric A. Cornell, Carl E. Wieman: Nobel Prize in Physics 2001 "for the achievement of Bose-Einstein condensation in dilute gases of alkali atoms, and for early fundamental studies of the properties of the condensates"

Trapping and cooling The most important condition in the quest for sub-microkelvin temperatures is total isolation from the outside world. This is achieved by spatial trapping of the gas in a magneto-optical trap. In the first step temperatures of order $10\mu K$ are attained by laser cooling. In the decisive step of evaporative cooling the most energetic atoms are thrown away from the trap, and hence the temperature of the remaining gas falls below the critical temperature. Thus atomic condensation is reached, because in the last step of the experiment the temperature is lowered faster than the atoms' density, resulting in an increase of the phase space density. More experimental details about these techniques can be found in [Pet02].

Transition characteristics One of the first images of the atomic condensation is presented in figure 1.3. Above the critical temperature, atoms are thermally distributed within the trap. As the critical temperature is reached, a sharp peak of atomic density emerges in the middle of the trap illustrating the formation of the condensate in the ground state. With further decrease of the temperature almost all particles are transferred into the condensate.

The typical lifetime of the atomic condensate is of order 10 s, giving the possibility to establish internal thermal equilibrium. Furthermore, interactions are very weak in diluted gaseous samples. Thus, in atomic condensation, the case of an ideal Bose gas can be approached.

It should be emphasized that the first claim for atomic condensation was solely based on the macroscopic occupation argument.

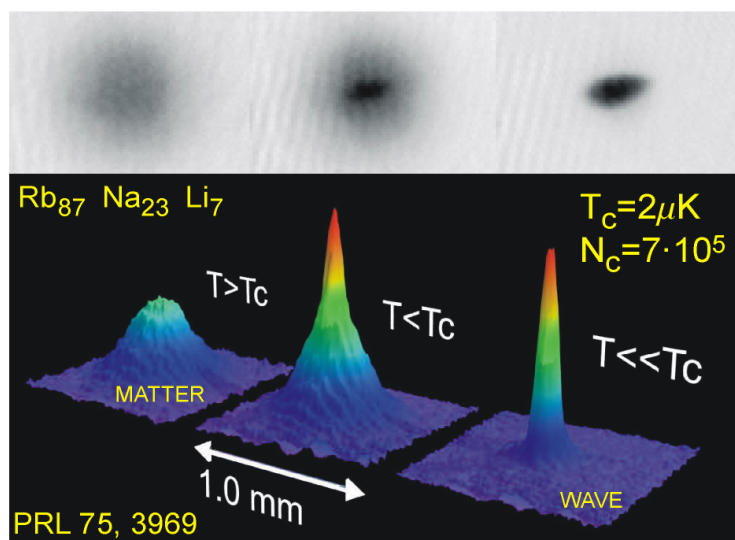


Figure 1.3: *One of the first images of atomic condensation. Above a critical temperature atoms are thermally distributed within the trap. At the critical temperature a sharp peak of atomic density in the center of the trap emerges, corresponding to formation of the condensate in the ground state. Far below the critical temperature, almost all atoms fall into the condensed state.*

Long range coherence It took more than one and half years to provide the ultimate proof for atomic condensation. Long range phase coherence was demonstrated in [Andr97]. The coherence properties were proven by observation of the interference fringes produced by two expanding condensates. Another beautiful result showing the onset of the spatial coherence over the entire cloud at the condensation threshold was published in [Blo00].

The second order spatial coherence of the atom laser was also confirmed recently [Sch05, Ott05].

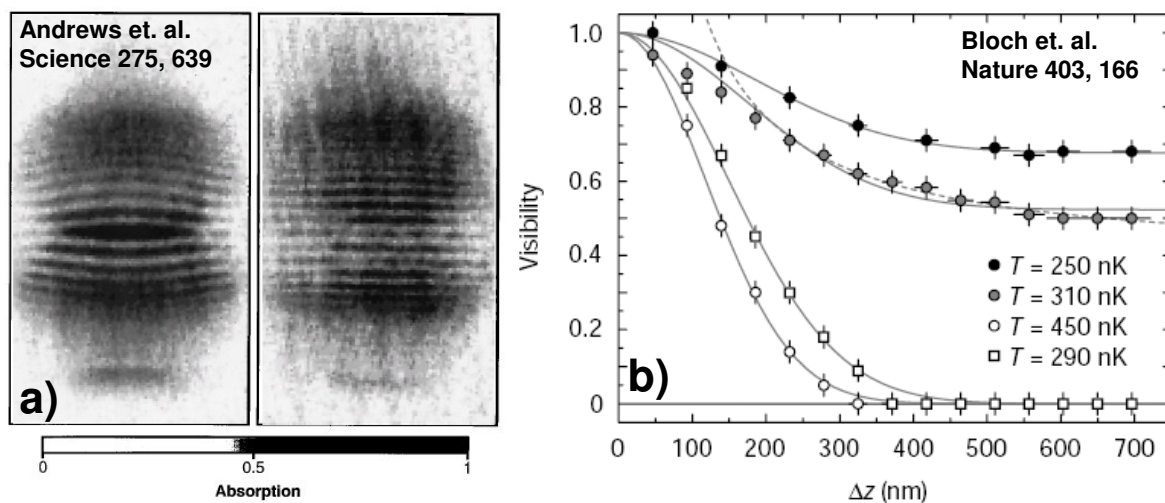


Figure 1.4: *Spatial coherence of the atomic condensates: a) After [Andr97]: interference pattern produced by two expanding condensates, b) After [Blo00]: Spatial coherence of the trapped Bose gas as a function of the slit separation for temperatures above T_{cr} (open symbols, for $T=290\text{nK}$ the density was decreased below the transition point) and below T_{cr} (full symbols). Above T_{cr} coherence disappears beyond the thermal length. Below T_{cr} strong spatial coherence is measured for the entire condensed cloud providing evidence for long range order.*

1.3 Related phenomena

Thanks to the very extensive theoretical studies in condensed matter physics it has been established that **the concept of spontaneous coherence unifies phenomena like the BEC, superfluidity, superconductivity and lasing**. For example, the BEC implies spontaneous coherence. Excellent review articles pointing out the connections and the differences between these phenomena are available in [Gri95, Noz03].

1.4 Towards condensation in solids

1.4.1 The exciton as a boson

A gas in a solid? Since the first proposals of Blatt [Bla62] and Moskalenko [Mos62] the BEC also has been searched for in solid state systems⁵. But, a gas in a solid...? How this can be possible? It turns out that the periodic potential produced by the crystal lattice introduces remarkable properties for the particles existing within it. The Bloch theory [Zim72] shows that a free carrier moving in the periodic potential can be described by the wave function:

$$\psi(\mathbf{r}, t) = u_{\mathbf{k}}(\mathbf{r}) \cdot e^{i(\mathbf{k}\mathbf{r} - \omega t)} \quad (1.5)$$

Thus the electron is moving through the lattice as a plane wave modulated by the periodic function $u_{\mathbf{k}}(\mathbf{r})$ whose period coincides with the lattice structure. The fact that its wave vector is conserved with time means that the electron moves through the dense medium without any scattering, nearly like in empty space. Thus the carriers in a crystal form a quantum gas which, in an ideal case, can be completely detached from the lattice.

Of course, any perturbation of the periodicity destroys this picture and carriers can be scattered, for instance, due to interactions with phonons.

The excitonic particle The periodicity of the crystal leads to formation of the band structure. It may happen that the top of the highest fully occupied band (valence band) and the bottom of the lowest empty band (conduction band) are separated by an energy gap. This is the case of a semiconductor⁶. Thanks to photon absorption (or thermal activation), an electron can be promoted from the valence band into the conduction band. The collective behavior of the remaining valence band electrons is described by the positively charged quasi-particle called a hole.

Since electron and hole are counter charged particles, they can form a bound state akin to positronium named an **exciton**. The energy of the exciton is:

$$E_X = E_{gap} + \frac{\hbar^2 K^2}{2M} + E_Q + E_{XB}(N) \quad (1.6)$$

where E_{gap} is the band gap, $M = m_e^* + m_h^*$ is the exciton mass, K is the exciton momentum, E_Q is the confinement energy relevant in lower dimensional structures. The exciton binding energy $E_{XB}(N)$ is given by the well known solutions of the particle with reduced mass $\mu = \frac{m_e^* m_h^*}{m_e^* + m_h^*}$ in the Coulomb potential:

$$E_{XB}(N) = -\frac{Ry^*}{N^2} \quad N = 1, 2, 3... \quad (1.7)$$

⁵For other early works devoted to the issue of Bose condensation in the solid state see [Kel67, Ger68, Gerg68].

⁶This is also the case of insulators. The difference between semiconductors and insulators is that in the former case there exists the possibility of introducing free carriers into the bands by doping.

where N is the principal quantum number ($N=1$ corresponds to the exciton's ground state, whereas $N=2,3..$ describe the exciton's excited states), $Ry^* = 13.6eV \cdot \frac{\mu}{\varepsilon^2 m_0} \approx 10meV$, because usually $\varepsilon \approx 10$ (dielectric constant) and $\mu \approx 0.1m_0$. This means that the ground state energy of the exciton is only a fraction of a percent of the band gap, which is of order several eV. Its Bohr radius is $a_B = 0.5\text{\AA} \cdot \varepsilon \cdot \frac{m_0}{\mu} \approx 50\text{\AA}$, and thus the exciton is spread over many lattice constants (Mott-Wannier exciton). This justifies the use of the dielectric constant. Equation (1.7) shows that the spectrum just below the absorption edge of a semiconductor is characterized by a hydrogen-like series [Din74].

The important characteristic of an exciton is its oscillator strength f_S , describing the capacity of the medium to couple with the photon field. It is proportional to the matrix element of the transition in the dipole approximation and the spatial overlap of the electron and hole wave functions. In particular, in the case of a quantum well, $f_S \propto a_B^{-2}$.

For a good introduction to the physics of excitons in semiconductor heterostructures the reader is referred to [Bas98]. Useful discussions of excitonic properties seen through the prism of microcavity polaritons can also be found in [Sav96, Boe00, Mul00, Sen01, Mox04, Per06, Kav03].

The exciton as a boson - main difficulties Even though the exciton consists of two fermions, it can be considered as a **composite boson** in the diluted limit. In this paragraph we wish to discuss the validity of this approximation.

The major advantage of the exciton in the context of the BEC is its low mass, four orders of magnitude smaller than atomic masses. This should favor bosonic degeneracy at temperatures accessible by cryogenic means. On the other hand, due to its small binding energy and large size, the exciton's bosonic nature is much more fragile than the atom's, and no longer holds at high density of its fermionic components. With increasing density of the electrons and holes the fermionic phase space starts to be significantly occupied. The Pauli exclusion principle intervenes:

- Excitons cannot be created, because the electron and hole states, out of which the exciton is constructed, are being filled - this is the **phase space filling** effect [Sch85, Sch89, Sen01].
- Carriers with the same spin avoid each other and hence acquire the **exchange** energy [Sch85].

Formally, the degradation of the bosonic character of excitons by phase space filling and exchange effects can be seen by calculating the excitonic commutator in the basis of electrons and holes. This leads to the relation:

$$[b_{\mathbf{K}}, b_{\mathbf{K}}^\dagger] \simeq 1 - O(n \cdot a_B^2) \quad (1.8)$$

Therefore, excitons can be considered as composite bosons as long as:

$$n \cdot a_B^2 \ll 1 \quad (1.9)$$

The limiting effective density, above which excitons no longer can be considered as bosons is called the **saturation density** and, according to [Sch85], can be expressed as:

$$n_{sat} = \frac{0.117}{\pi \cdot a_B^2} \quad (1.10)$$

This shows that excitons are more robust in the large gap materials where the exciton Bohr radius is small. In particular, CdTe QWs are more advantageous for studies of high occupancy effects than GaAs QWs: $n_{sat}^{CdTe} \simeq 5 \times 10^{11} \text{cm}^{-2}$ ⁷, whereas $n_{sat}^{GaAs} \simeq 5 \times 10^{10} \text{cm}^{-2}$.

Phase space filling and exchange decrease exciton binding energy (and increase Bohr radius), which can be effectively described by the density dependent effective dielectric constant [Dam90]:

$$\varepsilon(n) = \frac{\varepsilon(0)}{1 - \frac{n}{2n_{sat}}} \implies E_{XB}(N) = E_{XB}(0) \left(1 - \frac{n}{2n_{sat}}\right)^2 \quad (1.11)$$

Screening is another mechanism influencing the exciton binding energy as the density is increased. It appears due to weakening of the electron-hole attraction in the presence of the other carriers. It is estimated that in 2D, which will be the case of this work, screening is a less important density effect than phase space filling and exchange [Sch85].

It can be concluded that with increasing density the exciton breaks down: its bosonic character diminishes as well as its oscillator strength. **Bleaching** of the excitonic transition occurs.

Excitons interact not only through their fermionic components but also can collide with each other. This **exciton-exciton** interaction is of a vital importance for polariton condensation. Of course excitons also interact with the lattice resulting in **exciton-phonon** scattering. They can also be localized by **disorder** present in every heterostructure.

The above remarks already demonstrate that an exciton gas is very far from an ideal Bose gas: excitons experience various interactions. Moreover, these interactions play a crucial role at the high densities needed for BEC.

The difficulty of obtaining an exciton BEC is illustrated in table 1.2 where the exciton's parameters are compared with the atom's. One can see that in spite of the light exciton mass, at cryogenic temperatures the degeneracy requires a density approaching n_{sat} , where the bosonic approximation is no longer valid.

Finally, excitons are not stable particles and convert into photons in their radiative lifetime, which is usually of order 10^{-9}s . This raises the question of whether, during their lifetime, excitons can relax toward the ground state and accumulate there forming a condensate. Similarly, one can ask whether relaxation processes are fast enough to establish thermalization and hence approach the thermodynamical aspect of the BEC. Thus, excitonic systems studied through optical methods are

⁷The upper boundary of the $n_{sat}^{CdTe} = 6.7 \times 10^{11} \text{cm}^{-2}$ is given in [Por02], whereas the lower one, $n_{sat}^{CdTe} = 2.5 \times 10^{11} \text{cm}^{-2}$, will be estimated in chapter 5.1.

always **open systems**: excitons are continuously created by optical pumping and then recombine, emitting photons. So researchers looking for an exciton BEC must inevitably be confronted with these non-equilibrium effects.

At this point we wish to remark that modern understanding of the BEC requires neither thermal equilibrium, nor even a steady state in the system [Leg01]. We also believe that, if we are looking for thermalization it doesn't have to be equilibration with the host lattice, but rather equilibration of condensing particles. This is exactly what happens in an atomic BEC, which is entirely detached from the environment. We can go even further and claim that one should rather decouple excitons from the lattice and hence prevent decoherence induced by the exciton-phonon interaction. Spontaneous coherence is much more important than thermal equilibrium.

Parameter	Atom	Exciton
$m [m_e]$	10^4	1
$T [K]$	10^{-6}	4
$\lambda_{dB} [\mu m]$	0.7	0.037
$n_{cr} [cm^{-2}]$	$2 \cdot 10^8$	$7 \cdot 10^{10}$
Life Time	"long" s	"short" $10^{-9} - 10^{-6} s$

Table 1.2: *The difference between atom and exciton considering the BEC. The exciton mass, being around four orders of magnitude smaller than the atom mass, favors condensation of excitons at higher temperatures. We can estimate (2D) critical densities for a BEC as $n_{cr} \simeq \lambda_{dB}^{-2}$. Thus at standard cryogenic temperatures the density required to obtain exciton condensation is very high, close to the limit where the bosonic approximation for excitons is questionable. Moreover, the exciton is unstable and is characterized by a very short radiative lifetime, making efficient filling of the ground state and thermalization difficult.*

1.4.2 Systems studied

After the proposals of Moskaleiko and Blatt the search for an excitonic BEC was concentrated at the beginning on excitons with long lifetimes. Good candidates seemed to be indirect bulk **excitons in Si and Ge** [Ger68, Gerg68, Sno02]. However, it was quickly established that, due to the small exciton binding energy in these materials, fermionic electron-hole droplets appear before a BEC could take place.

The situation is much better in **Cu₂O**. Here excitons have very special properties. In this material with a direct gap, the dipole excitonic transition is highly forbidden due the conduction and valence band having the same parity, which results in an extremely long exciton lifetime reaching 10^{-6} s and hence favors thermalization with the lattice. Moreover, the high exciton binding energy of 153 meV implies stable excitons that can be safely considered as a diluted gas at densities much higher than the one required for a BEC at cryogenic temperature. Symmetry leads also to the ground state splitting into paraexciton (singlet state) and, situated 12 meV

above it, orthoexciton (triplet state). Because luminescence of the orthoexciton is weakly allowed, it is this state that can be explored by optical experiments. But interestingly, up till now all attempts to increase the excitonic phase space density led to the onset of a very efficient non-radiative recombination channel for excitons. In this Auger process, excitons collide and one of them annihilates, yet its energy is not released as a photon but is transferred to the second exciton ionizing it. Thus, due to this process, not only the density diminishes but also the exciton gas heats up, preventing condensation. The BEC in cuprous oxide has been widely discussed in the literature. For a review see Wolfe in [Gri95] and references therein. Experimental work is still in progress with new promising results⁸.

More recently, very serious candidates for a BEC in excitonic systems are **indirect excitons in coupled quantum wells**. An indirect exciton is a bound state of an electron in one quantum well and a hole in the other. Reduced overlap of the carrier wave functions enhances the exciton lifetime up to hundreds of ns. Furthermore, spatial separation prevents agglomeration into a fermionic electron-hole liquid. Indeed, very strong luminescence, localized in real space has been observed recently. The critical behaviour of such photoluminescence was demonstrated revealing the degeneracy of the exciton gas in this system [But01, Bu02, Buto02, Snoise02]. Nevertheless, the statistics of the excitons trapped in the in-plane potential is still under discussion. Neither is clearly established in this system that defining characteristics of BEC, i.e. long range, spatial coherence are present.

Very recently a BEC was claimed in a **bilayer electron system** [Eis04] by performing transport measurements under high magnetic field and mK temperatures. A filling factor 1/2 is obtained in both electron layers. This is accompanied by the collapse of the Hall voltage, which proves that, effectively, inter layer excitons are created. These excitons have a unique feature: they do not recombine into photons and hence are in thermal equilibrium. A critical enhancement of tunneling rate between the layers with temperature and magnetic field was observed [Spi00] and interpreted as a sign of a long range coherence.

An interesting observation of linear and gapless excitation spectra (Goldstone mode) in a **magnetic insulator** was also tentatively attributed to a BEC [Rue03].

Finally there are exciton polaritons, on which our own efforts were focalized with the aim of demonstrating condensation in the solid state. The results presented in this work demonstrate that condensation of exciton polaritons is achieved.

Conclusions In this chapter the origin of the BEC was discussed. We have shown how this phenomenon inevitably emerges from the symmetry properties of bosons. Two "smoking guns" of condensation were pointed out:

- Massive occupation of the single particle state
- Spontaneous phase coherence across the entire condensate

⁸prof. M. Bayer - private communication

The demonstration of the BEC in a diluted atomic gases was recalled. It was mentioned that the concept of the spontaneous phase coherence unifies phenomena like: the BEC, superfluidity, superconductivity and lasing.

Next, the exciton was presented as a natural candidate for achievement of a BEC in solid state. In spite of many years of research, excitonic BEC has not been fully accepted in the scientific community. The advantages and difficulties of the exciton as concerns the BEC were discussed. The systems, where excitonic BEC are being searched for were briefly presented.

Chapter 2

Why polariton condensation?

Why, from all the candidates described above, have we chosen exciton polaritons to achieve condensation in solids? The discussion of this issue is given in the present chapter. The origin of polaritons is a strong exciton-photon coupling regime. Thus we start this part by pointing out conditions for strong light-matter coupling. This situation is particularly favored by inserting an active medium (atoms, excitons) inside a cavity. If the finesse of the resonator is sufficiently high and the active medium has a significant oscillator strength, Rabi oscillations between exciton and photon modes can occur. New, mixed exciton-photon states arise named exciton polaritons. As they are a superposition of bosonic particles, they can be considered as composite bosons in the same limits as excitons. The experimental signature of strong coupling is observation of the energy splitting and anticrossing of coupled states. This situation has a particular impact on the dispersion branches of the polariton states: in a very narrow range of wave vectors (up to around $2 \times 10^5 \text{ cm}^{-1}$), in the center of reciprocal space, a characteristic potential minimum is formed that will be used to realize polariton condensation. Polaritons in the neighborhood of this potential minimum carry a special bonus: Owing to the extremely steep dispersion in this zone, they are characterized by an effective mass 4-5 orders of magnitude smaller than the exciton's mass. Hence, in theory, degeneracy conditions can be achieved at high temperatures ($T \sim 20\text{K}$) in a diluted limit ($n \sim 5 \times 10^8 \text{ cm}^{-2}$). Moreover, thanks to this steep dispersion and conservation of the in-plane wave vector, one can monitor the polariton distribution in momentum space by performing angle resolved experiments. Furthermore, a strong coupling regime guarantees that the energy, polarization and coherence properties of the outgoing photons are the same as those of polaritons. Thus, we see that strong coupling introduces several major advantages for polariton BEC. They can however be obscured by another feature of the same origin. Due to the strong coupling, the photonic component imprints on the polariton its very short lifetime of around several ps, making it very difficult to get efficient populating of the polariton ground state and thermalization within the trap. Fortunately, under high excitation conditions exciton-polariton scattering is fast enough to bring polaritons into their ground state at rate at least as high as the radiative lifetime, enabling phenomena like thermalization, stimulated scattering and finally condensation.

Contents

2.1 From exciton to microcavity polariton	16
2.1.1 Weak versus strong exciton-photon coupling	16
2.1.2 Cavity effect: Purcell effect or Rabi oscillations?	17
2.2 Polariton dispersion: the key for condensation	21
2.2.1 Polariton trap in momentum space	21
2.2.2 Momentum space mapping	23
2.2.3 Peculiar polariton relaxation	25

2.1 From exciton to microcavity polariton

2.1.1 Weak versus strong exciton-photon coupling

The excited medium (atom, exciton) can relax towards its lower energy states through emission of a photon. In general, emission of light can occur in two distinct regimes, depending on the nature of coupling between the active medium and the electromagnetic field. The first one is the **weak coupling** (known also as perturbative) regime. In this situation, a photon emitted into the given mode has a negligible probability of being reabsorbed by the medium. Thus the excitation of the medium is dissipated. This regime is usually observed when the transition occurs into the continuum of photon states. Here the emission is governed by the Fermi golden rule (see eq. 2.1), resulting in exponential time decay of the population of the excited state.

A qualitatively different behavior is seen in the **strong coupling** (also called non-perturbative) regime, when the photon emitted into a given mode can be recaptured and reexcite the medium. In this regime excitation is coherently shifting back and forth between the medium and the mode of the electromagnetic field. However, these **Rabi oscillations** are damped by the decoherence present in the system. Energy is dissipated within a time comparable with the coherence time of the uncoupled states. In the spectral domain, Rabi oscillations are revealed by an energy splitting Ω (called Rabi splitting or normal mode splitting) and the anticrossing behavior of the coupled states.

The regime of strong coupling is more difficult to achieve, since it requires a high probability of photon reabsorption by the medium: the Rabi frequency has to overwhelm damping rates. In particular, it is facilitated when the optical transition is resonantly coupled with a well isolated photon mode. For this reason strong coupling is favored as soon as an active medium is inserted inside a cavity. The examples of the systems that can operate in the strong and weak coupling regimes are presented in table 2.1.

For formal introduction into the issue of light-matter coupling the reader is referred to [Coh88, Coh96, Man95].

Coupling	Emission	Examples
Weak	irreversible $P \sim e^{-\Gamma t}$	free atom free quantum dot free QW exciton
Strong	reversible $P \sim \cos^2\left(\frac{\Omega t}{2\hbar}\right)$	exciton polaritons quantum dot in a cavity atom in a cavity

Table 2.1: *Distinction between emission in the weak and strong coupling regimes. In the weak coupling regime emission is irreversible. The optical transition is coupled to the continuum of photon modes. The excitation (P) is dissipated with the characteristic rate Γ , given by the Fermi golden rule (see eq. 2.1). In the strong coupling regime, the optical transition is close to resonance with the specified photon mode. Excitation oscillates between optical mode and matter excitation giving rise to the normal mode splitting. In practice these oscillations are damped by the decoherence.*

2.1.2 Cavity effect: Purcell effect or Rabi oscillations?

An emitter existing in a free space (usually modeled as a two level system) decays spontaneously by interaction with the vacuum at a rate proportional to the density of modes at the transition energy $\rho(E_{ph})$. The spontaneous emission rate Γ is governed by the Fermi golden rule:

$$\Gamma = \frac{2\pi}{\hbar} |\langle \phi_0 | W | \phi_1 \rangle|^2 \rho(E_{ph}) \quad (2.1)$$

The density of modes of the radiation field is modified inside a cavity. Also, confined photon modes are characterized by large spatial variations of their amplitude \mathbf{A} that, combined with the dipole transition operator \mathbf{p} defines the dipole matrix element $W \propto \mathbf{p} \cdot \mathbf{A}$. Therefore the emission rate Γ of the emitter placed inside a cavity can be modified, yielding the **Purcell effect** [Pur46]: by a proper manipulation of the cavity design the emission rate can be enhanced [Goy83, Ger01] or suppressed [Gab85, Har89].

In 1983 researchers were on the edge of the "strong-coupling era". In [Goy83] we can read:

"With a tenfold increase of Q [...] an emitted photon would be stored in the cavity long enough for the atom to be able to reabsorb it. This would correspond to a regime of quantum mechanical oscillations between a two-level atom and a single electromagnetic field mode."

And indeed, very quickly, the same group increased the number of atoms in the cavity, yielding the pioneering demonstration of the strong light-matter coupling regime [Kal83]. Since then strong coupling phenomena were intensively studied in atomic physics [Rai89, Tho92, Bru96]. This activity spread into semiconductor physics in 1992, when it was shown that an exciton in quantum well can strongly couple to the microcavity mode giving rise to exciton polaritons [Wei92]. Starting

from this point, research for strong coupling phenomena in semiconductors dispersed into many directions (for an excellent review see [Vah03]). For instance, this phenomenon was recently shown for the quantum dot embedded either in a photonic crystal nanocavity [Yos04] or in a pillar microcavity [Rei04].

We use the strong exciton-photon coupling regime in a Fabry-Perot like microcavity as a starting point for the demonstration of Bose condensation in the solid state. In a single quantum well structure (QW) the in-plane translational invariance imposes that an exciton within the light cone couples to the photon of the same in-plane wave vector (k_{\parallel}). But, this selection rule does not hold in the growth direction (k_z), where the translational symmetry is broken. Thus, the bare QW exciton can be coupled with the continuum of photon states in the z direction, resulting generally in the dissipation of excitation and emission in the weak coupling regime.

In order to facilitate strong exciton-photon coupling, the density of photon modes in the z direction has to be discretized. As shown in figure 2.1, this is what happens when a QW is dressed by a planar microcavity. When the Rabi frequency exceeds the decoherence rates of exciton and photon (Γ_X, Γ_{PH}), strong coupling is reached and exciton polaritons are created. Decoherence of the excitons is induced by the structural disorder of the QW and interactions with other excitons, free carriers and phonons, whereas photon decoherence is mainly due to the finite radiative lifetime in a cavity.

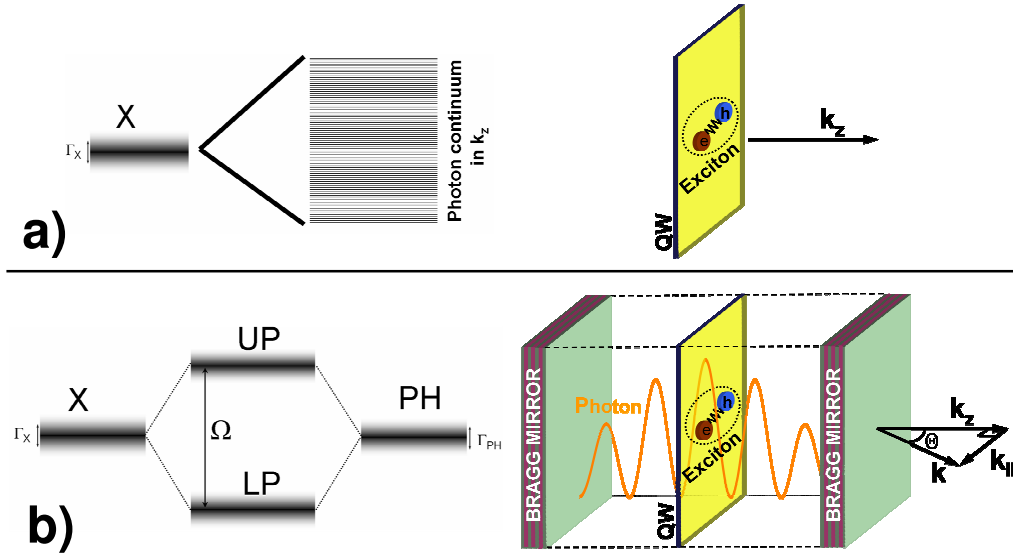


Figure 2.1: *Free-standing QW versus strong coupling microcavity emission: An exciton in a QW is coupled to the continuum of photon modes, resulting most often in emission in the weak coupling regime (a). A QW Exciton embedded in a planar microcavity is coupled to a well defined, discrete photon mode, favoring the attainment of the strong exciton-photon coupling regime (b).*

Thus a long intra-cavity photon lifetime τ_{PH} is the crucial parameter for achievement of strong coupling. Starting from the description of the Fabry-Perot cavity it

can be shown [Mul00] that this depends on three parameters: optical length of the cavity $n_c L$, incidence angle θ , and most critically on reflectivity of the mirrors R :

$$\tau_{PH} = \frac{\pi\sqrt{R}}{1 - \sqrt{R}} \frac{n_c L \cos(\theta)}{2c} \quad (2.2)$$

For this reason the mirrors of the microcavity considered in this work are realized by distributed Bragg reflectors (DBR). In principle, they are one dimensional photonic crystals. They consist of alternating $\lambda/4$ layers of materials with different refractive indexes n_1 and n_2 , schematically presented in figure 2.2.

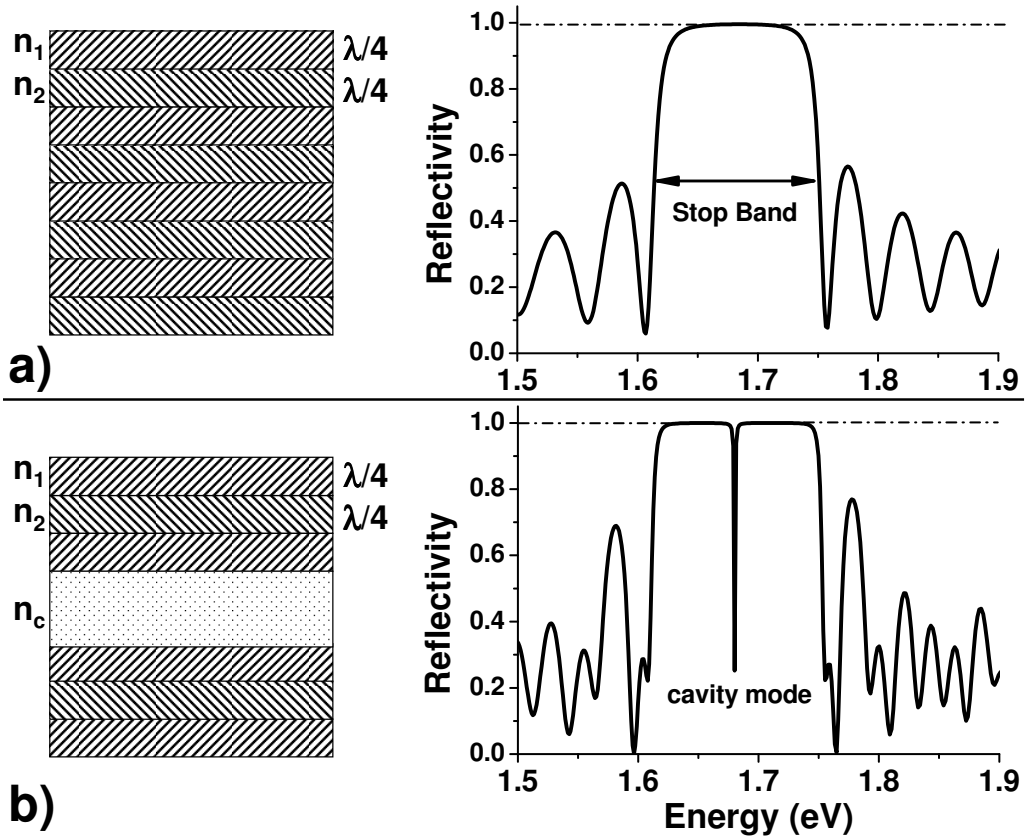


Figure 2.2: *Bragg mirror and microcavity: structure and optical response. a) A Bragg mirror acts as an interferential mirror. Its periodic structure produces a stop band for the propagating photons. b) A microcavity results, when the translational symmetry of the Bragg mirror is broken. An additional mode (cavity mode) in the gap arises. The reflectivity spectra were calculated by using the transfer matrix method for $\lambda = 735\text{nm}$. a) 23 stacks of $\text{Cd}_{0.4}\text{Mg}_{0.6}\text{Te}/\text{Cd}_{0.75}\text{Mn}_{0.25}\text{Te}$, b) same as a) with a cavity of around $1\mu\text{m}$.*

A photon of wavelength λ propagating through such a structure will experience periodic changes of the refractive index. In a good analogy with an electron moving in a crystal, a photonic gap centered at λ is created. Its width is governed by the

difference between n_1 and n_2 :

$$\delta\lambda = \frac{4\lambda}{\pi} \arcsin\left(\frac{|n_1 - n_2|}{n_1 + n_2}\right) \quad (2.3)$$

The cavity mode arises as soon as the periodicity of the DBR is affected. In our case the difference between refractive indexes is small ($\sim 13\%$) so the photon field penetrates deep into the mirrors producing an effective cavity length L_{eff} . Therefore, at normal incidence, the spectral position of the cavity mode depends not only on the cavity width L_c but also on the refractive indexes:

$$L_{eff} = L_c + \frac{\lambda n_1 n_2}{n_c |n_1 - n_2|} \quad (2.4)$$

The fundamental advantages of DBRs are the following:

- they are characterized by an extremely high reflectivity. The quality factor⁹ of planar semiconductor microcavities based on DBRs nowadays reaches $Q \sim 3 \times 10^4$ [San05]
- their absorption losses are negligible
- their mode structure allows one to properly couple nonresonant excitation with the intracavity field; this has particular importance in our experiments.

Exciton polaritons existing in a semiconductor microcavity operating in a strong coupling regime can be described by the coupled oscillator model. This approximation is well justified close to the exciton-photon resonance and is a limiting case of a full quantum mechanical approach [Sav96]. Polaritons treated as coupled oscillators are in the simplest form described by the hamiltonian:

$$\mathcal{H} = \begin{pmatrix} E_X(k_{\parallel}) & \frac{\Omega}{2} \\ \frac{\Omega}{2} & E_{PH}(k_{\parallel}) \end{pmatrix} \quad (2.5)$$

where Ω is the Rabi splitting [Sav95]:

$$\Omega^2 \propto \frac{(1 + \sqrt{R})^2}{\sqrt{R}} \frac{f_S}{L_{eff}} \quad (2.6)$$

The eigenstates of \mathcal{H} describe polariton states:

$$|LP\rangle = c_{L,PH}|PH\rangle + c_{L,X}|X\rangle \quad |UP\rangle = c_{U,PH}|PH\rangle + c_{U,X}|X\rangle \quad (2.7)$$

with the Hopfield coefficients:

$$c_{L,PH} = c_{U,X} = \sqrt{\frac{1}{2} - \frac{\delta(k_{\parallel})}{2\Delta(k_{\parallel})}}, \quad c_{U,PH} = -c_{L,X} = \sqrt{\frac{1}{2} + \frac{\delta(k_{\parallel})}{2\Delta(k_{\parallel})}} \quad (2.8)$$

⁹ $Q = \frac{E}{\delta E}$, with δE the homogeneous linewidth of the cavity mode

where $\Delta(k_{\parallel}) = \sqrt{\Omega^2 + \delta(k_{\parallel})^2}$ and $\delta(k_{\parallel}) = E_{PH}(k_{\parallel}) - E_X(k_{\parallel})$ is the photon-exciton detuning. Therefore the exciton and photon fractions in polariton states are governed by the Rabi splitting and photon-exciton detuning. The eigenvalues for the lower and upper polariton energies are:

$$E_{LP} = \frac{1}{2}(E_X + E_{PH} - \Delta), \quad E_{UP} = \frac{1}{2}(E_X + E_{PH} + \Delta) \quad (2.9)$$

2.2 Polariton dispersion: the key for condensation

2.2.1 Polariton trap in momentum space

The most interesting physics of exciton polaritons concern their dispersion properties in plane of the microcavity. Polariton dispersion relations can be obtained by taking into account the exciton and photon dispersion in eqs. (2.9):

$$E_X(k_{\parallel}) = E_X(k_{\parallel} = 0) + \frac{\hbar^2 K^2}{2M_{\parallel}}, \quad E_{PH}(k_{\parallel}) = \frac{\hbar c}{n_c} \sqrt{\left(\frac{\pi}{L_{eff}}\right)^2 + k_{\parallel}^2} \quad (2.10)$$

Let us first develop photon energy around $k_{\parallel} = 0$:

$$E_{PH}(k_{\parallel} \approx 0) = E_{PH}(k_z) \sqrt{1 + \left(\frac{E_{PH}(k_{\parallel})}{E_{PH}(k_z)}\right)^2} \approx E_{PH}(k_z) + \frac{\hbar^2 k_{\parallel}^2}{2 \frac{E_{PH}(k_z) n_c^2}{c^2}} \quad (2.11)$$

One can see that the formula $E_{PH}(k_z) n_c^2 / c^2$ has the meaning of an effective photon mass of around $10eV/c^2$, which is 4-5 orders of magnitude less than the exciton mass ($M_{\parallel} \sim m_e = 0.5MeV/c^2$). This is illustrated in figure 2.3, where the dispersions of the uncoupled states and the polaritons are plotted. It is shown that the dispersion of the cavity photon is much steeper than that of the exciton.

The strong exciton-photon coupling results in the formation of the polariton branches with a marked anticrossing behavior, as can be seen in the inset of figure 2.3. It should be emphasized that the coupling is efficient only in a very narrow range of the Brillouin zone, up to around $2 \times 10^5 cm^{-1}$ (in our case). Outside this range the excitonic branch is preserved.

Unusually strong photon dispersion creates the most striking polariton feature: a characteristic potential minimum is formed in the center of the zone. The polariton effective mass near the ground state is radically reduced, accordingly to the photon mass, by 4-5 orders of magnitude with respect to the exciton's mass. A polariton, as a superposition of a composite boson and photon, can be considered as a composite boson in the same limits as an exciton. But, **this extremely light mass means that at cryogenic temperatures the bosonic degeneracy for polaritons is revealed at densities where the exciton can be considered to be in the diluted limit** (see table 2.2). This is the key feature of the polariton as a candidate for Bose condensation in the solid state.

It is also worth noticing that, because of the energy-momentum conservation rules, polaritons are decoupled from phonon interaction. In this sense polaritons

are isolated from the lattice and from phonon induced decoherence. The polariton internal temperature can also differ from the lattice temperature. Furthermore, the depth of the potential minimum of around 10 meV is larger than the thermal energy at low temperature (for instance $20K \sim 1.7meV$). Therefore at low temperatures polaritons in the strong coupling zone cannot be thermally scattered back into exciton states. Thus the polariton dispersion produces a kind of thermodynamic trap around the ground state. So it is well justified to call the central part of the polariton dispersion in momentum space a **polariton trap**. This vocabulary will be used further along in this work.

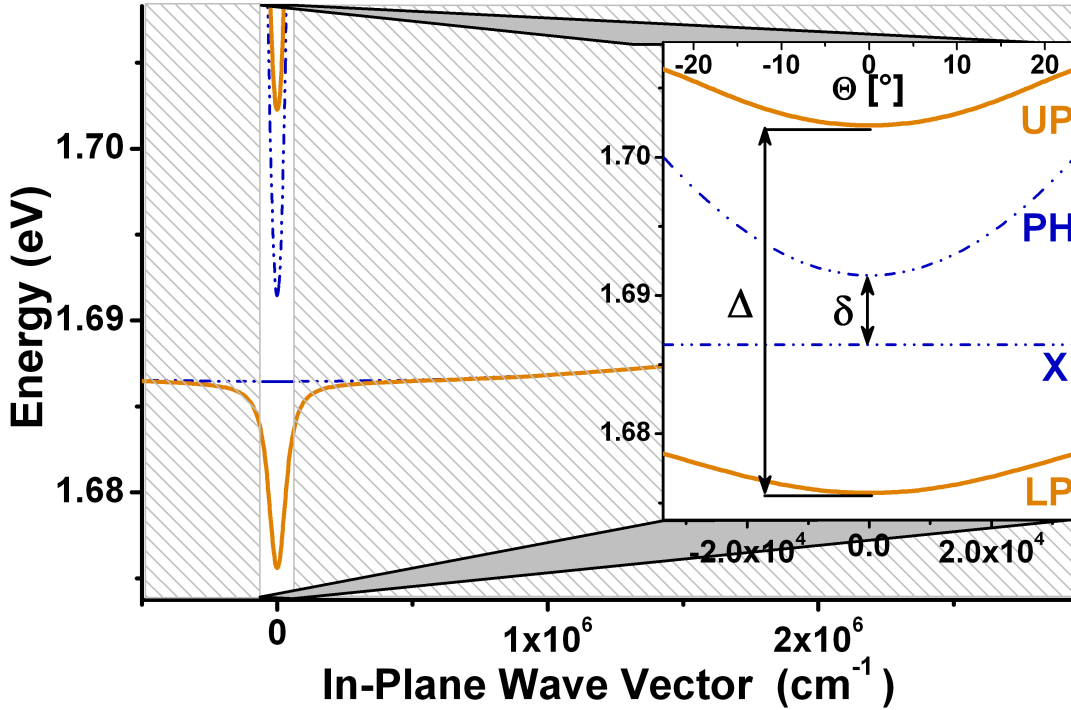


Figure 2.3: *In-plane dispersion of the exciton polariton. The strong exciton-photon coupling regime leads to formation of the lower (LP) and upper polariton (UP) branches. In the center of the zone a polariton trap is formed, which will be used to demonstrate polariton condensation. The coupling is efficient only in a very narrow range of wave vectors (non-shaded area). Inset: A zoom into the strong coupling zone. The shape of the polariton branches is governed by two parameters: the photon-exciton detuning $\delta = E_{PH} - E_X$, and the Rabi splitting Ω . The splitting $\Delta = \sqrt{\Omega^2 + \delta^2}$.*

We wish to remark that, in comparison with bulk polaritons, the ground state of microcavity polaritons is well defined, thanks to the photon confinement. Indeed, polaritons were first proposed [Hop58] and observed [Hen65] in 3D samples, where strong coupling is favored by the full translational symmetry and where one-to-one exciton-photon coupling occurs. However, as shown in figure 2.4, in the 3D case, due to the linear photon dispersion, the polariton becomes purely photonic when

Parameter	Atom	Polariton
$m [m_e]$	10^4	10^{-4}
$T [K]$	10^{-6}	20
$\lambda_{dB} [\mu m]$	0.7	3
$n_{cr} [cm^{-2}]$	10^8	$5 \cdot 10^8$
Life Time	"long" s	"very short" $10^{-12}s$

Table 2.2: The difference between atom and polariton considering BEC. Degeneracy conditions for polaritons can be reached in diluted limit at temperatures 7 orders of magnitude higher than for atoms. This huge advantage may be obscured by a very short polariton lifetime.

approaching the zero momentum state and, strictly speaking, the ground state does not exist.

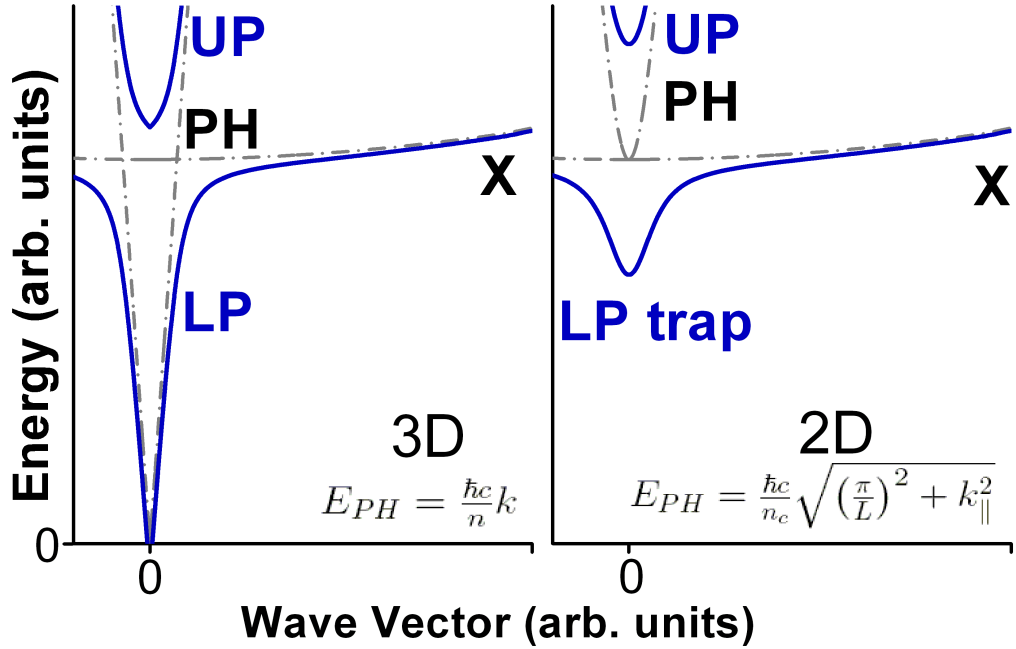


Figure 2.4: The conceptual difference between 3D and 2D polaritons. In the 3D case the ground state is not defined, since the $k=0$ state has vanishing energy. In 2D, owing to the photon confinement, the lower polariton ground state is well defined.

2.2.2 Momentum space mapping

Polaritons are detected by measuring their photon part leaking out of the microcavity, due to the finite reflectivity of the mirrors. Thus polaritons are directly coupled with the modes in the light cone:

$$E = \hbar c \sqrt{k_x^2 + k_y^2 + k_z^2} \quad (2.12)$$

Owing to the conservation of the in-plane wave vector (k_x, k_y) and of the energy E , the k_z component of the mode that is coupled to the polariton is unequivocally defined:

$$k_z = \sqrt{\left(\frac{E}{\hbar c}\right)^2 - k_{\parallel}^2} \quad (2.13)$$

As one can see in figure 2.5, we have:

$$\tan(\theta_{ext}) = \frac{k_{\parallel}}{k_z} = \frac{k_{\parallel}}{\sqrt{\left(\frac{E}{\hbar c}\right)^2 - k_{\parallel}^2}} \implies k_{\parallel} = \frac{E}{\hbar c} \sin(\theta_{ext}) \quad (2.14)$$

Thanks to the rotational symmetry, the azimuthal angle φ is conserved. Thereby, **in a microcavity system, we have the unique chance to probe polariton momentum space by performing angle resolved measurements:**

$$(k_x, k_y) \iff (\theta_{ext}, \varphi) \quad (2.15)$$

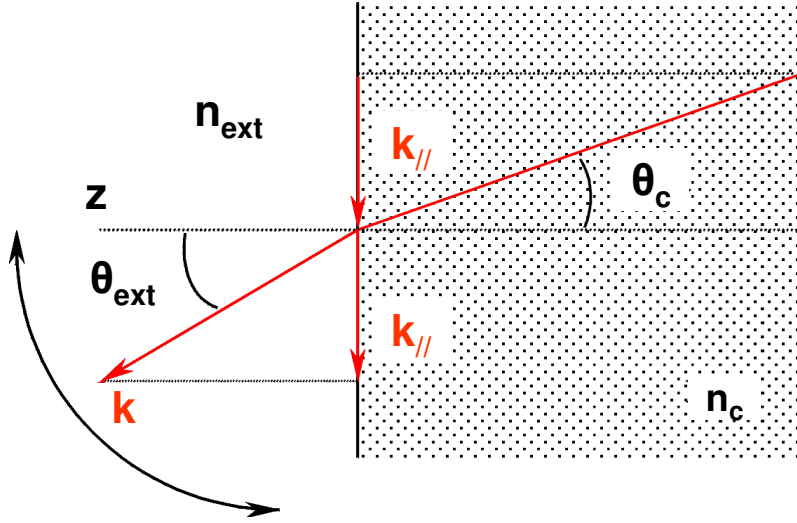


Figure 2.5: *Energy and in-plane momentum conservations enable probing of the polariton states by angle resolved measurements: $k_{\parallel} = \frac{E}{\hbar c} \sin(\theta_{ext})$.*

We will make use of this property throughout all this work. In particular, as described in chapter 4 and shown in figure 2.6, we will use the far field imaging technique to obtain information about the polariton population distribution within the trap: in the momentum plane as well as in the dispersion plane.

Finally, it should be pointed out that the population, polarization and coherence properties of the polaritons are coded by the light emitted by the microcavity since the outgoing photons represent a part of the polariton wavefunction [Baa06, Kar04, Karr04].

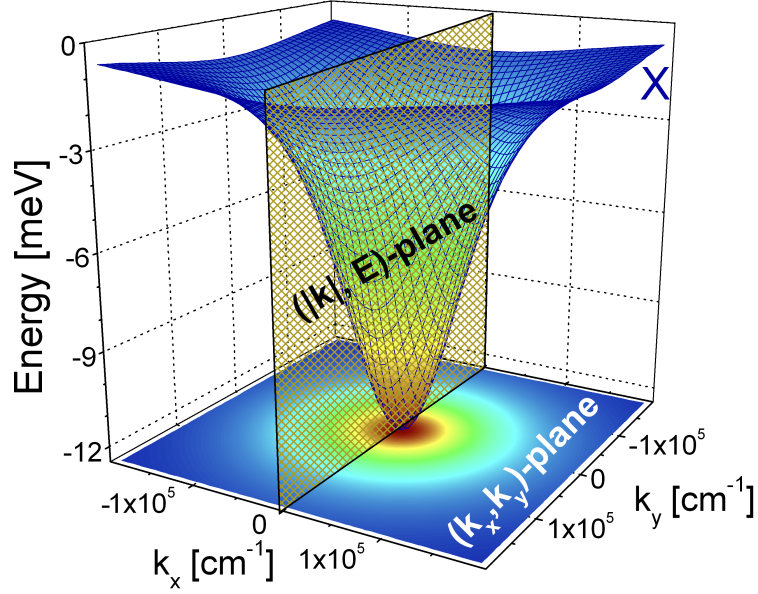


Figure 2.6: *The far field imaging as a tool for the momentum and dispersion space mapping. Each point in the far field of the polariton emission correspond to the polariton with a different in-plane momentum. By projecting the far field on the spectrometer slit the dispersion image can be directly obtained.*

2.2.3 Peculiar polariton relaxation

Nowadays, the major obstacle for polariton condensation is the polariton's extremely short radiative lifetime. Owing to the strong coupling regime, this lifetime is of the same order as the photon radiative lifetime in a microcavity τ_{PH} , given by eq. (2.2). In the microcavities used in this work, the polariton lifetime is 1-2 ps, approximately two orders of magnitude shorter than the relaxation time through phonon scattering [Mul00]. Thus at first sight it seems to be difficult, if not impossible, to efficiently populate polariton states.

Indeed, in the weak excitation regime, when relaxation is dominated by phonons, the occupancy factors in the vicinity of the ground state are very small ($\sim 10^{-3-4}$ for $\sim 0.01P_{thr}$). The polariton trap is empty most of the time and relaxation suffers from a strong **bottleneck effect** (discussed further in chapter 6.3). In CW excitation, the polariton occupancy of the given state is governed by the relaxation time towards this state with respect to its dephasing and radiative lifetime. In the weak excitation regime and negative detuning, when the lower polariton states are mostly photon-like, the maximum of the polariton population is located on the edge of the polariton trap, forming a bottleneck-like emission, shown in figure 2.7. In k -space the bottleneck is seen as a homogeneous ring. With increasing detuning towards more positive values, the polariton lifetime increases and the trap becomes shallower. The exciton fraction in the lower polariton branch increases, facilitat-

ing relaxation towards the ground state. This is very clearly observed in figure 2.7: the ring in momentum space shrinks and the population falls deeper into the ground state. However, even for deep positive detuning, a bottleneck persists and the polariton population is not thermalized.

In order to overcome the bottleneck effect and to efficiently populate polariton states, we need a mechanism that will scatter polaritons into their ground state with a rate comparable to the polariton radiative lifetime. Fortunately, such a mechanism exists. With increasing pump power and exciton density, a new scattering channel is triggered. In this process two excitons from the reservoir collide, one of them becomes hot and the second one is scattered into the trap [Por02]. This fast type of scattering is able to trigger stimulated scattering towards the polariton ground state.

It should be pointed out that the **exciton-polariton scattering** mechanism proposed in [Por02] is possible only because of the peculiar polariton dispersion curve shape. Such a process would not be possible for instance in the parabolic potential, where the energy and momentum conservation conditions cannot be simultaneously fulfilled [Bau02].

Conclusions In this chapter we have presented the exciton polariton as our candidate for achievement of Bose condensation in the solid state. The discussion can be summarized by the following points:

- A QW Exciton can strongly couple to the mode of a planar microcavity, giving rise to exciton polaritons.
- The small polariton effective mass $m_{LP} \simeq 10^{-4-5}m_X$ enables attainment of bosonic degeneracy at standard cryogenic temperatures in a diluted limit for excitons.
- A characteristic polariton trap is formed in the dispersion plane (in contrary to bulk polaritons).
- Polariton states can be investigated by angle resolved measurements, in particular, by the far-field imaging technique. Moreover, the outgoing photons code information about polariton polarization, population and coherence.
- The major problem with polaritons in the quest for polariton condensation is their very short radiative lifetime (several ps). This lifetime is limited by the finesse of the microcavity.
- Polariton states can be populated thanks to the exciton-polariton scattering mechanism. This opens the possibility of polariton thermalization and condensation.

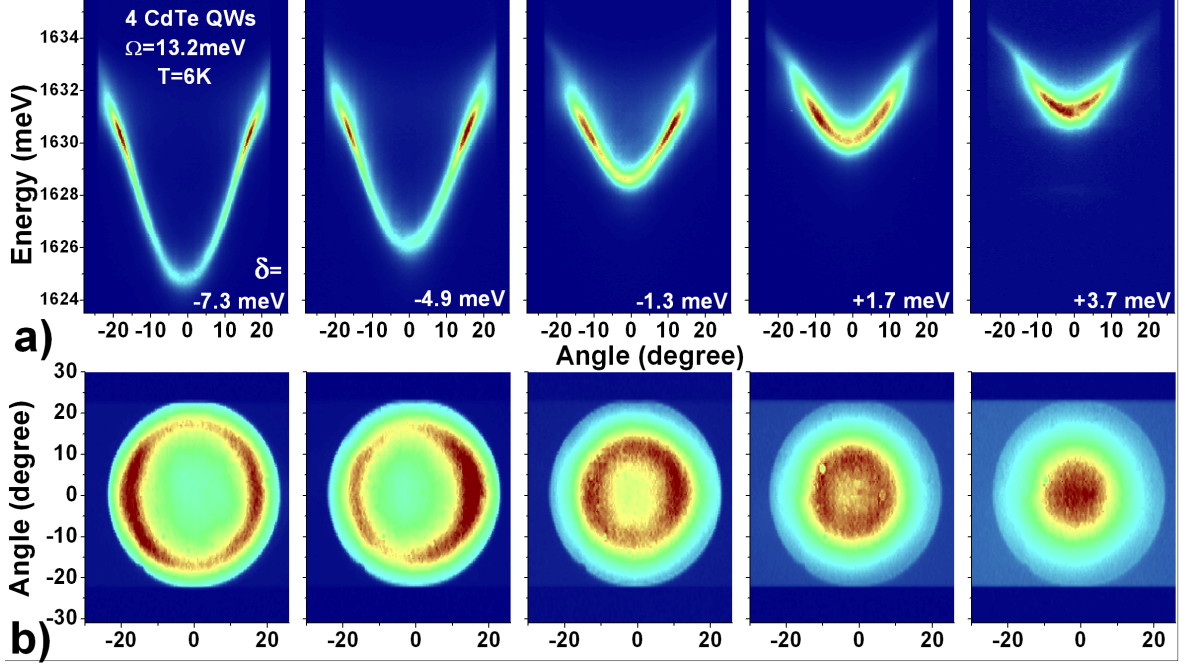


Figure 2.7: Evolution of the polariton distribution as a function of detuning. a) Dispersion plane image, b) momentum plane image. For details about the experimental technique see chapter 4. The false color scale goes from blue to red. Weak ($P \simeq 20\text{W}/\text{cm}^2$), non-resonant ($E_{\text{laser}} \simeq 1.75\text{eV}$) excitation regime at $T=6\text{K}$. The polariton distribution in k -space is governed by the interplay between the relaxation time and the radiative lifetime. For negative detuning, the polariton population is mostly gathered in the bottleneck, which can be seen as a homogeneous ring in the momentum plane. In the dispersion plane, the bottleneck effect gives a strong emission from excited polariton states. With increasing detuning towards more positive values, the polariton radiative lifetime and relaxation rate towards the ground state are enhanced. This corresponds to a shrinkage of the bottleneck ring in momentum space and a fall of the polariton population towards the bottom of the trap observed in the dispersion plane. However, in the weak excitation regime, a thermalized polariton population is **not** achieved. The experiments shown are performed on a CdTe-based microcavity containing 4 CdTe/CdMgTe QWs giving a Rabi splitting $\Omega = 13.2\text{ meV}$. The energy scale is conserved for all panels.

Chapter 3

Polariton condensation - state of the art

Strictly speaking, polariton condensation cannot be considered as a classical BEC, which deals with an ideal 3D gas of noninteracting bosons. Here, we have a finite 2D system, so true long range order cannot be attained. Due to the Coulomb and saturation interaction, the physics soon exits the regime of weakly interacting bosons. The lifetime is short enough that we must confront the role of non-equilibrium physics. Nevertheless, the main characteristic of BEC; i.e. massive occupation of the ground state through the stimulated scattering process, occurs in the polariton system. In this chapter we give a brief overview of the efforts and progress towards achievement of condensation in the solid state with polaritons. The first step towards condensation is the demonstration of the stimulated emission of polaritons in the strong coupling regime under non-resonant excitation conditions.

Contents

3.1 GaAs	28
3.2 CdTe	31

3.1 GaAs

The pioneering work of Weisbuch et al. [Wei92] initiated active research on the light-matter interaction in semiconductor microcavities. Soon after a proposal of Imamoglu et al. [Ima96] the idea of polariton BEC at high temperature excited and intrigued the scientific community.

The first claim for a "boson" [Pau96] could not withstand many criticisms [Kir97] and had to be withdrawn [Cao97] finally. Another early claim for observation of the stimulated scattering of polaritons [Sen99] was based on the observation of the quadratic nonlinearity of the LP ground state emission. In a following article [Sen00] the authors retreat from their previous interpretation. The detailed analysis shows,

that the nonlinearity occurs for an occupancy factor of 10^{-3} , so it cannot be the result of a stimulation process, but is due to binary collisions of excitons.

The initial enthusiasm was restrained by the following findings. A strong bottleneck in the exciton relaxation towards polariton states at $k_{\parallel} \sim 0$ was observed. In GaAs microcavities existing to date, attempts to increase occupancy of the polariton states led to the increase of exciton density beyond the screening density, when using strictly non-resonant pumping. Ionization of excitons in the reservoir occurred and strong coupling was lost before polariton stimulation could take place [Shu98], [Hou95], [But02], [Sko02]. Observed nonlinearities were due to the cavity's lasing in the weak coupling regime¹⁰.

The bleaching may be however prevented in resonant pumping experiments, when polaritons are directly injected in the trap. In this way one can attain high occupancy factors at a low exciton density. The first breakthrough came with the demonstration of stimulated emission from the polariton ground state in the parametric scattering process [Sav00]. Weak optical pulses were applied to seed the parametric gain, when the polarization and phase matching conditions for the pumping beam were fulfilled. In subsequent works [Bau00], [Erl01], self-stimulation¹¹ of the polariton ground state and stimulated removal from the pump beam were reported. Coherence properties of a parametric scattering process were investigated and proven in [Kun03]. High temporal coherence of the polariton population in the signal state was reported, as well as the phase matching between signal and idler states. Stimulated removal from the pump state was reconfirmed.

To sum up, resonant excitation experiments have left no doubt about the bosonic behavior of polaritons in their scattering process. At the same time, stimulation and coherence were strongly driven by the excitation laser itself. In other words, the transition observed was a transfer of coherent population produced by the pump into coherent population of the signal. Thus the nonlinear and coherent effects obtained in resonant experiments cannot be considered as a condensation, which is a spontaneous phase transition from incoherent into coherent state. However, this field is still a playground to demonstrate general features of quantum mechanics. Beautiful examples can be found in [Lan02] and [Sav05].

The need for non-resonant excitation conditions led to a few ideas that could overcome the problem of low saturation densities for excitons in GaAs. The first concept is based on embedding multiple QWs in a microcavity, so that the exciton density is divided between many QWs. The Rabi splitting is increased thanks to the increase of the total oscillator strength. The strongest claim to date for polariton condensation is made in ref. [Den02]. A microcavity with 12 QWs is pumped¹² at a high angle into exciton states. The polarization studies published afterwards [Den03] show that this kind of pumping cannot be considered as strictly non-resonant, since polarization of the LP emission depends on the polarization state of the pump. Strong nonlinear emission from the polariton ground state and the shortening of the

¹⁰For review articles see [Hou05], [Sko98], [Yam00]

¹¹without a seeding beam

¹²The use of pulsed excitation rules out a steady state regime

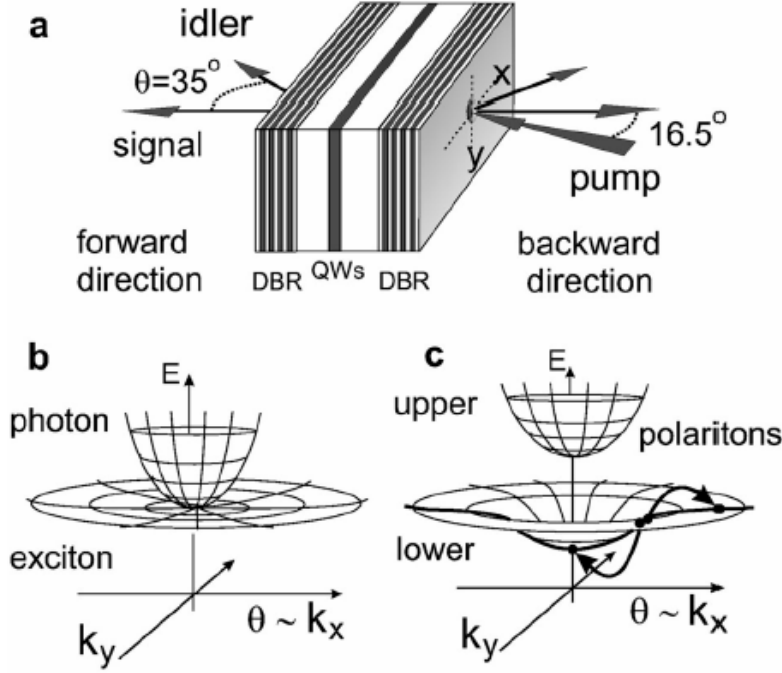


Figure 3.1: *The geometry of a parametric scattering experiment. Polaritons are created directly in the trap. Scattering of the pump polaritons leads to formation of signal at the polariton ground state and idler at high k_{\parallel} . Figure copied from [Bau00].*

decay time is reported. Line narrowing is not visible on the PL spectra presented. The formation of a quantum coherent state at $k_{\parallel} = 0$ is investigated in second order temporal coherence measurements. The second order correlations are found to be quasi-thermal at the stimulation threshold - $g^2(0) = 1.8$, and astonishingly remain far from that expected for a coherent state - $g^2(0) = 1$ at pumping as high as $P = 18P_{thr}$ - $g^2(0) = 1.48$. In [Den03] authors seem to back-down themselves from their initial statement.

The other mechanism to overcome the bottleneck effect and favor polariton thermalization was proposed in [Mal02]. In this work, electron-polariton scattering is found to be helpful to bring the reservoir population towards the ground state. Indeed, enhancement of the polariton relaxation by polariton-free carrier scattering was recently confirmed experimentally [Tar03], [Qar03], [Lag03], [Per05], [Per06], but up to now the results remain much less spectacular than the theoretical predictions.

The onset of polariton stimulated scattering is governed by the ratio between escape time of the polariton out of the microcavity (polariton lifetime) and relaxation time towards the ground state (relaxation time). Therefore, another idea to facilitate polariton condensation is to increase the polariton lifetime with ultra high finesse cavities to improve occupancy of the polariton ground state. It is estimated, that increasing the photon lifetime up to $\tau \sim 100$ ps should enable polariton condensation in GaAs.

3.2 CdTe

Finally, the remedy for low saturation density is the use of materials in which excitons are more robust, like II-VI compounds or GaN. As we will show in this dissertation, polariton condensation **does indeed occur** in CdTe microcavities. The key advantage with respect to GaAs, is increased saturation density, thanks to the higher exciton binding energy. The exciton density needed to trigger stimulated polariton-polariton scattering from the reservoir towards the trap [Por02], [Huy03] is an order of magnitude lower than the saturation density. The physical situation of a non-resonant excitation experiment is presented in figure 3.2.

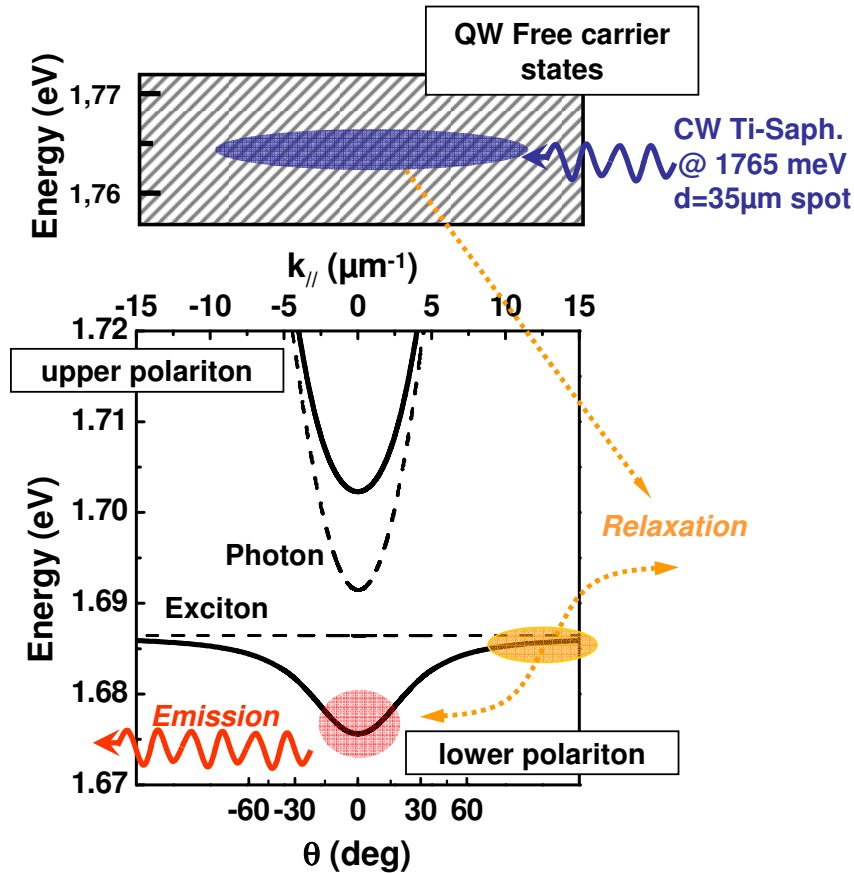


Figure 3.2: *Physical situation of a non-resonant experiment. The optical pump creates free carriers, which form excitons. The excitons cool down through interaction with LO phonons, forming the exciton reservoir. Increasing density in the reservoir launches schematically indicated polariton-polariton scattering from the reservoir towards the trap. If the scattering rate is higher than the polariton escape rate, condensation can occur.*

The first successful growth of the CdTe-based microcavities was realized in 1997 by R. André [And97]. Quantum degeneracy of the CdTe microcavity polaritons was rapidly reported [Dan98]. It was shown that, above a certain threshold of the pump

power, the ground state polariton emission could exhibit a significant nonlinearity, while the linewidth showed significant narrowing. These results provided evidence for polariton stimulation in the strong coupling regime under strictly non-resonant excitation conditions. This interpretation was confirmed by the existence of a second threshold towards the weak-coupling regime. For pumping power two orders of magnitude higher than needed for polariton stimulation, lasing from the cavity mode occurs. Further proof was given by the study of the threshold pump power for stimulation. It was found that this does not depend on the number of QWs in a cavity [Boe00]. The foregoing observations rule out any interpretation based on lasing due to localized exciton population inversion [Fan97]. Further investigation of the polariton dynamics also showed that observed non-linearities stem from a stimulated relaxation process [Mul00]. The abrupt reduction of the decay time from 100-400 ps below threshold down to 3 ps at threshold is noted, demonstrating stimulated relaxation.

Applying k-space and real space imaging opened up new possibilities for experimentalists and quickly enriched understanding of the system. In 2005 it was explicitly demonstrated that polaritons accumulate in the bottom of the lower polariton branch, forming a non-equilibrium condensate [Mox05]. The additional argument of spatial coherence was provided. At the condensation threshold, dramatic changes take place in real space: the spatially homogenous luminescence of the spontaneous regime breaks down at the condensation threshold into a few bright spots with a characteristic size of 3-5 microns. Surprisingly the angular pattern of those spots was much narrower than the angular emission of a few micron source and indeed corresponded to the size of the entire excitation spot. It was then argued that formation of a single, coherent state had been observed. Theoretical analysis in the framework of the Gross-Pitaevskii equation suggested that the observed object corresponded to the time-averaged condensate wave function experiencing a random, localizing potential. This potential was resulted from the photonic disorder of the microcavity.

Finite \mathbf{k} stimulation Earlier, in 2004, an other set of experiments was published giving evidence for the coherent nature of the phase transition in CdTe microcavities [Mox04, Max05]. The use of a small excitation spot ($3\mu\text{m}$ diameter) prevented relaxation into the lowest polariton energy states: polariton stimulation occurred in a degenerate ring of excited states¹³ (see figure 3.3), and thus was only remotely connected with BEC. Nevertheless, above the nonlinear threshold, macroscopic coherence in the momentum plane was demonstrated by the build-up of speckled patterning and by the formation of interference fringes, produced by a Billet interferometer.

At the first glance stimulation on the ring of excited states was quite puzzling. First, let us point out that a characteristic non-dispersive bar inside the polariton dispersion always appears in the stimulated regime. To understand the origin of this geometrical artefact, let's note that a stimulated state of a given $|\mathbf{k}|$ has a given

¹³Similar effect can be already found in [Hua02].

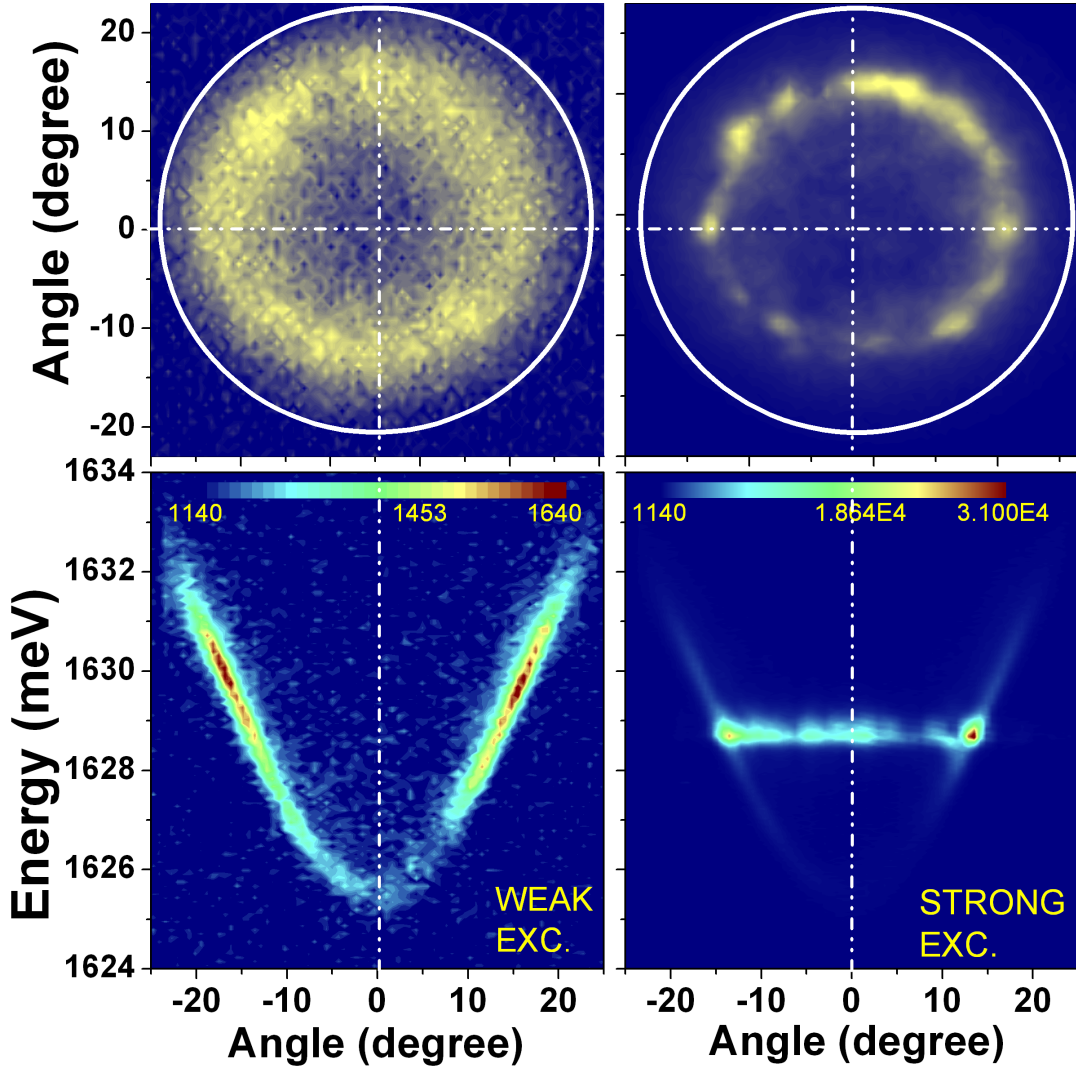


Figure 3.3: *Example of condensation on a degenerate ring of excited states. Upper row: polariton population distribution in momentum space (far field image). At the weak excitation regime a broad, homogeneous ring corresponding to the bottleneck emission is observed (left). Above threshold (right) stimulated emission occurs on a degenerate ring of excited states. Its speckled pattern indicates coherent properties of emission (speckles appear as a result of the diffusion of coherent light on the static disorder). Lower row: polariton distribution in the dispersion plane. The bottleneck emission in a weak excitation regime (left) and stimulation into the finite k polaritons (right) are observed. The "horizontal bar" is observed due to the very strong emission on the ring of excited states, whose "wings" contribute onto the monochromator slit. The energy of the stimulated polariton states depends on the size of the excitation spot and on the local disorder. 4 QW CdTe microcavity at $T=7.5K$. All parts of the panel share the same energy and angle scale.*

angular width in θ and dominates completely the spectrum. Thus, by selecting a narrow stripe in the far field with the slit, we will detect the stimulated emission not only from the states of opposite wave vectors: \mathbf{k} and $-\mathbf{k}$, but we will gather also some signal from the angular wings of the other states on the ring. This "stray light" was very useful for the transverse coherence measurements [Max05]. This effect is visible not only in the stimulated regime but also when the bottleneck effect is well pronounced as presented in figure 3.4.

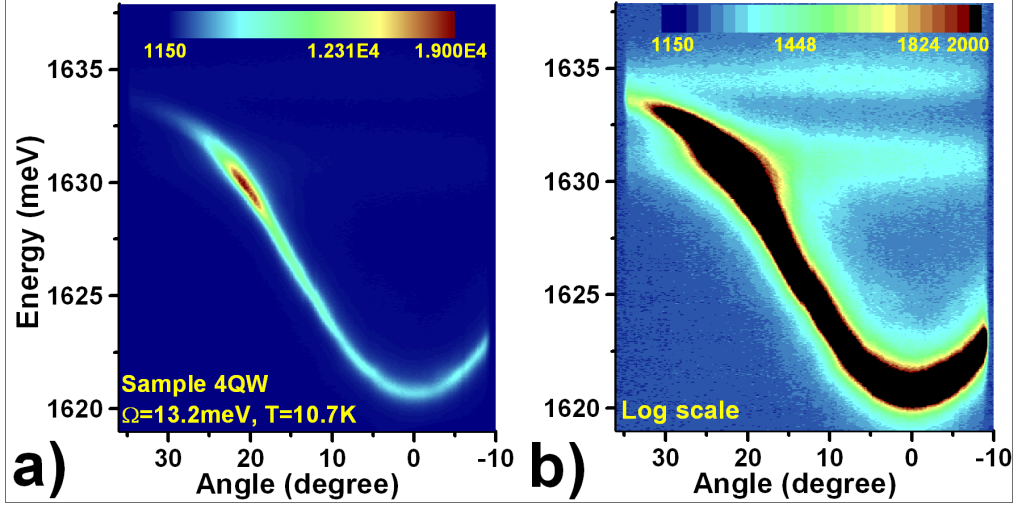


Figure 3.4: The light diffused from the bottleneck emission can also produce the effect of "non-dispersive bar". **a**: the polariton dispersion image in PL measured for 4 QW CdTe microcavity at $T=10.7K$ for $\delta = -11.6 meV$. The bottleneck emission is well pronounced. **b**: the same image as **a** on the different (saturating at black) color and log scale. The emission from the bottleneck at $\sim 1630 meV$ gives rise to the artefact of "non-dispersive" segment. The exciton dark states at $\sim 1635 meV$ are also visible.

Today it is clear, that this unusual stimulation is connected with the size of the excitation spot. Figure 3.5 summarizes the effect of the spot size on the energy of the stimulated states. When decreasing the spot size - d , condensation occurs in the ground state down to around $d = 25\mu m$. Further reduction of d increases the energy of stimulated states. When the spot size is reduced down to $d \simeq (2 - 5)\mu m$, it becomes comparable with the characteristic size of the photonic disorder of the microcavity (see chapter 9). Thus by moving on the sample surface an excitation spot of the size of a few μm we can probe locally spatial disorder experienced by polaritons. In these conditions the energy of stimulated state is very sensitive on the spatial size of the localizing potential: its value can jump even more than 1 meV when moving of a few microns on the sample.

The simple hypothesis that could explain finite k stimulation is based on the observation of the strong spatial trapping of the polaritons in the stimulated regime when the small spot size is used. In the spontaneous regime relaxation time from the reservoir towards the polariton states is governed by phonons and therefore is long

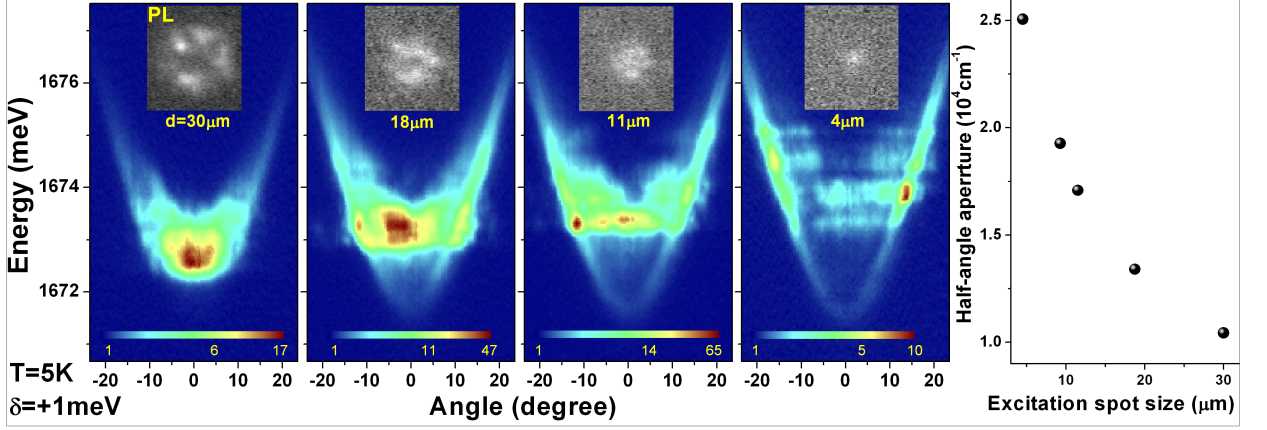


Figure 3.5: *Spot-size dependence of the energy of the stimulated states. For the spot-size down to 25 μm the stimulation of the ground state occurs. Further diminishing of the excitation spot size results in a stimulation on the ring of the polariton excited states. The logarithmic color scale is used. The insets show a real space pattern corresponding to the given excitation spot. Right: a half angular aperture as a function of the spot size.*

(100-400 ps - dependently on the photon-exciton detuning). So the free carriers have enough time to diffuse in the plane of the microcavity before forming polaritons. In stimulated regime, thanks to the exciton-polariton scattering, the relaxation speeds-up to around 5-10 ps [Mul00]. Thus polaritons are immediately created and trapped in the local minima of the in-plane potential. Stimulated nature of the process forces polaritons to be scattered towards these spatial traps.

Yet, the real and k-space patterns are conjugated by the Fourier transform. The ring in the k-space is formed, since its Fourier transform gives a strongly localized real space pattern. In particular, the spatial localization corresponding to this ring is more pronounced than the Fourier transform of the polariton ground state that would have a gaussian shape.

This can be illustrated by the following analytical argument. The ring in the k-space can be described as follows:

$$A(k) = \delta(k - k_0) \otimes e^{-\frac{k^2}{\Delta k^2}} \quad (3.1)$$

Its Fourier transform yields:

$$A(k) \xrightarrow{\text{FT}} A(r) \propto J_0(k_0 r) \times e^{-\frac{r^2 \Delta k^2}{4}} \quad (3.2)$$

where J_0 is the Bessel function. Width of the J_0 in the first order is $\Delta r_{J_0} \simeq \frac{1.5}{k_0}$, whereas width of the gaussian is $\Delta r = \frac{2}{\Delta k}$. Thus by taking, radius of the ring larger than its width, for instance $k_0 = 10 \cdot \Delta k$, we notice that the ring in the k-space represents the state that is much more spatially localized (width $\frac{1.5}{10 \cdot \Delta k}$) than the state at $k=0$ (width $\frac{2}{\Delta k}$).

The presence of the Bessel function in eq. (3.2) indicates that the Fourier transform of the ring in the k-space should produce concentric rings in the real space. Interestingly, such rings were indeed observed - see Fig. 9.4 in [Mox04].

Conclusions The first step towards polariton condensation has already been done before this thesis. The bosonic character of the polariton scattering was demonstrated in resonant experiments. The stimulated emission from the bottom of the polariton trap in a strong coupling regime under non-resonant pumping was observed in CdTe microcavities. The signs of the formation of the coherent state were also noticed. The main advantage of CdTe structures with respect to GaAs is larger exciton binding energy. This allows one to increase excitonic density and trigger stimulated exciton-polariton scattering. The rate of this process, being comparable to the polariton escape time, enables efficient populating of the polariton states.

Chapter 4

Experimental methods

This chapter contains a detailed description of the experimental setup. The experimental conditions will be also specified.

Contents

4.1 Cryostat	37
4.2 Excitation	38
4.2.1 Laser	38
4.2.2 Acousto-optic modulator	39
4.2.3 Formation of the excitation spot	39
4.2.4 White light	40
4.3 Detection	41
4.3.1 Real and k-space imaging	41
4.3.2 Monochromator and CCD camera	43
4.3.3 Michelson interferometer	43
4.3.4 Photon correlator	44

4.1 Cryostat

The heart of the experimental setup is a cold finger cryostat "MicrostatHe" provided by Oxfords Instruments. A calibrated temperature sensor and a heater coupled with Oxford Instruments temperature controller ITC502 allows to set the operating temperature from 4.8K up to 300K with an accuracy of 0.1 K. The sample is glued on the cold finger with vacuum grease, which ensures a good thermal contact (the temperature is measured just on the opposite side of the sample holder). The cryostat is mounted on XYZ Micro-controlle translation stages to permit sample alignment with respect to the optical axis of the setup (Z axis). The cryostat can be tilted around the X and Y axes, which can be useful to probe polaritons with large in-plane $k_{||}$.

The sample stability is estimated to be $0.5 \mu\text{m}$ and is limited by the sample holder drift and vibration. The main source of noise are the vibrations of the helium transfer tube. In order to reduce them, the helium container is stabilized. The optical measurements are simplified by the wide optical window of the cryostat - diameter 25 mm, thickness 1.5 mm, angle of admittance 144° .

4.2 Excitation

The schema of the excitation part of the setup is presented in figure 4.1.

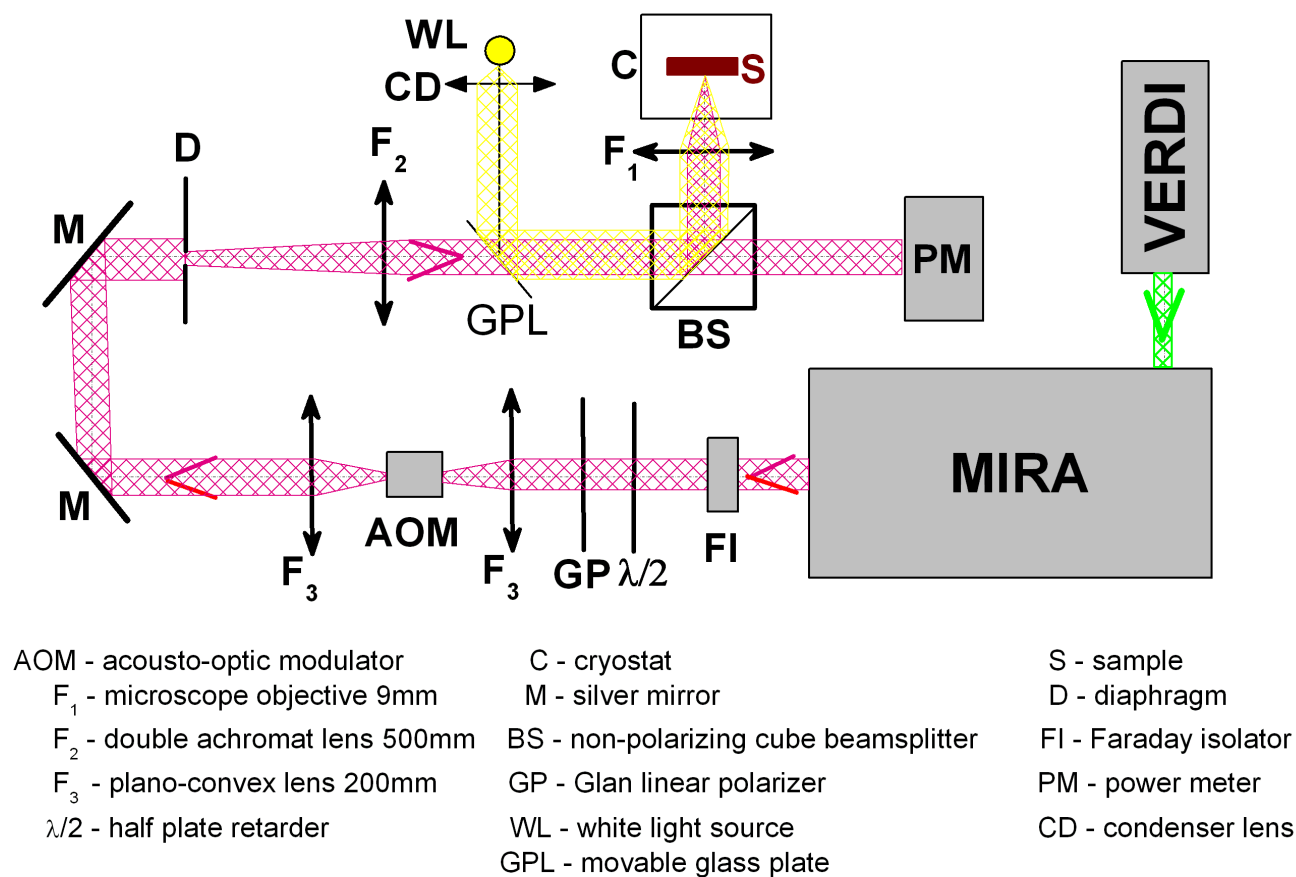


Figure 4.1: The schema of the excitation part of the experimental setup.

4.2.1 Laser

One of our most important experimental requirements is the condition of non-resonant excitation, which ensures that initially injected polaritons are incoherent. For this reason the pump energy is set to $\lambda_{exc} \simeq 701 \text{ nm}$ (1.768 eV), more than 90 meV above the polariton ground state, creating hot electron-hole pairs in QWs. The

excitation is coupled to the intra-cavity field by the first reflectivity minimum of the Bragg mirror, on the high energy side of the stop band.

The powerful tool, that gives us a high excitation intensity at λ_{exc} is a titanium:sapphire laser, a Coherent Mira 900. This laser contains two switchable cavities, which allow us to work in pico- or femtosecond mode-locking operation. It can, of course, work also in a CW mode. Thanks to the excellent quality of the optics and perfect alignment of the laser cavity, we obtain (in CW operation) a high output power of up to 1W for λ_{exc} for pumping power of $P_{pump} = 5.5W$ ¹⁴. In most of our experiments a steady state of the polariton system is required, and this is why we will mainly work in the CW mode.

The Mira is pumped by a *Verdi*TM/V-5 diode-pumped ring laser, also provided by Coherent. The gain medium in Verdi is $Nd : YVO_4$. It is pumped by diode laser bars (~ 808 nm). The cavity chooses the vanadate emission at $\lambda_V = 1064$ nm. This wavelength is doubled with a LBO second harmonic generator. Finally, the output is a single mode $\lambda = 532$ nm beam with the power of up to $P_{pump} = 5.5W$

The high quality of the system is reflected in a good power stability of the output beam of 0.2%. The output beam passes through the Faraday isolator, which prevents back reflections into the cavity, thus protecting the stability of the laser.

The Mira output is linearly polarized along the horizontal direction. Optical attenuation of the beam power is realized by combining a $\lambda/2$ plate and a Glan linear polarizer¹⁵.

The excitation power is monitored, just before focalizing the beam on the sample, with the Coherent FieldMateTM power meter. The power arriving on the sample is 0.7 of the device readout (as the excitation additionally passes through the microscope objective and the window of cryostat).

4.2.2 Acousto-optic modulator

In order to reduce sample heating in CW operation, the excitation beam is "chopped" with an acousto-optic modulator. Pulses of duration 1 μs with a duty cycle of 1% are used. The pulse duration is sufficiently long (by four orders of magnitude) in comparison with characteristic times of the microcavity to guarantee a steady state regime.

4.2.3 Formation of the excitation spot

To provide uniform excitation of the sample, the laser beam is carefully shaped into a "top hat" intensity profile (see figure 4.2). The excitation laser is projected onto the diaphragm. First, the central part of the gaussian profile of the beam is selected by the diaphragm. Next, the image of the diaphragm is formed on the sample

¹⁴Note that this wavelength is close to the limit of the gain curve of the Ti:Saph laser. Maximum output power corresponds to the maximum of the gain curve at $\lambda = 800$ nm: $P_{out} = 1.4W$ for $P_{pump} = 5.5W$

¹⁵All optics are optimized to work in the near infra-red zone: 700-1000 nm

surface with magnification of $\gamma = 1.8 \cdot 10^{-2}$. Just by changing the diameter of the diaphragm one can adjust the excitation spot size from a few μm up to $50 \mu\text{m}$.

The beam is focused on the sample with a high quality microscope objective Olympus LMPLFL $20 \times / 0.40$ mounted on XYZ Microcontrolle translation stages. The objective provides magnification of $\gamma = 20$. The high working distance of 12 mm allows us to work outside of the cryostat. The focal length is $f=9$ mm. The objective is corrected for spherical¹⁶ and chromatic aberrations. As pointed out below, the big advantage is its large numerical aperture of $\text{N.A.}=0.4$.

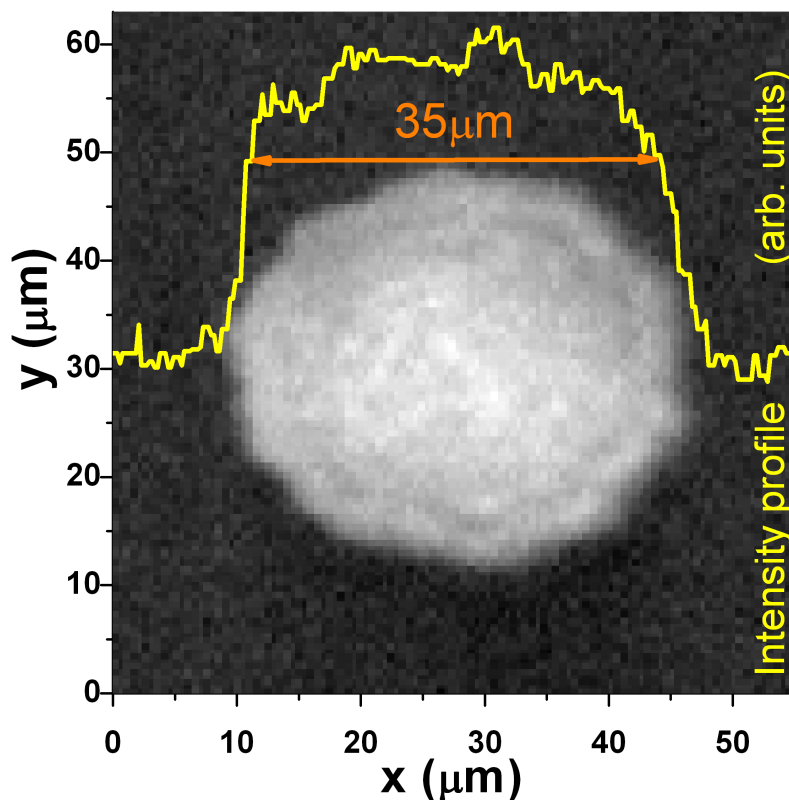


Figure 4.2: *Formation of the excitation spot on the sample surface.*

4.2.4 White light

We have also the possibility of injecting white light into the objective. This allows us to perform reflectivity measurements and to control the quality of the sample surface. For reflectivity measurements, white light is strongly attenuated for photon energy above 1.75 eV, to reduce excitation of the LP photoluminescence. The reflectivity spectrum may also be obtained by operating the laser in the femtosecond mode¹⁷, when probing of small sample region (down to a few microns) is required.

¹⁶We obtain a sharp image in the whole field of view

¹⁷Spectral width of 10 nm

4.3 Detection

The schema of the detection part of the setup is presented on the figure 4.3.

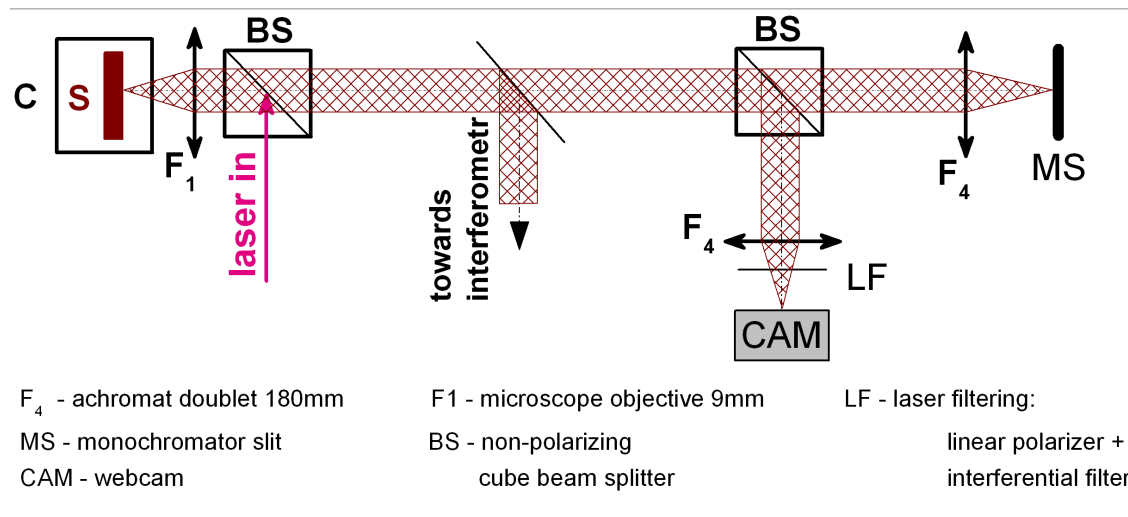


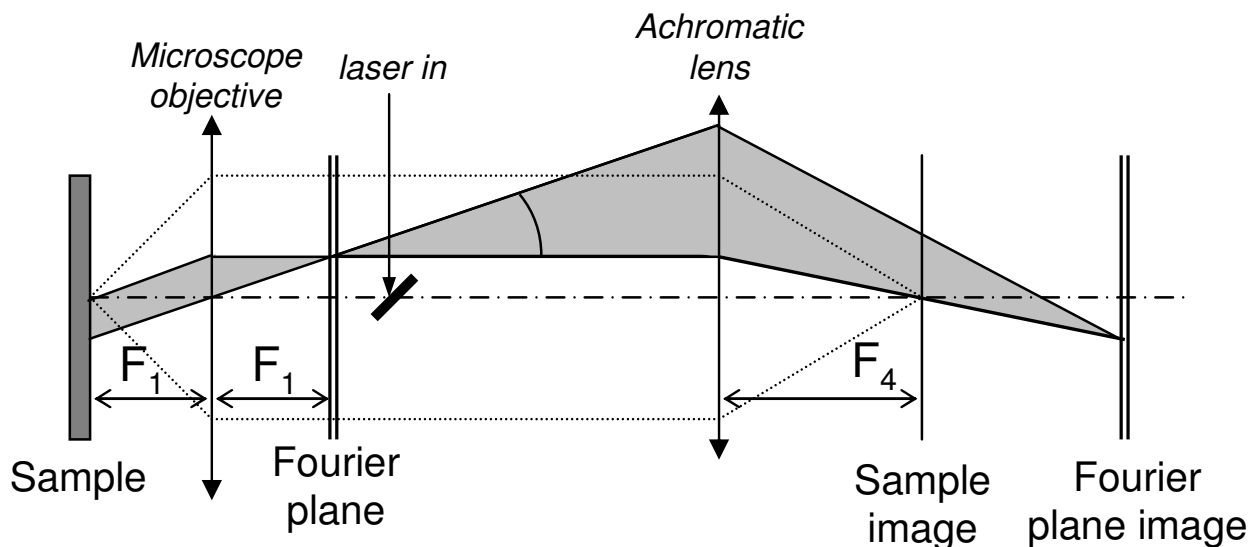
Figure 4.3: *Schema of the detection part of the optical setup.*

4.3.1 Real and k-space imaging

Practically, throughout all our work, we will need to conjugate spectral and spatial properties of the emitted signal. To allow simultaneous analysis of the near-field (real space image of the sample surface) and the far-field (angular diagram of the emission), a setup was built, in which the sample response is imaged **at the same time** on the chip of a very simple camera (a webcam) and on the monochromator slit. The PL signal is collected by the same objective as used for the excitation and focused on the entrance slit of a monochromator by an achromatic doublet lens of focal lengths $F_4 = 180$ mm, which produces an image of the emitting spot magnified by a factor $\gamma = 20$.

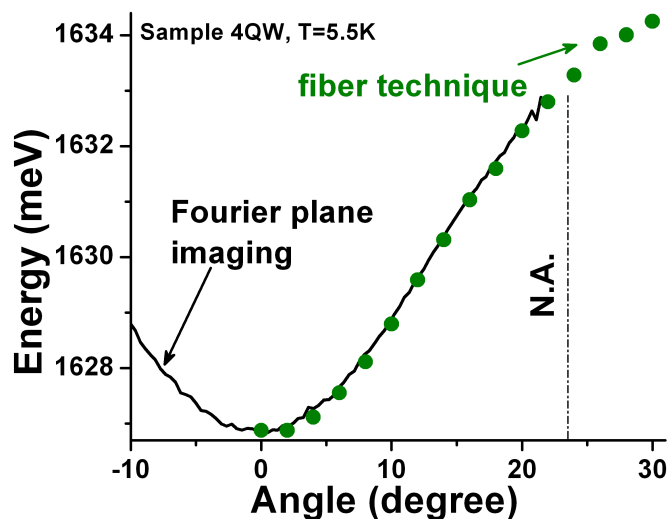
On the chip of the web camera and on the slit of the monochromator, we can form not only an image of the emitting spot, but also an image of the Fourier plane. This is done just by changing the position of the F_4 lens (see figure 4.3). The position is determined by the lens equation. In figure 4.4 the idea of k-space imaging is shown.

The possibility of Fourier plane imaging has for us a particular meaning. The Fourier plane is the plane on which each point corresponds to the far field emission (θ, φ) of the emitting spot. As stated earlier in section 2.2.2, for microcavities optical selection rules require that the in-plane wave vector of the emitted photon be equal of the recombining polariton: $k_{\parallel photon} = k_{\parallel polariton} = \frac{E}{\hbar c} \sin(\theta_{ext})$. Thus, the image of the Fourier plane carries vital information about the polariton distribution inside the trap in the momentum space. The high numerical aperture N.A.=0.4 means that we can collect photons emitted within the angles -23.4° to 23.4° , and thus

Figure 4.4: *The principle of real and k-space imaging.*

reach polariton states up to $k_{\parallel} = 3.37 \cdot 10^4 \text{ cm}^{-1}$. If needed, this value can be almost doubled by tilting the cryostat with respect to the standard optical axis of the setup. The angular resolution of the Fourier plane analysis is limited by the pixel size of the CCD camera of the monochromator, which is $25 \mu\text{m}$.

The calibration of angle in the Fourier plane image is checked by comparing the polariton dispersion measured with the imaging technique and with an optical fiber technique (see [Mox04], figure 4.5).

Figure 4.5: *Polariton dispersion measured with the Fourier plane imaging technique (solid line) and with the optical fiber technique (solid circles). No significant difference can be observed between two techniques.*

4.3.2 Monochromator and CCD camera

The light emitted (or reflected) by the sample is analyzed spectrally by a Jobin Yvon THR1000 monochromator of 1 m focal length. The dispersive element is a holographic grating with 1200 grooves/mm. A spectral resolution of $60 \mu\text{eV}$ at 1675 meV is achieved with $40 \mu\text{m}$ slit width. The absolute wavelength is calibrated with a mercury lamp. The grating efficiency as a function of the energy is known for vertical and horizontal linear polarizations of the incident light. Imaging properties of the monochromator are improved by using mirrors of a high optical quality.

The spectrally analyzed light is detected by a liquid nitrogen cooled CCD camera, the Spectrum One (1024×256 , quantum efficiency - 50% at 750 nm).

4.3.3 Michelson interferometer

Polariton condensation is accompanied by the spontaneous development of coherence. To study the first order temporal and spatial correlations $g^1(\delta\vec{r}, \delta t)$, a Michelson interferometer¹⁸ was used (see figure 4.6).

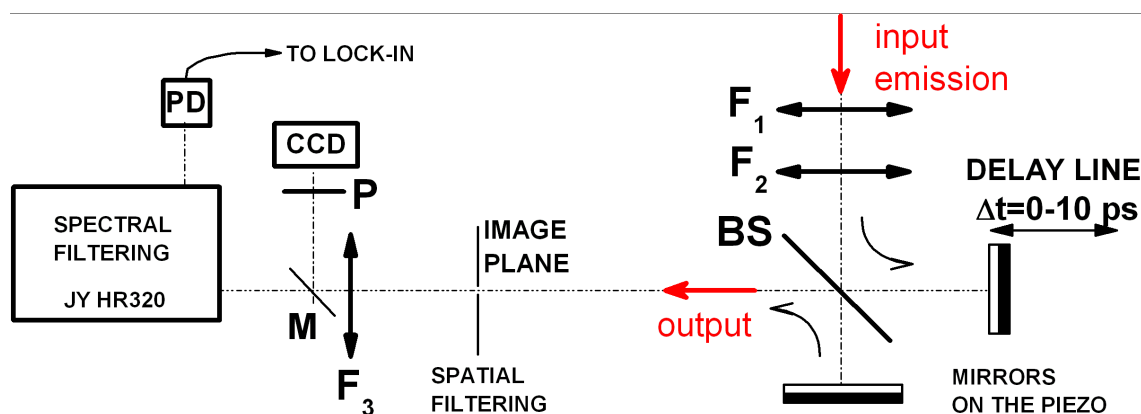


Figure 4.6: *Interferometry setup: $F_1 = 50 \text{ mm}$, $F_2 = 2000 \text{ mm}$, $F_3 = 100 \text{ mm}$. After exiting the output of the interferometer, the signal is spatially and spectrally filtered (temporal coherence). The PL signal is detected by a photodiode (PD) and sent to a lock-in amplifier. The signal can be directed towards a CCD camera by a movable mirror (M). Image on the CCD is magnified by a factor $\gamma = 40$. Laser scattering is eliminated by the spatial and polarization (P) filtering.*

This interferometer consists essentially of two movable mirrors forming two arms and a high quality pellicle (thin film) beam splitter. The input signal is split and sent into the two arms. Reflected signals are superimposed at the output. The mirrors are mounted on piezo-electric components, allowing tuning of the difference between

¹⁸All first order coherence measurements with the Michelson interferometer were performed at Ecole Polytechnique Fédérale de Lausanne in B. Deveaud's group. The interferometer was designed and built by S. Kundermann. People directly involved in the experiment were: M. Richard, S. Kundermann, A. Baas, P. Jeambrun and myself. I participated directly only in the temporal coherence experiments.

optical paths in both arms with an accuracy of around 10 nm. For a given delay between both arms the relative phase between the interfering PL signals is scanned over 6π , providing interference patterns. The signal is detected by the photodiode and sent to a lock-in amplifier. The interference contrast $c = \frac{I_{max} - I_{min}}{I_{max} + I_{min}}$ is measured as a function of the delay¹⁹. Precautions were taken to eliminate scattering of the excitation laser by using spatial, spectral and polarization filtering²⁰.

The advantage of this system is the presence of an active stabilization loop [Weh97, Sab02]. The light from a mono-mode, stabilized He-Ne laser is injected into the interferometer during measurements. The He-Ne interferometry feedback loop is used to lock the relative distance between both arms with a sub-wavelength precision of 10 nm, allowing one to realize relative phase resolved measurements.

Another feature is the entire computer control of the experiment. A LabView program has been written to control movements of the arms. One can choose the number of steps to scan the phase and the number of delay points. The contrast value is automatically calculated and plotted for each delay.

Care has to be taken to choose correctly the zero delay point between both arms and to properly superimpose the signals from the two arms spatially. This situation corresponds to the maximum contrast value for the given experimental conditions.

4.3.4 Photon correlator

For the second order temporal coherence studies, $g^2(t)$, we have used two single photon counting modules, id100-20, manufactured by id Quantique. Thanks to the small size (20 μm) of the active chip of these avalanche photo-diodes (APDs) their time resolution is as high as 70 ps. A very low dark current of 30 photons/s is observed. In order to study photon statistics, a photon correlator was built. The schema and a picture of the correlator are presented in figure 4.7.

The photoluminescence signal, selected by the monochromator, is collimated by the lens F_1 and then split by the non-polarizing cube beam splitter (BS) and focused on the APD chips by lenses F_2 with a magnification of $\gamma = 0.25$, forming a spot of size around 25 μm . The APD modules are mounted on XYZ Micro-control translation stages. The whole optical path is shielded by elastic tubes. The electronic signal from one of the APDs triggers the voltage ramp of the time to amplitude converter (TAC) of the Becker&Hickel's SPC-630 correlation card. The response of the second APD stops the TAC. The measured tension on the TAC is translated into the delay between start and stop signals²¹. The histogram of the number of coincidences in function of the relative delay between the start and stop signals is formed by the multi-channel analyzer (MCA). The time resolution of the photon correlator is 120 ps for counting rates $2 - 5 \cdot 10^5 s^{-1}$ ²².

¹⁹The phase is scanned over a distance 100 times smaller than the incremental delay, typically 0.5 ps or 150 μm .

²⁰Polarization filtering was used only in spatial coherence measurements

²¹The zero delay is determined by the difference between the cable lengths connecting the APDs with the correlation card. 20 cm of the cable corresponds to 1ns of the delay.

²²Time resolution starts to be degraded for counting rate higher than $8 \cdot 10^5 s^{-1}$

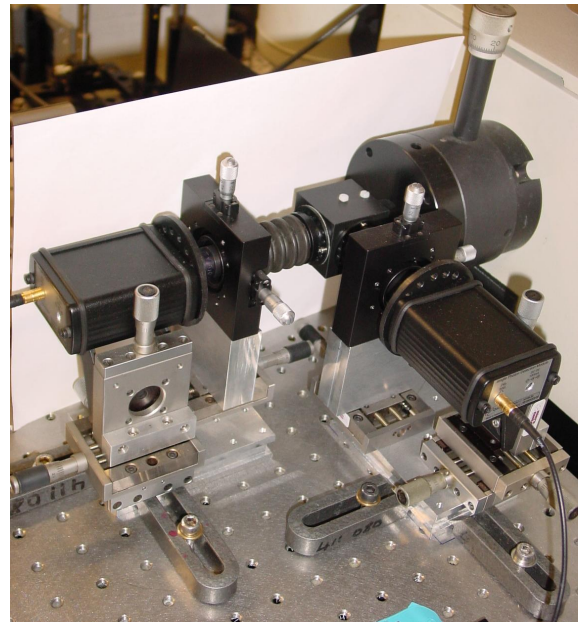
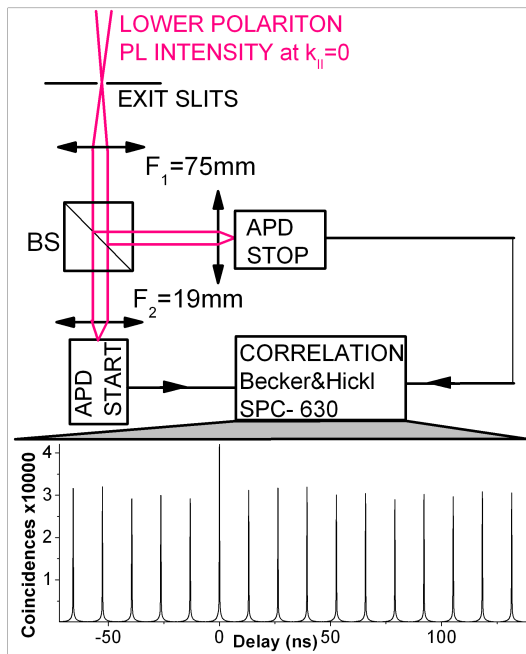


Figure 4.7: Photon correlator schema (a), and picture of the setup (b).

Conclusions The experimental methods used along this work were presented. The crucial experimental conditions were specified.

Chapter 5

Sample description and evidence for strong coupling

In this chapter we will present the 16 QW sample chosen for the demonstration of polariton condensation. We will also show evidence for the strong exciton-photon coupling regime. The strong coupling persists up to room temperature.

Contents

5.1 Microcavity sample	46
5.2 Evidence for strong coupling	48
5.3 Polaritons at room temperature	50

5.1 Microcavity sample

Our monolithic, MBE-grown microcavity sample consists of 16 $CdTe/Cd_{0.4}Mg_{0.6}Te$ 5 nm quantum wells (QWs) embedded in a 2λ Fabry-Perot like cavity. The design of the cavity places its fundamental optical mode at $\lambda \approx 735.5$ nm, in resonance with the excitonic transition in the QW. The resonator mirrors are Bragg reflectors, which are stacks of 23 (for the bottom mirror) and 17.5 (for the top mirror) pairs of lattice matched $Cd_{0.4}Mg_{0.6}Te/Cd_{0.75}Mn_{0.25}Te$ $\lambda/4$ layers. A refractive index contrast in the Bragg mirrors of 13% is sufficient to create a photonic stop band of width around 150 meV.

Of course, further increase of Mg content would increase the dielectric contrast, and so the photon confinement (see eq. (2.4)). One should keep in mind however that there is a significant difference in lattice constant between each member in the telluride family of materials (CdTe/MgTe - 0.9%, CdTe/MnTe - 2.2%, CdTe/ZnTe - 6%). Moreover, CdMgTe alloy is known to oxidize very rapidly for high Mg content, so the sample's lifetime would go down dramatically. Finally, the choice of alloys to build II-VI photonic structure is imposed by a compromise between obtaining a high dielectric contrast while maintaining a low lattice mismatch. Even if $\lambda/4$ layers

are intended to be lattice matched, we should keep in mind that a residual strain may be still present in the Bragg mirrors. Notably, because of the lattice mismatch between $CdTe$ and $Cd_{0.4}Mg_{0.6}Te$, QWs are strained.

A schema of the structure is presented in figure 5.1.

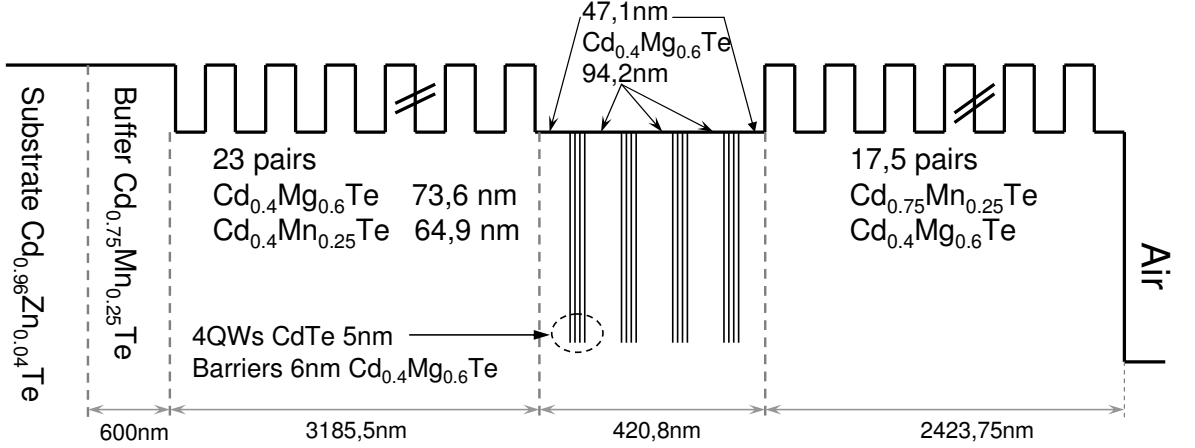


Figure 5.1: *Sample structure.*

For supplementary details about the growth process of CdTe-based microcavities see [And98], [Boe00], [Mul00], [Mox04]. The profile of the QWs may be investigated by means of the resonant Raman scattering technique [Bru06].

The great efforts made in the difficult task of fabrication of CdTe based microcavities proved very worthwhile, as soon as one wants to enter the strong light-matter interaction regime, and study high exciton density effects.

The higher ionicity of CdTe with respect to GaAs means that the excitonic Bohr radius (a_B) is 3 times smaller in CdTe QWs (3.9 nm). This value was estimated using equations 2b and 29 of [Mat92], with exciton binding energy in bulk CdTe $E_0 = 11\text{meV}$ and $E_{2s} - E_{1s} = 22\text{meV}$ - see figure 5.3. As explained above in section 1.4.1, reduced a_B has an impact on the oscillator strength of the excitonic transition and implies that the Rabi splitting Ω obtained for a single CdTe QW is much higher (7 meV) than for GaAs QW (2.5 meV). We also note that smaller a_B means that the exciton saturation density for CdTe QWs is one order of magnitude higher ($\sim 2.5 \cdot 10^{11}\text{cm}^{-2}$) than for GaAs QW. So excitons in CdTe QWs keep their bosonic nature for much higher densities. This advantage is crucial for condensation studies.

In order to maximize photon-exciton coupling, QWs are placed in each of the 4 nodes of the optical mode (4 QWs per node). The presence of 16 QWs increases the total excitonic oscillator strength which, combined with the excellent optical quality of the structure, leads us into the strong exciton-photon coupling with a Rabi splitting of $\Omega = 26\text{meV}$. As already stated in section 2.1, the strong coupling is demonstrated experimentally by the anti-crossing behavior of the formed polariton states. Thus, an experimental parameter to control the relative energy change of

exciton and photon modes is required. Mutual tuning may be realized in various ways. The exciton energy may be influenced by applying either an external electric [Fis95] or magnetic [Bru05] field or by changing the temperature [Lau90]. In our microcavity an additional degree of freedom is given by the existence of the thickness gradient along the sample. The variation of the cavity width along the sample has a sharp influence on the photon energy. The same percent of change of the QW width has only a very small effect on the exciton position, as only the confinement energy is affected.

Another straightforward method of observation of the strong coupling is a direct investigation of the polariton dispersion [Hou94].

5.2 Evidence for strong coupling

We now present the optical characterization of the sample by reflectivity measurements. The experiment is performed by collecting white light reflected from the sample and by imaging its far field onto the monochromator slit. The dispersed image of the slit give us a direct access into the polariton dispersion curve. By closing the slit vertically we can also choose a normal incidence reflectivity with accuracy of 1° . The signal obtained is normalized to the optical setup response, given by the reflectivity signal of a silicon mirror placed inside the cryostat. The mirror has a flat reflectance in the spectral range under consideration. The sample temperature is $T=5\text{K}$.

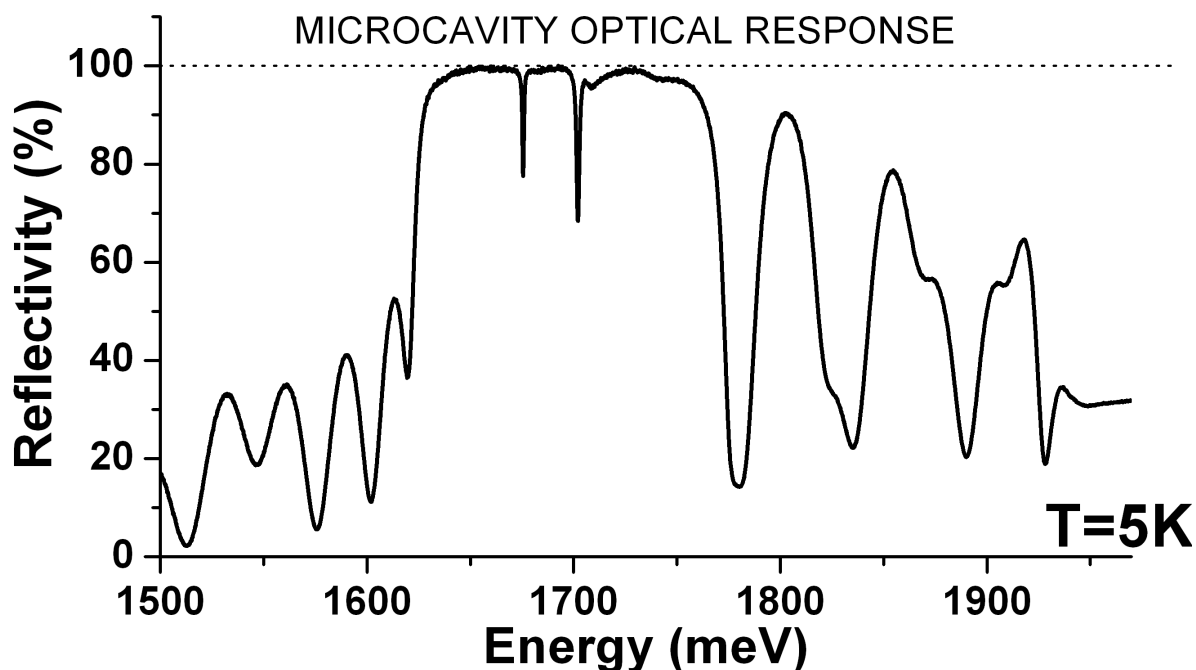


Figure 5.2: *Reflectivity spectrum.*

The normal incidence reflectivity is shown in figure 5.2. One can clearly see

two sharp peaks in the middle of the stop band. These correspond to the LP and UP states. A set of lateral lobes, corresponding to the "leaky modes" of the Bragg mirrors, is present on the low and high energy side of the spectrum.

The experiment is repeated for many points along the sample. The position of the polariton peaks as a function of the first high energy lobe (i.e. as a function of position on the sample) is plotted in figure 5.3. Three anti-crossings are clearly visible. This graph gives the evidence for strong exciton-photon coupling.

In fact, we deal here with a quite complicated polariton system: we observe not only the main anti-crossing of the photon mode $|PH\rangle$ with the heavy hole exciton $|X\rangle$, but also a clear anti-crossing with the 2S heavy hole exciton $|X_{2S}\rangle$, and the light hole exciton $|X_{LH}\rangle$. These states are identified by their energy difference and the ratio of the oscillator strengths with respect to the $|X\rangle$ [And98].

The spectra around the resonances are presented in the right part of figure 5.3. The high quality of the sample is confirmed by the splitting - linewidth ratio of 33²³. The linewidth of the upper polaritons increases due to the interaction with the continuum of the exciton states. The data presented in figure 5.3 are particularly useful for determining the detuning in photoluminescence experiments.

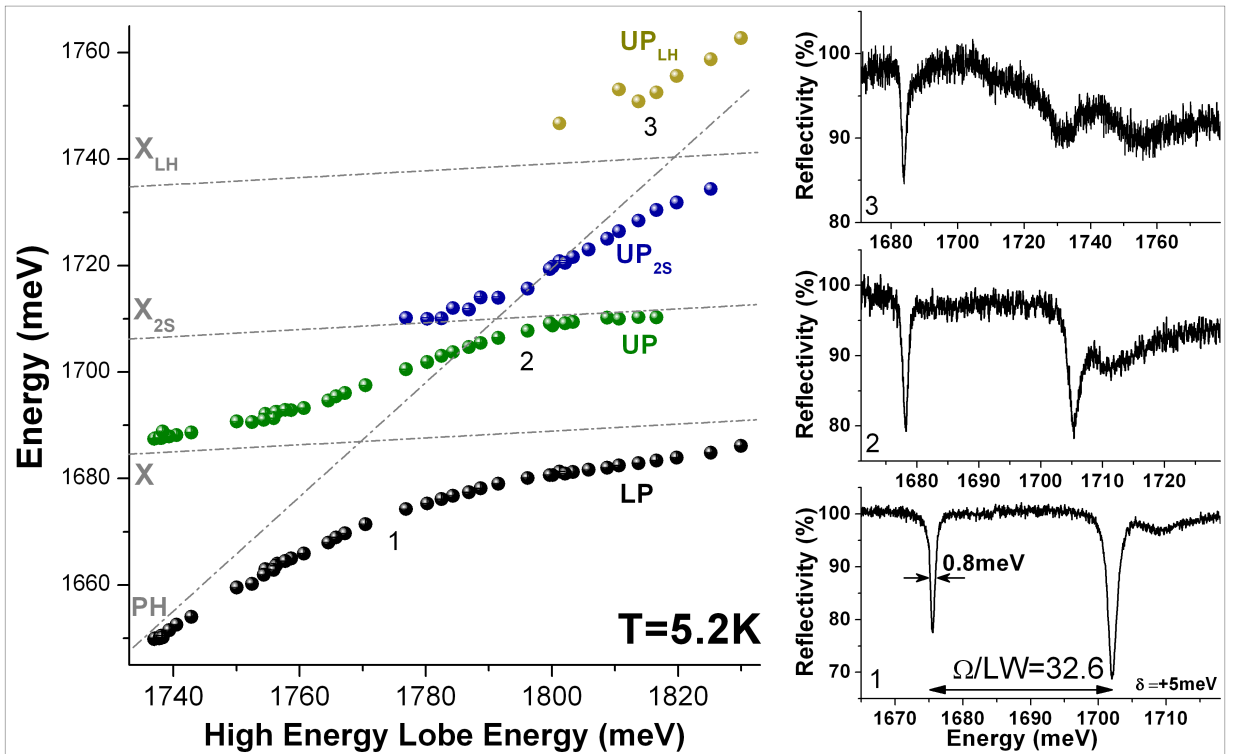


Figure 5.3: *Energy of polariton peaks vs. cavity energy (points). Dashed lines: energy of the uncoupled states. The anti-crossing behavior for the polariton states is clearly visible, demonstrating the strong coupling regime. Right panels: spectra around the resonances. The measured Rabi splitting is $\Omega = 26$ meV.*

²³An inhomogeneous broadening of $\Gamma = 0.1 - 0.2$ meV is present due to use of the $150\mu\text{m}$ spot.

As could be expected, the temperature tuning also exhibits anti-crossing feature and reconfirms the strong coupling regime (see figure 5.4).

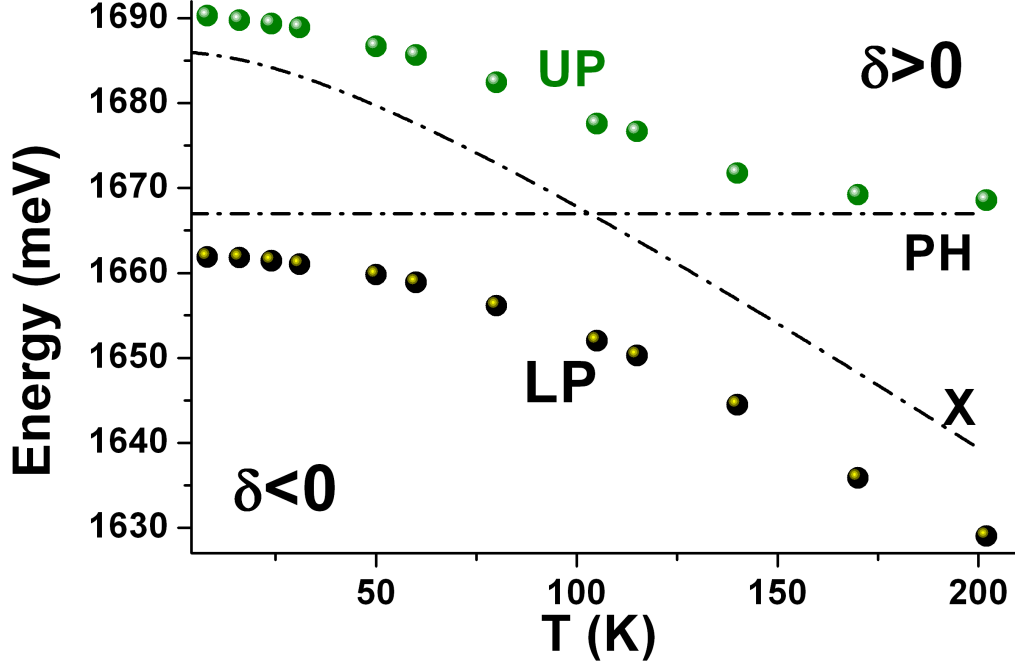


Figure 5.4: Energy of polariton peaks at normal incidence in reflectivity experiment as a function of temperature. Dashed lines: energy of the uncoupled states. The exciton energy depends strongly on the temperature [Lau90], whereas the cavity energy is not significantly affected. The anti-crossing behavior for the polariton states is clearly visible.

We demonstrate the strong coupling regime also by direct imaging of the polariton dispersion in the reflectivity configuration. The results showing anti-crossing of the polariton branches for four detunings are shown in figure 5.5.

5.3 Polaritons at room temperature

The same experiment as in figure 5.3 was performed also at room temperature. The result is shown in figure 5.6. An anti-crossing is clearly visible corresponding to a Rabi splitting of $\Omega_{300K} = 13$ meV²⁴. This strong reduction with respect to the low temperature Rabi splitting $\Omega = 26$ meV is due to the exciton-phonon interaction which results in an homogenous broadening of the exciton of $\sim 15 - 20$ meV at room temperature in a CdTe QW [Pel92, Nei93]. Figure 5.7 shows images of the polariton photoluminescence along the dispersion curve measured at $T=300K$. No stimulated emission in either the strong or weak coupling regime has been observed on this sample at room temperature.

²⁴For the temperature dependence of the Rabi splitting Ω in CdTe-based microcavities see [And98, Boe00]

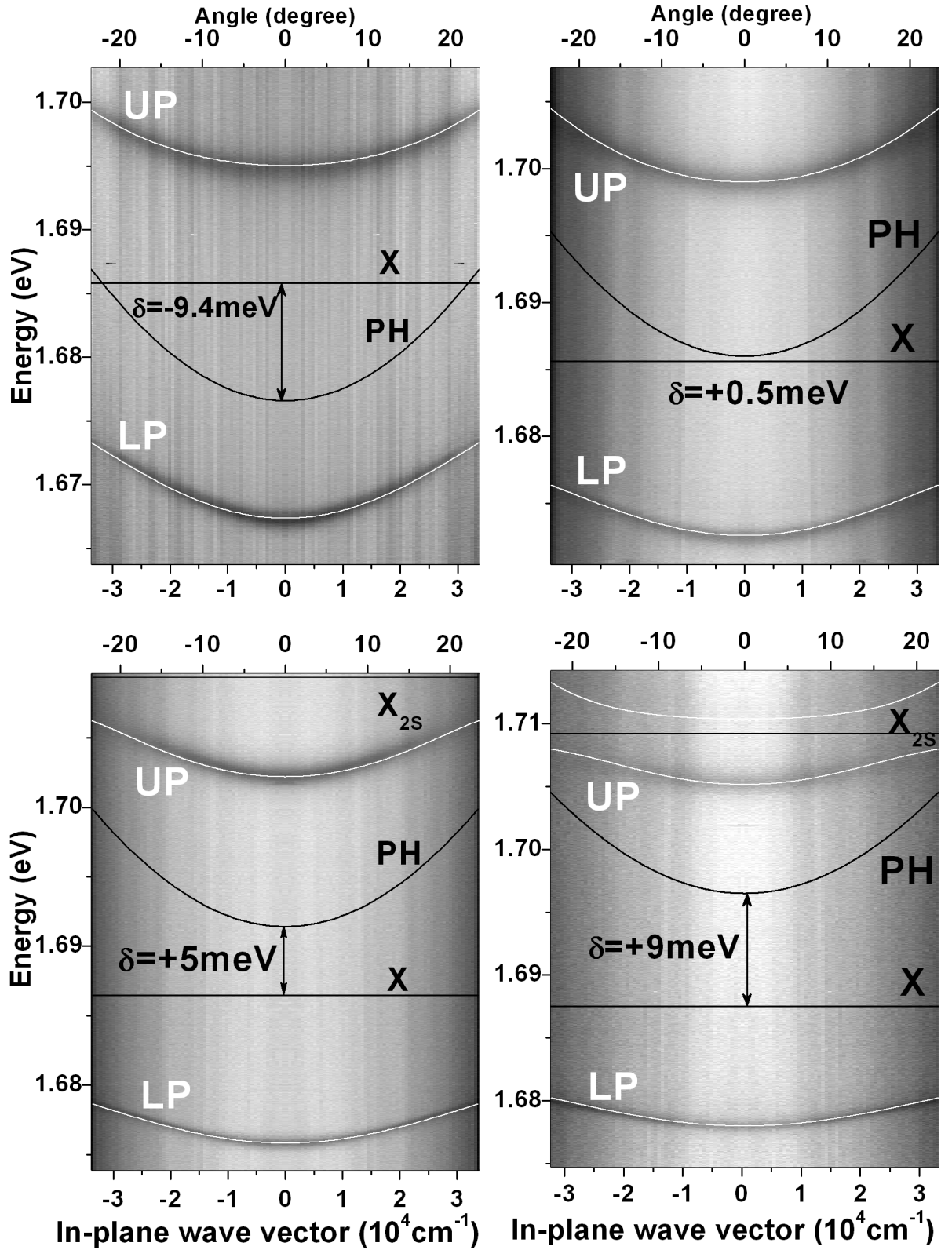


Figure 5.5: *Polariton dispersion in an angle resolved reflectivity experiment. Each image corresponds to a different detuning δ . The white lines are the result of the fit of the coupled oscillator model. The black lines correspond to the uncoupled exciton and photon states.*

It is worth noting that $\Omega_{300K} = 17.5$ meV has been obtained with a 24 QW microcavity.

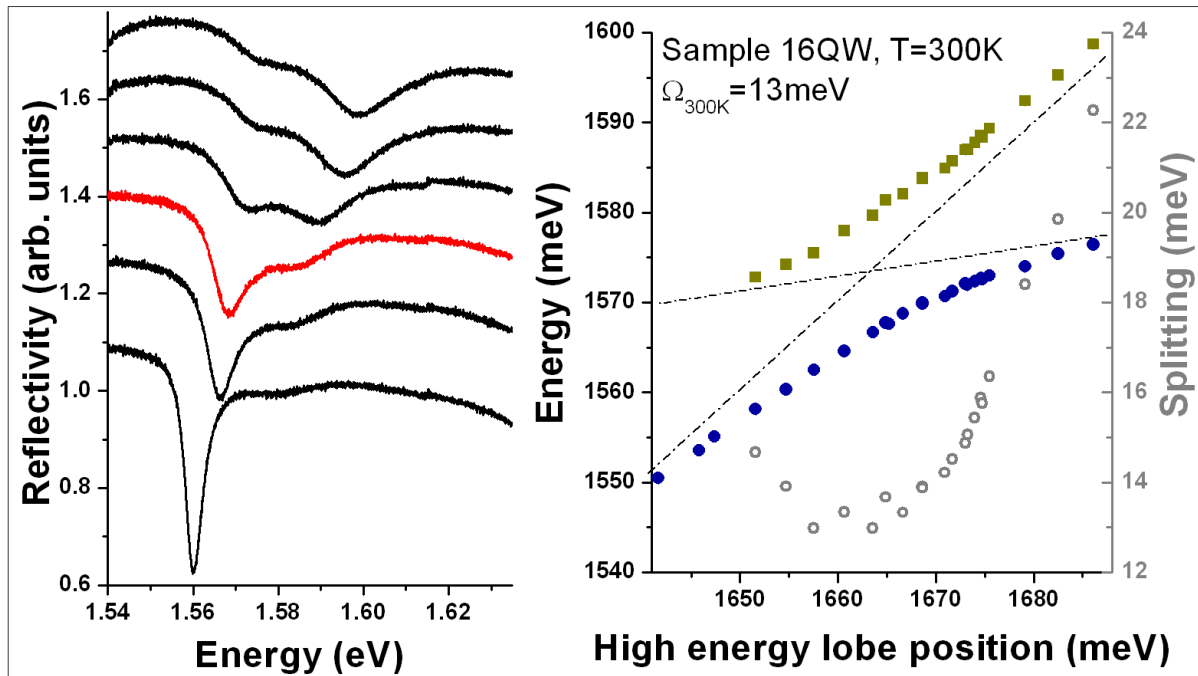


Figure 5.6: Sample characterization at $T=300K$. Left: the reflectivity spectra measured for different detunings. The spectrum at resonance is drawn in red. Right: the anti-crossing of the states demonstrating the strong coupling regime with $\Omega_{300K} = 13$ meV.

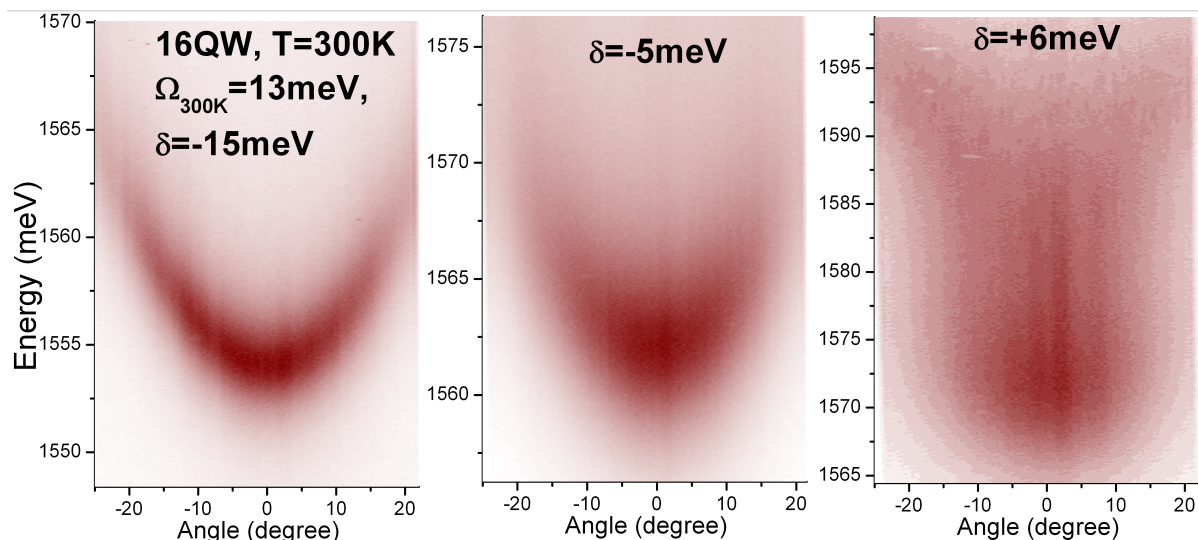


Figure 5.7: 2D images of the polariton photoluminescence along the dispersion curves at $T=300K$ for three detunings.

Conclusions The 16 QW microcavity sample used for our studies was presented. It exhibits the strong coupling regime with $\Omega = 26$ meV at T=5K and $\Omega_{300K} = 13$ meV at room temperature. The width of the lower polariton line at resonance is 0.6 meV at low temperature.

Chapter 6

Polariton condensation in momentum space

This chapter presents a detailed study of polariton condensation in momentum space at $T_{crysto} = 5K$.

We prelude the analysis with a brief summary of the major obstacles to realize the condensation in the solid state. The main advantages of the microcavity polariton system are pointed out once again.

After recalling the experimental details, we demonstrate that, in spite of the short polariton lifetime, polaritons can thermalize within the trap under well defined experimental conditions. The key point here is a high exciton fraction in the polariton. Increasing exciton density in the reservoir provokes **polariton-polariton** scattering towards the bottom of the trap, which becomes highly efficient for positive detunings. Enhanced polariton dynamics is illustrated by decrease of the dephasing time of the polaritons in excited states. The **full thermalization** of the polariton population below the condensation threshold is reported with an **internal polariton temperature** of $T_{eff} = (16 - 20)K$. Further increase of the polariton density results in spontaneous phase condensation. Above a critical density, **polariton condensation** in the bottom of the trap occurs: massive occupation of the polariton ground state and saturation of the excited states are observed. The internal temperature is well defined and does not change much across the transition. The critical density for the phase transition, the ground state occupancy and the condensate fraction are estimated. The dramatic change in the near field emission pattern through the transition is signalized. In this chapter, the onset of **spontaneous coherence** reflects only in the line narrowing at the condensation threshold, corresponding to increasing coherence time²⁵. With further increase of the polariton density, interaction induced decoherence is visible. The role of interactions in the condensate is examined and the nature of the polariton condensation is commented within the frame of the theoretical model.

We demonstrate that thermalization of the polariton population is an exceptional

²⁵For the complete discussion of the coherence properties of the polariton condensate see chapter 11.

effect of positive detuning. By changing the exciton-photon balance towards a more photon-like nature, the thermalization is quickly lost. In negative detuning the relaxation is strongly inhibited. A bottleneck effect in the emission angular pattern dominates. The polariton-polariton scattering mechanism is less active as shown by the linewidth analysis. However, increasing the excitation power triggers polariton ground state stimulation in the presence of a bottleneck, and non-equilibrium polariton condensation occurs.

The strong coupling regime is well preserved for all the experiments presented in this chapter.

Contents

6.1 Peculiarities of the condensation in the solid state	55
6.2 Polariton condensation in internal equilibrium - positive detuning	57
6.3 Non-equilibrium polariton condensation - negative detuning	72
6.4 The nature of the polariton condensation - theoretical remarks	76

6.1 Peculiarities of the condensation in the solid state

Bose-Einstein condensation as originally proposed applies to an infinite, three dimensional gas of non-interacting bosons, conserved in time and without internal structure. For a finite number of trapped, non-interacting particles in 2D the macroscopic occupation of the single particle state is also possible [Bag91, Ket96, Pet00]. The modern definition of BEC requires not only massive occupation of the single particle state, but also spontaneous development of long range correlations [Leg01, Pit03].

The BEC observed in atomic physics, even if **very close** to the proposal of Einstein, does not reach the ideal case. Interatomic interactions, though strongly quenched in diluted atomic vapors, can be still important [Bur99]. For example, they are responsible for depletion of the condensate. The number of particles is finite. At the same time condensation of cold atoms takes place on the second-like time scale compared to the micro-second thermalization time [Dav95]. So an atomic system can be considered to be in thermal equilibrium, with well defined thermodynamic functions. The modern criterion of the BEC, i.e. development of long range correlations extending over the whole condensed cloud, is clearly demonstrated (see figure 1.4).

The attempts to demonstrate BEC in a semiconductor system meet difficulties that are hard to overcome (see chapter 1.4). The major obstacle here is the fact that quasi-particles in solids, such as excitons, are characterized by finite lifetime. The

ideal case of a BEC in a real thermal equilibrium is hardly imaginable. Moreover, the center of the Brillouin zone is almost not dispersive. Thus, the methods used to demonstrate exciton equilibration by spectroscopic means are not straightforward. Excitons in solids are usually created by photon absorption. Therefore, permanent optical pumping is required to sustain exciton population. For the above mentioned reasons, the studies of condensation in solid state must inevitably confront the impact of non-equilibrium physics due to the pumping/decay process [Szy06].

The second problem arises from the fact that the excitons in solids, are composite bosons consisting of two fermions. Therefore they experience strong mutual interactions. Due to their fermionic origin and the Coulomb forces, effects coming from the Pauli exclusion rule (like phase space filling and exchange) cannot be neglected for high exciton densities. A small exciton binding energy (5-10 meV in semiconductors like GaAs) means that the bosonic nature of an exciton is rather fragile and is rapidly lost when increasing the carrier density. As the saturation density depends on the exciton Bohr radius, the bosonic character of an exciton is much better preserved in wide band gap semiconductors.

In the realm of solid state quasi-particles, 2D microcavity polaritons are promising candidates to attain condensation in an excitonic system. The polariton, having a partially excitonic nature, inherits "excitonic problems" as concern condensation. However, the photon part of the polariton introduces some important features making the polariton system worthy of interest. In particular, there is an unusually steep in-plane dispersion $E(k_{\parallel})$ for polaritons as compared to excitons. For the lower polariton branch a characteristic trap in reciprocal space is formed within the strong coupling zone. The polariton mass around the bottom of this trap is 4-5 orders of magnitude lower than the pure exciton mass. This radical reduction makes it possible to reach high occupancy factors for the LP ground state in the low exciton density limit - more than an order of magnitude lower than the exciton saturation density for CdTe-based microcavities. Moreover, thanks to the two-dimensional nature of the system and strong polariton dispersion, one is able to probe the polariton relaxation towards the ground state by means of angle resolved measurements. The characteristics of the LP trap, flexibility for its engineering (by the coupling strength and the detuning) and the facility of monitoring the relaxation within the LP trap are big advantages which, combined together, make the polariton system convenient for studying BEC in the solid state.

At the same time the strong mixing with the photon turns out to be a drawback when we consider polariton lifetime, which is in our case 1-2 ps. This value is generally much shorter than the relaxation time towards the ground state by phonon interaction. Therefore, the polariton population distribution is normally out of thermodynamical equilibrium with the host lattice and suffers from the relaxation bottleneck effect: photoluminescence comes mainly from high energy states in the LP trap. In this chapter we demonstrate that this obstacle can be overcome by optimizing the exciton fraction of the LP. Polariton thermalization below the condensation threshold is reached under positive detuning.

6.2 Polariton condensation in internal equilibrium - positive detuning

Experimental conditions Observation of the polariton far-field emission allows us to investigate the polariton distribution in k-space and along the dispersion curve. Careful detuning studies in the range $(-0.77 \leftrightarrow 0.4)\Omega$ are performed. An experimental driving parameter for the transition towards the condensed phase is the excitation power i.e. the injected carrier density. The microcavity is excited by a CW-Ti:Sapphire laser, combined with an acousto-optic modulator (1 μs pulse, 1% duty cycle) to reduce sample heating. The use of **continuous excitation** ensures the steady state regime and is a necessary condition for demonstrating thermal equilibrium. The laser beam was carefully shaped into a "top hat" intensity profile in order to provide an **uniform excitation spot** of about 30-35 μm diameter on the sample surface. The excitation energy was set at around 100 meV above the polariton ground state. This ensures that **exciton polaritons initially injected in the system are incoherent**, which is an important condition for demonstrating a spontaneous phase transition. The excitation beam is coupled to the intra-cavity field via the first reflectivity minimum of the Bragg mirrors.

Results We start the analysis by presenting the spectral and angular distribution of the emission as a function of the excitation power for a few positive detunings. The upper set of panels in figures 6.2 displays pseudo-3D images of the angular distribution of the spectrally integrated emission for detuning $\delta = +7.7$ meV. Below threshold (left), the emission exhibits a smooth distribution around the ground state. When the excitation intensity is increased, **the emission from the zero momentum state becomes predominant at threshold (centre) and a sharp peak forms at $k_{\parallel} = 0$ above threshold (right)**. At the same time **emission from the excited states saturates** above threshold. The lower panels of figure 6.2 show the energy and angle resolved emission intensities. It can be seen that the width of the momentum distribution shrinks with increasing excitation intensity, and above threshold, the emission mainly comes from the lowest energy state at $k_{\parallel} = 0$. The same qualitative behavior is found for different points on the sample corresponding to the detunings $\delta = +10.7, +7.2, +6.5, +5.4$ and $+5.3$ meV. Typical results are displayed in panels 6.3 A) and B).

Condensation of polaritons in reciprocal space should be reflected by a macroscopic phase coherence of their wave-function in real space. The various aspects of polariton condensation in real space are discussed in chapter 9. At this point, we mention only that, in agreement with previous studies [Mox05], dramatic changes take place in the near field emission pattern. In the weak excitation regime the emission pattern is homogenous and corresponds to the shape of the excitation laser spot. Above condensation threshold, the emission pattern breaks up into a few strongly localized, bright spots - see figure 6.1.

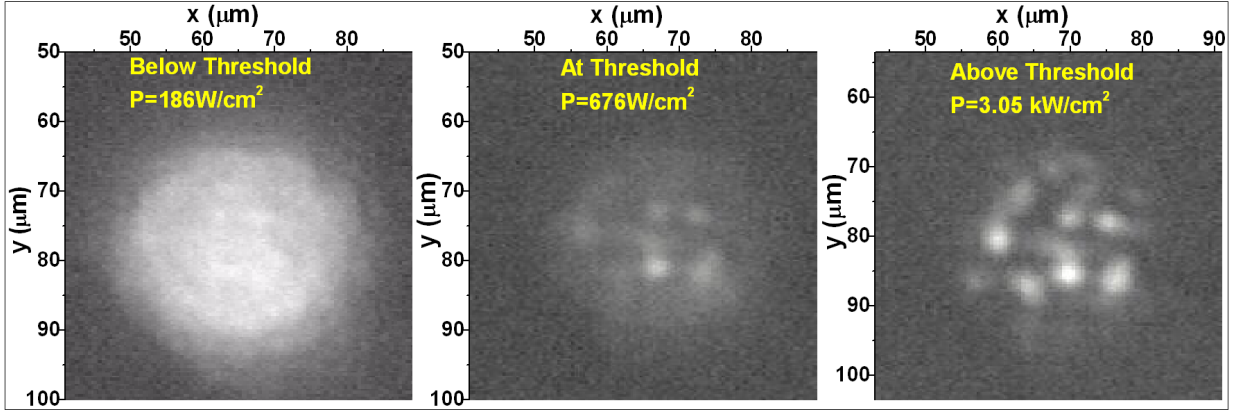


Figure 6.1: *Two-dimensional images of the near-field polariton PL for different pumping powers. Above condensation threshold polariton emission mainly comes from a few micron-size, strongly localized, spots. Vertical and horizontal axes are in-plane coordinates on the sample surface. PL intensity increases from black to white. Detuning $\delta = +5.4$ meV (the corresponding far field emission is shown in figure 6.3).*

Thermalization and condensation. Polariton internal temperature. The occupation of the polariton states can be extracted from the emission resolved in energy and angle by taking into account the radiative lifetime of polaritons. We concentrate first on the analysis of the data presented in panel 6.2. Figure 6.4 a) shows the occupancy of the $k_{\parallel} = 0$ ground state, its emission energy and linewidth as a function of the excitation power. With increasing excitation, the occupancy increases linearly at first. Then the exponential growth with a sharp threshold-like behavior is seen. It should be noted that the occupancy at threshold is estimated to be of the order of unity (see next paragraph). This is consistent with a polariton relaxation process stimulated by the polariton population in the ground state, which is a specific feature of boson driving mechanism of BEC. The emission blue-shift was measured to be a tenth of the Rabi splitting at a excitation power 10 times greater than the nonlinear threshold, confirming that the microcavity is unambiguously in the strong coupling regime. The origin of this blue-shift is discussed later on.

The linewidth of the $k_{\parallel} = 0$ emission shows significant narrowing at the nonlinear threshold, down to a third of the polariton linewidth in the linear regime. As is shown in chapter 11, this narrowing corresponds to the spontaneous increase of the coherence time. Line broadening observed at higher excitation is due to phase diffusion induced by polariton self-interaction [Por03].

Figure 6.4 b) displays the occupancy of polariton states as a function of their energy on a semi-logarithmic scale, for various excitation powers. At very low excitation power (shown in figure 6.5), the polariton occupancy is not thermalized [Mox05, Tas97]. Close to threshold ($P = 0.86 \cdot P_{thr}$), the occupancy can be fitted with a Maxwell-Boltzmann distribution, indicating a polariton gas in internal equilibrium at around 16 K. Above threshold, one can clearly observe a bimodal dis-

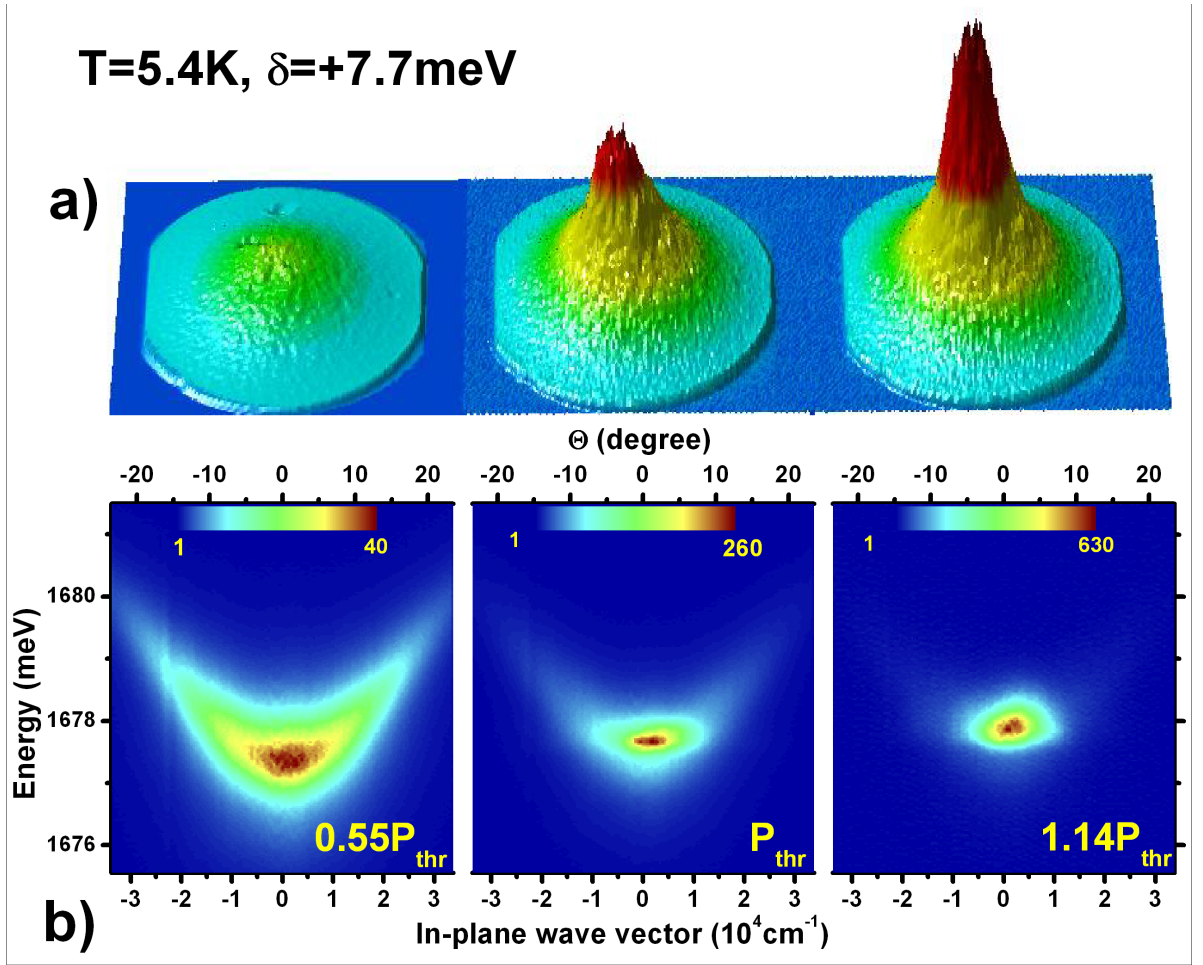


Figure 6.2: *Far-field emission measured at $T=5.4\text{ K}$ for three excitation intensities: $0.55 \cdot P_{thr}$ (left panels), P_{thr} (centre panels), and $1.14 \cdot P_{thr}$ (right panels); $P_{thr} = 1.67\text{kW} \cdot \text{cm}^{-2}$ is the threshold power for condensation. (a) Pseudo-3D images of the far-field emission within the angular cone of $\pm 23^\circ$, with the emission intensity displayed on the vertical axis (in arbitrary units). With increasing excitation power, a sharp and intense peak is formed in the center of the emission distribution ($\Theta_x = \Theta_y = 0^\circ$), corresponding to the lowest momentum state $k_{||} = 0$. Note that the intensity from excited states is saturated. The color and intensity scale in (a) is the same for all three figures. (b) Same data as in (a) but resolved in energy. For such a measurement, a slice of the far-field emission corresponding to $\Theta_x = 0^\circ$ is dispersed by a spectrometer and imaged on a CCD-camera. The horizontal axis displays the emission angle (top) and the in-plane momentum (bottom); the vertical axis displays the emission energy in a false color scale (different for each panel). Below threshold (left panel), the emission is broadly distributed in momentum and energy. Above threshold, the emission comes almost exclusively from the lowest energy state $k_{||} = 0$ (right panel). A small blue-shift of about 0.5 meV , or 2% of the Rabi splitting, is observed for the ground state, which indicates that the microcavity is in the strong coupling regime.*

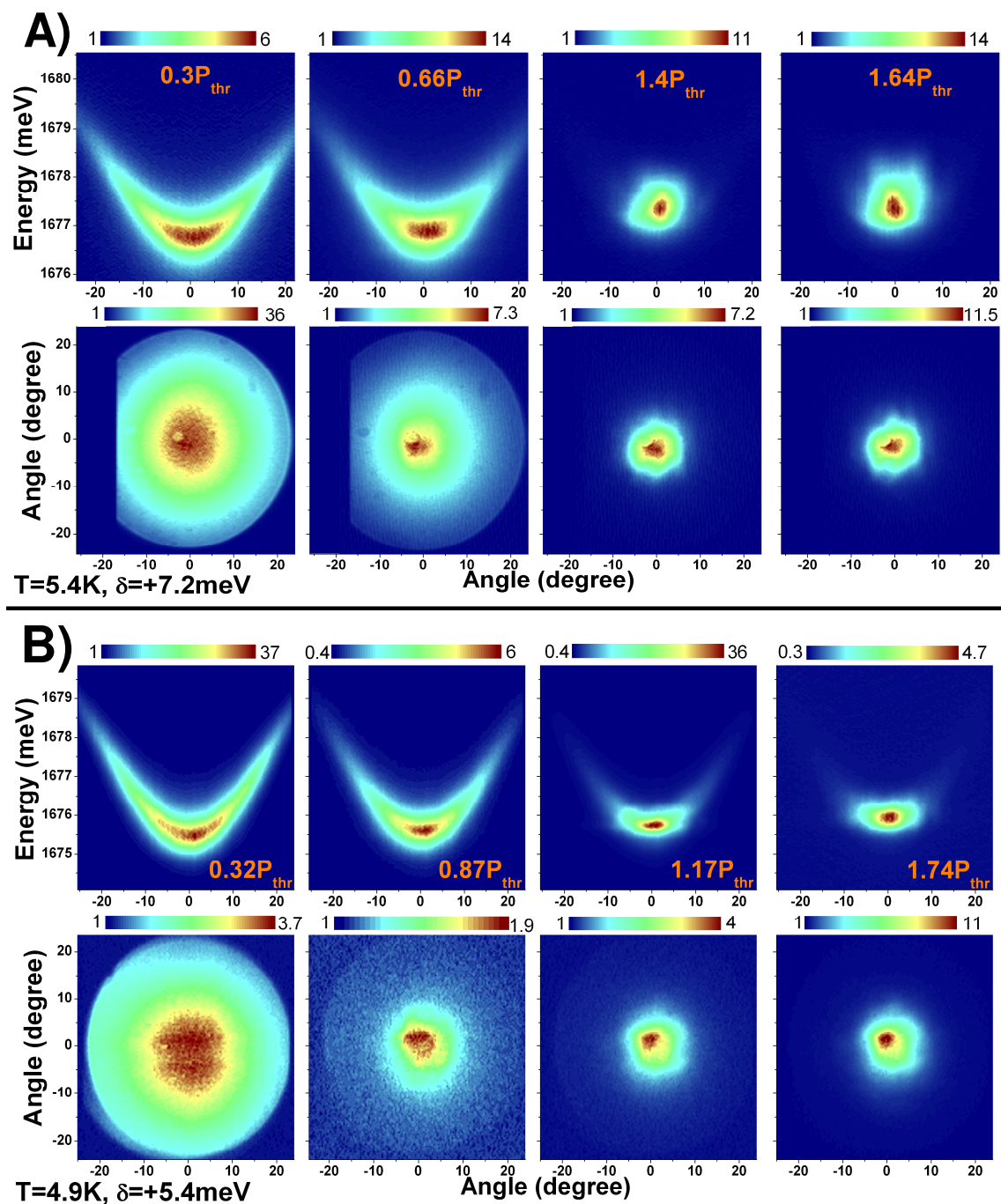


Figure 6.3: Far-field emission measured at low temperature for four excitation intensities and detunings $\delta = +7.2 \text{ meV}$ - A and $\delta = +5.4 \text{ meV}$ - B. With increasing excitation power, a sharp and intense peak is formed in the center of the emission distribution ($\Theta_x = \Theta_y = 0^\circ$), corresponding to the lowest momentum state $k_{\parallel} = 0$. Upper parts of each panel present the spectrally resolved far field emission. The horizontal axis displays the emission angle; the vertical axis displays the emission energy in a false color scale (different for each panel). Below threshold (left part of the panel), the emission is broadly distributed in momentum and energy. Above threshold, the emission comes almost exclusively from the lowest energy state (right panels) $k_{\parallel} = 0$.

tribution marked by saturation of the excited state population and the formation of a condensate in the ground state. Such a behavior is typical of a BEC. We additionally illustrate saturation of the excited states in figure 6.6, where the angularly and spectrally resolved polariton emission under excitation power around threshold are plotted on the same color scale. For the data taken at $\delta = +7.7$ meV we cannot obtain a reasonable fit for the low energy part of the occupancy using a Bose-Einstein distribution. This is not surprising, since in a non-ideal Bose system, interactions are responsible for changes in the density of states and depletion of the condensate in favor of excited states. This constitutes a caution against over-interpretation of the Bose-Einstein distribution for non-interacting particles when far into the condensed regime [Gri95, Ens96].

In figure 6.5 we present an analysis of the data shown in figure 6.3 B). As in figure 6.4 one can see, a clear threshold for turn-on of the stimulated scattering, accompanied by line narrowing and blue-shift of the emission. We now present the analysis of the polariton population along the dispersion curve, as a function of the excitation power. For this set of data, the thermal part can be fitted with a Bose-Einstein distribution with good accuracy. Thus, in this case polariton gas is approaching the ideal Bose gas. The saturation of the excited states is also well marked. The common error bar (drown in the middle of the figure) corresponds to the uncertainty of the occupancy estimate and the characteristic polariton linewidth. Bose-Einstein distribution above threshold was also observed for the other set of data corresponding to detuning $\delta = +5.3$ meV - not shown. The results of the fit are displayed in figure 6.5 b. The data are fitted with a function:

$$n(T_{eff}, \mu_{eff}) = \frac{N_0}{e^{\frac{E - \mu_{eff}}{kT_{eff}}} - 1} \quad (6.1)$$

The fitting parameters are: μ_{eff} - effective chemical potential, T_{eff} - effective polariton temperature. For a very low pumping, the system is not thermalized. Just below threshold for condensation the polariton population reaches an internal equilibrium with the $T = (18.6 \pm 0.7)K$. Above threshold, the polariton distribution clearly deviates from classical Maxwell-Boltzmann statistics and takes the form corresponding to quantum, Bose-Einstein statistics. The polariton distribution above threshold is fitted with the same effective temperature and with the negative effective chemical potential approaching zero (see inset in figure 6.5 B)). We emphasize that T_{eff} does not change across the the transition, which means that the increase of the pumping rate only increases the number of particles in the system without heating it.

Thermalization of the polariton population below the condensation threshold is confirmed for a relatively narrow detuning range of $+0.19\Omega$ to $+0.4\Omega$ i. e. $+5$ to $+10.7$ meV. As we show in section 6.3, the polariton population can no longer thermalize for negative detuning, because of the lower efficiency of the scattering mechanism within the trap and the shorter polariton lifetime.

Increasing the detuning results in an increase of the polariton lifetime. This should favor condensation at lower pump powers, since the stimulation starts as soon as the filling rate starts to be comparable with the emission rate from the

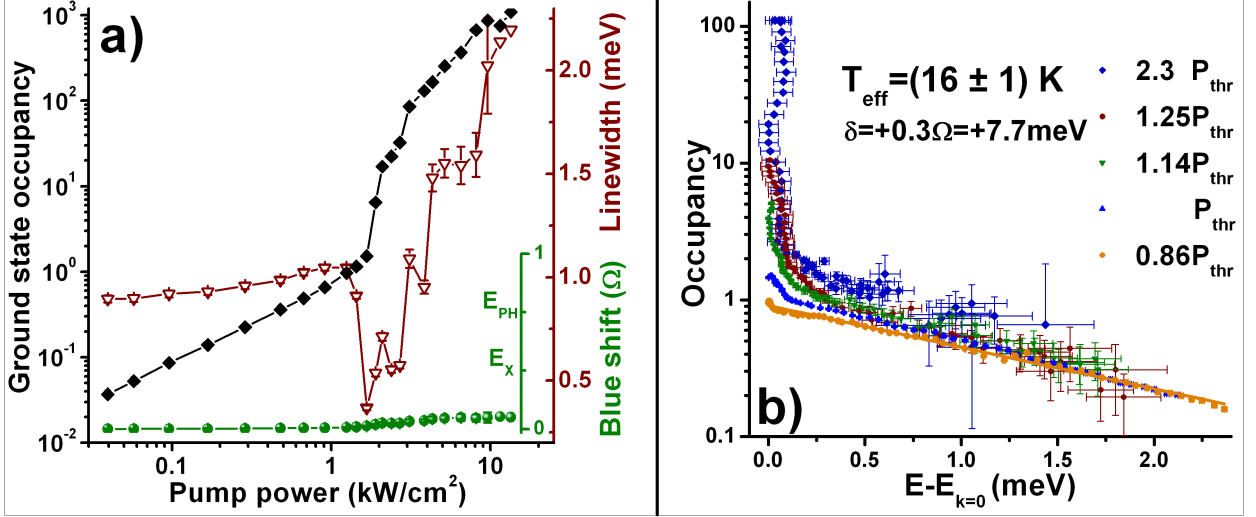


Figure 6.4: Polariton occupancy measured at 5.4 K. A: Occupancy of the $k_{\parallel} = 0$ ground state (solid diamonds), its energy blue-shift (solid circles) and linewidth (open triangles) versus the excitation power. The blue-shift is in units of the Rabi splitting $\Omega = 26$ meV. For low excitation, the ground state occupancy increases linearly with the excitation then exponentially right after threshold. This sharp transition is accompanied by a decrease of the linewidth by about a factor 3, corresponding to an increase of the polariton coherence. Further increase of linewidth is due to interaction between polaritons in the condensate. The polariton ground state slightly blue-shifts, by less than 10 % of the Rabi splitting for excitation about 10 times the threshold power, staying well below the uncoupled exciton (E_X) and photon mode (E_{PH}) energies. This is a clear evidence of the strong coupling regime. B: Polariton occupancy in ground and excited levels is plotted in a semi-logarithmic scale for various excitation powers. For each excitation power, the zero of the energy scale corresponds to the energy of the $k_{\parallel} = 0$ ground state. The occupancy is deduced from far-field emission data (see figure 6.2), taking into account the radiative lifetime of polaritons. At excitation power just below threshold ($0.86 \cdot P_{thr}$) the polariton gas is fully thermalized, as evidenced by the exponential decay of the occupancy distribution. Above threshold a bimodal distribution is observed: the ground state becomes massively occupied whereas the excited states are saturated, which is typical of BEC. The polariton thermal cloud is at 16 K and not significantly changed when increasing the excitation to twice the threshold power.

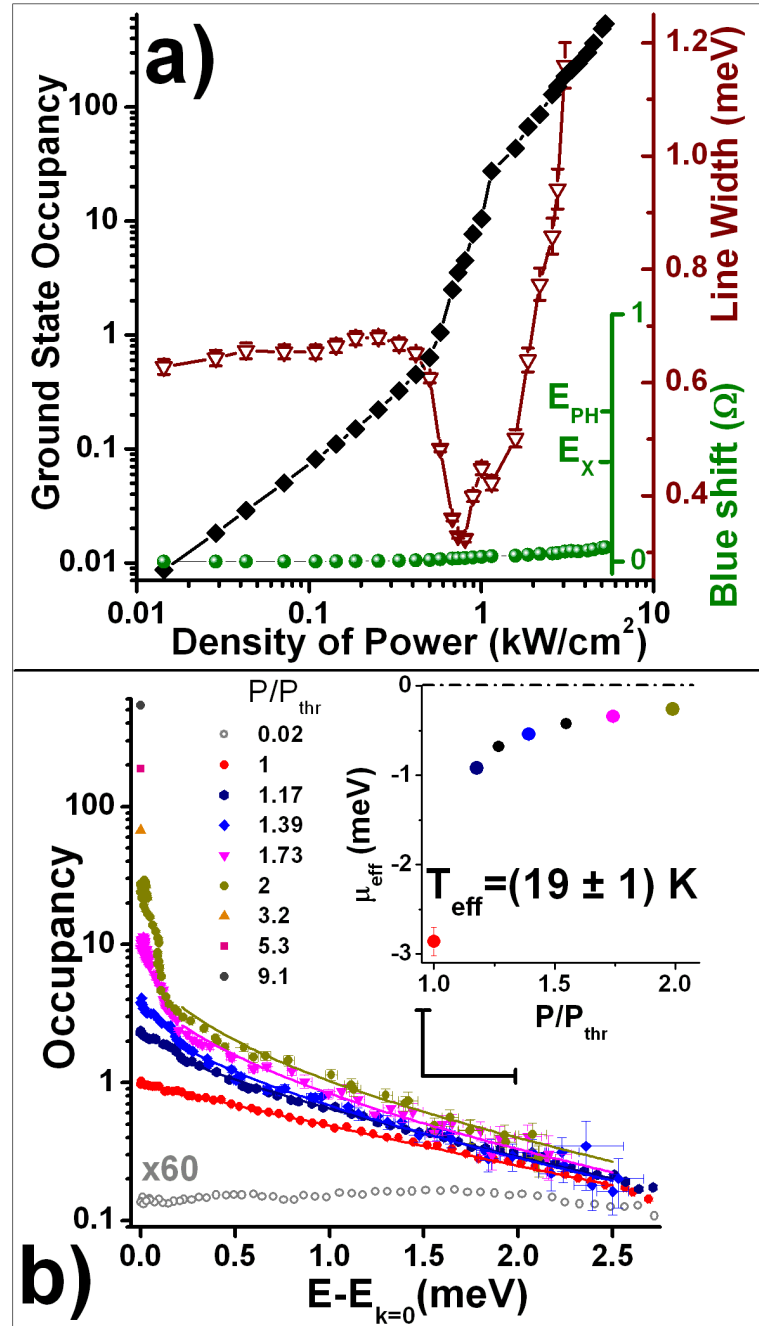


Figure 6.5: Polariton state occupancy measured at 4.9 K for $\delta = +5.3$ meV. a): as in figure 6.4, b): Polariton occupancy in ground and excited levels is plotted in a semi-logarithmic scale for various excitation powers. The occupancy is deduced from far-field emission data (see figure 6.3 B), taking into account the radiative lifetime of polaritons. For very low excitation level ($0.02 \cdot P_{thr}$) the polariton distribution is not thermalized. At the stimulation threshold the polariton gas is in internal equilibrium, as shown by the exponential decay of the occupancy distribution. Above threshold, the ground state becomes massively occupied whereas the excited states are saturated, which is typical of a BEC. The thermal part of the distribution can be fitted with a Bose-Einstein statistics with a constant $T_{eff} \approx 18.6$ K and μ_{eff} approaching zero above threshold. For the highest pump powers, the emission is entirely dominated by the condensate emission, preventing analysis of the thermal tail. Black error bar represents the total uncertainty of occupancy and energy.

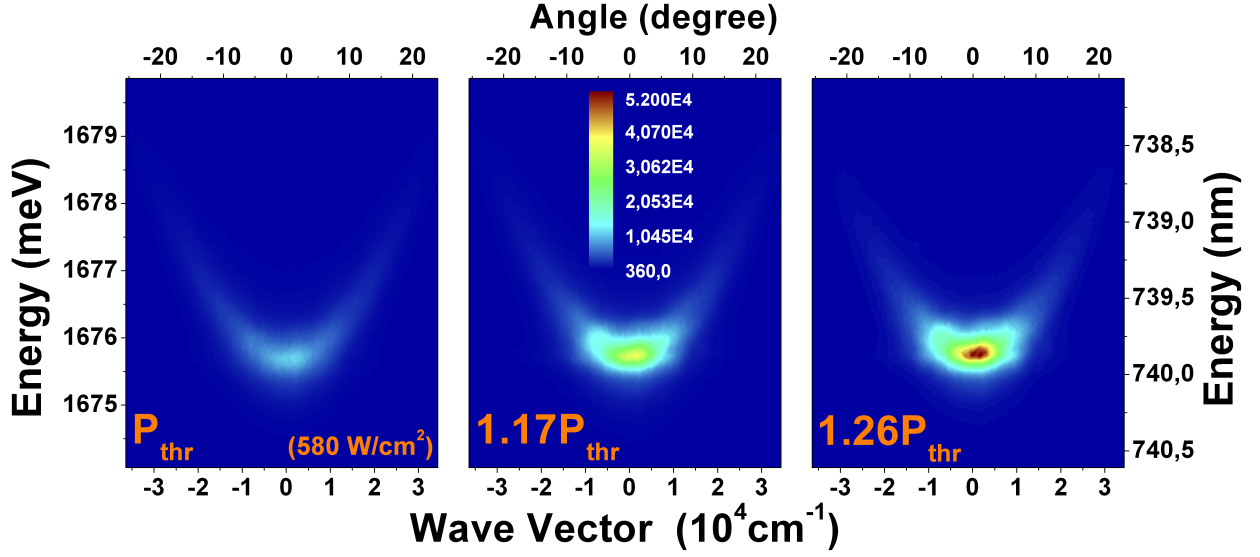


Figure 6.6: Saturation of the polariton excited states at threshold, $\delta = +5.4 \text{ meV}$. Increasing the excitation power results in adding the particles into the ground state, whereas the excited states becomes saturated. This is a typical characteristic of BEC. The color scale is the same for the three excitation powers.

ground state. The opposite is seen: With increasing the detuning towards more positive values, rapid increase of the threshold excitation density is observed. This is possibly due to increase of the polariton density of states around the bottom of the trap. This phenomenon is illustrated in figure 6.7, where the threshold pump power is presented as a function of the detuning.

Acceleration of the polariton dynamics - linewidth analysis The observation of a polariton gas in internal thermal equilibrium is surprising and could appear puzzling considering the short polariton radiative lifetime (1-2 ps). The necessary condition to attain equilibrium is for the polariton scattering rate to be faster than the radiative decay time. The collisional broadening of the polariton as a function of the pump power and the detuning has been already studied by using an angle resolved four wave mixing technique [Huy03]. It was found that the polariton dephasing time decreases with increasing pump power and angle. The similar conclusion can be extracted from [But02], where a strong increase of the linewidth is seen for the polariton excited states when the pump power is increased. Only the very recent data show that in a GaAs-based microcavity for positive detuning and high pump power the thermalization time can be as much as 10 times shorter than the radiative lifetime [Den06].

In fact, in our case, for positive detuning, strong broadening of the polariton emission along the dispersion curve is observed for excitation around threshold. This indicates that the dephasing time due to polariton-polariton scattering is shorter than the polariton lifetime by a factor of 2 (figure 6.8 A). Such a mechanism has been proposed for polariton BEC [Por02] and, as we have seen, indeed permits

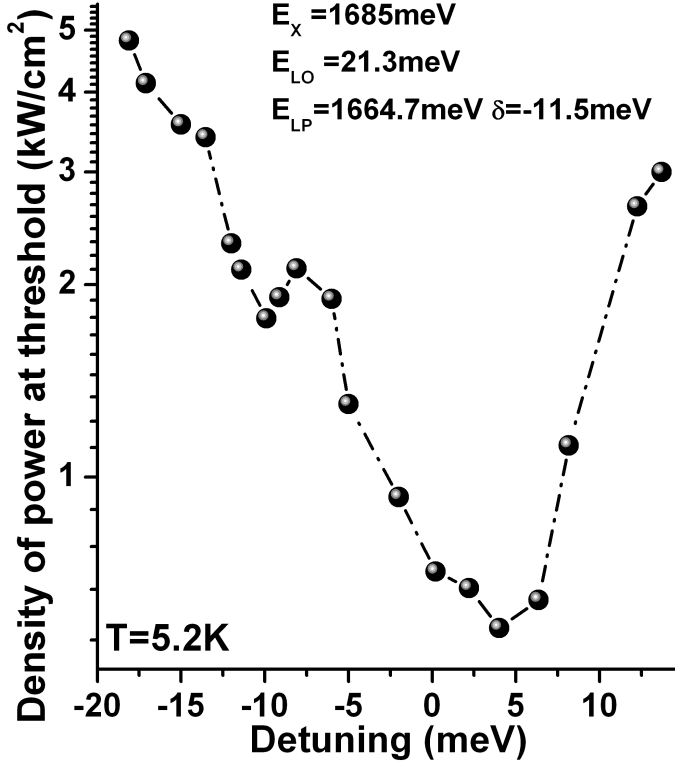


Figure 6.7: Threshold pump power for condensation as a function of detuning, $T=5.2K$. For positive detuning the threshold power grows very rapidly due to increase of the polariton density of states at the bottom of the trap. For negative detuning the threshold power also grows due to a decrease of polariton-polariton scattering efficiency. The lowest threshold occurs for detunings $+(2-5)$ meV. The local minimum, visible for $\delta = -11.5$ meV, corresponds to the increase of the polariton relaxation due to the resonance between the optical phonon energy and the difference between the exciton level and the polariton ground state level [Boef00].

attainment of internal thermal equilibrium before the escape of polaritons out of the microcavity. It is interesting to perform the linewidth analysis also for negative detuning, where thermalization is not attained (figure 6.8 B). In this situation no significant broadening of the polariton excited states is observed. The polariton dephasing time remains longer than the radiative lifetime. As could be expected, the polariton-polariton scattering efficiency decreases in negative detuning precluding polariton thermalization.

Some estimates: density of injected carriers, saturation density, critical density and occupancy factor It is instructive to give some estimates of the characteristic densities in the system. First, let us evaluate the density of injected carriers per quantum well at condensation threshold:

$$D[\text{cm}^{-2}] = \frac{DoP}{En} \times (1 - R) \times \tau_x \times \alpha_{QW} \approx 1.4 \cdot 10^{10} \text{cm}^{-2} \quad (6.2)$$

, where

- $DoP \approx 1 \text{ kW} \cdot \text{cm}^{-2}$ - a typical density of the excitation power at threshold
- $En \approx 1.76 \text{ eV}$ - energy of the pump
- $R \approx 0.15$ - reflectivity of the microcavity for the pump energy

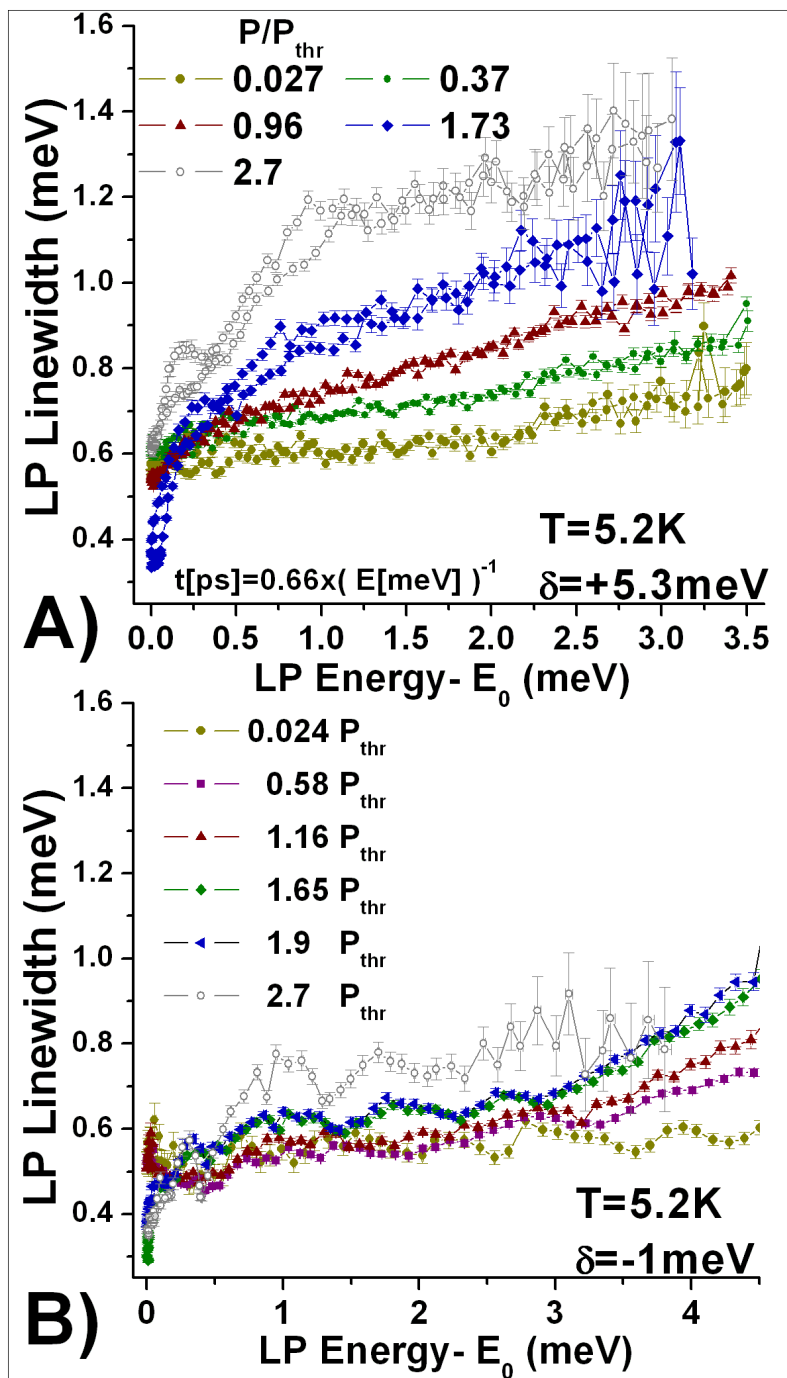


Figure 6.8: Acceleration of the polariton dynamics: linewidth analysis for detunings $\delta = +5.3\text{ meV}$ - A) $\delta = -1\text{ meV}$ - B). For positive detuning the polariton-polariton scattering mechanism is efficient. This causes the dephasing time to be shorter than the radiative lifetime enabling thermalization of the polariton population. For negative detuning, the collisional broadening of the polariton excited states is reduced, illustrating a lower efficiency of the polariton scattering process, which prevents equilibration of the polariton population.

- $\tau_x \approx 140ps$ - the lifetime for an exciton in a reservoir [Poh92]
- $\alpha_{QW} \approx 3\%$ - absorption coefficient of the quantum well

The value obtained gives the upper limit of the exciton density in the reservoir per quantum well. Of course, not all electron-hole pairs form excitons. Moreover, most of the created excitons will instantaneously recombine into the leaky modes of the Bragg mirror. This process is particularly efficient in microcavities. It is estimated that 90% of the excitons recombine through this channel [Tas96, Blo97] and only a small part of the excitons created feed the polariton trap.

Without any doubts, the **exciton density at threshold**, $D \sim 10^{10}cm^{-2}$, **remains far below the saturation density for CdTe QWs**. Following [Sch85] and taking an excitonic Bohr radius of $a_B = 28 \text{ \AA}$ [Dan98] we find:

$$n_{sat} = \frac{0.117}{\pi \cdot a_B^2} = 4.75 \cdot 10^{11}cm^{-2} \quad (6.3)$$

Indeed, strong coupling is lost and the transition towards the weak coupling regime is observed for a pumping rate corresponding to $\sim 50 \cdot P_{thr}$ (see chapter 8). Thus, we can assume that our estimate of the exciton density at threshold is correct.

Only about 10% of the excitons relax into the strong coupling zone and fill polariton states. The condensation occurs when the ground state occupancy is of order unity. One can ask what is the critical polariton density (n_{cr}) for condensation? It should be emphasized that n_{cr} describes occupancy of the polariton states in the strong coupling region and is expected to be much lower than the exciton density. First, we demonstrate that the onset of the stimulated scattering towards the ground state corresponds to a ground state occupancy of order unity. We use the data presented in figure 6.2. At threshold, rate of emission of photons by the polariton ground state is:

$$N_{PH}[s^{-1}] = \frac{N}{D.C. \times intT \times eff} \sim \frac{7.64 \cdot 10^5}{1\% \times 0.2 \times 2.1\%} \sim 1.82 \cdot 10^{10}[s^{-1}] \quad (6.4)$$

, where

- N - number of CCD counts detected at threshold for an angular range of 0.37°
- $D.C.$ - duty cycle of the acousto-optic modulator
- $intT$ - integration time
- eff - overall efficiency of the experiment

The efficiency of the experiment for detection wavelength $\lambda = 740 \text{ nm}$ takes into account:

- quantum efficiency of the CCD camera, $\sim 50\%$
- efficiency of the monochromator grating, $\sim 60\%$

- transmission of the monochromator mirrors, $\sim 95\%$
- transmission of the optics in the detection line:
 - window of the cryostat, $\sim 88\%$
 - objective, $\sim 95\%$
 - two beam splitters, $\sim 24\%$
 - lens, $\sim 95\%$
 - polarizer, $\sim 77\%$
- half of the emission goes into the substrate and is lost, $\sim 50\%$

N_{PH} can be transformed into the ground state occupancy ²⁶ :

$$n_{pol} = \frac{N_{PH} \times \tau_r}{DoS \times c_{PH}^2} \sim \frac{1.82 \cdot 10^{10} \times 10^{-12}}{2.86 \cdot 10^{-2} \times 0.37} \sim 1.7 \quad (6.5)$$

Here:

- τ_r - radiative lifetime of the ground state polariton ($\simeq 1$ ps)
- DoS - number of states contained within one pixel of the Fourier plane image formed on the CCD camera [[Mox04](#)]
- c_{PH}^2 - photon fraction of ground state for detuning $\delta = +7.7$ meV

This rough estimate is consistent with the bosonic final state stimulation process: bosonic stimulation is triggered when the occupancy factor of the state is of order unity. Even if the uncertainty of such a calculation is rather large, the same conclusion can be found in many works exploring stimulated emission of polaritons [[Blo05](#), [Hua02](#), [Den02](#)]. An occupancy factor of the order of one at the onset of stimulated scattering was confirmed also for different detunings: $\delta = +5.4$, $\delta = -9.5$ meV.

Having the above information, n_{cr} can be estimated by integrating photoluminescence from the polariton trap at threshold and dividing it by the excitation area. Performing this operation we end up with:

$$n_{cr} \sim 5 \cdot 10^8 \text{ cm}^{-2} \quad (6.6)$$

This value is much lower than the estimated exciton density. Further comments on this value are included in part [6.4](#) of this chapter.

²⁶the similar estimation for the photon rate was obtained by using single photon counting device instead of the CCD camera as a detector

Origin of blue-shift: Coulomb interaction or saturation effects? Figure 6.9 a shows the lower polariton branch dispersion for detuning $\delta = +7.7$ meV (see figure 6.2), measured for increasing pump power. Two main features may be distinguished in this graph. First, with increasing power a blue-shift of the dispersion curve is visible. Second, the bottom of the polariton dispersion flattens when approaching the condensation threshold. This flattening phenomenon may be explained in different ways. It may be considered as a signature of the condensation in the presence of pump and decay process [Szy06]. It can be also more easily understood by the consequence of the real space localization of the condensate. It is also interesting to note that what we observe is not a rigid shift of the lower polariton branch: the blue-shift of the bottom of the branch is larger than the one of the polariton excited states.

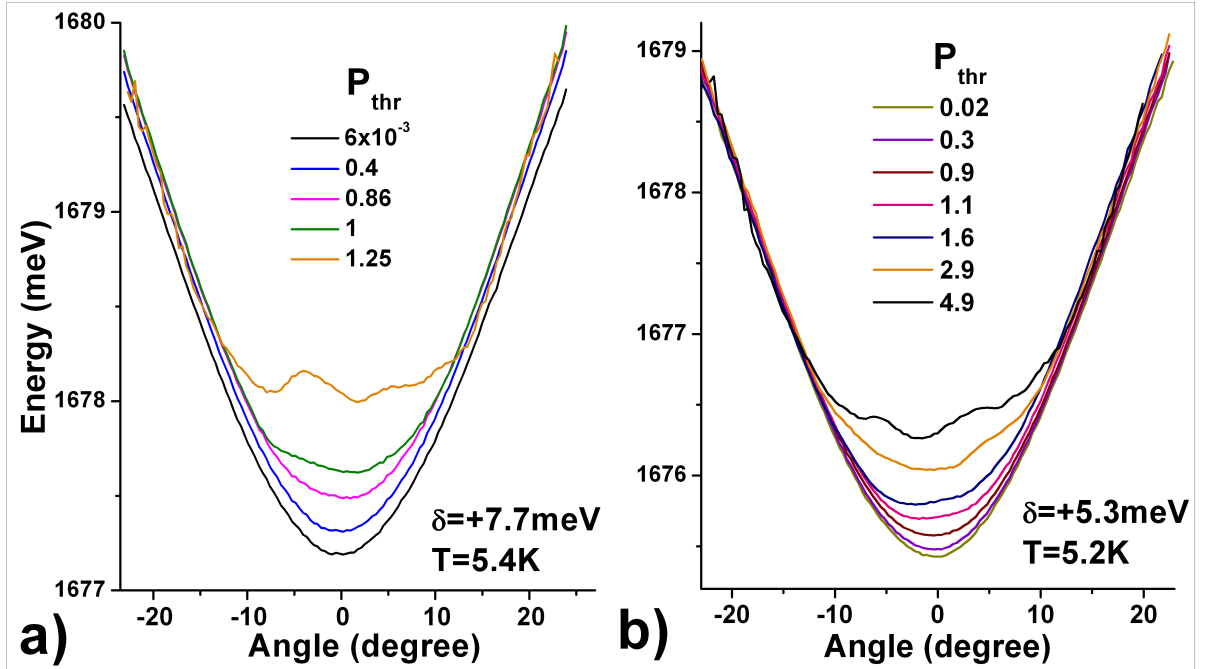


Figure 6.9: *Evolution of the dispersion curve, a: $\delta = +7.7$ meV, b: $\delta = +5.3$ meV. With increasing power a blue-shift of the dispersion curve is visible. The dispersion is flattened around the ground state. Flattening may appear as a consequence of presence of the pump and decay process [Szy06] or as a result of the polariton localization in real space.*

In this paragraph we wish to investigate the origin of the observed blue-shift. This phenomenon can occur as a consequence of the following two different effects:

- The inter-exciton Coulomb interactions, which lead to the blue-shift of the exciton energy, and consequently of the upper and lower polariton lines.
- The saturation effects, describing decrease of the exciton oscillator strength when increasing the exciton density, due to phase space filling and exchange

effects. This phenomenon leads to decrease of the Rabi splitting, and thus to blue-shift of the lower polariton and red-shift of the upper polariton.

To check which mechanism dominates in our case, the energy shift of the upper state has to be measured. Due to the large Rabi splitting, this experiment has to be performed at elevated temperature ($T=28\text{K}$), when the upper polariton states start to be thermally occupied. The result is presented in figure 6.10.

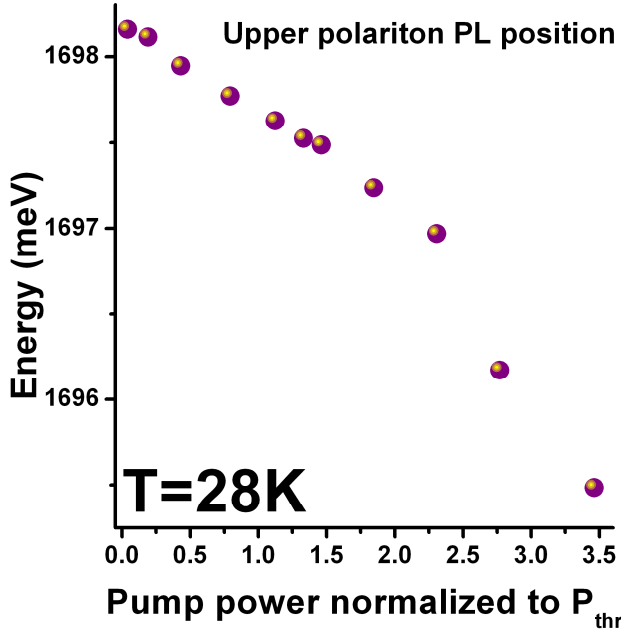


Figure 6.10: *With increasing power a clear red-shift of the upper polariton is observed. This behavior suggests that the spectral shift of the polariton states is mainly governed by the saturation effects, $T=28\text{K}$.*

With increasing power a clear red-shift of the upper polariton is observed. This behavior suggest that at $T=28\text{K}$ the spectral shift of the polariton states is mainly governed by **saturation effects**, and not by Coulomb interaction. Similar behavior at $T=15\text{K}$ has been already seen in time-resolved experiments [Boe00].

Condensate fraction The main signature of condensation is a massive occupation of the ground state. Thus, estimate of the condensate fraction permits to show that, when condensed, number of particles in the ground state becomes comparable with a total number of particles in the system. From theoretical point of view, condensate fraction is an important number, since - first of all - it indicates that transition occurs, but also it permits to calculate the strength of interaction in the system. For instance, in highly diluted atomic condensates the interactions are weak, allowing to obtain condensate fraction close to unity [Ens96]. On the other hand, in strongly interacting Bose-condensed systems the interactions prevent from forming a large condensed part. The well known example is superfluid helium, where the condensate fraction does not exceed 10% [Bal03].

It is thus instructive to determine the condensate fraction for the polariton condensate. We analyze the data presented in figure 6.2 in the following way. The dark counts are subtracted from the k -space maps. The photoluminescence is converted into the occupation taking into account the change of photon fraction and density

of states with increasing in-plane wave vector. The k-space maps are integrated and give the estimate of the total number of polaritons in the strong coupling zone (N_{total}). The number of condensed polaritons (N_{cond}) is estimated by integrating the ground state emission over its angular FWHM (N) (as is presented in the inset of figure 6.11) and subtracting the number of polaritons in the ground state at condensation threshold ($N_{P_{thr}}$). Finally, condensate fraction holds:

$$\frac{N_{cond}}{N_{total}}\left(\frac{P}{P_{thr}}\right) = \frac{N - N_{P_{thr}}}{N_{total}}\left(\frac{P}{P_{thr}}\right) \quad \text{for} \quad P \geq P_{thr} \quad (6.7)$$

The obtained condensate fraction as a function of the normalized to threshold pump power is displayed in figure 6.11.

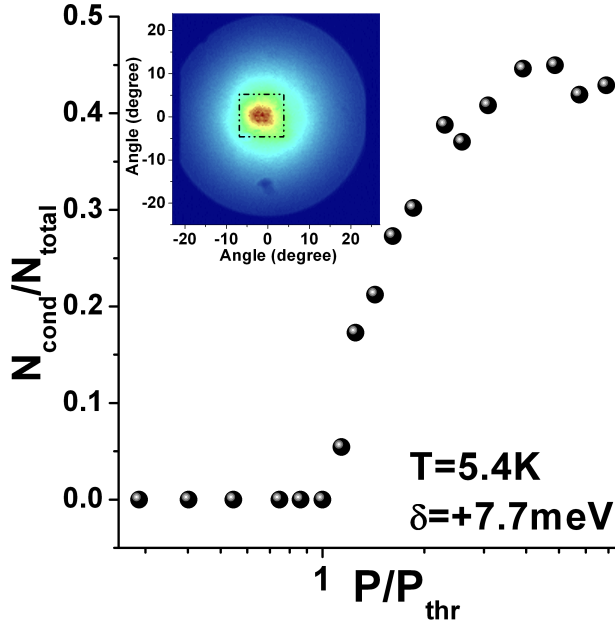


Figure 6.11: The condensate fraction as a function of the normalized to threshold pump power. Analysis of the data presented in figure 6.2. With increasing pump power the condensate fraction saturates after reaching value of 0.4. Inset: the k-space maps are used to calculate N_{total} . N_{cond} was calculated by integrating the ground state emission as indicated by the central rectangle.

Indeed, one can see that number of condensed polaritons in the trap becomes macroscopic: above threshold, condensed part grows rapidly reaching the value of 40% at $2.3 \cdot P_{thr}$. This value places polariton condensate between atomic BEC and liquid He. Anticipating the results discussed in the chapter 11, it is interesting to note that the parallel estimation of the condensate fraction can be given by the spatial coherence measurements. There, the onset of the spatial coherence directly reflects growth of the condensate with the condensate fraction given by the value of the interference contrast for $d > \lambda_{dB}$. In figure 11.5 it can be seen that for $P = 1.9 \cdot P_{thr}$ long range correlation reaches 40%, which is remarkably consistent with the estimation performed in this paragraph.

6.3 Non-equilibrium polariton condensation - negative detuning

We finish the analysis of polariton condensation in momentum space by presenting the results for negative detuning. The lower part of panels 6.12 A), B) shows intensity maps of the far-field polariton emission for increasing pump power. By spectrally resolving the far-field emission, an intensity map of the polariton dispersion emission is obtained and presented in the upper part of panels 6.12 A), B). The photon-exciton detuning is set to $\delta = -9.5$ meV - panel A) and $\delta = -1$ meV - panel B).

For negative detuning, at low pumping, light is mostly emitted from the so-called "bottleneck" region of the polariton dispersion curve [Mox05]. This can be explained as follows. Electron-hole pairs are created by the non-resonant pump and very quickly form excitons, which relax efficiently along the exciton-like part of the LP branch by interaction with optical and acoustic phonons (~ 30 ps, [Blo05]). At the strong coupling region, the LP becomes photon-like, characterized by an effective mass four orders of magnitude lighter than the exciton mass and a short lifetime (1-2 ps). In the low pumping regime, the relaxation time in this region is much longer (a few hundred ps) than the radiative life-time. So, excited polaritons do not reach the ground state at $k_{\parallel} = 0$, but remain mainly near the transition region of the strong coupling, forming an incoherent reservoir of exciton-polaritons. The emission is quite broad both in energy and angle. As shown in panels 6.12 and in figure 2.7, a characteristic bottleneck ring is formed in the k-space.

As we have seen before, increasing the pumping power speeds up the relaxation kinetics. In figure 6.12 B) one can see that for $\delta = -1$ meV the distribution of the polariton population shifts towards lower energies while remaining broad in energy and wave-vector in this regime. For more negative detuning, $\delta = -9.5$ meV, polariton-polariton scattering within the trap is inefficient due to the low exciton fraction (~ 0.33) in the lower polariton state. As can be seen in figure 6.12 A), polariton distribution remains practically unchanged when approaching the stimulation threshold. The intensity emitted by the ground state increases linearly with pumping in this intermediate regime. At stronger pumping, the average occupation of the lowest energy polariton state reaches unity. From this point on, scattering of polaritons to the ground state becomes much more effective due to the bosonic final state stimulation effect. Above this threshold, the rate for polariton-polariton scattering, with one polariton going towards the ground state, is enhanced by a factor $N_0 + 1$, where N_0 is the ground state population. This leads to an avalanche-like process which results in an exponential increase of the ground state population (see figure 6.13). However, analysis of the polariton distribution along the dispersion curve shows that in negative detuning the buildup of the ground state population starts when the system is not in internal equilibrium (figure 6.14).

It is interesting to compare the evolution of the linewidth as a function of the pump power for different detunings. Independently from the detuning, the condensation threshold is accompanied by the onset of temporal coherence, which results

6.3. Non-equilibrium polariton condensation - negative detuning

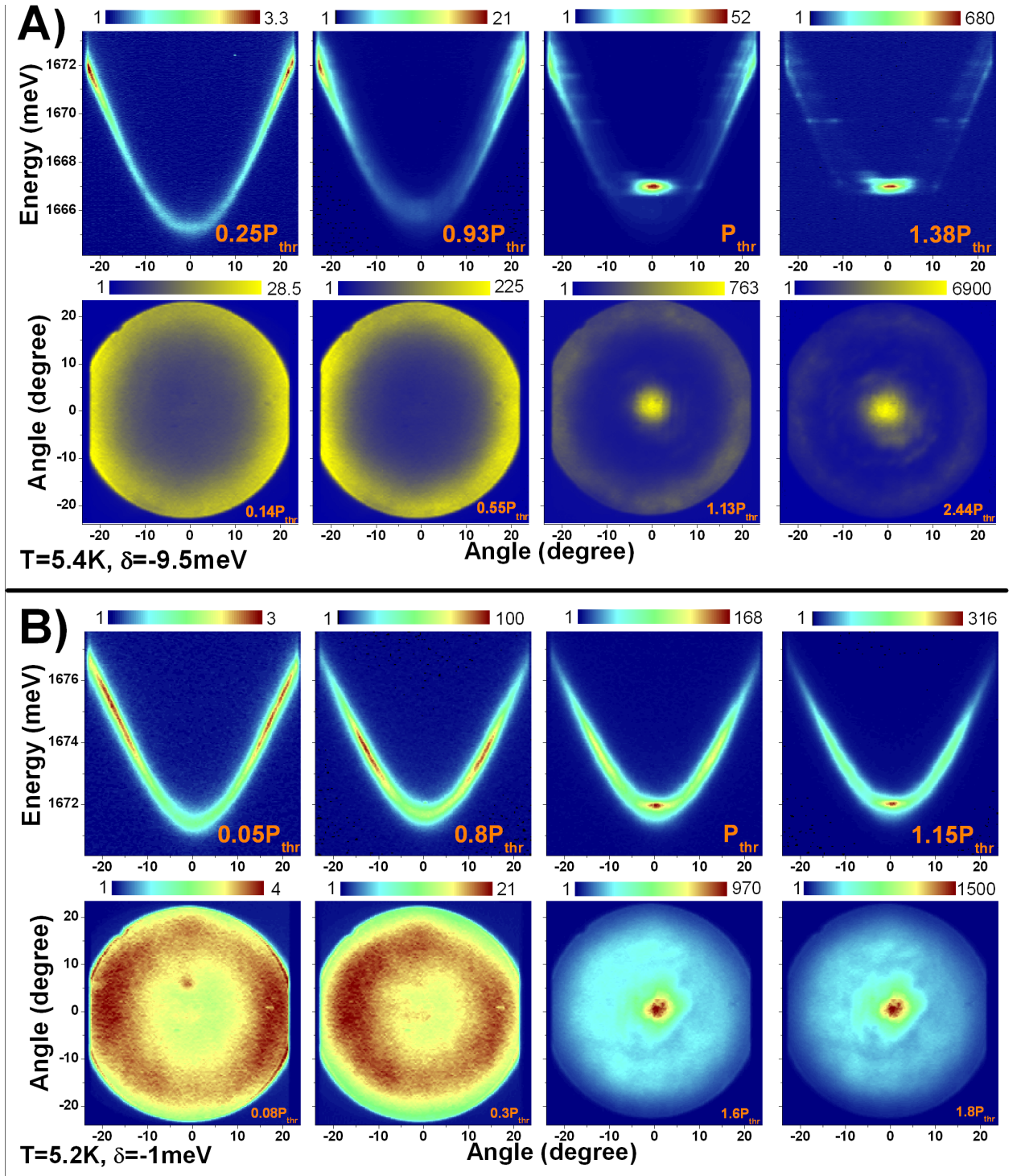


Figure 6.12: Non-equilibrium polariton condensation in phase space. A): $\delta=-9.5\text{ meV}$, $T=5.4\text{K}$. Lower part: the far-field polariton emission for different excitation powers. Upper part: The spectrally resolved far-field emission for different excitation power. Left part: the polariton relaxation is inhibited resulting in the "deep" bottleneck effect. Right part: Non-equilibrium polariton condensation occurs in the presence of the bottleneck. B): $\delta=-1\text{ meV}$, $T=5.2\text{K}$. The higher exciton fraction for $\delta=-1\text{ meV}$ with respect to $\delta=-9.5\text{ meV}$ results in higher efficiency of the polariton-polariton scattering mechanism. With increasing excitation power the bottleneck effect is partially suppressed: the maximum of the polariton distribution is pushed towards the bottom of the trap. But still polariton ground state stimulation starts when the polariton population is not yet thermalized.

in a significant line narrowing. It can be seen that for large positive detuning (figure 6.4) line broadening starts from pump power $2 \cdot P_{thr}$, whereas for an exciton-photon balance more photon-like, the linewidth of the polariton ground state emission above threshold remains narrow for pump power as high as $8 \cdot P_{thr}$ (figure 6.13). This behavior is intuitively comprehensible. Decoherence of the condensate is driven by interactions within the condensate. Of course, by increasing the exciton fraction in the polariton, effects of interactions will be revealed sooner than for negative detuning. This interaction-induced decoherence should be considered as a drawback of a polariton laser and makes this device different from a laser: in a standard laser, coherence properties increase with the number of photons in the lasing mode, while increase of the polariton condensate population finally degrades its coherence [Por03].

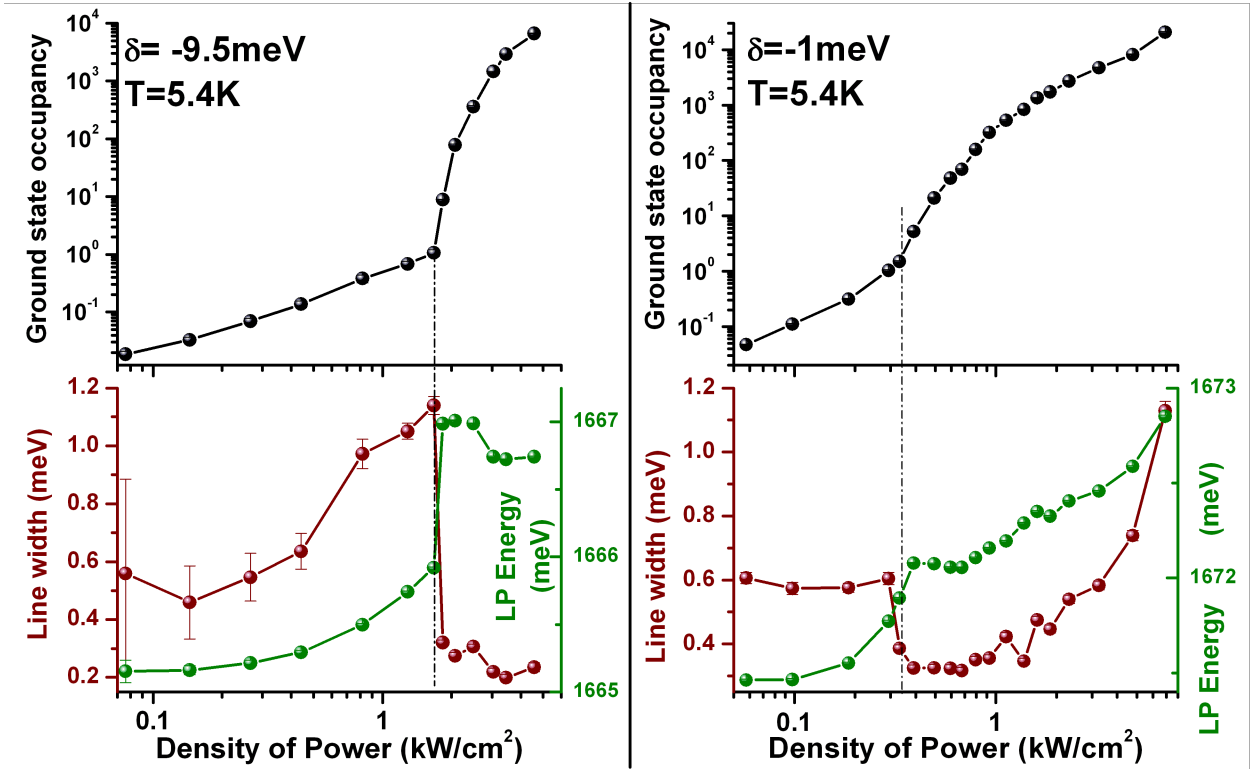


Figure 6.13: Characteristics of the polariton ground state emission vs. pump power under negative detuning. Left: Analysis of the data from figure 6.12 A), $\delta = -9.5 \text{ meV}$, $T = 5.4 \text{ K}$. At threshold the linewidth is reduced by a factor 5.5 indicating high coherence properties of the emission. Right: Analysis of the data from figure 6.12 B), $\delta = -1 \text{ meV}$, $T = 5.2 \text{ K}$.

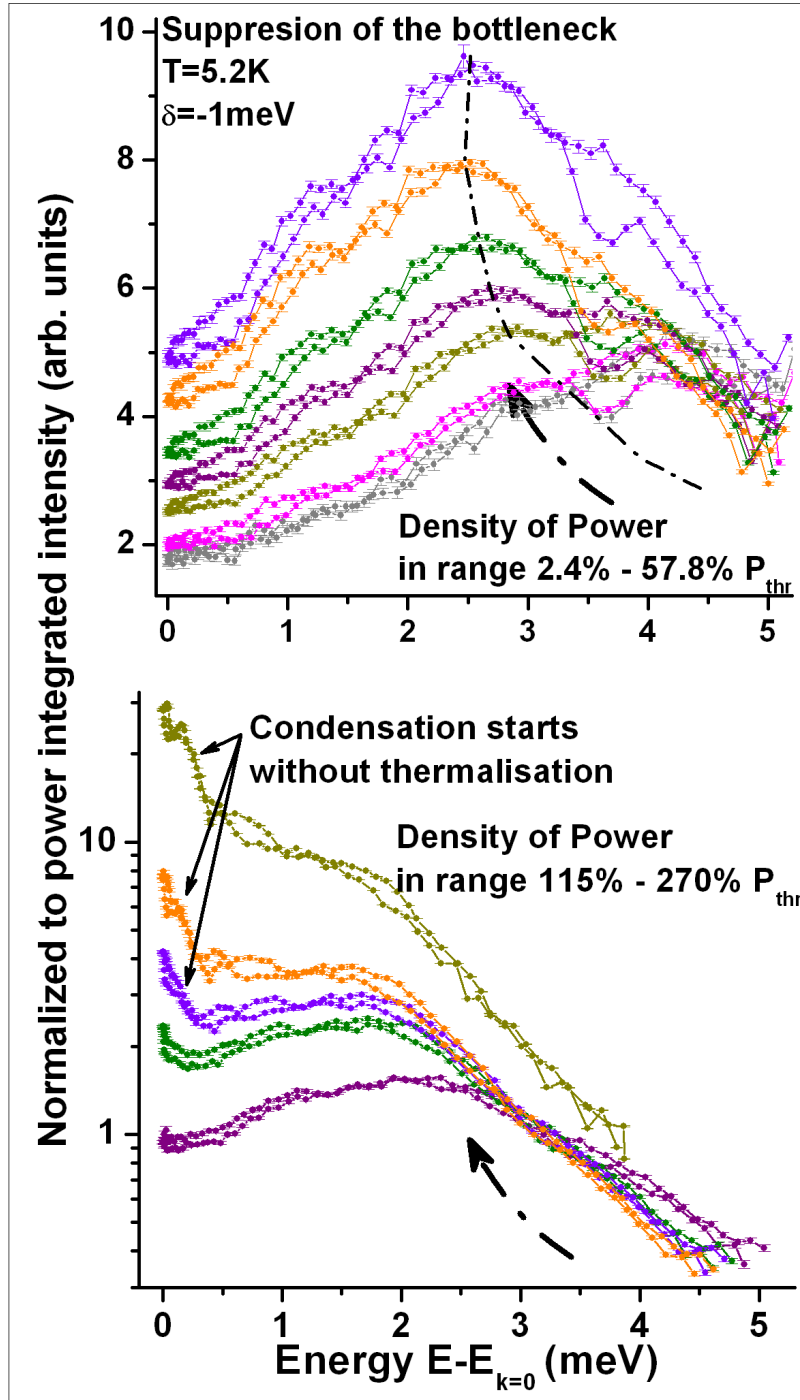


Figure 6.14: Polariton distribution along the dispersion curve for $\delta = -1$ meV, $T=5.2$ K. Left: For low pumping power the bottleneck effect in the polariton relaxation is well marked for negative detuning. Increasing the power partially suppresses the bottleneck. Nevertheless stimulated scattering towards the ground state switches on when the polariton distribution is still far from equilibrium (B): the "hunch" in the polariton distribution is not surveyed even far above threshold. The dashed arrows indicate increase of the pump power.

6.4 The nature of the polariton condensation - theoretical remarks

This section is based on the notes written by M. Szymańska (Oxford University), F. Marchetti, J. Keeling and P. Littlewood (Cambridge University). These comments give theoretical background for polariton condensation and confront the results with the theoretical model.

The system of semiconductor microcavity polaritons studied here consists of a finite, two dimensional gas of interacting particles in a disordered potential, which have internal structure and a finite lifetime. It is therefore natural to ask about the nature of condensation, its defining signatures, and the conditions under which it should be observed, when all the above features are taken into consideration. We discuss below how the evidence for polariton condensation collected experimentally relates to that expected theoretically. In particular, we show that the conditions under which such signatures were observed match well the predictions of a model which takes into account features like reduced dimensionality, interaction, internal structure of polaritons and their finite lifetime.

Interactions Although a three dimensional gas of non interacting bosons may condense, many of the interesting features that are associated with condensation require interactions. Macroscopic occupation of a single state, rather than occupation of a number of nearly degenerate states, can be explained by considering the energetic cost of exchange terms for an interacting Bose gas (P. Nozières p.15 in [Gri95]). It is this argument which explains why for the system in consideration condensation should naturally be associated with a single polarisation and macroscopic phase coherence. As discussed further below, interactions can modify the predictions of expected critical densities, and are of particular importance in understanding the nature of the phase transition in a two dimensional system.

The effects of interactions must also be considered when interpreting the occupation of states of the condensed system (i.e. when fitting the occupation data to the Bose-Einstein distribution that would be expected for non-interacting bosons). As is well known [Pit03] and discussed further, interactions will modify the polariton spectrum in the presence of a condensate. In addition, while the chemical potential in the condensed phase will lock to the bottom of the polariton spectrum, interactions mean that the bottom of the spectrum and thus the chemical potential continue to increase with increasing density. For these reasons, although the temperature can be well estimated from the tail of the occupation data (figures 6.4, 6.5), the estimate of the chemical potential in the condensed phase from the fit to the BEC distribution is not expected to be very accurate [Ens96].

Phase transitions and finite two dimensional systems An infinite, non-interacting two dimensional gas of bosons has no phase transition and never develops spontaneous coherence. However, adding interactions leads to the Berezinski-Kosterlitz-Thouless (BKT) transition, below which power law correlations, and su-

perfluidity can develop [Nel83]. For a finite, trapped two dimensional system of non interacting particles, macroscopic occupation of a single particle state can also occur [Bag91, Ket96, Pet00]. In a finite, interacting, two-dimensional system, it is clear that at low enough temperatures, deep in the condensed region, there should be coherence extending across the entire cloud. The question is whether such complete coherence arises at the phase boundary as in [Ket96] (finite size BEC) or whether coherence decays in space with a power law (the BKT transition) and then smoothly crosses over to full coherence when the thermal length reaches the cloud size. The answer to this question also determines how the expected critical density at a given temperature should be estimated.

However, for the experimental system under consideration here, there is another consideration. The discussion of the BKT and finite size BEC transitions are normally made for structureless bosons, i.e. the particles that exhibit bosonic behavior independently on their density. If there is no internal structure, then mean-field theory does not predict a transition temperature and one must always consider fluctuations; i.e. the population of excited modes. In the experiments described here, the temperature is a significant fraction of the Rabi splitting ($\simeq 6\%$), and so, the internal structure of polaritons is relevant and cannot be neglected. Including this structure, the phase boundary can be described by a mean-field theory [Mar06] with finite corrections due to occupation of fluctuations [Kee04]. At the temperatures of the current experiment, these fluctuations have a small effect on the prediction of critical density. At even lower temperatures and densities, such fluctuation corrections recover the results that would be found neglecting the internal structure: In this case it is worth understanding whether finite size effects are expected to play a role in determining the critical density.

Finite size BEC describes the transition when the effect of interactions can be neglected, compared to the effect of finite level spacing due to a trapping potential. Although the density profile is strongly affected by photonic disorder (see figure 6.1), the overall size of the cloud depends on the size of the spot, as polariton lifetime prevents any further expansion. A cloud size that is limited by the inability of polaritons to travel further, due to their finite lifetime, is distinct from a cloud size set by a large scale trapping potential. Such a mechanism would neither lead to a quantisation of energy levels, nor modify the density of states as required in [Ket96]. Further, if finite size quantisation effects were significant compared to interaction effects, one would expect to observe a quantisation of energy levels with spacing larger than the observed blue-shift. The opposite is seen: interaction effects are strong, and quantisation effects are weak. For these reasons, it appears that finite size effects should not be significant for the prediction of critical density in these systems.

The impact of the dimensionality, interactions and finite size on the possibilities of the phase transitions are summarized in the table 6.1.

Internal polariton structure The effect of the internal structure of polaritons, and their long-range interactions, can be for example described by the model dis-

Dimension	Interactions	Trap/Infinite	Transition
3	Yes/No	Infinite	BEC
3	Yes/No	Trap	BEC
2	Yes	Infinite	BKT
2	Yes	Trap	BEC/BKT
2	No	Trap	BEC/no transition
2	No	Infinite	no transition

Table 6.1: *The impact of the dimensionality, interactions and size of the system on the possibilities of the condensation. We are not concerned by $dim < 2$.*

cussed in [Mar06]. This model makes use of a realistic description of the disorder present in the quantum wells and takes into account the composite fermionic nature of the excitons. The importance of saturation effects in the polariton shift in energy when increasing the pump intensity is supported directly by experiment, as was discussed before (see figure 6.10).

Further support for this model, comes from the very good agreement between predictions of polariton density and experimental estimates. Starting from such a model, one can describe both the low density (fluctuation dominated) [Kee04] and higher density (long-range interaction dominated) regimes [Mar06, March06]. At very low temperatures and densities, the critical density for condensation is controlled by the photon mass, rather than the interaction strength. In other words, at very low densities when polaritons can be treated as structureless bosons, the effective polariton mass m_{pol} (given in $\frac{eV}{c^2}$) uniquely determines the critical temperature and density, which are linearly related:

$$n_{cr} = \frac{m_{pol} 2k_B T}{\pi \hbar^2} \quad (6.8)$$

However, when the temperature becomes a significant fraction of the Rabi splitting, polaritons start overlapping because of their photonic component, revealing their internal structure. Here, the critical density can be described by a mean-field theory, uniquely determined by the long-range nature of the polariton interactions [Kee04, March06]. In this regime, the dependence of critical temperature on density is much slower than linear.

For the particular characteristics of the CdTe microcavity considered in experiments, the crossover between the linear and the long-range interaction dominated regimes happens for a critical temperature and density around $T \simeq 19K$ and $n_{cr} \simeq 9 \times 10^7 cm^{-2}$.

To see which regime is appropriate to the experimental conditions requires an estimate of the temperature of the system, and the total density of the polaritons. Fitting the thermal tail of the occupation (figure 6.4) above threshold gives an estimate of the effective temperature around $T_{eff} = (16 \pm 1)K$. Theoretical estimates of the density can instead be obtained from the measured blue-shift of the lower polariton at $k_{||} = 0$.

The previously known expressions for the energy blue-shift for a weakly interacting gas of polaritons [Ciu00, Roc00], $\delta E_{Coul} \sim Ry \times n \times a_B^2$ and $\delta E_{sat} \sim \Omega \times n \times a_B^2$, where Ry is the excitonic Rydberg, Ω the Rabi splitting and a_B the excitonic Bohr radius, are not suitable in our case, since they take into account excitons with momentum up to $q < 1/a_B \simeq 3 \cdot 10^6 cm^{-1}$. Thus they include not only thermalized polaritons, but also most of the excitons in the reservoir. Supposing that the main contribution to the blue-shift comes from the saturation effects, these formulas allow one to estimate the excitonic density at threshold: At pump powers just below the non-linear threshold, where thermalization, but not condensation, is observed ($P \simeq 1.4 kW cm^{-2}$ of the data presented in figure 6.4), the measured blue-shift $\delta E \simeq 0.3 meV$ corresponds, to a total (exciton+polariton) density of around:

$$n \simeq \frac{0.3 meV}{26 meV \cdot (3 nm)^2} \simeq 1.3 \times 10^{11} cm^{-2} \quad (6.9)$$

This matches remarkably well with our experimental estimate of a total (in all 16 QWs) exciton density at condensation threshold: $n \simeq 16 \cdot 10^{10} cm^{-1}$.

But what we are interested in, is rather **a critical density of thermalized polaritons**. This value can be extracted from the model presented in [Mar06]. It includes a realistic description of the disorder present in the quantum wells and takes into account the composite, fermionic nature of the excitons.

The blue-shift of the lower polariton mode with increasing density can be predicted within this theory [Mar06, March06]. In particular, one can show that in the noncondensed regime, at these low temperatures, the blue-shift increases linearly with density, with a typical coefficient either determined by the temperature, $\delta E \sim \frac{\hbar^2 \Omega}{m_{pol} k_B T} \times n$, or by the disorder present in the quantum well, $\delta E \sim \frac{\hbar^2 \Omega}{m_{pol} W} \times n$ (here, W is the energy scale controlling the low energy tail of the excitonic density of states and m is exciton effective mass), respectively when $k_B T > W$ or $k_B T < W$. In contrast, just above the critical density for condensation, the increase of the blue-shift follows the increase of the chemical potential; this is initially faster than linear and then tends to saturate, in quantitative agreement with the data shown in figure 6.15.

Making use of this model, the blue-shift measured just below threshold, $\delta E \simeq 0.3 meV$, corresponds, at a temperature of $T = 16 K$ and a detuning of $\delta = +8 meV$, to a density of $n \approx 3 \times 10^8 cm^{-2}$. This estimate of the polariton density can be compared to an independent estimate of density extracted from the luminescence as in the previous section. The obtained experimental value of $5 \times 10^8 cm^{-2}$ is in remarkably good agreement with the density estimate from blue-shift.

Comparing this estimate of experimental temperature and threshold density to the theoretical phase boundary, it is therefore clear they fall close to the crossover regime. Thus for higher temperatures the transition would be dominated by the long-range interaction only, while at lower temperatures the transition would be controlled by the polariton mass only. Although the above estimates seem to suggest that the experimental values of density and temperature at threshold lie very close to the phase boundary, but just within the condensed phase, the effects of pumping

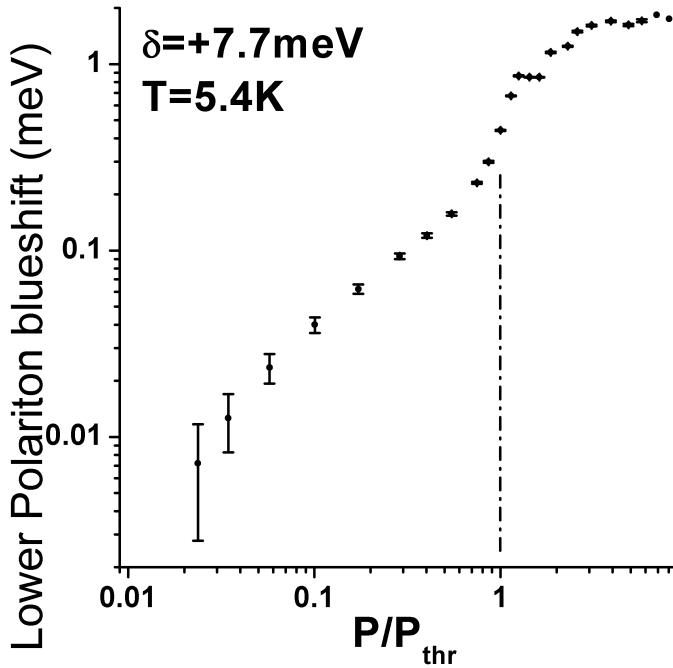


Figure 6.15: *Blue-shift of the lower polariton at $k_{||} = 0$ versus the density of incident pump power for the data shown in figure 6.4. Below condensation threshold, the lower polariton energy increases linearly. At threshold a faster increase and then saturation are seen.*

and decay will, as discussed below, increase the critical density.

Finite lifetime, non-equilibrium effects Polaritons have short lifetimes and so continuous pumping is needed to sustain the steady state. This leads naturally to the questions: Is condensation possible with incoherent pumping and decay? If so, how does it relate to condensation in an isolated system, and how does it differ from the spontaneous coherence in a strongly pumped system such as a laser? As discussed in [Szy06], spontaneous coherence in an incoherently pumped system is possible, and can be distinct from lasing, for example it does not require population inversion. For a range of parameters describing pumping and decay, condensation appears robust to such dissipative and non-equilibrium conditions and shares many fundamental features with that of closed systems in thermal equilibrium. The following discussion, of how pumping and decay modify the signatures of and conditions for condensation, summarizes results discussed more fully in [Szy06].

One important feature shared with an isolated system is that condensation occurs when an effective chemical potential reaches the bottom of the polariton band, and the normal state becomes unstable. Approaching the phase transition, the occupation function, even out of equilibrium, develops a divergence at some energy, defining an effective chemical potential. When this reaches the bottom of the polariton dispersion, fluctuations about the normal state grow, and the normal state becomes unstable. This mechanism is seen in experiment by the approach of fitted chemical potential to the bottom of the polariton band.

The above mechanism also leads naturally to a reduction of the homogeneous linewidth of polaritons as the transition is approached. The divergence of the occupation function discussed above is related to a zero of the imaginary part of the

inverse retarded Green's function. Defining polariton modes by poles of the retarded Green's function, the imaginary part of the inverse retarded Greens' function also describes the homogeneous width of these modes. Thus condensation, where the effective chemical potential reaches the bottom of the polariton band, implies a reduction of the linewidth near the bottom of the band.

Condensation of interacting particles is connected with broken phase rotation symmetry; as a consequence there exist modes of global phase rotation with no energy cost – the sound modes. They can be derived in Bogoliubov approximation, which leads to the following excitation spectrum ([Pit03], [Kav03]: chapter 6.2):

$$E_{Bog}(\mathbf{k}) = \sqrt{E(\mathbf{k})[E(\mathbf{k}) + 2N_{cond} \cdot V_{\mathbf{k}}]} \quad E_{Bog}(\mathbf{k} \sim 0) \simeq \sqrt{\frac{N_{cond} \cdot V_0}{m_{pol}}} \hbar k \quad (6.10)$$

Thus in the absence of the condensate an unaffected parabolic dispersion in the vicinity of the ground state is found. On the other hand, when the system is condensed linear excitation spectrum arises with the (superfluid) velocity $\sqrt{N_{cond}V_0/m_{pol}}$ ²⁷.

However, in a dissipative system, like the exciton polariton one, the excitation spectrum is changed. In the condensed state dissipation changes the low momentum fluctuations from linear dispersion to diffusive (i.e. dispersionless), which is expected to affect superfluid properties of polariton condensates. For a two dimensional system, such as the experiment here, this leads to a change in the power laws that would control the decay of correlations in an infinite system. Such a flattening of the dispersion is indeed visible (figure 6.9), but the answer, whether it is connected with above mechanism, needs further investigations.

Dissipation can also change the critical density required at a given temperature. In order to overcome the decay, a certain level of pumping is required to provide sufficient gain. This required level of pumping can be expected to increase the critical density at a given temperature. Calculations using the model discussed in [Szy06] support this conclusion: the transition in the presence of pumping and decay requires larger critical density. Unfortunately, the qualitative comparison between theory and experiment is not straightforward.

²⁷The observation of the sound mode in the excitation spectrum provide an evidence for condensation of liquid helium below λ -point.

Conclusions In this chapter the **polariton condensation in momentum space was presented**. The driving parameter of the transition is the polariton density i.e. the exciting laser power. By analyzing the far field emission of the polariton photoluminescence we demonstrated that in spite of short lifetime, polaritons in CdTe microcavity can thermalize within the strong coupling zone, thanks to the very high exciton-polariton scattering rate. Enhanced scattering rate and dephasing are manifested by line broadening of the polariton excited states when approaching the condensation threshold. These observations enable us to claim that **internal equilibrium can be reached in polariton system** with effective temperature of $T_{eff} = (16 - 20)K$. Then **condensation in the ground state takes place, with the condensate fraction up to 0.4, accompanied by marked saturation of the excited states**. Condensation is possible thanks to the populating rate of the ground state being faster than its radiative decay rate. Unambiguously, transition occurs in a strong coupling regime. It was shown, that thermalization occurs in a narrow range of positive detunings.

With increasing photon fraction, scattering efficiency diminishes and thermalization is quickly lost. However, exciton-polariton scattering in the exciton reservoir is still fast enough to fill polariton states and start stimulated scattering towards the ground state, resulting in non-equilibrium polariton condensation.

Strictly speaking, the reported condensation is not a standard BEC because **polaritons are not ideal (non-interacting) bosons**, and are not in thermal equilibrium with the phonon bath. Moreover the **polariton system is not conservative**, in the sense that polaritons continuously leak out of the microcavity.

The nature of the polariton condensation was commented in the theoretical frame. The results were examined along the theoretical model that takes into account peculiarities of the microcavity polariton system.

Chapter 7

Temperature dependence studies

In the preceding chapter the transition towards the condensed state was driven by increasing the polariton density at a fixed cryostat temperature. As we are dealing here with a thermodynamic phase transition, the possibility of provoking condensation with the temperature as a control parameter is expected. In this chapter we describe experiments that demonstrate polariton condensation induced by lowering the temperature. In the second part polariton condensation at high temperature is discussed. In particular, this phenomenon is reported up to cryostat temperature $T_{cryo} \simeq 50K$. These measurements are the first step towards experimental investigation of the polariton condensation phase diagram: the dependence of the critical density as a function of the critical temperature for condensation.

Contents

7.1	Temperature dependent polariton condensation	83
7.2	Polariton condensation at high temperature - towards the phase diagram	89

7.1 Temperature dependent polariton condensation

In the case of polaritons, in contrast to the atomic experiments, the straightforward method to increase the phase space density is by increasing particle density. As we have shown in the preceding chapter, with increasing pump power, the polariton gas first reaches internal equilibrium, establishing an effective temperature (in a certain range of detuning) and then condenses at fixed polariton temperature.

The second method to provoke polariton condensation is by decreasing the cryostat temperature at a given excitation density. At this point a few remarks should be given. First, keeping the same excitation density does not mean that the polariton density in the strong coupling region is constant for different temperatures. With increasing cryostat temperature, the onset of various exciton non-radiative recombination channels is expected, depleting the occupancy of the exciton reservoir

and of the polariton states. Moreover, as was shown in [Por02] (eq. 14), the scattering rate from the exciton reservoir towards the strong coupling zone is inversely proportional to the exciton temperature²⁸ and to the square of the exciton density in the reservoir. Hence, the higher the temperature the lower the occupancy factor that can be reached at given pump power. Finally, the response of the polariton effective temperature to changes of the cryostat temperature is unknown. Thus, we should keep in mind that, in the experiments described below, the temperature tuning influences not only the polariton effective temperature, but also the polariton density.

When performing temperature variation studies there is another complication that cannot be neglected. The temperature tuning changes the absolute exciton energy due to the change of the band gap (figure 7.1). At the same time the effective refractive index, and so the energy of the photon mode, is very weakly sensitive to the temperature. As a result, the photon-exciton detuning is not the same for different temperatures when investigating a fixed point on the sample surface. In the previous chapter it was shown that the relaxation processes and the threshold power for condensation depend dramatically on the detuning. Hence, in order to keep the same relaxation mechanisms, one should compensate these temperature induced detuning changes by choosing different, appropriate point on the sample for different temperatures. On the other hand, each time the position is changed on the sample, the polariton condensate that is created experiences a different photonic disorder.

In what follows, we present two different studies that demonstrate polariton condensation induced by lowering the temperature: in the first study, a different point on the sample is chosen to compensate the detuning change for each temperature, and in the second study, the point on the sample is kept fixed.

Fixed photon-exciton detuning The 16 QW sample is excited as described in the previous chapter with a constant power density of $\sim 1kW/cm^2$. The polariton photoluminescence along the dispersion curve is recorded for different cryostat temperatures. A photon-exciton detuning of $\delta \simeq +6.8$ meV is fixed by changing the point on the sample for different temperatures. In this way the temperature dependence of the detuning is compensated, as is presented in figure 7.1.

The results are presented in panel 7.2. The transition towards the condensed state occurs approximately for $T_{cr} \simeq 20K$. For $T=5K$ the emission pattern is dominated by the condensate. The presence of the thermal cloud is brought out by the logarithmic color scale. The onset of the nonlinear emission is observed in figure 7.3 a, where the temperature dependence of the ground state emission intensity, its linewidth and blue-shift are presented.

It is instructive to analyze the polariton occupancy along the dispersion branch as a function of the temperature - see figure 7.3 b. At high temperature ($T=40K$)

²⁸The long exciton lifetime in the reservoir (~ 100 ps) justifies the assumption that the excitons in the reservoir are thermalized and can be described by a temperature close to the lattice temperature.

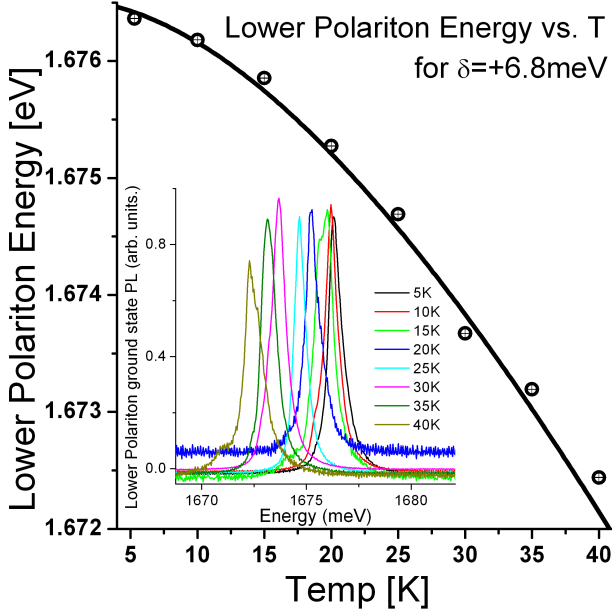


Figure 7.1: Lower polariton energy for $\delta = +6.8 \text{ meV}$ as a function of the temperature. With increasing temperature the CdTe band gap shrinks as described in [Lau90] (solid line). In order to keep the same detuning for each temperature, a different point on the sample is chosen (open circles). In the range of temperatures 5K-70K the changes of the Rabi splitting are negligible [Boe00]. Inset: PL spectra for weak excitation at different temperatures and fixed detuning.

polaritons are in internal equilibrium, but the fitted effective temperature is lower than the lattice temperature. **Decreasing cryostat temperature has an impact on the polariton population distribution and the effective temperature.** As is shown in figure 7.3 b, the steepness of the distribution increases, manifesting changes of the effective polariton temperature. Owing to this cooling process, the occupancy of the polariton ground state increases. At critical temperature of $T_{cr} \simeq 20\text{K}$, a buildup of the ground state occupancy is seen. Condensation occurs and is accompanied by a depletion of the excited states, as can be seen for $T=20\text{K}$, $T=5.3\text{K}$. This demonstrates polariton transfer from the excited states towards the condensate with decreasing temperature. The transition is described by Bose-Einstein statistics. The effective temperature and chemical potential are plotted in the inset. The uncertainty of this three parameter fit is rather large, hence the plotted values of T_{eff} and μ_{eff} are only approximate. Surprisingly, for $T_{cryo} > 25\text{K}$, the fitted T_{eff} is smaller than the cryostat temperature. We will comment on this striking effect in the next section of this chapter.

Fixed position on the sample In the following experiment, polariton condensation is achieved, as described in the previous paragraph, with the temperature as a controlling parameter. However, this time the position on the sample is fixed, and thus the photon-exciton detuning changes from $\delta_{5K} = +6.5 \text{ meV}$ at $T=5\text{K}$ to $\delta_{40K} = +10.8 \text{ meV}$ at $T=40\text{K}$. As was shown before, the threshold power increases rapidly when increasing the detuning towards more positive values (figure 6.7). Hence, in this configuration, the temperature tuning not only cools down the polariton gas, but also strongly influences the polariton density in the strong coupling zone. The higher the temperature, the more positive the detuning that is obtained. At the same time the exciton scattering efficiency decreases. As the result, a significantly lower polariton density is achieved. The transition into the

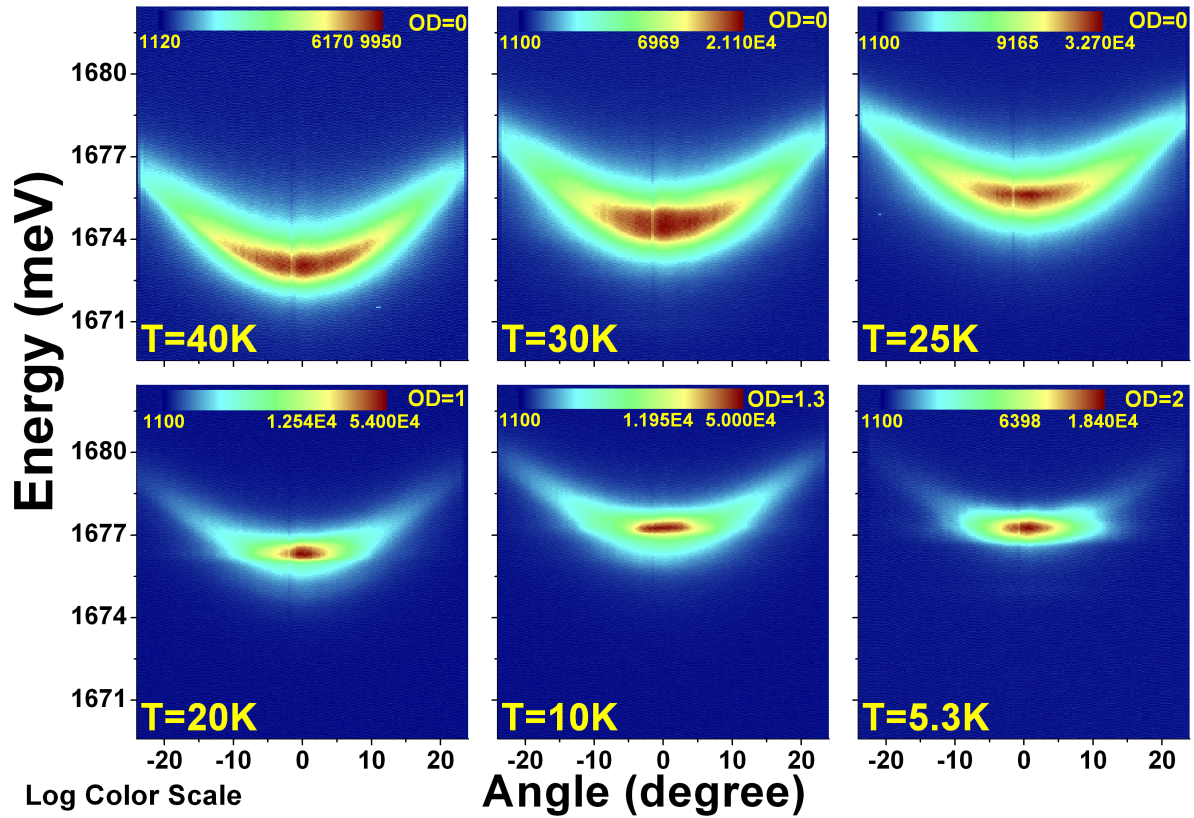


Figure 7.2: *Polariton condensation induced by lowering the cryostat temperature at fixed detuning. The excitation power $\sim 1\text{kW}/\text{cm}^2$ and the detuning $\delta \sim +6.8\text{ meV}$. With decreasing cryostat temperature, polaritons cool down along the branch and condense at cryostat temperature of around $T \simeq 20\text{K}$. A logarithmic color scale is used to emphasize the presence of the thermal cloud above threshold. Non-resonant ($\sim 1768\text{ meV}$), quasi-CW ($1\mu\text{s}$ pulses, duty cycle 1%) excitation. Optical densities (OD) are added in the detection line to prevent saturation of the CCD.*

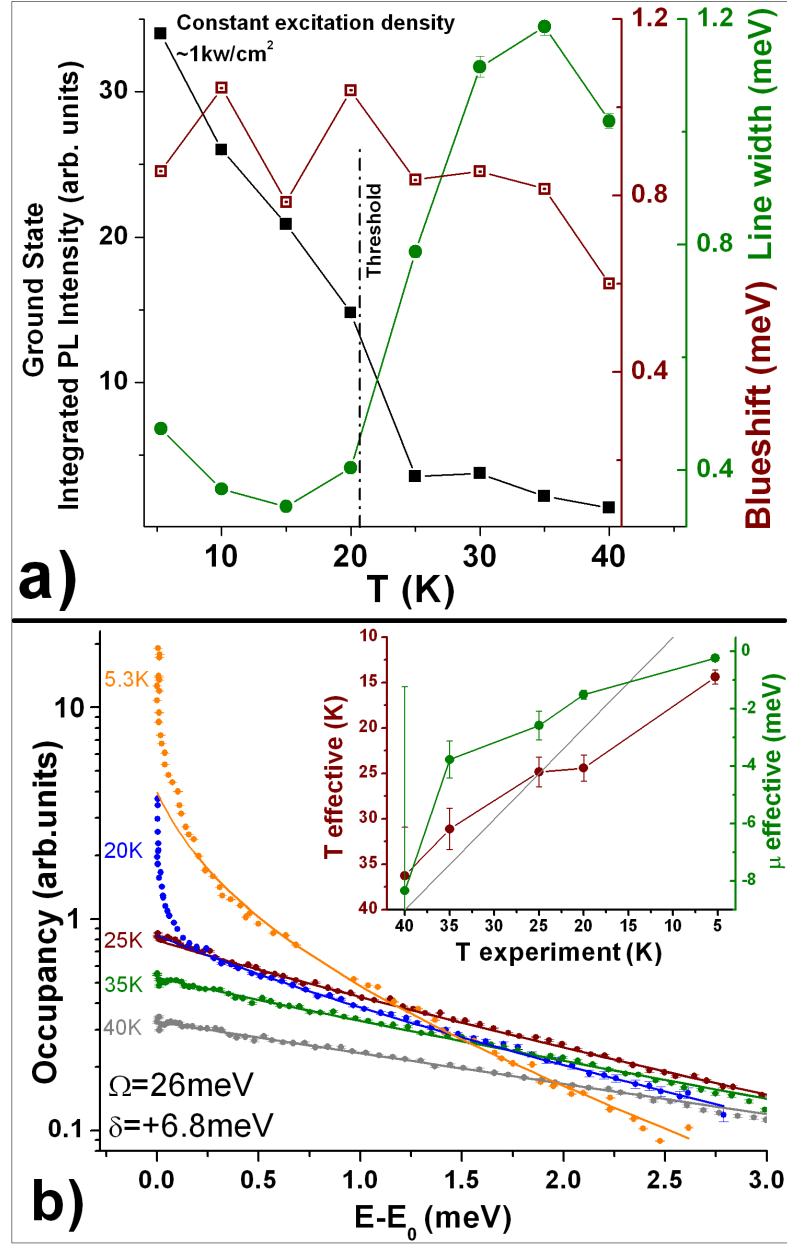


Figure 7.3: *Polariton condensation induced by lowering the cryostat temperature. a: Transition characteristics. Above threshold the ground state intensity becomes nonlinear. Line narrowing and blue-shift are observed. b: Polariton statistics along the branch as a function of the temperature. At high temperature ($T_{cryo} = 40K$) polaritons are thermalized with their temperature lower than the lattice. Decreasing cryostat temperature influences the polariton effective temperature: the increased steepness of the distribution demonstrates the lowering of the T_{eff} and the polariton cooling towards the ground state. Below a critical temperature of $T_{cr} = 20K$, the ground state occupancy explodes and depletion of the excited states is seen. The polariton population at the transition is fitted with the Bose-Einstein distribution, with an effective temperature and a chemical potential (inset). Up to $T_{cryo} = 25K$, T_{eff} is higher than T_{cryo} . For $T_{cryo} > 25K$, T_{eff} is lower than T_{cryo} . Such behavior indicates that the polariton effective temperature is established by a polariton-polariton scattering mechanism and not by the phonon interactions, i.e. that the polaritons in the trap are detached from the lattice. Gray, solid line: $T_{eff} = T_{cryo}$.*

condensed state is presented in figure 7.4. Below $T_{cr} \simeq 25K$ the polariton ground state starts to be massively occupied. Again, use of a logarithmic scale allows us to observe the thermal cloud of excited states.

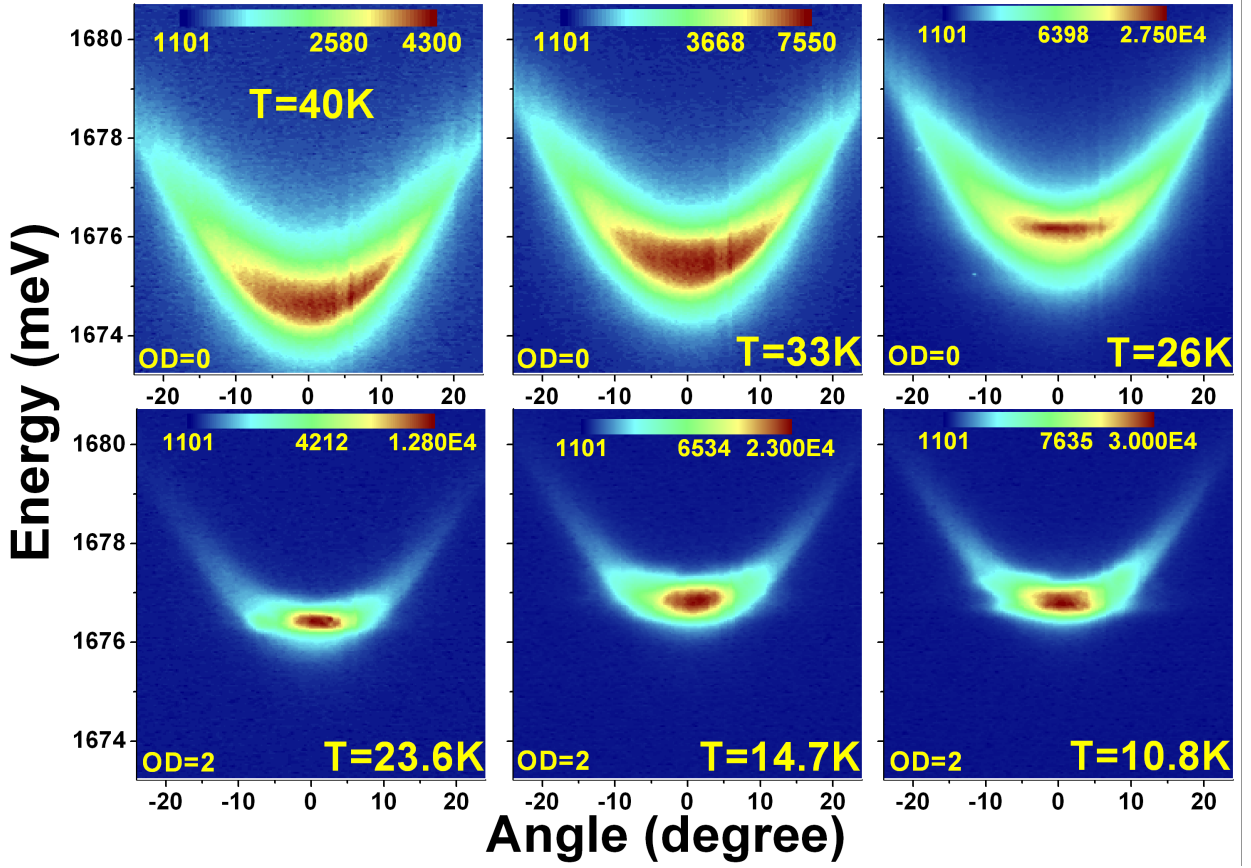


Figure 7.4: *Polariton condensation induced by lowering the cryostat temperature and varying of the detuning. The position on the sample is fixed. Excitation power $\sim 0.7kW/cm^2$. With increasing temperature the detuning increases from $\delta \sim +6.5 meV$ at $T=5K$ to $\delta \sim +10.8 meV$ at $T=40K$. Decreasing cryostat temperature increases the polariton density and cools polaritons along the branch. The condensation occurs at $T_{cr} \simeq 25K$. The logarithmic color scale is used to emphasize the presence of the thermal cloud above threshold. Non-resonant ($\sim 1768 meV$), quasi-CW ($5 \mu s$ pulses, duty cycle 5%) excitation. Optical densities (OD) are added in the detection line to prevent saturation of the CCD.*

The analysis of these data is presented in figure 7.5. At high temperature $T=40K$ and larger detuning ($\delta_{40K} = +10.8 meV$) the polaritons are not fully thermalized. Decreasing the temperature and the detuning increases the efficiency of scattering towards the polariton trap, increasing the polariton density and cooling down the polariton gas towards the ground state. Below a critical temperature of $T_{cr} \simeq 25K$ the ground state emission becomes nonlinear and line narrowing is seen (inset of figure 7.5).

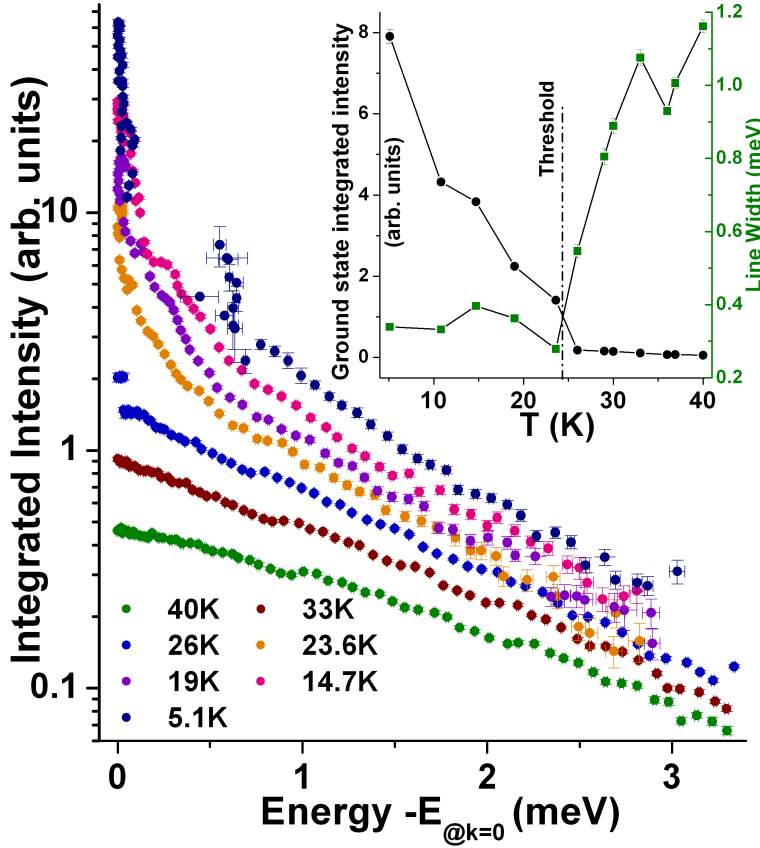


Figure 7.5: *Polariton condensation induced by changing the temperature. The analysis of the data presented in figure 7.4. For $T=40\text{K}$ and detuning $\delta = +10.8\text{ meV}$, polaritons are not thermalized. With decreasing temperature and decreasing detuning, the polariton density increases and at $T \simeq 26\text{K}$ thermalization is reached. Below the critical temperature of $T_{cr} \simeq 25\text{K}$, condensation occurs and the threshold is marked by a strong increase of the ground state occupancy and a significant decrease of the linewidth (inset).*

7.2 Polariton condensation at high temperature - towards the phase diagram

Experimental observations In this section we will push the limit of polariton condensation in a CdTe microcavity up into higher temperatures. The spectrally resolved far field images of the polariton emission as a function of the pump power are measured for different temperatures (12K, 15K, 20K, 25K, 28K, 35K, 44K, 50K and $T=60\text{K}$). The experiments are performed for positive photon-exciton detuning $\delta = +(3 - 9)\text{ meV}$. Our first observation is plotted in figure 7.6, which presents the threshold pump power for the onset of nonlinear emission from the ground state as a function of the cryostat temperature. It can be seen that the threshold power increases linearly up to $T \simeq 30\text{K}$. With further increase of the temperature, the threshold power increases much faster, reaching a value of $P_{60\text{K}} \simeq 6.3P_{4.8\text{K}}$. This significant increase of the threshold for stimulated emission can be interpreted as due to a decrease of the efficiency of scattering towards the ground state [Por02] and a heating of the polariton gas.

Figure 7.7 presents dispersion images for lower polariton PL as a function of the pump power at high temperatures: 35K, 50K and 60K. The condensation into the polariton ground state is unambiguously seen up to the lattice temperature of $T=50\text{K}$ (rows A and B of panel 7.7). We notice that with increasing temperature

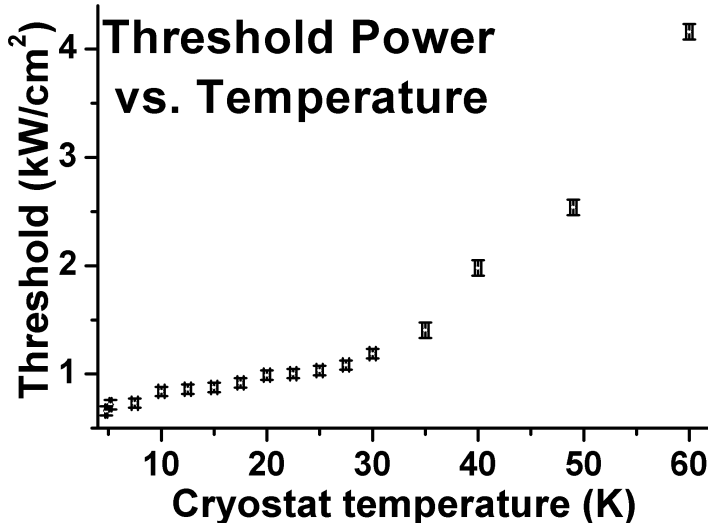


Figure 7.6: *Threshold power for the non-linear ground state emission as a function of the cryostat temperature. The threshold increases with temperature due to the polariton heating and the decrease of the efficiency of scattering of the exciton-polariton towards the ground state. Detuning $\delta \simeq +6$ meV.*

the blue-shift of the polariton ground state at threshold gets larger. The linewidth of the ground state polariton emission in the linear regime also increases considerably with pump power at high temperatures. This can be understood as the effect of the increase of the exciton density at threshold with increasing temperature. The characteristics of the transition at high temperatures are shown in figure 7.8.

At temperature higher than $T=50$ K the situation is no longer clear. At the threshold for nonlinear emission, a jump of the emission energy is seen, questioning whether stimulation occurs in the strong coupling regime above $T=50$ K. An example of such a strong blue-shift of more than 4 meV is seen in row C of panel 7.7. The uncoupled exciton and photon states are still far above (6 meV and 11 meV respectively) the energy of the nonlinear emission. This behavior can be explained by a strong saturation of the Rabi splitting in the localized points, appearing in real space at the condensation threshold (see figure 9.1), at increased temperatures and high densities. This hypothesis could be checked by studying the energy position of the upper polariton state at high temperature and exciton density. At present, the origin of such a jump-like blue-shift remains unclear.

As shown in figure 8.2, at even higher temperature ($T=106$ K) the nonlinear emission evidently occurs in a weak coupling regime.

Towards the phase diagram - polariton distribution at high temperatures

The results presented above can be considered as a starting point for the investigation of the phase diagram of the polariton condensation, i.e. the relation between polariton critical density and polariton effective temperature. In this sense, the data presented in figure 7.6 are still far from the sought-after phase diagram: neither the relation between lattice temperature and polariton internal temperature, nor the relation between the pump power and polariton density is known.

In order to investigate the polariton effective temperature at high cryostat temperatures, the polariton distribution is analyzed as in figure 6.4. The results for cryostat temperatures 25K, 35K, 44K and 50K are presented in figure 7.9 a, b, c, d

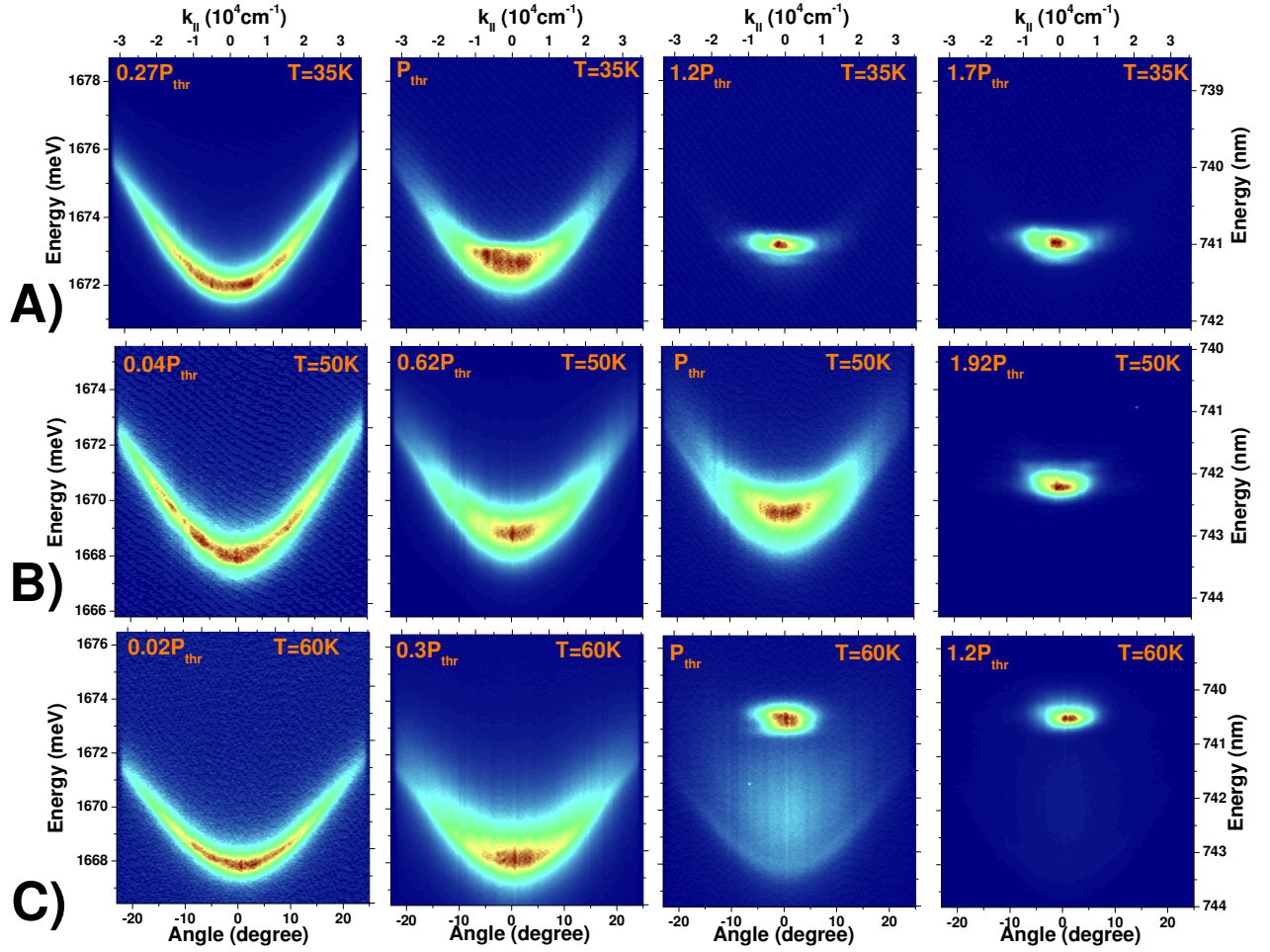


Figure 7.7: Polariton condensation at high temperatures. Condensation into the polariton ground state is observed up to $T=50\text{K}$ (rows A and B). Above $T=50\text{K}$ a strong jump towards the blue is seen at the onset for nonlinear emission. At $T=106\text{K}$ (see figure 8.2) stimulated emission certainly occurs in the weak coupling regime.

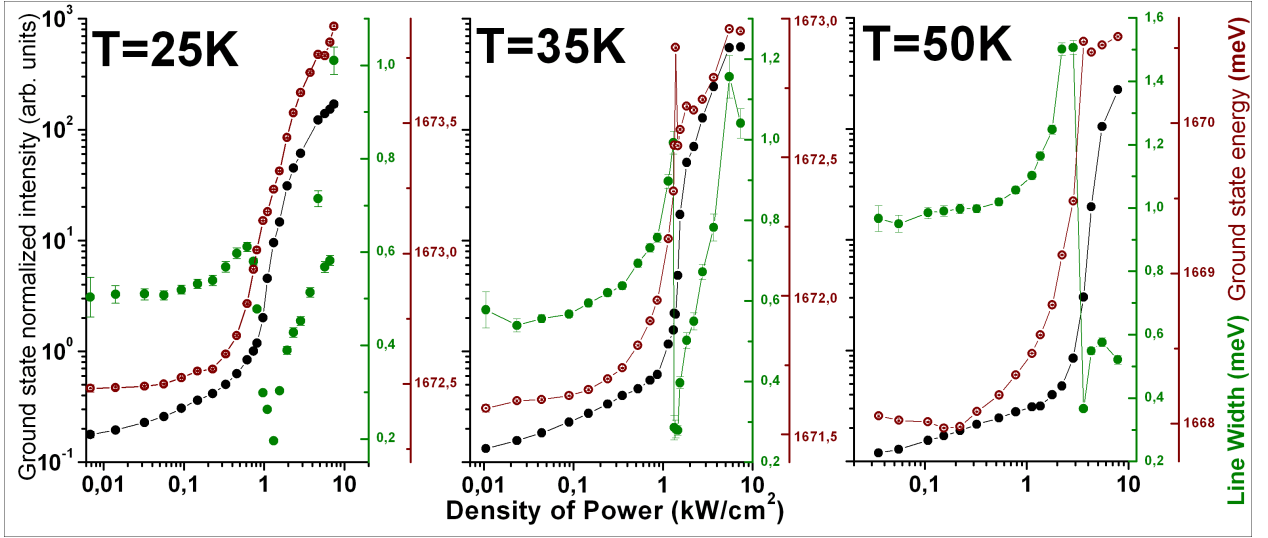


Figure 7.8: *The characteristics of the ground state polariton emission as a function of the pump power at high temperatures: 25K, 35K and 50K. Black circles: integrated intensity normalized to pump power, brown open circles: energy blue-shift, green circles: emission linewidth. A progressive increase of the emission linewidth and of the blue-shift just below threshold are observed when rising the temperature.*

respectively. In spite of the high temperature, a bottleneck effect is still present under weak excitation conditions. Increasing the pump power allows us to reach polariton thermalization at threshold (a, b, c). Yet systematically, we obtain $T_{eff} < T_{cryo}$. This surprising result indicates that polaritons are weakly coupled to the lattice. Their T_{eff} is established thanks to the collisions between polaritons and not due to interactions with phonons. Changing the lattice temperature influences T_{eff} indirectly by modifying the efficiency of polariton-polariton scattering. This statement is confirmed by analyzing the polariton population for $T_{cryo} = 50K$ (part d of panel 7.9). In spite of the high temperature, polaritons are no longer thermalized, owing to a decreased scattering rate towards the trap. In particular, the polariton occupancy extracted from figure 5.7 shows that at $T=300K$ and under weak excitation conditions, polariton thermalization is not reached.

In order to understand this nonintuitive behavior we should once more realize that their short lifetime and the peculiar shape of their dispersion curve inhibit the interactions of polaritons with phonons, and this isolates the polaritons from their environment.

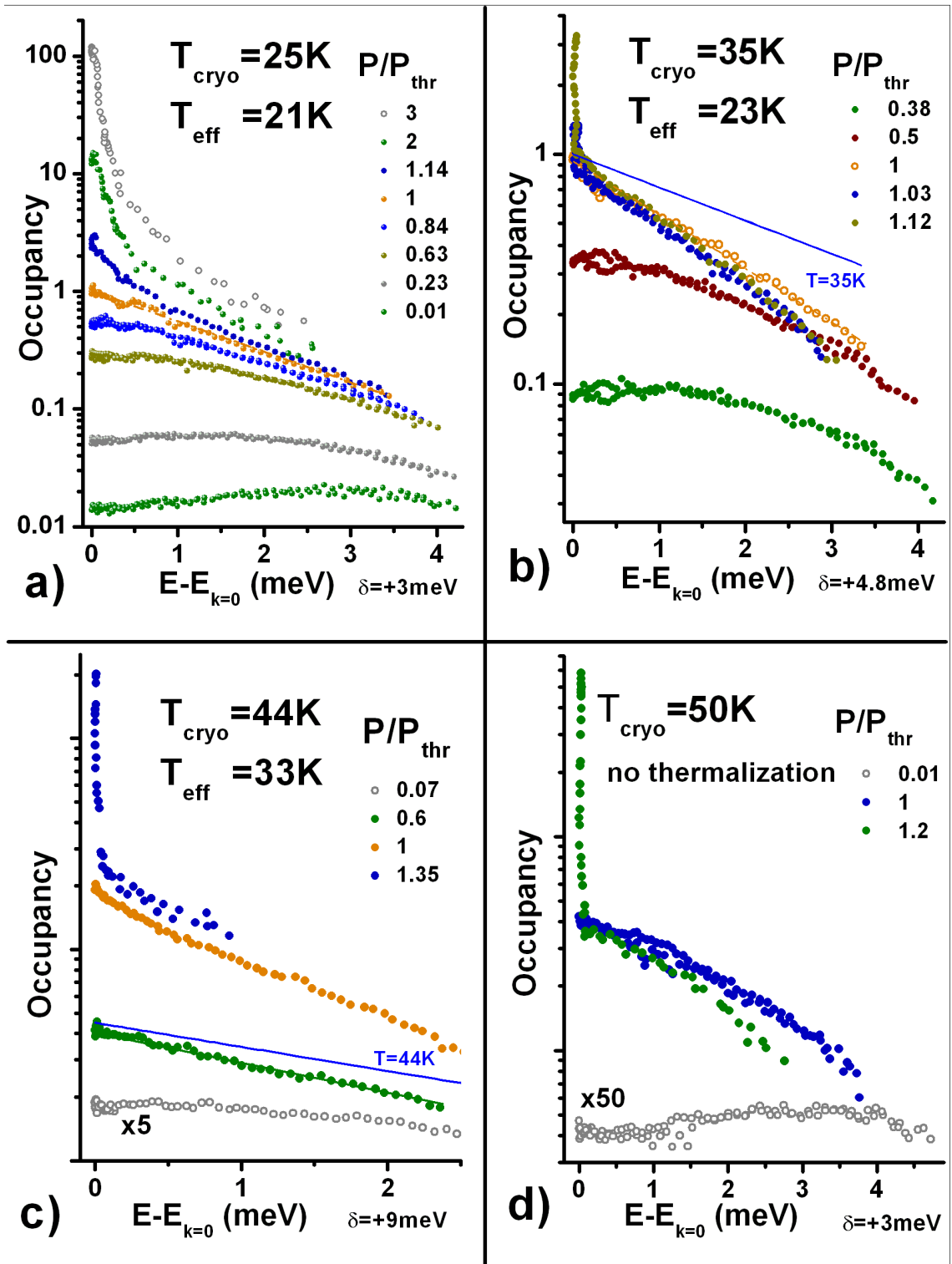


Figure 7.9: Polariton distribution at high cryostat temperatures. Under weak excitation, polaritons are still not thermalized: the bottleneck effect is present. With increasing pump power, thermalization of the polariton population is attained at 25K, 35K and 44K (parts a, b, c of the panel). But interestingly, T_{eff} is not directly related to T_{cryo} . In particular we obtain $T_{\text{eff}} < T_{\text{cryo}}$.

Conclusions In the previous chapter it was shown that there exists a critical polariton density for polariton condensation. Here, we demonstrate that **polariton condensation can also be achieved with the temperature as a controlling parameter**. It is emphasized that temperature tuning influences the scattering rate from the exciton reservoir into the neighborhood of the ground state, and hence changes the polariton density in the strong coupling zone. It is also shown that **there exists a relation between cryostat temperature and polariton effective temperature**. The high temperature limit ($T \simeq 50K$) for polariton stimulation in the strong coupling regime in a CdTe-based microcavity is determined. The results obtained provide a starting point for experimental investigation of the phase diagram for polariton condensation.

Chapter 8

Transition into the weak coupling regime

In this part the optical response of the microcavity under extremely strong pumping conditions is investigated. The transition from strong coupling into the weak coupling regime is demonstrated. In chapter 3 it was emphasized that the main advantage of the CdTe-based microcavities is a higher exciton binding energy with respect to the GaAs structures. The higher exciton saturation density enables the unambiguous observation of the polariton stimulation in strong coupling regime [Dan98]. But increasing the excitation power, and thus the exciton density, induces also in our case decrease of the exciton binding energy and bleaching of the exciton oscillator strength. The degradation of the exciton binding energy is mainly due to **the phase space filling** effects, which can be described as a carrier density dependent effective dielectric constant (see equation 1.11 and [Dam90]). With increasing carrier density the transition into the weak coupling regime finally occurs [Hou95, But02]. The main point of this chapter is to demonstrate that at low temperature the transition to weak coupling takes place for an excitation density more than 50 times higher than the threshold for polariton condensation.

Contents

8.1 T=5.3K	95
8.2 T=106K	96

8.1 T=5.3K

In order to demonstrate the transition into the weak coupling regime the microcavity is pumped in the pulsed mode. This enables us to provide very high instantaneous excitation densities with a relatively low average power and prevents sample damage. The dynamic polariton condensation under the pulsed excitation condition in T=5.3K is presented in figure 11.13. Let us see how the spectrally resolved far-field

emission evolves with increasing excitation power (in the same experiment as shown in figure 11.13). The result is displayed in figure 8.1. We see that for pump power as high as $30P_{thr}$ emission comes from the polariton states, and the strong coupling regime is preserved. For pump power $80P_{thr}$ the emission from the cavity mode starts to be visible, showing the transition towards a weak coupling regime. Finally, for the maximum available pump power $143P_{thr}$ the maximum of the emission is displaced towards the cavity mode. As this time integrated experiment is performed in a pulsed mode, all the transitory stages between strong and weak coupling regime are mixed. That's why emission for energies between polariton and cavity mode is observed.

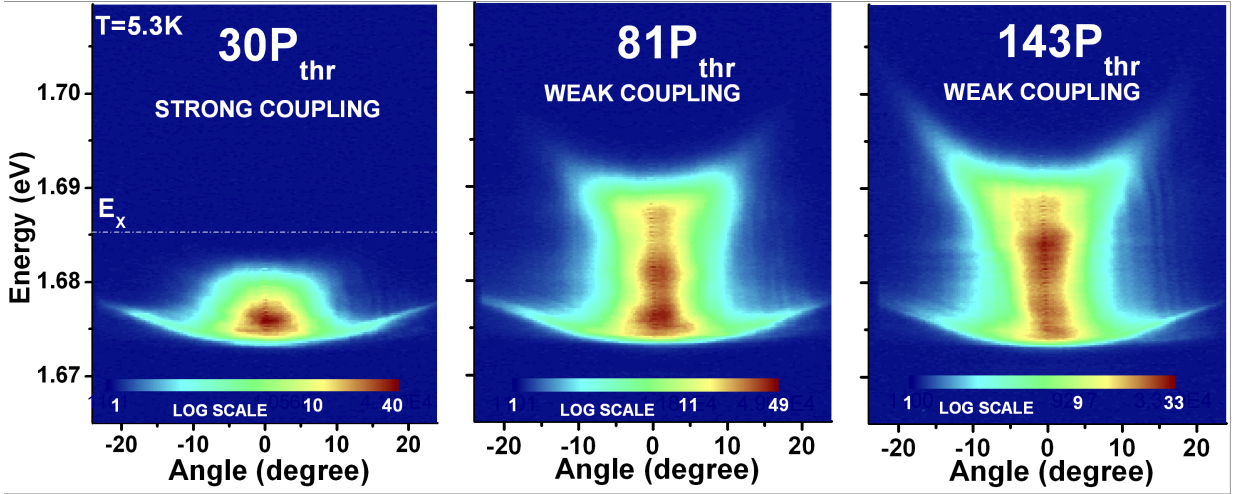


Figure 8.1: The transition towards the weak coupling regime at $T=5.3K$. The strong coupling regime persists up to the pump power as high as $50P_{thr}$. Due to the exciton phase space filling and screening effects the strong coupling is lost for the highest accessible pump powers. The logarithmic color scale is used to point out the appearance of the cavity mode. Intermediate stages between the stimulated emission in the strong coupling and weak coupling regimes are seen due to the pulsed excitation.

8.2 $T=106K$

The situation is different at elevated temperature. The result of the power resolved studies of the polariton emission at $T=106K$ is presented in figure 8.2. At $T=106K$ the upper polariton states are thermally occupied and in the low excitation limit photoluminescence of both polariton branches is visible, clearly demonstrating strong coupling regime. In these conditions, the saturation density is reduced with respect to the low temperature studies. The increase of the carrier density provokes ionization of the excitons. As a consequence the strong coupling is lost before polariton stimulation could take place. The emission from the cavity mode followed by the sharp threshold of the photon lasing occurs. In these conditions microcavity operates in a weak coupling regime like a vertical cavity surface emitting laser.

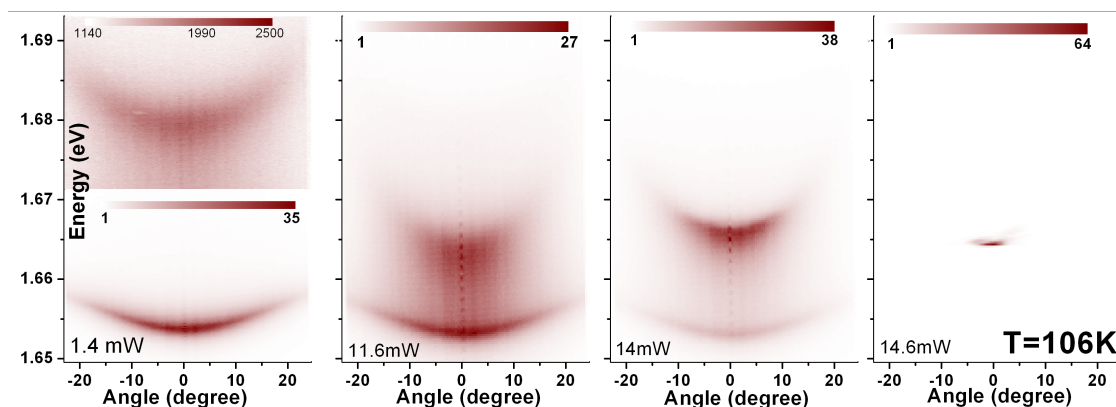


Figure 8.2: *Photon lasing in the microcavity at $T=106K$. Exciton energy: $E_x = 1666$ meV, Rabi splitting: $\Omega = 25$ meV, detuning, $\delta = -1$ meV. Due to the elevated temperature the upper polariton states are thermally occupied and the photoluminescence of both polariton branches is visible. The saturation density is reduced with respect to the measurements at $T=5K$. At $T=106K$ polariton stimulation no longer occurs, but increasing the excitation power destroys excitons, and cavity lasing then occurs.*

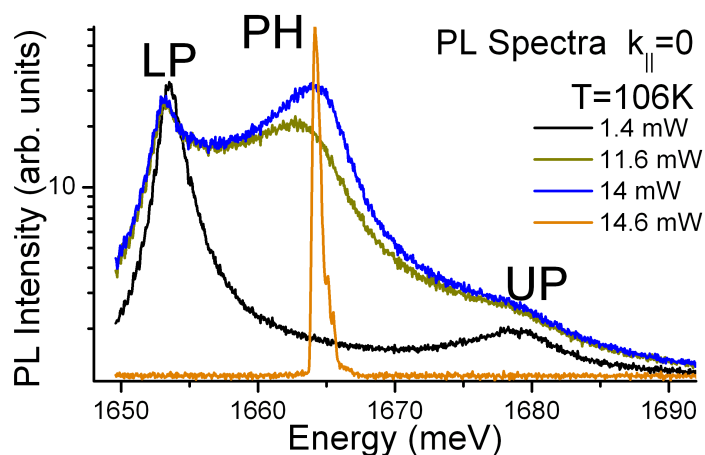


Figure 8.3: *PL spectra at $k_{\parallel} = 0$ at $T=106K$ with increasing pump power. Cavity lasing in a weak coupling regime occurs.*

Conclusions It was shown that the strong coupling regime at $T=5K$ is present up to $P = 50P_{thr}$. The transition towards the weak coupling regime is demonstrated by the appearance of the emission from the cavity mode above $P = 80P_{thr}$.

At $T=106K$ the saturation density is reduced, hence the strong coupling regime is lost before polariton condensation could take place. Instead the standard, photon lasing occurs at the cavity mode and the microcavity operates in the VCSEL mode.

A huge difference in the threshold power for the polariton condensation and the photon lasing confirms distinct physical origin of these two phenomena. The differences between the polariton and the photon lasing are discussed in detail in appendix A.

Chapter 9

Polaritons in real space

In this chapter we will investigate real space emission of the polariton condensate. It will be shown that the spectacular localization in the near-field emission pattern occurs when condensation in momentum space is observed. The origin and consequences of this localization will be discussed. Characterization of this phenomenon is given by the detuning studies and spectrally resolved spatial emission measurements.

Contents

9.1 Spatial localization of the polariton condensate	98
9.2 Characterization of localization	100

9.1 Spatial localization of the polariton condensate

As was mentioned before (see figure 6.1), dramatic changes are seen in the real space emission pattern, when the transition towards the condensed state occurs. Below threshold, the emitting spot is homogeneous and reflects the shape of the excitation spot, whereas above threshold the emission collapses into a small number of 2-5 μm size areas. An example of such a transition for detuning $\delta \simeq +5$ meV is displayed in panel 9.1. One can see that, deep in the condensed state the emission comes almost exclusively from localized zones, showing that there is a localizing potential that cannot be treated as a weak perturbation of the condensate wave-function.

The origin of this remarkable localization needs to be explained. We believe that of the major role here is **photonic disorder** of the microcavity. The characteristic, micron scale of the observed disorder shows that the localization is connected with the photon part of the polariton and not with the exciton part. Previous studies [Mox04] have characterized the nature of disorder and have shown that it cannot be neglected. It was found that the energy of the lower polariton mode can fluctuate up to as much as 1 meV over a characteristic distance of 10 μm . Parallel studies on GaAs microcavities also confirm that the photonic disorder of the Bragg mirrors

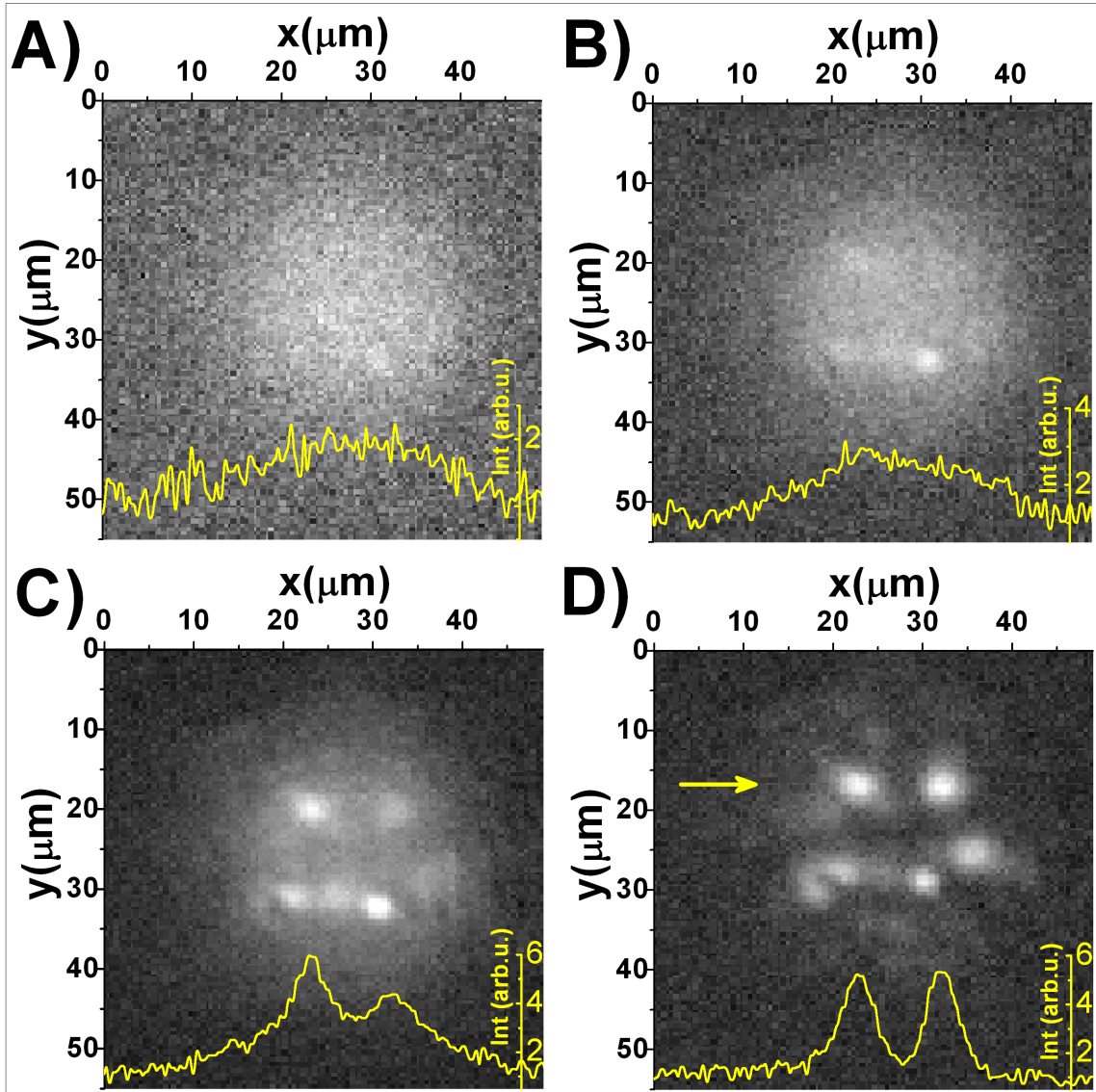


Figure 9.1: *Two-dimensional images of the near-field polariton PL for different pumping powers, $T=5.4\text{K}$. Below threshold (A, B) the emission is homogenous and reflects the shape of the excitation power. Above condensation threshold (C, D) the polariton emission breaks down into a small number of a few micron-size, strongly localized spots. Vertical and horizontal axes are in-plane coordinates on the sample surface. PL intensity increases from black to white. The intensity profiles along the x direction at the y position, indicated by an arrow in the panel D, are plotted on the bottom of each figure. Far above threshold the emission comes almost exclusively from localized areas.*

plays the main role in the shape of the emission pattern in the parametric oscillation regime [San06]. The preliminary results in GaAs show that polaritons are trapped in the local minima of the photonic disorder in the non-linear regime.

The fascinating observation of our studies is that, even though their spatial separation is much longer than the thermal length (2-3 μm), strong mutual coherence between localized spots is measured (see chapter 11), providing direct proof for a long range correlation of the polariton condensate. The first argument for spatial coherence of the polariton condensate was given in [Mox05]. It was perceived that spatial localization of polaritons is not accompanied by angular broadening of the far field emission spectrum. Because of the laws of diffraction, we must conclude that the different localized areas have the same mutual phase and form a single 20-30 μm emitting object, justifying the narrow angular emission pattern.

One starts to fully appreciate this argument when the laser spot is decreased to a size comparable with a localizing potential - 1-3 μm . As is shown in [Max05] and in section 3.2, in this condition, strong localization prevents the condensation into the ground state. The characteristic stimulation on the ring of the excited states is seen (see figure 3.3). In those experiments a spontaneous transition towards the coherent state is proved by appearance of a speckling pattern²⁹ of the stimulated ring, and by observation of a strong interference pattern produced by the Billet interferometer in the transverse plane. Furthermore, additional, concentric rings in real space are seen, showing the Fourier relation between near-field and far-field emission, hence demonstrating a high degree of spatial coherence of the source.

9.2 Characterization of localization

Photonic disorder vs. condensation The appearance of a stationary interference pattern in real space (chapter 11) and a common linear polarization of the emitting spot (chapter 10) are strong proofs that condensation into a single state, that is a single wavefunction with well defined energy, takes place. But how can this be confronted and reconciled with the presence of the photonic disorder, causing fluctuations of the polariton energy comparable with its linewidth? It should be emphasized in this place that the degree of spatial and temporal coherence strongly depend on the point on the sample. There are areas where spatial contrast does not appear above a non-linear threshold, and the contrast in the temporal coherence experiment does not build up significantly but exhibits beatings, thus showing that the spectral difference between localized points exceeds its linewidth. In order to demonstrate condensation into the single state, those points on the sample are chosen where the fluctuations of the emitting energy over the excited area are the smallest possible, much smaller than the polariton linewidth.

(x, λ) measurements In order to show that one can easily find the points on the sample where condensation towards the single state (i.e. with the same energy across

²⁹The speckles appear when coherent light is scattered by the static disorder. They can be produced, for instance, by diffusing the laser light on a rough surface.

the entire excitation spot) occurs, spectrally and spatially resolved studies were performed as follows. The emission of the polariton condensate can be imaged on the CCD camera by setting the grating to zero order. By closing the monochromator slit horizontally and by changing the lateral position of the entrance lens one can sweep the image of the emitting area in front of the slit and, in particular, choose a zone with bright points. Image of the slit can be dispersed by setting the grating to the polariton emission wavelength. An example of such a spatial selection within the emitting spot is presented in figure 9.2.

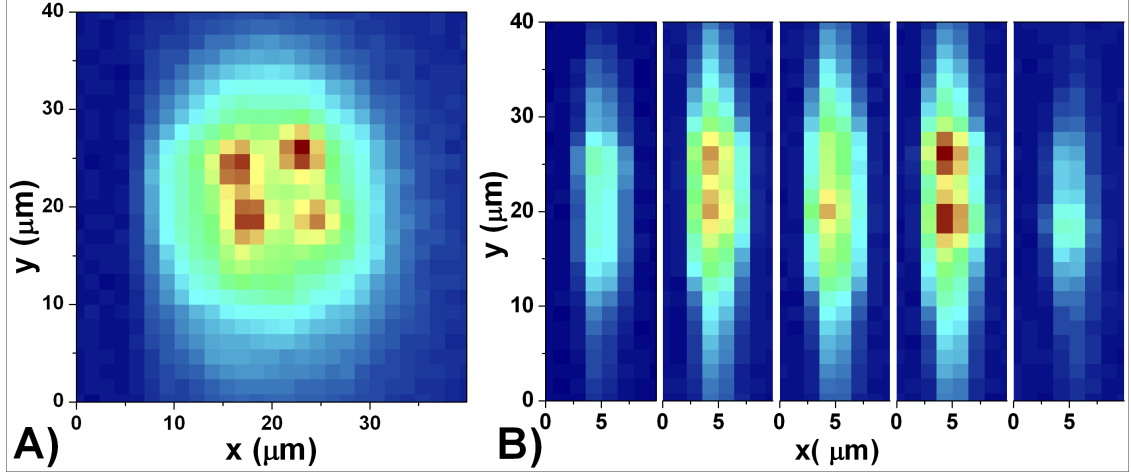


Figure 9.2: *A: Image of the condensate emission on the CCD camera. B: Spatial selection of the emitting area within the excitation spot.*

Typical results of a spectral analysis along the slit are presented in figure 9.3. Points where different bright spots emit exactly at the same wavelength can easily be found. However, careful studies also reveal cases when the energy of the neighboring points is different. But their spectral superposition is still large, enabling their mutual coherence. It is interesting to note that the characteristic fluctuation of the emission energy between different localized spots is (0.2-0.5) meV. This corresponds to the jump of the cavity photon energy caused by a change of the cavity length of one atomic step³⁰. These energy fluctuations contribute to the inhomogeneous broadening of the polariton emission.

The same experiment was performed in the weak excitation regime. The result is presented in figure 9.4. Each part of this panel presents the spectral analysis of different areas (stripes) within the emitting spot. Some spatial fluctuations within the energy of polariton emission are clearly observed. Because in this configuration the emission is distributed over all the angles detected within the numerical aperture of microscope objective, the observed energy distribution is spread over a few meV.

Detuning dependence Polariton localization is connected with the photonic part of the polariton wave-function. One can thus expect that the efficiency of the local-

³⁰ $\delta d = \frac{\delta\lambda}{\lambda} \times d = \frac{0.15nm}{740nm} \times 1480nm = 0.3nm$, where d is the cavity length and $\delta\lambda$ is the emission energy fluctuation in nm.

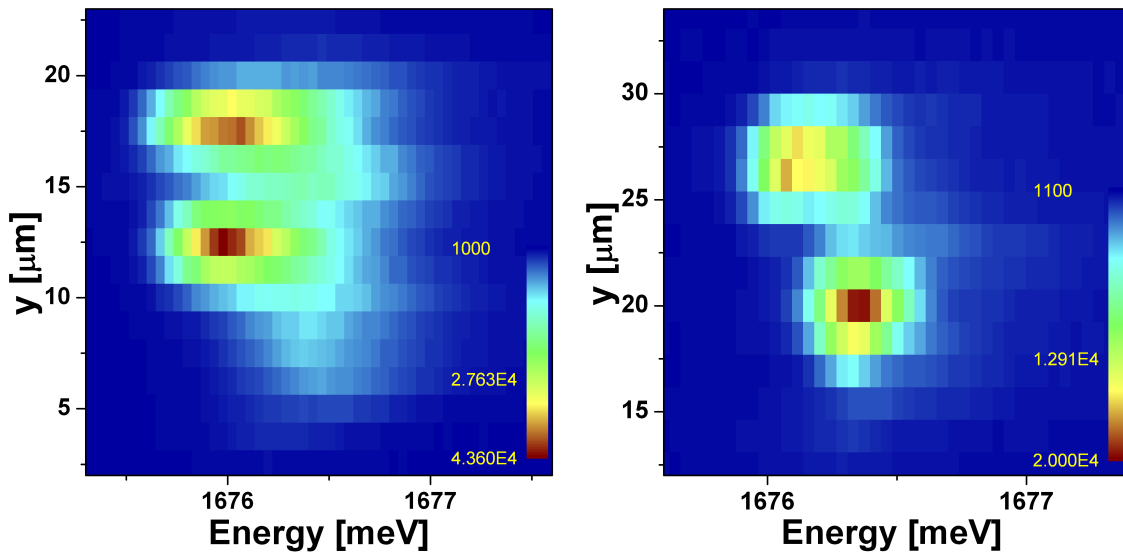


Figure 9.3: Spectrally resolved near-field image of the polariton condensate emission, $T=5K$. Left: Localized spots emit exactly the same energy. Right: The energy of localized spots is not the same and fluctuates within the linewidth.

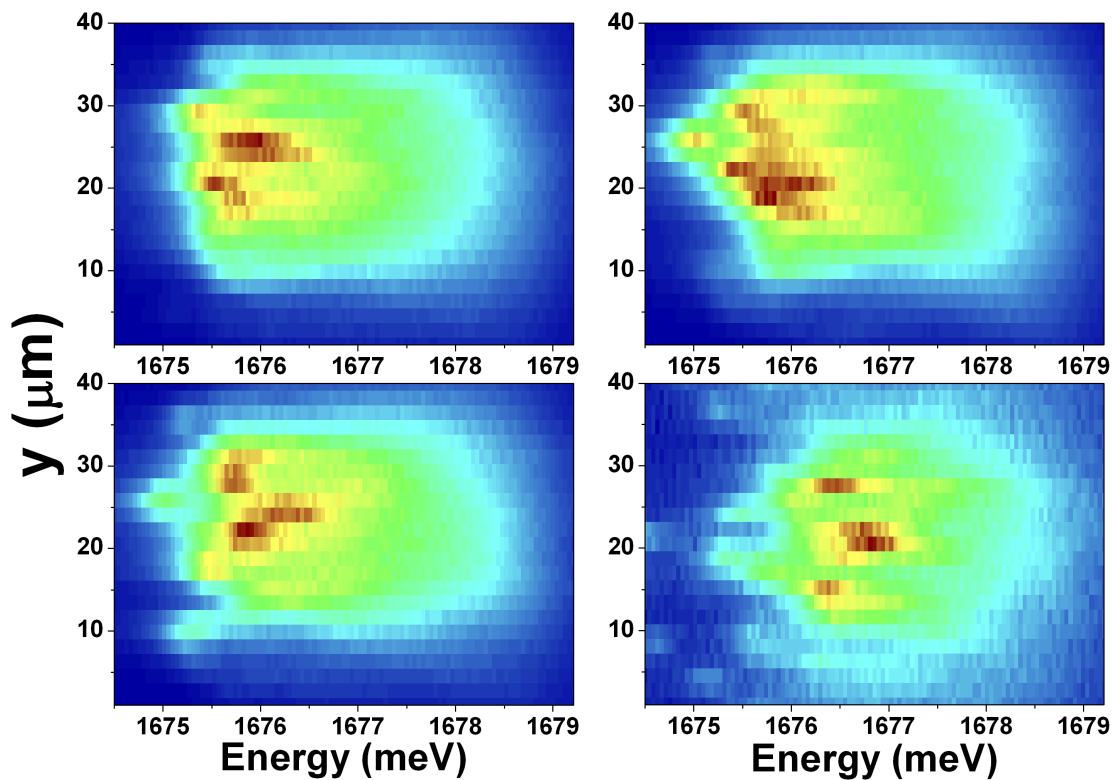


Figure 9.4: Spectrally resolved near-field image of the polariton emission in the weak excitation regime. The disorder is clearly observed within the emitting spot.

ization mechanism depends on detuning. Such a relationship is indeed found: the number of localized points within the excitation spot increases on going towards positive detuning. Statistically, for negative detuning 1-2 bright spots are visible, whereas in positive detuning within the same size of the excitation spot the number of localized spots increases up to 5-7. This tendency is plotted in figure 9.5.

This behavior is not fully understood at present. We might argue that it is connected with the weaker localizing potential experienced by polaritons as the detuning is varied from negative towards more positive values. This hypothesis is illustrated in figure 9.6. We have simulated behavior of the lower polariton branch as a function of the detuning, with the additional, random energy fluctuations. As can be seen in this figure, we have chosen the amplitude of the photonic disorder to be significantly larger than the excitonic one. Thus, in these conditions it is obvious that under negative detuning the disordered potential experienced by polaritons is governed by the photonic fluctuations. As the detuning is swept towards positive values, the lower polariton branch is "smoothed" i.e. the potential traps in the real space become shallower, hence polariton wave function is more delocalized. This could explain why in the condensed regime the number of localized spots increases with detuning.

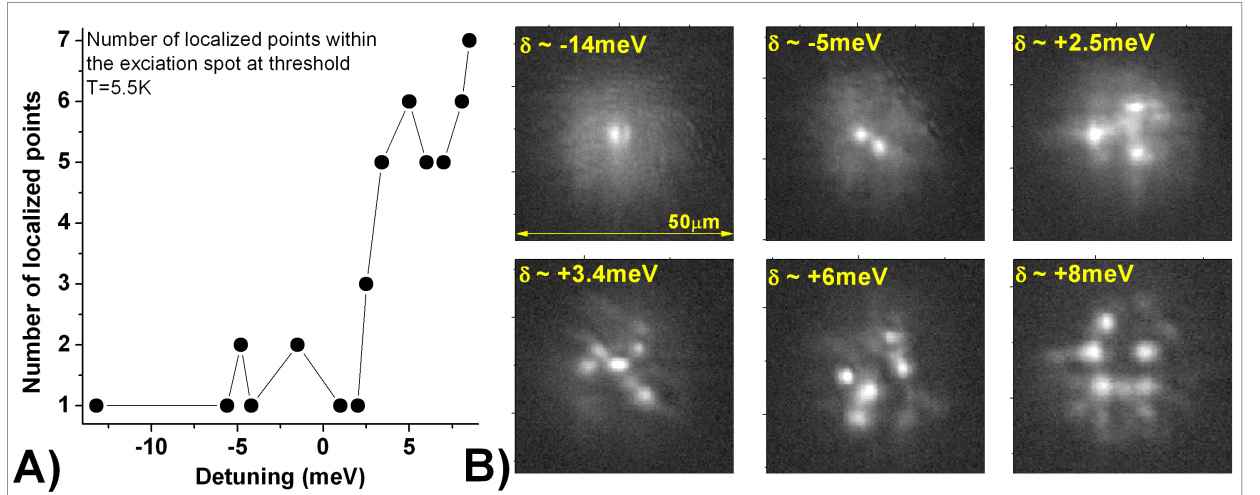


Figure 9.5: *Number of localized spots as a function of the detuning. A: When going towards positive detuning the number of localized spots within the excitation spot increases from 1-2 to 5-7. B: Near-field images of the polariton emission in condensed regime for different detuning. The excitation spot size around 35 μm .*

Conclusions We have discussed the real space properties of the polariton emission. In the weak excitation regime the emitting spot is homogenous and corresponds to the excitation spot shape. It was shown that, when condensed, the polariton emission is strongly peaked around kind of traps produced by the photonic disorder of a microcavity. In spite of the energy fluctuation due to the photonic disorder one can find areas, where the spatial energy fluctuations of the emitting spot are negligible

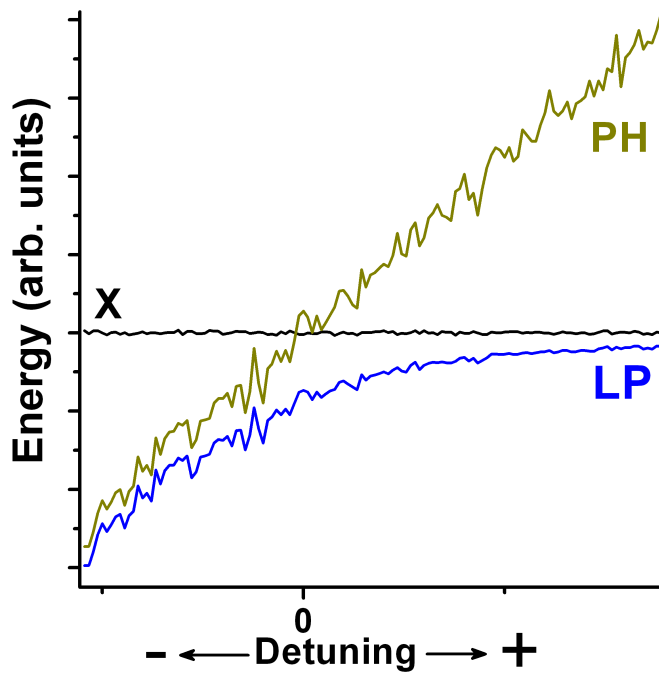


Figure 9.6: *Effect of the photonic disorder on the lower polariton branch as a function of detuning. Under negative detuning disorder has dominantly photonic origin. Increasing detuning results in the "smoothing" of the lower polariton branch. Under positive detuning polaritons are less sensitive on the photonic disorder.*

with respect to the emission linewidth, justifying the claim of condensation into the single quantum state. These findings are the starting points for investigations presented in chapters 10 and 11.

Chapter 10

Polarization

Polariton condensation into a single state should manifest itself as the emission with a well defined polarization state. In this part, we present experiments that demonstrate spontaneous development of linear polarization in the emission from the condensed state. The real space observations confirm the **collective** phenomenon of the condensation and strongly suggest **formation of a single quantum state**. The origin of the linear polarization is discussed. A splitting of the order of $\epsilon \sim 0.1 - 0.2$ meV between two linearly cross-polarized emissions from a polariton ground state is found. In spite of the fact that $\epsilon \ll k_B T = 1.6$ meV, the system chooses the lower state in the stimulated scattering process.

Contents

10.1 Experimental procedure	105
10.2 Build-up of linear polarization	106
10.2.1 Detuning $\delta = +5$ meV	106
10.2.2 Detuning $\delta = 0$ meV	108
10.3 Origin of the linear polarization	110
10.3.1 Linear polarization as a signature of symmetry breaking	110
10.3.2 Ground state splitting	110

10.1 Experimental procedure

The microcavity sample is excited non-resonantly by a laser operating in a quasi-CW mode. The linear polarization of the laser can be turned by a $\lambda/2$ retarder plate placed before a non-polarizing beam splitter cube BS (see figure 4.1). The excitation can be also made circularly polarized by replacing the half-wave plate by a quarter-wave plate oriented at 45° with respect to the direction of linear polarization of the laser. To prevent parasite effects, non-polarizing optics is used in the detection path. The monochromator grating is known to have significantly different efficiency

for both linear polarizations³¹. To suppress this effect, a constant polarization is sent into the monochromator by putting a linear polarizer in front of the slit. To probe the linear polarization properties, a half-wave plate is rotated in front of a polarizer from 0 to 180 degrees. The far field and the near field emission are investigated for different detunings and different samples.

10.2 Build-up of linear polarization

10.2.1 Detuning $\delta = +5$ meV

The linear polarization degree of the polariton ground state ($\alpha = \frac{I_{max}-I_{min}}{I_{max}+I_{min}}$) as a function of the pump power is plotted in figure 10.1³². Below threshold emission is depolarized. At condensation threshold the linear polarization degree increases abruptly reaching the value of 85% above threshold.

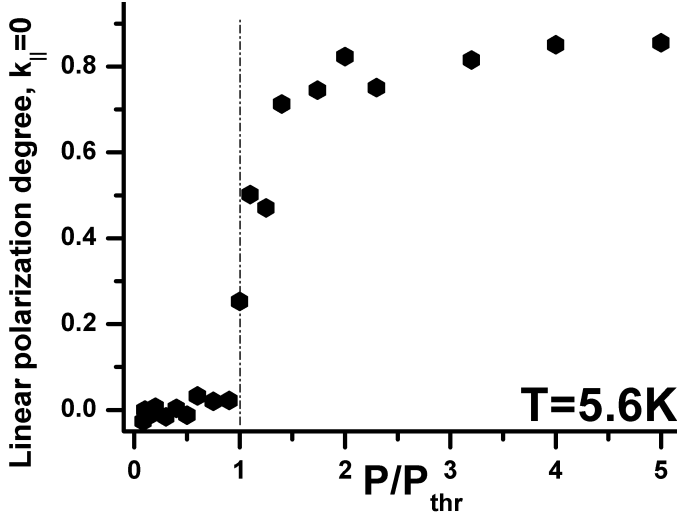


Figure 10.1: *Linear polarization degree of the polariton ground state as a function of the pump power. Below threshold emission from the ground state is depolarized. At threshold a rapid onset of the linear polarization degree is observed reaching value of around 0.85 above threshold.*

The polariton dispersion below threshold ($P \sim 0.28P_{thr}$) and above threshold ($P \sim 1.6P_{thr}$) for two cross-polarized directions is presented in figure 10.2 b, c, d, e. The photon-exciton detuning is $\delta = +5$ meV. Below threshold the emission appears to be completely depolarized with an accuracy of 1%. Above condensation threshold, the degree of polarization of the ground state emission increases by up to 83%. The polarization direction is oriented along a well defined crystallographic direction (probably [110]) with a standard deviation of 15° . A very strong linear polarization is observed only from the polariton condensate; the thermal cloud stays unpolarized.

The direction of the polarization emission is probed as a function of the polarization state of the pump. Regardless of the polarization direction of the pump, the

³¹At 740 nm, 60% and 30% for light polarized perpendicular to and parallel to the grating lines, respectively.

³²The results presented in figure 10.1 were exceptionally performed on the twin copy of the sample used throughout this work.

polarization direction of the ground state emission remains the same [Mar05]. Using a circularly polarized pump does not change this result. Thus, the **polarization is developed by the system itself and not by the excitation laser**. This observation confirms that the excitation conditions are strictly non-resonant. The electron-hole pairs are created 82 meV above the exciton reservoir. In the exciton formation and cooling process the coherence and polarization memory of the pump is lost due to many scattering events.

Figure 10.2 a shows a polar plot of the intensity of the ground state emission as a function of the polarization direction, below and above condensation threshold. Lack of any relation between outgoing polarization state and intensity and polarization direction of the pump is demonstrated as well.

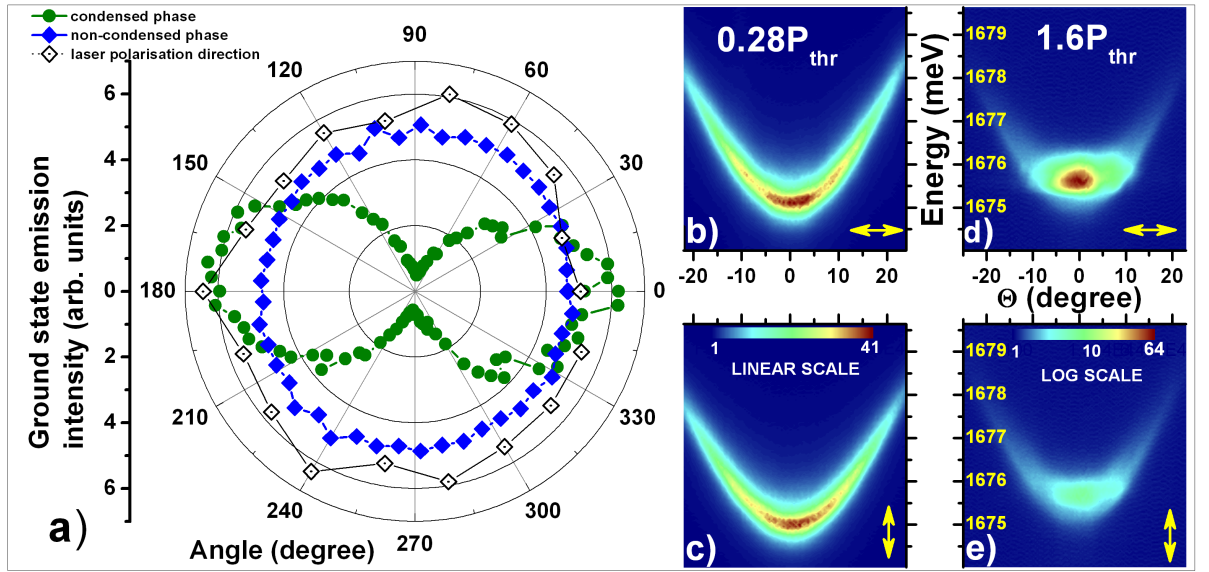


Figure 10.2: *Polarization properties of the polariton emission. Exciton-photon detuning is $\delta = +5$ meV. (a) The polar plot displays the intensity of the ground state emission at $k_{\parallel} = 0$ (angular width of 0.4°) measured as a function of the angle of the linear analyzer. Below threshold (solid blue diamonds), the emission is completely depolarized for linear and circular (not shown) polarization, whereas above threshold (solid green circles) a linear polarization exceeding 80% is observed. The linear polarization is "horizontal" ($0, 180^{\circ}$), roughly aligned along $[110]$. Open diamonds represent the intensity of the linearly polarized emission above threshold measured as a function of the linear polarization angle of the excitation laser: No correlation can be found between the excitation polarization and the polariton polarization. Panels (b-e): Analysis of the linear polarization of the polariton emission below threshold (b, c) and above threshold (d, e). Below threshold, polaritons all along the dispersion curve are not polarized: their emission intensity is the same for horizontal (\leftrightarrow) and vertical (\updownarrow) polarizations. Above threshold, emission from the excited states remains depolarized, but emission from the ground state is strongly linearly polarized. Note the linear and logarithmic scales used for the emission intensity measured below and above threshold, respectively. b, c, and e share the same x and y axis scale as d.*

In a second set of polarization studies, the polariton emission in real space was investigated. Below threshold the emission is again homogenous and unpolarized. Above threshold the spatial emission exhibits strongly localized pattern. The linear polarized probing shows a very high degree of linear polarisation. Moreover, the polarization state of each of the localized points is the same. This **collective phenomenon** strongly suggest that a single state is formed. Images of the polariton emission in real space below and above threshold for the cross-polarized direction are shown in figure 10.3.

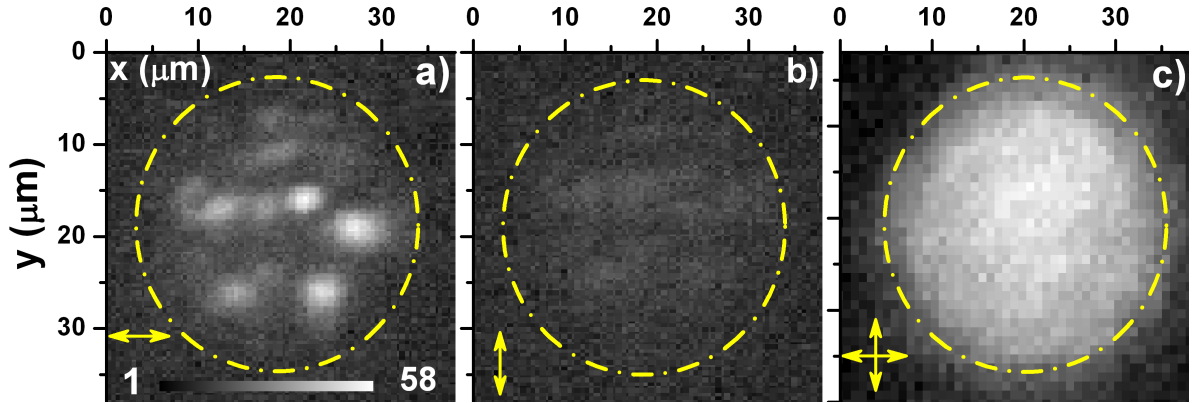


Figure 10.3: Analysis of the linear polarization of the emitting spot below threshold (c) and above threshold (a, b). Exciton-photon detuning is $\delta = +5$ meV. Below threshold the emission appears homogeneous and depolarized (not shown). Above threshold, the emitting spot becomes inhomogeneous: several bright small spots, due to structural inhomogeneities, are observed within the excitation area, yet they emit with the same linear polarization, consistent with the development of a single condensate. The grey scale in a) and b) is the same.

10.2.2 Detuning $\delta = 0$ meV

The polarization characteristics were also studied for the point on the sample which corresponds to zero exciton-photon detuning. The result is shown in figure 10.4. The polarization direction is still aligned along [110] direction and no dependence between outgoing polarization state and pump polarization state is detected. Because of the less positive detuning thermalization below threshold is no longer attained. The degree of linear polarization above threshold is 55%. Below threshold differences between cross polarizations can be noticed. The intensity emitted from the bottleneck region is not the same and a TM-TE splitting of 0.2-0.35 meV is visible. This polarization splitting of the polariton excited states is a consequence of the different effective refractive indexes of a microcavity for light cross- and co-polarized with respect to the incident plane [Per05, Kav04, Pan99]. Being connected with the optical properties of the microcavity, the TM-TE splitting is more pronounced for negative detunings. The real space emission pattern for the cross-polarized configuration is presented in figure 10.5. In this case only one polarized spot is visible.

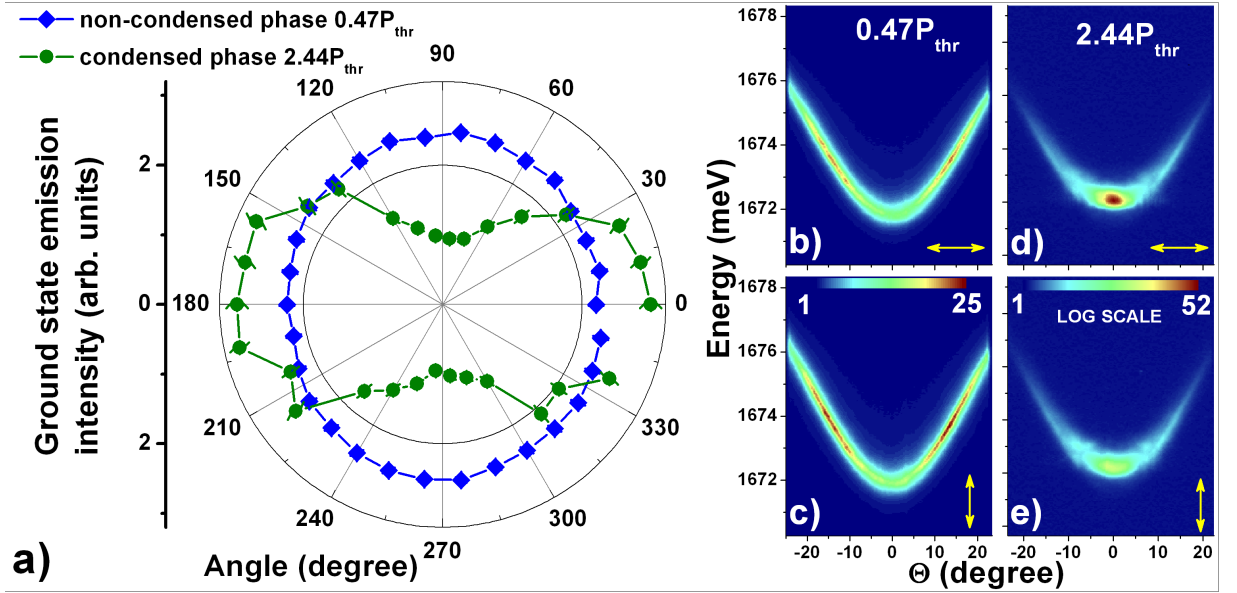


Figure 10.4: *Polarization properties of the polariton emission for photon-exciton detuning $\delta = 0$ meV. (a) The polar plot displays the intensity of the ground state emission measured as a function of the angle of the linear analyzer. Below threshold (solid blue diamonds), 4% polarization is measured. Above threshold (solid green circles) a linear polarization of 55% is observed. The linear polarization is "horizontal" ($0, 180^\circ$), roughly aligned along $[110]$. Panels (b-e): Analysis of the linear polarization of the polariton emission below threshold (b, c) and above threshold (d, e). Below threshold, a TM-TE splitting is visible. The color scale is the same in pairs (b,c) and (d,e). b, d and e share the same x and y axis scale as c.*

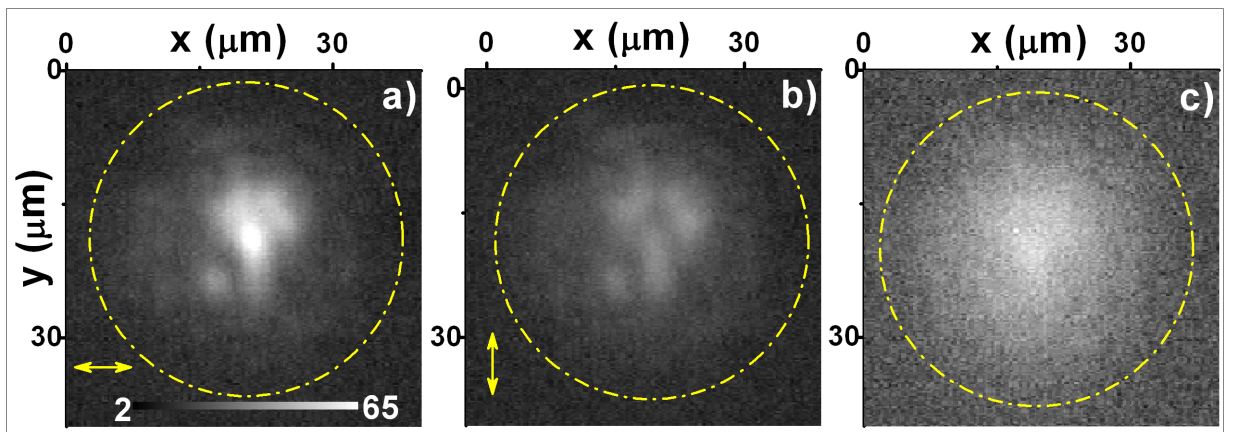


Figure 10.5: *Analysis of the linear polarization of the emitting spot below threshold (c) and above threshold (a, b). Photon-exciton detuning is $\delta = 0$ meV. The grey scale in a) and b) is the same.*

10.3 Origin of the linear polarization

10.3.1 Linear polarization as a signature of symmetry breaking

Bose condensation is a phase transition linked with the appearance of a well-defined phase in the system. As emphasized in [Lau04, Lau06], the development of this phase is manifested by appearance of linear polarization for the condensate emission. In [Lau06] the polariton ground state considered is degenerate with respect to the spin. Namely, when a non-resonantly pumped system condenses, two condensates with spin-up and spin-down are formed: a_{\uparrow} , a_{\downarrow} . The authors demonstrate that **the appearance of the non-zero order parameter in each of the circularly polarized components results in the appearance of the linear polarization**. It was also pointed out that in a system that is perfectly isotropic in the plane, the direction of the polarization is random.

10.3.2 Ground state splitting

Where does the linear polarization in the condensed state come from in our case? The mechanism of 10.3.1 is very tempting, but other possibilities ought to be checked. A good hint is given by detailed studies of the polariton dispersion. First, we repeat that, because of the TM-TE splitting, polariton states exhibit polarization splitting, except for the $k_{\parallel} = 0$ state (see figure 10.6). Surprisingly, as shown in figure 10.6, **the ground state is not degenerate**, but a splitting of $\epsilon \sim 0.1$ meV is found. It is most probably due to the presence of anisotropic strain producing a slight birefringence (prof. A. Kavokin, dr Ł. Kłopotowski - private communications, [Klo06]) in the cavity. The difference in refractive indexes for two crossed polarizations of order of 0.02% results already in the anisotropic splitting of around 0.1 meV³³.

It is worth noting that the condensation occurs always in the lower state. The observation of ϵ and a roughly constant polarization direction rule out the origin of the explanation for linear polarization given in 10.3.1. Apparently, our system is not isotropic in the plane. The cavity environment defines the state into which stimulation occurs, so the "symmetry breaking" is not fully spontaneous. However, the fact that $\epsilon \sim 0.1\text{meV} \ll k_B T = 1.6\text{meV}$ means that the selection is much narrower than the thermal energy. This strongly suggests that the phase transition occurs [Ste98].

Conclusions In this chapter we have investigated polarization properties of the polariton emission. **Strong linear polarization degree** is observed for the condensed state. The observed transition is **spontaneous** in the sense that the polarization state of the condensate does not depend on the polarization state of the pump.

³³ $\delta E \simeq \frac{\delta n}{n} E = \frac{2 \cdot 10^{-4}}{3} 1686\text{meV} = 0.11$ meV

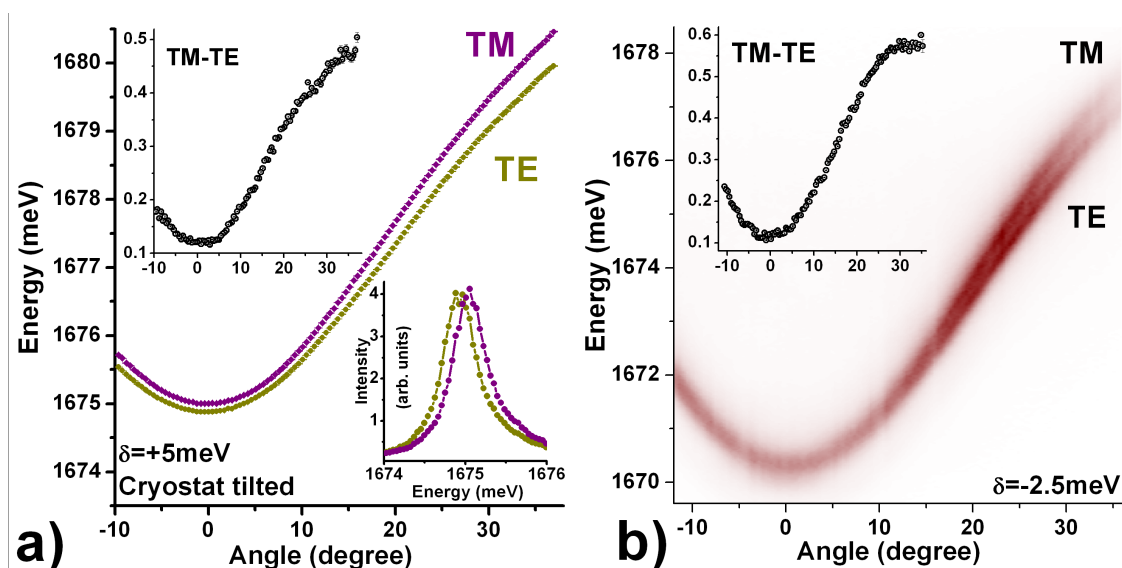


Figure 10.6: *Polarization splitting of the polariton emission for detuning +5 meV (a) and -2.5 meV (b). By tilting the cryostat the light emission at angles up to 37 degrees is detected. TM and TE branches are clearly visible. For negative detuning, the splitting becomes larger than the linewidth. Insets: the TM-TE splitting increases with angle. Surprisingly, the ground state is not degenerate. The cross polarized spectra at $k_{\parallel} = 0$ explicitly show the ground state splitting.*

The real space studies show collective polarization phenomena and strongly suggest **formation of a single quantum state**.

The detailed investigation proves that the **degeneracy of the ground state is lifted** and that the condensation occurs in the lower energy state. This selection in energy, being much narrower than the thermal energy, suggests that a phase transition occurs.

The orientation of the polarization plane is found to be pinned to one of the crystal axes, most probably due to the slight optical anisotropy of the cavity. The effect persists at different detunings between the cavity and exciton modes.

This is this small ground state splitting that fixes direction allowing us to observe a high polarization degree for the condensate emission. The build-up of the linear polarization degree can be indeed interpreted theoretically as an evidence for formation of the polariton condensate. The degree of linear polarization is governed by the number of condensed polaritons, the polariton effective temperature, the polariton interaction constants and the anisotropic ground state splitting (prof. A. Kavokin - private communications). On the other hand, our results cannot be interpreted as a manifestation of a spontaneous symmetry breaking [Lau06]. The symmetry is already broken by the cavity environment.

Chapter 11

Coherence

In this part we investigate coherence properties of the polariton condensate³⁴. First, the spontaneous build-up of the **first order temporal coherence** $g^1(\delta\mathbf{r} = 0, \tau)$, is demonstrated by using a Michelson interferometer. The results confirm that the coherence time of the condensate is longer than the photon lifetime in the cavity, i. e. the phase of the outgoing photons is imprinted by the condensate during up to $\tau = 8$ ps. Next, combining the interferometer with an imaging setup, we study **the first order spatial coherence** $g^1(\mathbf{r}_1, \mathbf{r}_2, \delta\tau = 0)$. A significant increase of the coherence length is observed. In particular, the **spatial correlation mapping** $g^1(\mathbf{r}, -\mathbf{r}, \delta\tau = 0)$ is presented, giving the proof for long range order extending over the excitation spot. A correlation length more than five times longer than the thermal de Broglie wavelength λ_{dB} is measured. Finally, **intensity correlations** $g^2(\tau)$ in CW and pulsed excitation conditions are investigated in a HBT experiment. The results demonstrate **the spontaneous phase transition from a thermal state towards a quantum coherent state** with increasing excitation density.

Contents

11.1 Field correlation	113
11.1.1 First order correlation function $g^1(\mathbf{r}_1, \mathbf{r}_2, t)$	113
11.1.2 First order temporal coherence $g^1(\mathbf{r}_1 = \mathbf{r}_2, \tau)$	113
11.1.3 First order spatial coherence $g^1(\mathbf{r}_1, \mathbf{r}_2, \delta\tau = 0)$	114
11.1.4 Spatial correlation mapping $g^1(\mathbf{r}_1, -\mathbf{r}_1, \delta\tau = 0)$	116
11.2 Intensity correlations	119
11.2.1 Second order coherence function $g^2(\tau)$	119
11.2.2 CW excitation	121
11.2.3 Pulsed excitation	124

³⁴All experiments presented in this chapter were done in T=(3.9-5.3)K

11.1 Field correlation

11.1.1 First order correlation function $g^1(\mathbf{r}_1, \mathbf{r}_2, t)$

In order to investigate the coherence properties of the polariton field, the classical first order correlation function [Gla63] of the polariton emission should be measured.

$$g^1(\mathbf{r}_1, \mathbf{r}_2, \tau) = \frac{\langle E^*(\mathbf{r}_1, t) \cdot E(\mathbf{r}_2, t + \tau) \rangle}{\langle E^*(\mathbf{r}_1, t) \rangle \cdot \langle E(\mathbf{r}_2, t + \tau) \rangle} \quad (11.1)$$

By imposing $\mathbf{r}_1 = \mathbf{r}_2$, the temporal correlations, i.e. the coherence time, can be measured. On the other hand, by putting $\tau = 0$ and $\mathbf{r}_1 \neq \mathbf{r}_2$ spatial correlations of the field between points \mathbf{r}_1 and \mathbf{r}_2 can be investigated.

11.1.2 First order temporal coherence $g^1(\mathbf{r}_1 = \mathbf{r}_2, \tau)$

As recalled in chapter 3.2, polariton condensation is accompanied by spontaneous development of temporal coherence. The measured linewidths are strongly reduced and may be as narrow as 0.18 meV. Let us show that this line narrowing corresponds to an increase of the coherence time³⁵.

The microcavity is non-resonantly excited as in chapter 6. The emission from the polariton ground state is sent to a Michelson interferometer as described in part 4.3.3. The contrast of interference fringes as a function of the delay between the arms is calculated as:

$$c(t) = \frac{I_{max}(t) - I_{min}(t)}{I_{max}(t) + I_{min}(t)} \quad (11.2)$$

For a monomode source, the contrast decays as

$$c(t) \propto \exp\left(-\frac{t}{\tau_c}\right) \quad (11.3)$$

, where the decay constant τ_c is the coherence time. In figure 11.1 the contrast as a function of the delay for different pump powers is plotted. The fitted coherence time is presented as a function of the pump power and the threshold behavior of the photoluminescence.

Below threshold the coherence time is found to be $\tau_c = 1.5$ ps, which corresponds to the polariton lifetime in the microcavity³⁶. At threshold, the coherence time clearly increases up to $\tau_c = 5$ ps and then saturates. In this experiment the accessible pump power is not high enough to induce a decrease of the coherence, as is observed in linewidth measurements (see chapter 6). Just above threshold, the coherence time can be as high as 8 ps. This brings us to the conclusion that the coherence time of

³⁵The $g^1(\mathbf{r}, \tau)$ and $g^2(\tau)$ measurements were performed on the same point on the sample corresponding to the detuning $\delta = +3$ meV. In $g^1(\mathbf{r}, \tau)$ experiments the excitation spot has a gaussian form and a diameter of $d=25 \mu m$. Polarization characteristics of this point are similar to those described in chapter 10: negligible linear polarization below threshold and 72% linearly polarized emission above threshold, independently of the pump polarization.

³⁶The LP luminescence linewidth around $\delta = 0$ meV in the spontaneous regime is $\Gamma = 0.6$ meV.

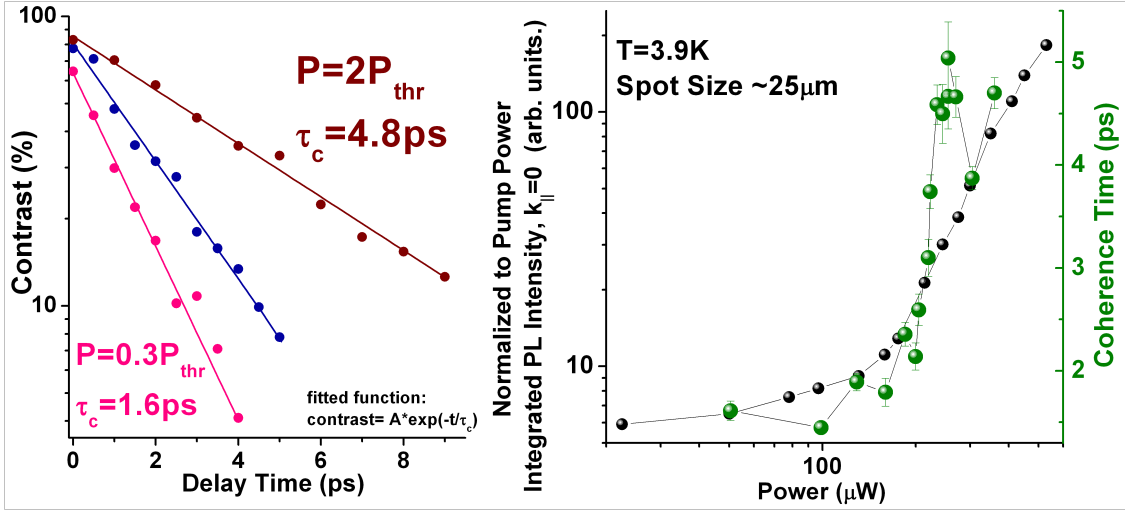


Figure 11.1: *The first order temporal coherence. Left: Measured contrast as a function of the delay for several pump powers. Right: Coherence time τ_c as a function of the pump power (green points) and threshold behavior of the LP photoluminescence (black points). Detuning $\delta = +3$ meV.*

the polariton condensate is around 5 times longer than the polariton lifetime. The coherence is preserved by the condensate itself and its phase is imprinted on the outgoing polaritons.

11.1.3 First order spatial coherence $g^1(\mathbf{r}_1, \mathbf{r}_2, \delta\tau = 0)$

The interferometer can also be used to study spatial correlations of the emitting spot. As shown in chapter 9, the condensate emission comes mainly from localized spots. We will show that the photons emitted by all of those spots are phase correlated.

Two 40 times magnified images of the condensate emitting spot are formed at the output of the interferometer. The two images, each coming from one arm of the interferometer, overlap in the image plane, forming an interference pattern. One image can be displaced with respect to the other by any vector simply by tilting a mirror of the interferometer, as shown in figure 11.2. The contrast of the interference is measured for each point of the image plane by scanning the relative phase of the interferometer over $\sim 6\pi$, providing a direct measurement of the spatial correlation function. The size of the probed area is typically (3-4) μm^2 . The contrast of the obtained interference pattern is directly related to the first order spatial coherence function (see chapters 10.3 and 10.4 of [Bor93]):

$$C(\mathbf{r}, \mathbf{d}) = \frac{I_{max} - I_{min}}{I_{max} + I_{min}} = \frac{2\sqrt{I(\mathbf{r})I(\mathbf{r} + \mathbf{d})}}{I(\mathbf{r}) + I(\mathbf{r} + \mathbf{d})} \times g^1(\mathbf{r}, \mathbf{r} + \mathbf{d}) \quad (11.4)$$

First, the autocorrelation³⁷ is measured, giving negligible changes in the interference contrast value below and above threshold. Next, two points separated by 8 μm

³⁷Interference of the point with itself.

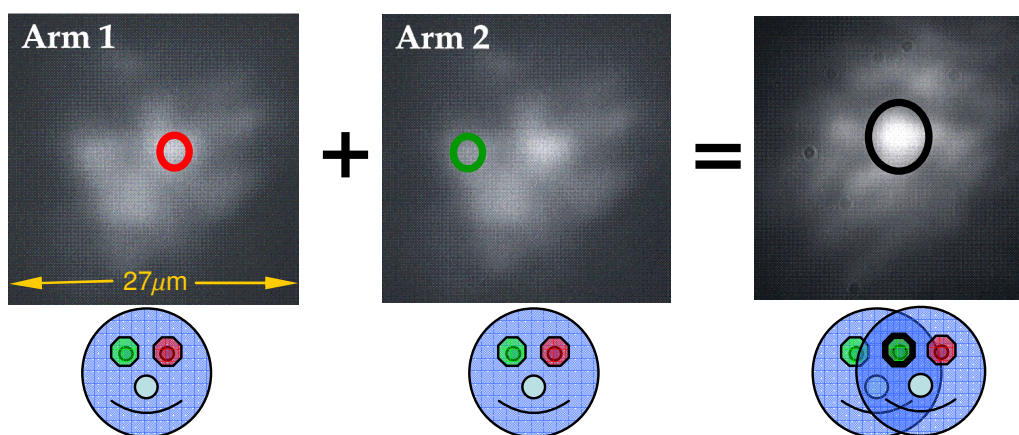


Figure 11.2: *Spatial correlation measurements by analyzing the interference pattern produced by overlapping the images from both arms of the interferometer. The relative distance between the images is tuned by tilting one of the interferometer mirrors. Thanks to the spatial filtering, only the emission from the black circle is detected and analyzed.*

(3 times the thermal de Broglie wavelength) are analyzed. The result is presented in figure 11.3. Below threshold the thermal coherence length is 3 times smaller than the distance between the selected points. The mutual phase is not correlated, resulting in a low contrast value of $c = 6\%$. Above threshold an interference pattern is formed with a contrast up to $c = 46\%$. This kind of experiment is repeated for all pairs of bright spots in the emitting spot, always giving a strong increase of the contrast at threshold. This shows that the first order coherence is extended in space over the whole condensate emitting spot.

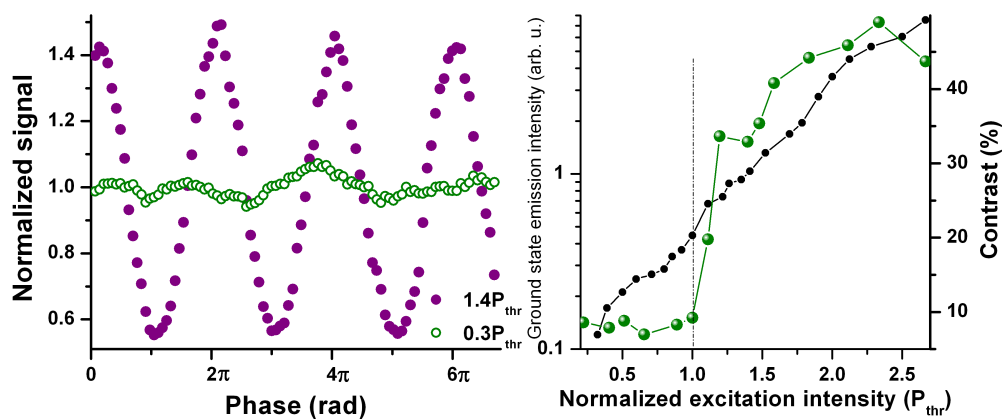


Figure 11.3: *Spatial correlations measured between two points separated by $8 \mu\text{m}$. Left: Interference pattern below (open symbols) and above (full symbols) condensation threshold. Right: Contrast as a function of the pump power. At threshold, the contrast increases by a factor 7, demonstrating the strong increase of the coherence length.*

11.1.4 Spatial correlation mapping $g^1(\mathbf{r}_1, -\mathbf{r}_1, \delta\tau = 0)$

As a second part of the spatial coherence studies, we measure the correlations between any pair of points \mathbf{r}_1 and \mathbf{r}_2 symmetric with respect to the center of the condensate. To do so, the mirror in one arm of the interferometer is replaced by a retroreflector to invert the image in a centro-symmetric way. In this new configuration we obtain a new interference pattern in the image plane (see figure 11.4). The contrast of these interferences carries information about the spatial coherence between points that are centro-symmetric with respect to the center of the condensate - $g^1(\mathbf{r}_1, -\mathbf{r}_1)$. This configuration has the advantage of simultaneously providing the correlation between pairs of points separated by the quantity $|\mathbf{d}| = 2 \cdot |\mathbf{r}_1|$.

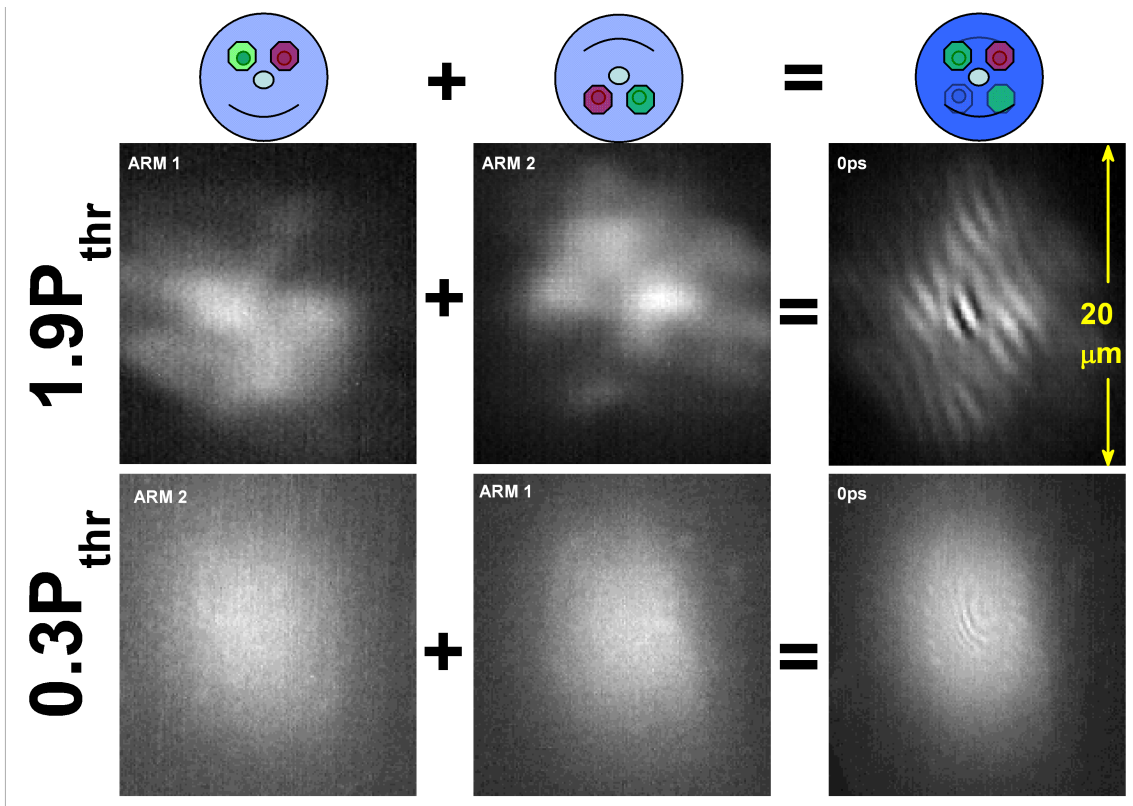


Figure 11.4: *The principle of spatial correlation mapping. Upper row: In the image plane, overlapping occurs (at zero delay) between the image from one arm and its centro-symmetric counterpart from the second arm. The calculated interference contrast carries information about $g^1(\mathbf{r}_1, -\mathbf{r}_1)$. Images from both arms of the interferometer and their spatial interference at zero delay above threshold (middle row) and below threshold (bottom row).*

Correlations measured for excitation power $P = 1.9 \cdot P_{thr}$ are displayed in figure 11.5. Apart from the high correlation peak at the center, which corresponds to the thermal de Broglie wavelength, several large islands with correlations exceeding 40% are observed for couples of points separated by $|\mathbf{d}| = 15 \mu m$. The extent of these correlations is limited only by the finite size of the condensate. The variety of island

shapes simply reflects the spatial inhomogeneity inherited from the in-plane disorder of the microcavity.

These correlations should be compared with those measured below the nonlinear threshold. For low pumping, the correlations vanish for distances as small as $2.6 \mu\text{m}$. This coherence length corresponds to the thermal de Broglie wavelength λ_{dB} of a homogenous thermalized polariton gas. The condensate cloud is several times larger than this length ($15 \mu\text{m}$ vs. $2.6 \mu\text{m}$), yet shows more than 40% of the phase correlations, providing direct evidence of coherence across the entire condensate.

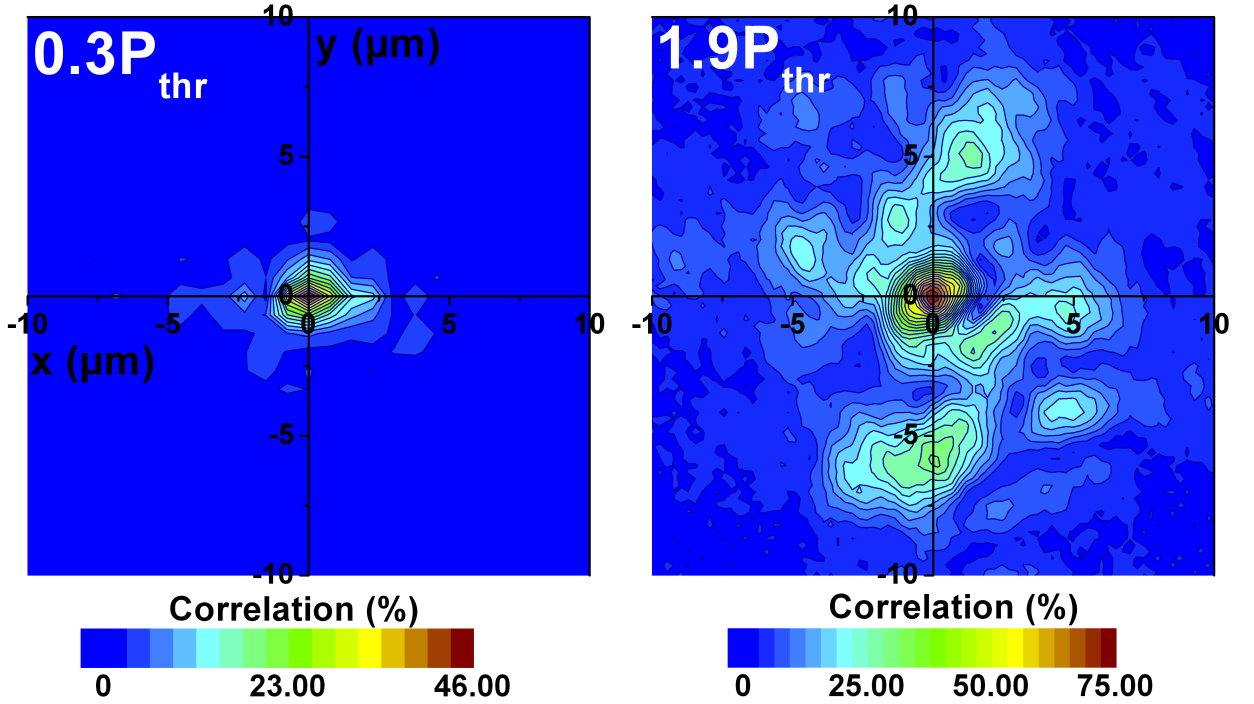


Figure 11.5: *Mapping of the contrast of the spatial correlations. Below threshold, short range, thermal correlations are present and disappear for $\lambda_{dB} = 2.6 \mu\text{m}$. Above threshold, the spatial coherence spreads over the whole excited area, demonstrating the formation of a spatially coherent state.*

To demonstrate the richness and flexibility of this method, let us just remark that by changing the delay between the arms and observing spatially the formed interference pattern one can observe directly the time evolution of the spatial coherence $g^1(\mathbf{r}_1, -\mathbf{r}_1, \tau)$. Thus, the coherence dynamics of the polariton condensate can be studied, giving one possible direction for further development of this work. An example of such a measurements is presented in figure 11.6.

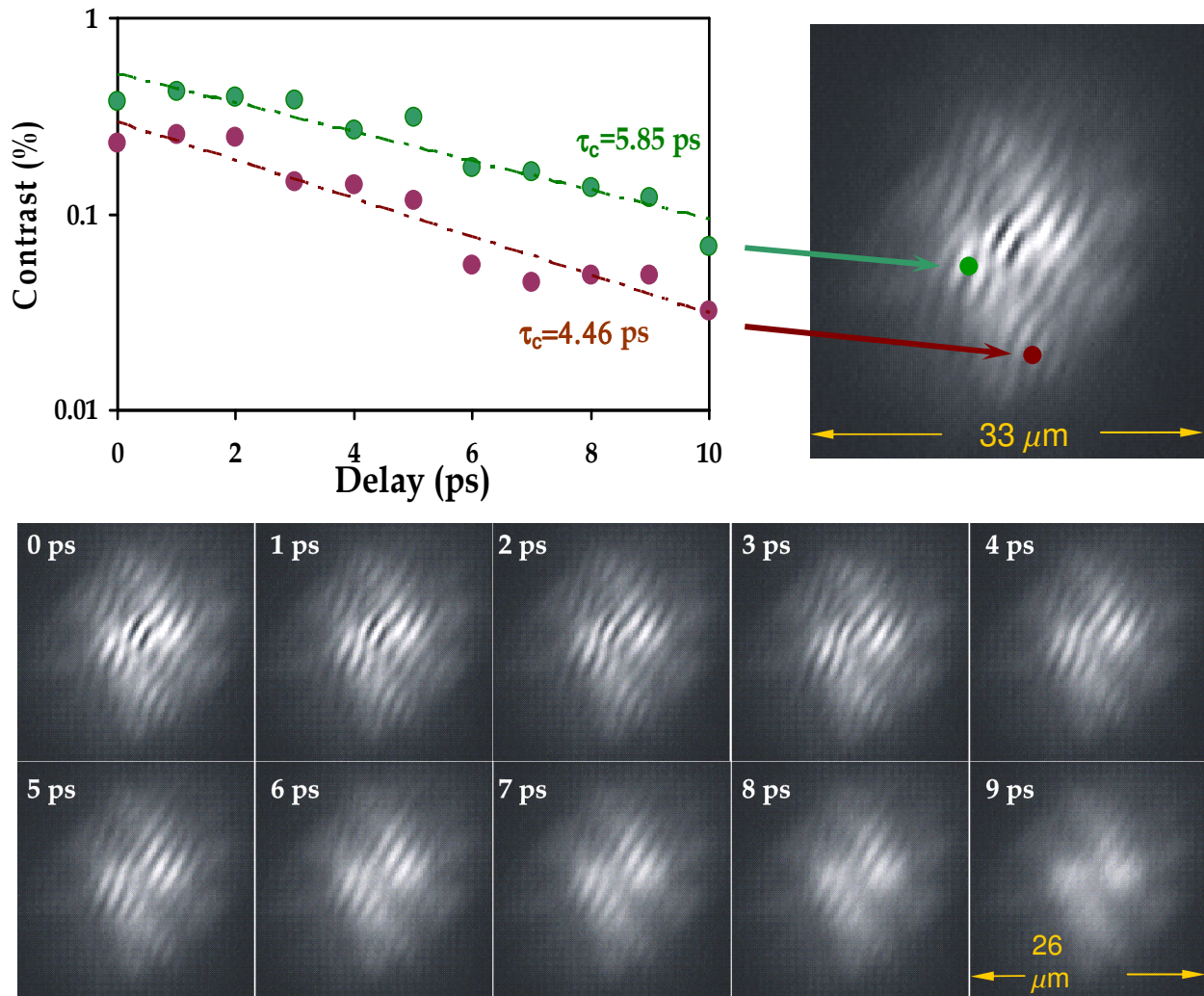


Figure 11.6: *Mapping of the time-resolved spatial correlations. By changing the relative time delay between the arms, one can obtain directly the coherence dynamics of the polariton condensate. Lower part: spatial interference pattern as a function of the time delay. Upper part: coherence time measured for two points of the interfering image of the polariton condensate.*

11.2 Intensity correlations

The term "**coherence**" of the optical field has been used historically to describe the possibility of such a field to produce interference fringes. With this "old" definition one cannot distinguish between the coherence level of sun (white) light filtered by a narrow band filter and of a laser: in both cases the coherence length ($\tau_c \cdot c$) can be long and an interference pattern with high contrast can be observed. Yet, the early stages of optical maser studies showed that these sources exhibit regularities that go beyond the coherence of a thermal source. For instance, different statistics was found for the photons in a thermal source and a laser beam. The concept of coherence had to be reformed and revised. In the mid-sixties R. J. Glauber published the set of articles which gave a basis for a modern understanding of coherence [Gla63, Glau63, Gla65, Gla66]³⁸. In particular, **coherence orders** were described and the fully coherent state was defined as a coherent in all orders. To sum up, in order to provide a complete description of the field coherence, the higher order coherence functions have to be measured. In this paragraph we investigate the second order coherence of the polariton field through the intensity correlation of the emission.

11.2.1 Second order coherence function $g^2(\tau)$

The statistics of photons from a thermal and coherent light source are not the same. It can be shown that photons emitted by a thermal source obey Bose-Einstein statistics [Sal91]. The high variance of this law means that small delays between the photons are privileged. The photons from a thermal source are said to be "bunched" [Sca66], [Mor66]. The situation is different for a coherent source like a laser. Here, the delay between the photons is dictated by Poisson statistics. This means that all delays between emission events are equally probable.

To investigate the statistical properties of light, the 2nd order coherence function has to be measured:

$$g^2(\mathbf{r}_1, \mathbf{r}_2, \tau) = \frac{\langle E^*(\mathbf{r}_1, t) \cdot E^*(\mathbf{r}_2, t + \tau) \cdot E(\mathbf{r}_1, t) \cdot E(\mathbf{r}_2, t + \tau) \rangle}{\langle E^*(\mathbf{r}_1, t) \cdot E(\mathbf{r}_1, t) \rangle \langle E^*(\mathbf{r}_2, t + \tau) \cdot E(\mathbf{r}_2, t + \tau) \rangle} \quad (11.5)$$

In what follows, we will concentrate on the temporal correlations. Thus, the function $g^2(\tau)$ takes the form:

$$g^2(\tau) = \frac{\langle I(t + \tau) \cdot I(t) \rangle_t}{\langle I(t) \rangle \cdot \langle I(t + \tau) \rangle} \quad (11.6)$$

This function is connected with statistical properties of the light through its first two moments: the mean \bar{n} and the variance σ^2 , in the following way [Lau06]:

$$g^2(\tau = 0) = 1 + \frac{\sigma^2 - \bar{n}}{\bar{n}^2} \quad (11.7)$$

³⁸The importance of these works for a modern quantum optics was honored by the Nobel Prize in Physics 2005: Roy J. Glauber "for his contribution to the quantum theory of optical coherence".

Moreover, it can be shown that for the thermal source:

$$g^2(\tau) = 1 + |g^1(\tau)|^2 = 1 + e^{-\frac{2|\tau|}{\tau_c}} \quad (11.8)$$

where τ_c is the coherence time. So the photon bunching for a thermal light source is reflected in $g^2(\tau = 0) = 2$. It decreases exponentially to 1 with time constant $\tau_c/2$. On the other hand, the coherent emission is non-correlated, which results in constant $g^2(\tau) = 1$ (see figure 11.7 and table 11.1).

Source	Thermal	Coherent
Statistics	B-E	Poisson
Probability	$\frac{1}{\bar{n}+1} \left(\frac{\bar{n}}{\bar{n}+1}\right)^n$	$\frac{\bar{n}^n e^{-\bar{n}}}{n!}$
Variance σ^2	$\bar{n} + \bar{n}^2$	\bar{n}
$g^2(\tau = 0)$	2	1
$g^2(\tau = \infty)$	1	1

Table 11.1: *Statistical properties of the thermal and coherent light. The probability of finding n photons in a given time interval is governed by different statistics during the coherence time. The large variance of the Bose-Einstein statistics for thermal light results in a photon bunching during a coherence time. The Poisson statistics for coherent light means that coherent emission is non-correlated. Beyond the coherence time the emission is non-correlated regardless of the emission's nature.*

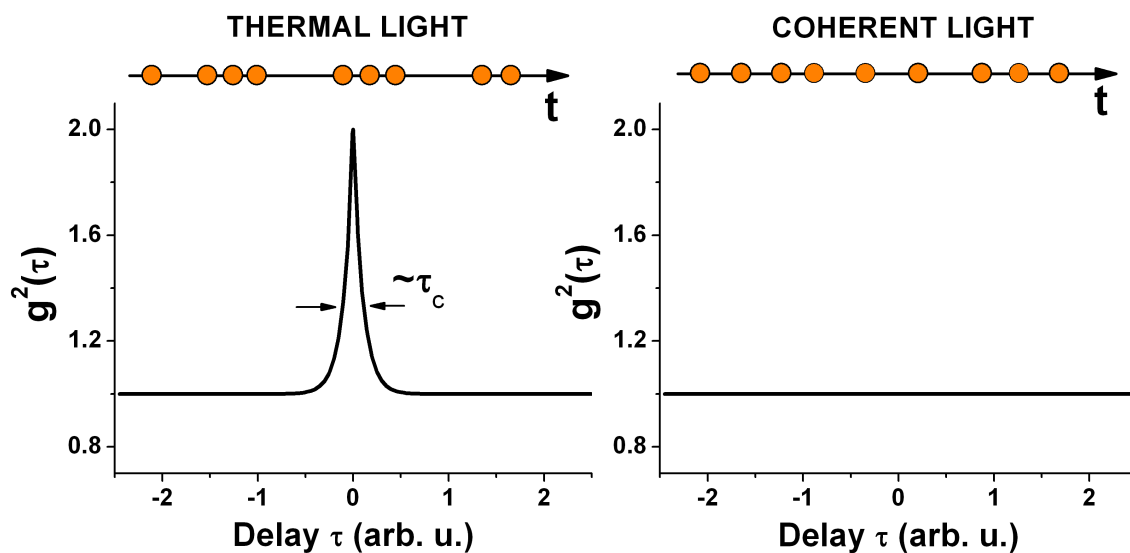


Figure 11.7: $g^2(\tau)$ function for thermal and coherent light. The high fluctuations in the intensity of thermal light result in $g^2(\tau) > 1$ for $\tau \sim \tau_c$.

11.2.2 CW excitation

To study the second order temporal coherence properties of the polariton emission the photon correlator described in part 4.3.4 is used. We work in the Hanbury Brown-Twiss configuration [Han56]: the signal is split by a beam splitter and detected by ultra-fast avalanche photo diodes. The histogram of the relative delays between the photons is constructed, yielding the photon statistics (see figure 4.7).

First, the experimental setup is checked and characterized by measuring the correlations of CW Ti:Sapphire laser light. No correlation in the laser signal is expected. Nevertheless, the oscillations in the laser intensity are clearly visible - figure 11.8.

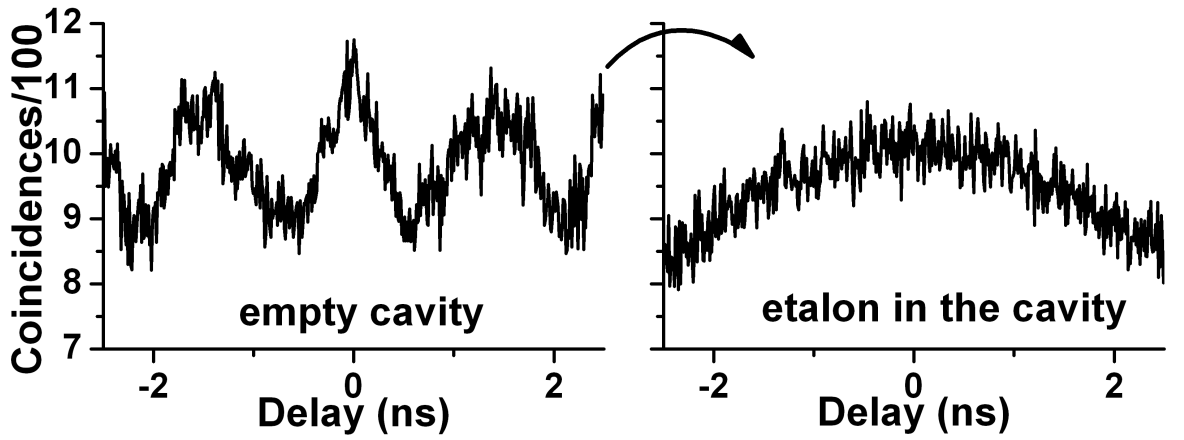


Figure 11.8: *The correlation signal measured on the Ti:Sapphire laser light. Left: dispersion compensation in the laser cavity leads to intensity oscillations. Right: the dispersion compensation is destroyed by inserting the etalon (dispersive element) into the laser cavity, permitting observation of changes in the photon statistics near zero delay. Number of coincidences per channel $N \simeq 1000$.*

This effect is explained as follows. The optics in our laser is optimized for pulsed operation. In particular, dispersion compensation [Coh] is introduced. Thus, the Ti:Sapphire laser has a natural tendency to lock the modes even in CW operation, resulting in a temporal oscillation of the output intensity. Yet, the dispersion compensation can be destroyed by inserting a dispersive element into the laser cavity. Here, an optical quality glass plate is used. As a result, the number of lasing modes is dramatically reduced and only the long period (~ 10 ns) oscillations are present (figure 11.8). To obtain $g^2(\tau)$, normalization with respect to these oscillations is performed. The histogram of the coincidences as a function of the delay τ is presented in figure 11.9. In particular, we see that no bunching is present around zero delay for the laser source. In this experiment number of coincidences per channel is $N \simeq 55000$, which results in a very low photon noise of $\frac{\sqrt{N}}{N} \simeq 0.4\%$. The standard deviation of the $g_2(\tau)$ function of our laser is around twice bigger. This additional noise is the token of multi-mode fluctuations of the laser field.

The same experiment is performed on the polariton ground state photolumines-

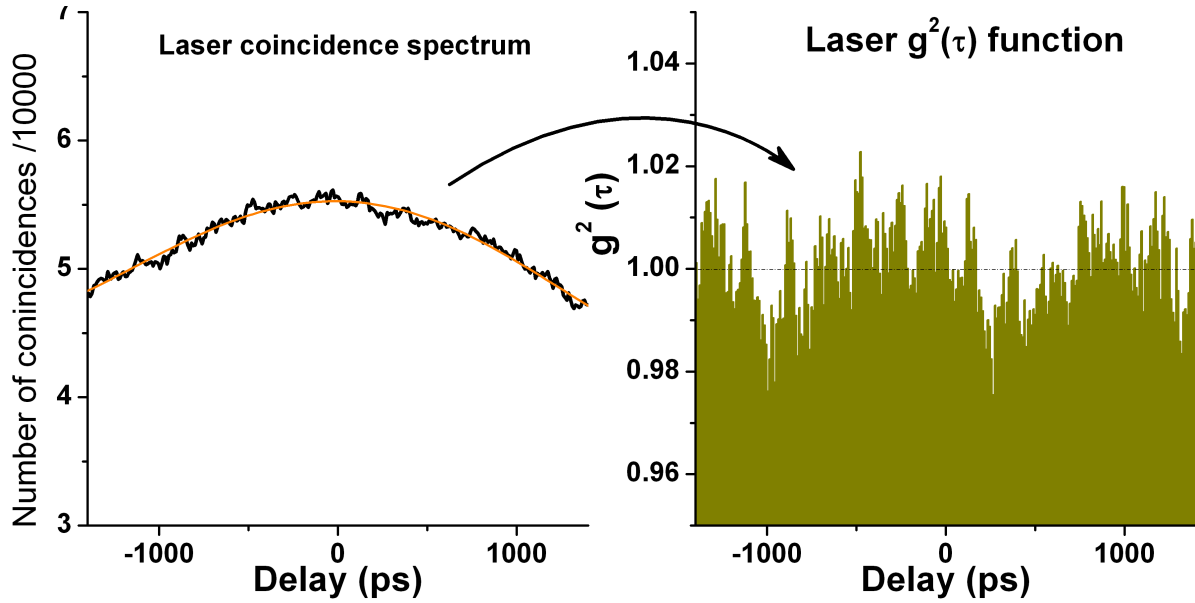


Figure 11.9: $g^2(\tau)$ for the CW-Ti:Sapphire laser light. The flat $g^2(\tau)$ function demonstrates coherence of the laser light. Intensity fluctuations of the laser are twice bigger than the photon noise possibly due to multi-mode emission, even if number of lasing modes was reduced.

cence to investigate the transition from thermal to coherent state. **The major difficulty of this measurement is to detect the photon bunching $g^2(\tau = 0) = 2$ in the weak excitation regime because of the small ratio between the coherence time ($\tau_c = 1.5 - 2$ ps) and the temporal resolution of the correlation setup ($\tau_r = 120$ ps)³⁹.** Consequently, only 1-2% of the measured signal will contain the excess due to the bunching. Thus, the measured value of $g^2(\tau = 0)$ will be an average between correlated events occurring during τ_c and non-correlated ones during $\tau_r - \tau_c \approx \tau_r$ and is expected to be of order 1-2%. In order to observe this small effect, the photon noise must be smaller than 1%, which requires an elevated number of events ($(3 - 4) \cdot 10^4$), i.e. long integration times (~ 3 hours for actual counting rate $(2 - 5) \cdot 10^5$ s⁻¹). The result of the experiment is presented in figure 11.10. The reduction of the photon noise with an increasing number of coincidences is shown in figure 11.12.

Indeed, photon bunching is clearly visible below the condensation threshold. The bunching level is 3% and the width of the peak corresponds to the temporal resolution of the setup. Therefore, below threshold polariton emission has a thermal characteristic. Above threshold, the bunching disappears, which is consistent with the formation of a coherent state. In other experiments we observe a significant reduction of the bunching value, but without its total disappearance, as displayed in figure 11.11.

³⁹This ratio could have been increased by the spectral filtering of a signal by the output slit, with maintaining a high number of coincidences.

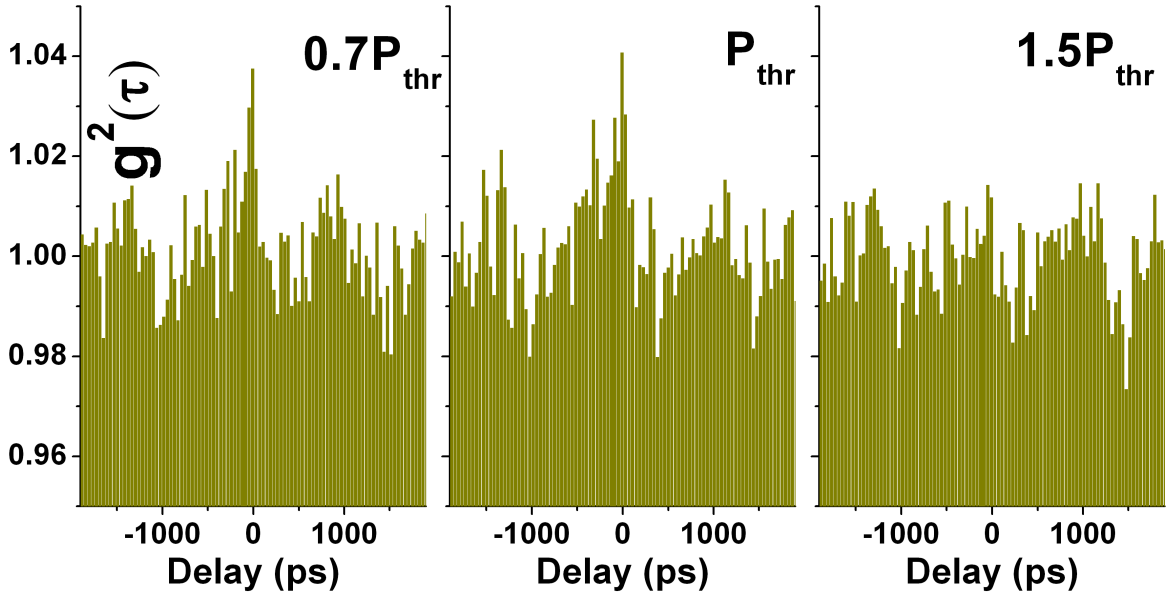


Figure 11.10: *Polariton transition from thermal towards coherent state in $g^2(\tau)$ experiment. Photon bunching disappears above the condensation threshold. Number of coincidences per channel N with increasing pump power is respectively around: 26000, 36000 and 33000.*

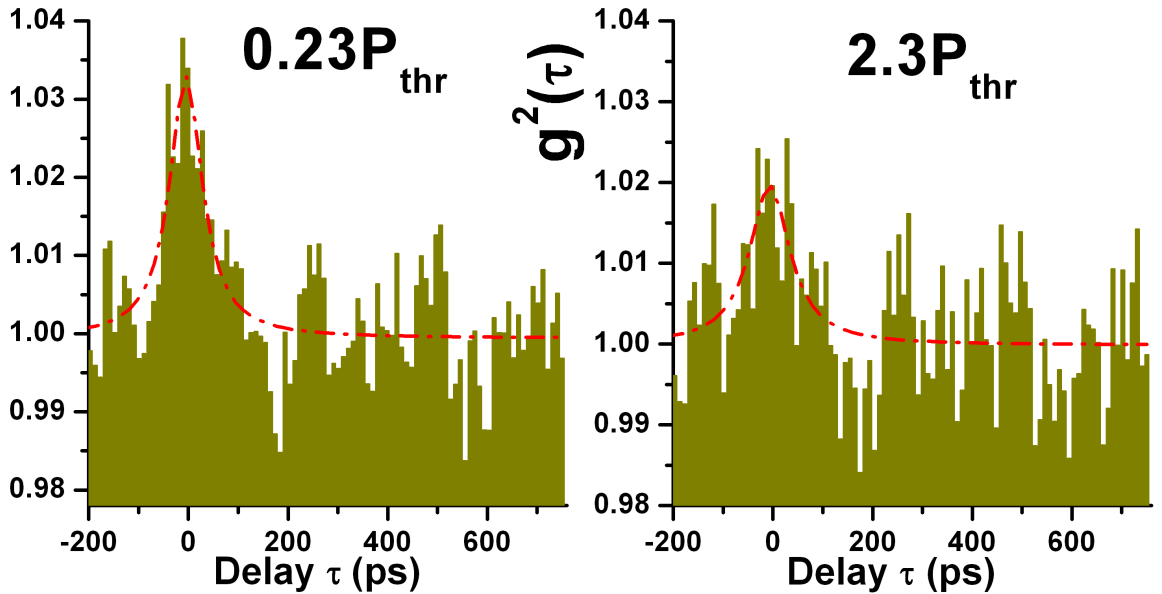


Figure 11.11: *The reduction of the thermal fluctuations in polariton transition towards condensed state observed in $g^2(\tau)$ experiment. Number of coincidences per channel in this experiment is $N \simeq 55000$.*

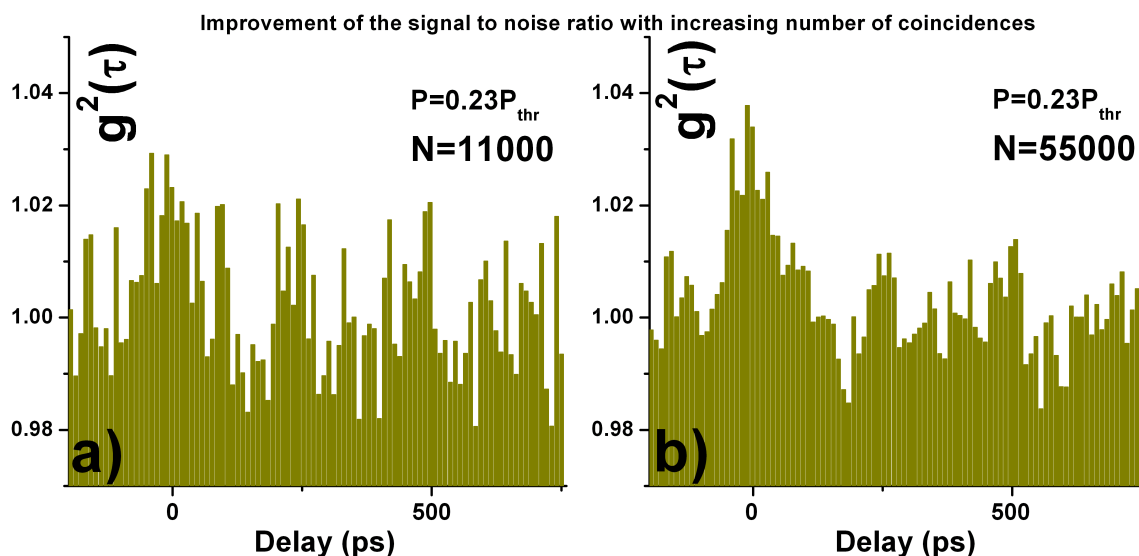


Figure 11.12: *The reduction of the photon noise with increasing number of coincidences. a:* The photon bunching at zero delay time is barely visible. Number of coincidences $N \simeq 11000$ yielding the photon noise of $N^{-\frac{1}{2}} \simeq 1\%$. *b:* Number of coincidences $N \simeq 55000$ resulting in the photon noise of 0.4% . Thanks to the high number of coincidences the photon bunching at zero delay is clearly visible. Experimentally measured photon noise (standard deviation of the non-correlated events in delay range 200-760 ps) are 1.06% and 0.067% for *a* and *b* respectively. $P = 0.23P_{thr}$.

11.2.3 Pulsed excitation

The use of a pulsed excitation rules out a steady state regime, and thus internal polariton equilibrium. The experiment consists of many events of creating and decaying of the condensate. The phase transition that occurs under pulsed excitation conditions will be called **dynamic polariton condensation**. The characteristics of the transition under pulsed excitation conditions are shown in figure 11.13.

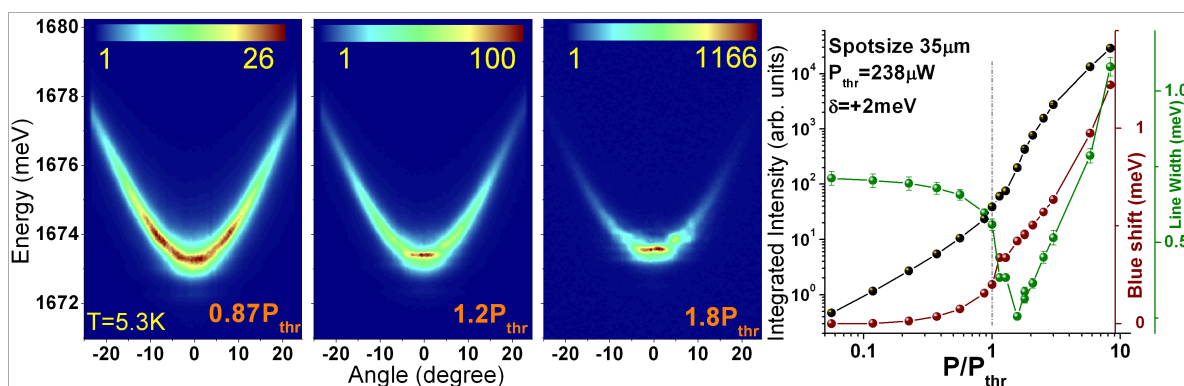


Figure 11.13: *Dynamic polariton condensation. Left: dynamic condensation in the k -space. Right: the threshold, the line narrowing, the blue-shift.*

Nevertheless, the use of pulsed excitation⁴⁰ has certain advantages when $g^2(\tau)$ is to be measured. First, the problem of the temporal resolution of the detectors is no longer present, unless the temporal resolution of the detectors is worse than the separation between pulses. Second, all the coincidences are now "squeezed" into a few channels corresponding to the correlation peaks. So, at the same counting rate⁴¹ the integration time significantly decreases with respect to a CW measurement, facilitating detailed studies. The above statement is illustrated by the following, realistic, experimental situation: In a CW mode integration time of the spectrum with number of channels around 1000 and with 40000 coincidences per channel took around 3 hours. In pulsed mode, with the same coincidence rate, the integration time of the spectrum with the same number of coincidences per channel (in the peaks) was reduced to around 9 minutes. Factor 20 corresponds to the ratio between the total number of channels (that are "used" in the CW mode) and the number of channels included within the correlation peaks (in a pulsed mode). The histograms of the coincidences obtained as a function of the delay are plotted in figure 11.14.

We must take considerable care in the analysis of these data. In the first place, the total number of coincidences, N , in each of the correlation peaks is calculated by integration over **equal** time intervals of 13.1 ns. Apparently, the number of coincidences decreases with increasing delay⁴², even if this is not visible in the raw data. This well known "pile-up" effect appears when the single photon detection regime is lost due to an elevated counting rate [Bec02]. The result of the integration and correction of the laser correlation signal is presented in figure 11.15. The correction is performed as follows. Photons can be correlated only within the zero delay peak. Thus, the zero peak is skipped and the pile-up is fitted only to the weight of the non-correlated (non-zero) delay peaks. By dividing the weight of the zero delay peak by the fit value for zero delay the $g^2(\tau = 0)$ function is found. The error bars are defined by the photon noise and are given by the number of coincidences according to $N^{-\frac{1}{2}}$. As we see, in pulsed mode the errors obtained correspond to the standard deviation of the total number of coincidences in the peaks.

The same procedure is performed for the polariton emission. The corrected histograms are presented in figure 11.16. Evidently, photon bunching of (0.5-1)% is present below condensation threshold. At condensation threshold, bunching of (2-3)% is still visible. For a very high pumping it increases even up to 35%. The ensemble of the results and their spectral linewidths is shown in figure 11.17 as a function of the pump power.

To finish this analysis, the role of the dynamics in a pulsed experiment should be taken into consideration. As stated before, the bunching appears only during the coherence time. Thus, the results should be compared with the ratio between the coherence time and the decay time - $\frac{\tau_c}{\tau_d}$, which is schematically explained in figure 11.18. As shown in [Mul00], due to the stimulated relaxation, the polariton kinetics changes dramatically when approaching the condensation threshold (see

⁴⁰The laser is set to mode-locking operation with a pulse duration of ~ 1 ps and a separation of 13.1 ns between the pulses.

⁴¹In this part of the experiment the counting rate is $(2 - 4) \cdot 10^5 \text{ s}^{-1}$

⁴²The additional delay of 72 ns is introduced by the difference between the cable lengths.

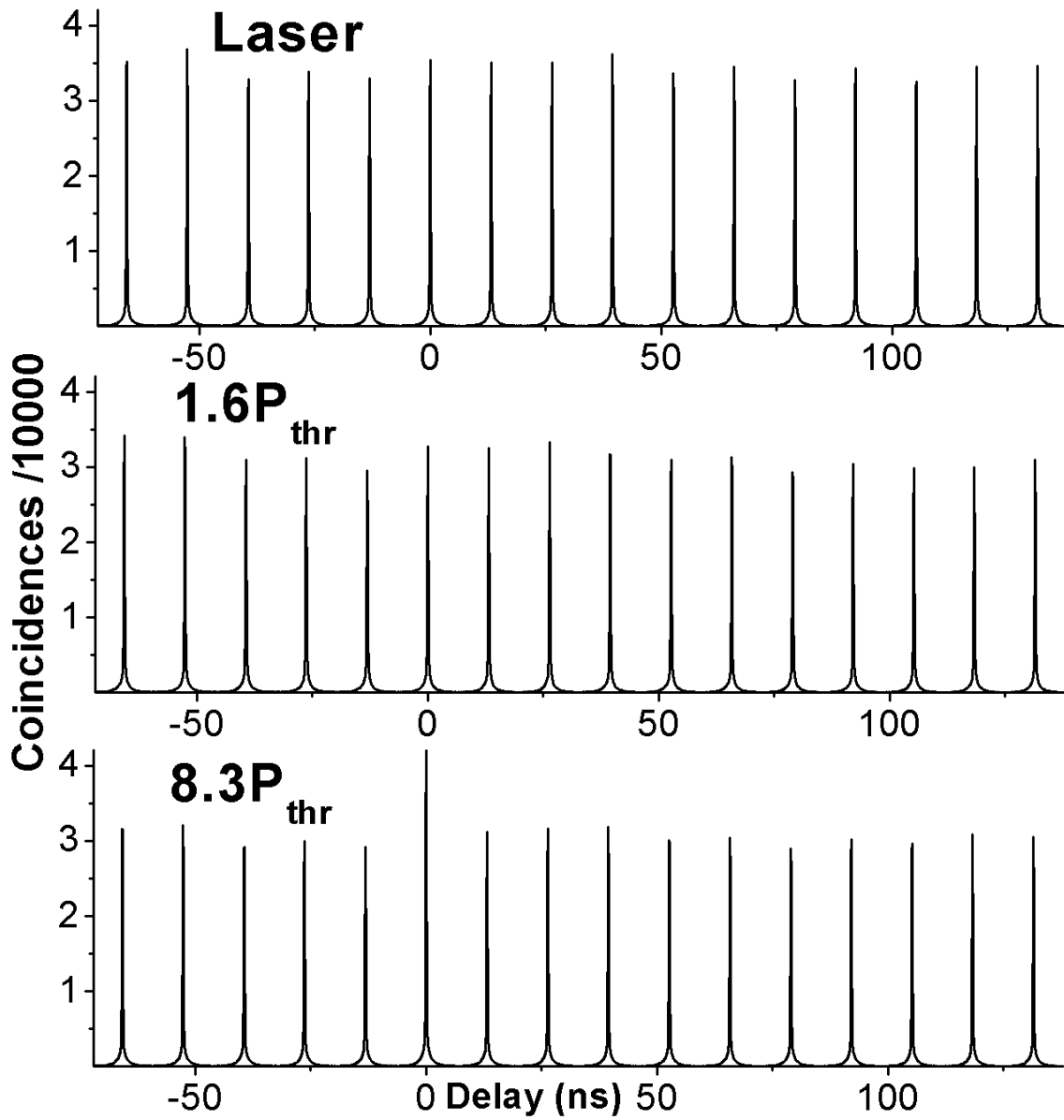


Figure 11.14: *The correlation peaks for the laser in the pulsed mode and the polariton emission above threshold.*

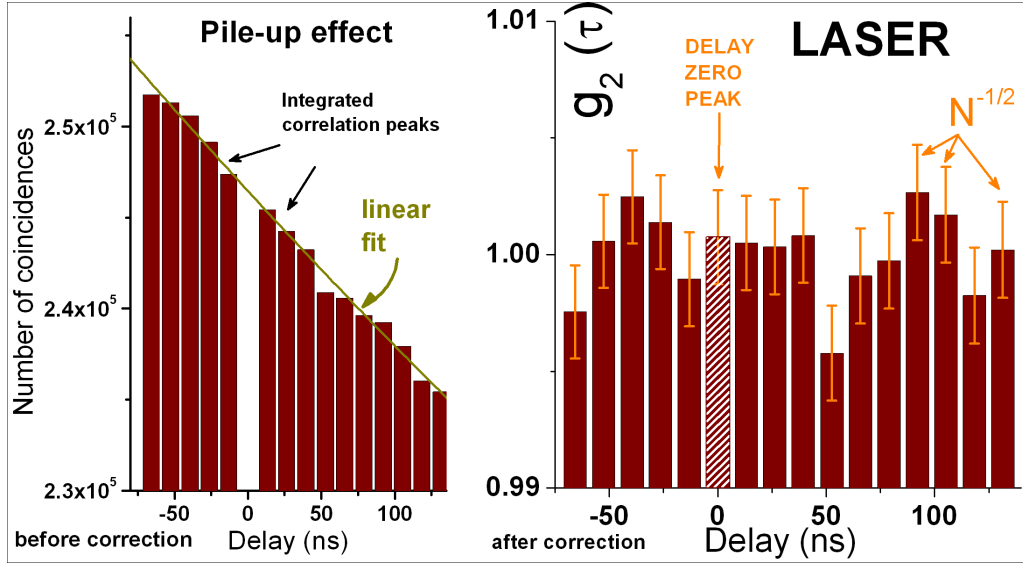


Figure 11.15: The correction of the "pile-up" effect and $g^2(\tau)$ for the laser in the pulsed experiment. The flat histogram demonstrates coherence of the laser. In pulsed mode a standard deviation of the weight of the coincidence peaks correspond to the photon noise: $\frac{\sqrt{N}}{N} = 0.2\%$.

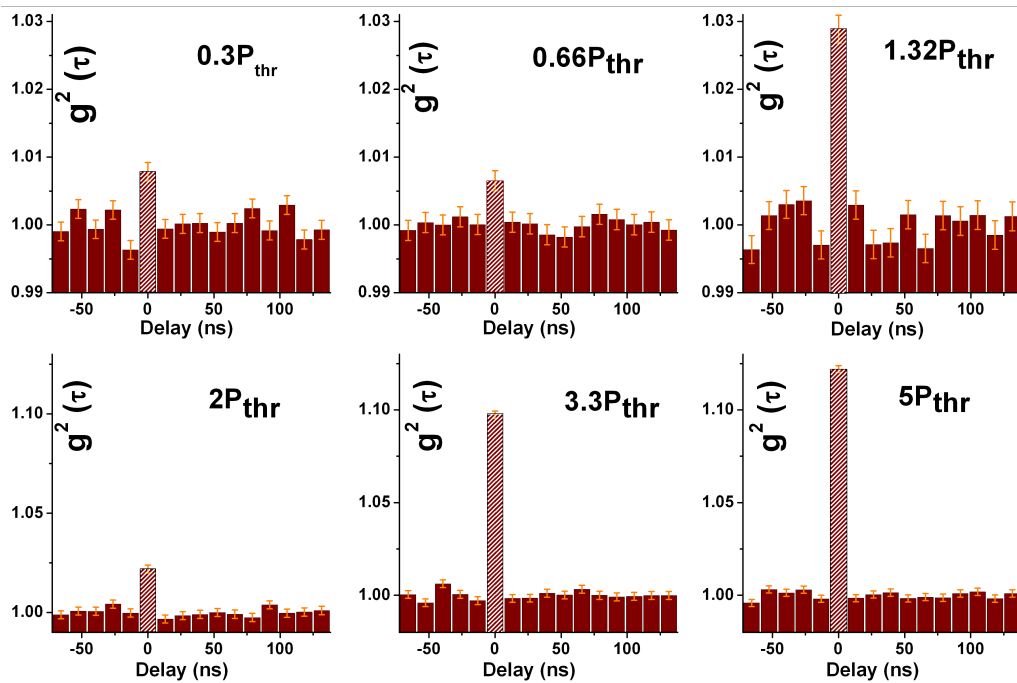


Figure 11.16: $g^2(\tau)$ for the polariton emission in the pulsed experiment.

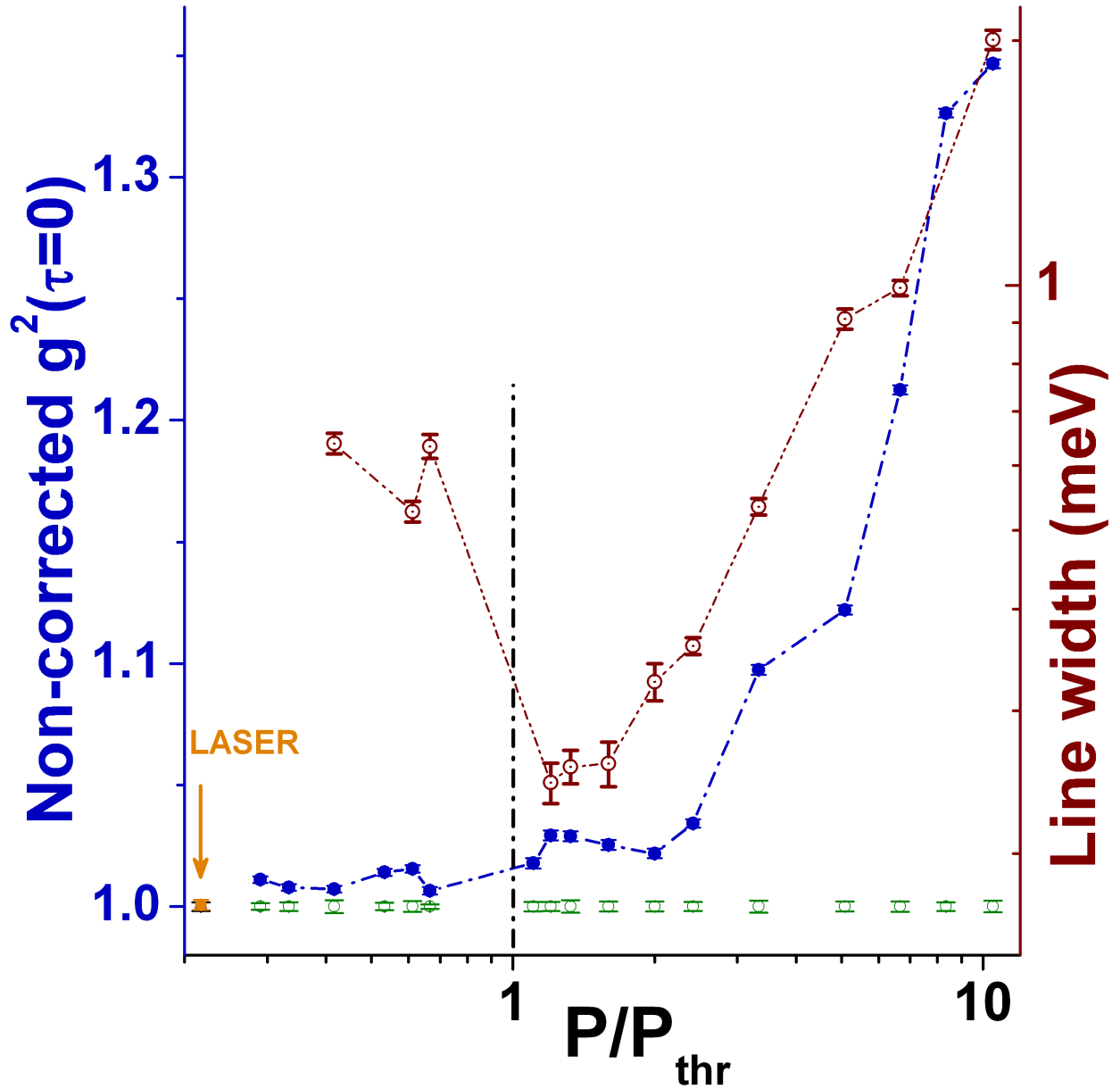


Figure 11.17: *Non-corrected $g^2(\tau)$ (full blue circles) and linewidths (open brown circles) as a function of the power. The spectral broadening of the polariton line is accompanied by increase of the bunching, showing strong decoherence of the polariton condensate far above condensation threshold.*

figure 11.19). The reduction of the decay time from 100-400 ps down to (3-7) ps above threshold was reported. Indeed, such acceleration is manifested in our case by a narrowing of the correlation peaks from almost 500 ps in weak excitation to the time resolution of the correlator, i.e. 120 ps, at and above threshold - figure 11.20.

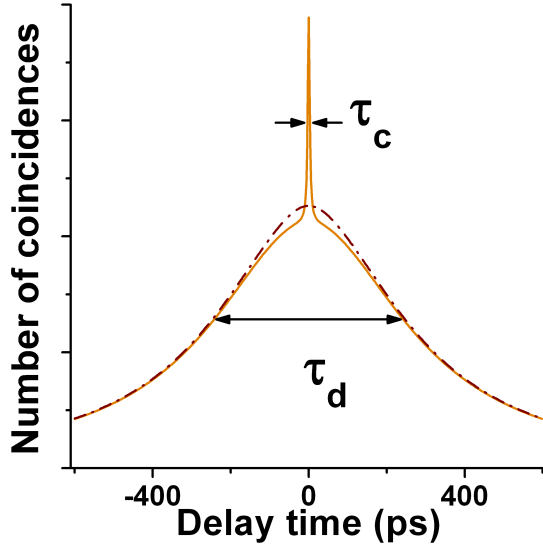


Figure 11.18: *Fine structure of the zero delay correlation peak below the condensation threshold. Supposing perfect time resolution of the correlator (orange line), photon bunching occurs only during coherence time $\tau_c \sim 1$ ps. When a realistic time resolution τ_r is taken into account, the convolution $\tau_r \otimes \tau_c$ smears out the bunching (dashed line). The normalization of measured $g_2(\tau)$ with respect to the ratio τ_c/τ_d , gives information about the $g_2(\tau)$ during coherence time.*

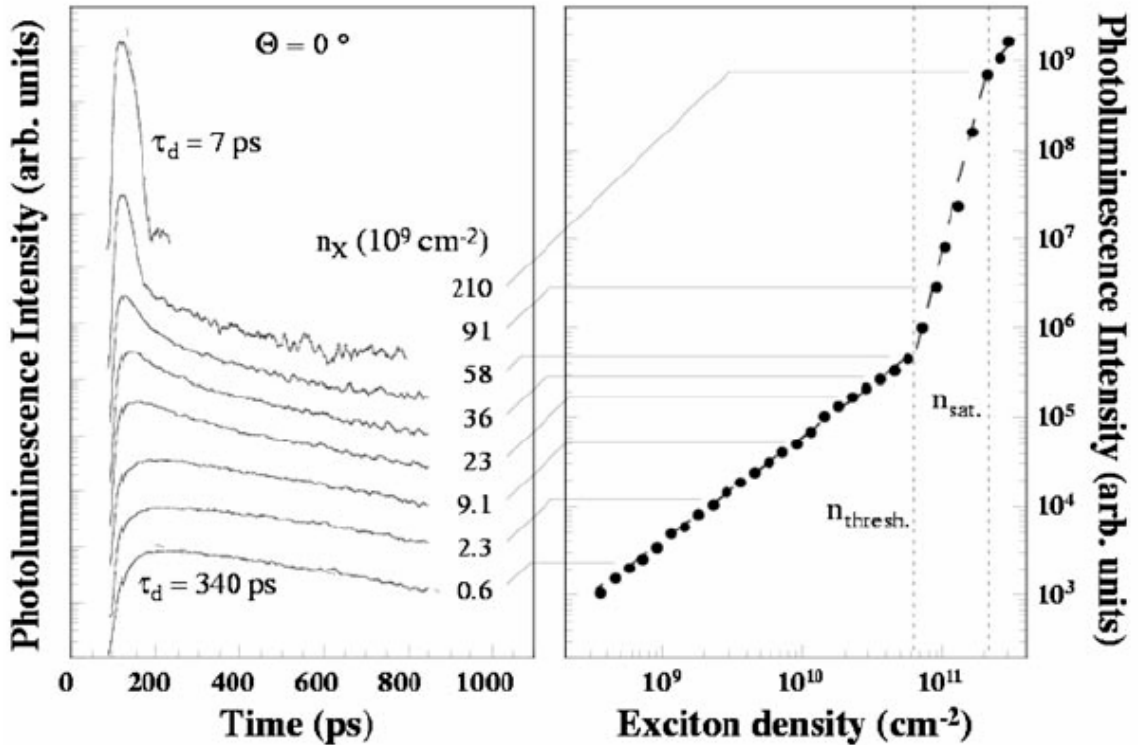


Figure 11.19: *The time resolved experiment from [Mul00] showing the turn-on of the stimulated relaxation.*

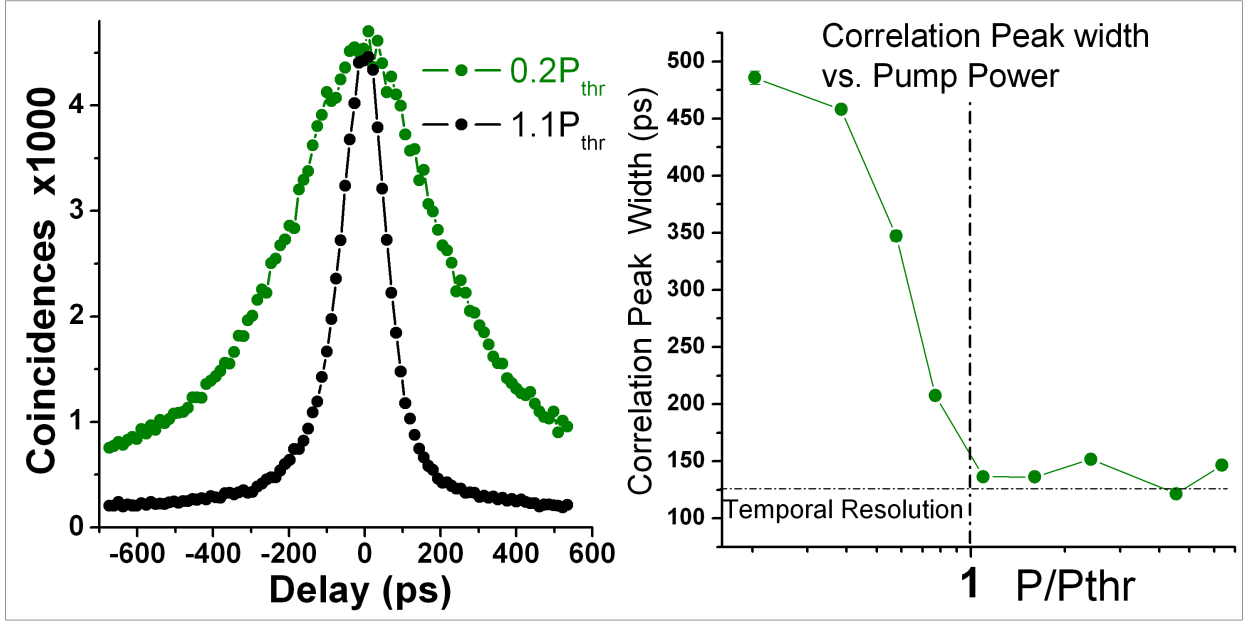


Figure 11.20: *The narrowing of the correlation peaks due to the reduction of the decay time.*

The overall conclusion is the following. To get information about the photon statistics during the time τ_c , measured $g^2(\tau)$ values should be normalized with respect to the $\frac{\tau_c}{\tau_d}$ ratio⁴³.

P/P_{thr}	τ_c [ps]	τ_d [ps]	$g^2(\tau)$	Corrected $g^2(\tau)$
<1	1-2	100-400	1.005-1.01	~ 2
(1,2.5)	5	5-7	1.02-1.03	1.02-1.1
>5	1	3-5	1.2-1.3	~ 2

Table 11.2: *The corrected $g^2(\tau)$ - values of the $g^2(\tau)$ during the coherence time in the pulsed experiment.*

As is shown in table 11.2, below the condensation threshold during the time τ_c , the strong bunching occurs showing the thermal statistics of the emission. The corrected correlation function decreases at the condensation threshold, approaching coherent statistics. However the value $g^2(\tau = 0) = 1$ expected for a coherent source (like a noiseless laser operating above threshold) is not reached. This is not surprising since the polaritons are interacting particles. Interaction induced decoherence is observed far above threshold: the $g^2(\tau)$ increases again demonstrating degradation of the coherence, which is also witnessed by the simultaneous linewidth measurements.

Up to date, only one experiment dealing with the second order coherence properties of the polariton emission has been published [Den02] (see figure 11.21). The

⁴³The exact values of the corrected $g^2(\tau)$ function require measurements of the decay time on the sample point under consideration.

main observations pointed out in that work are as follows. First, below threshold no bunching effect is observed in [Den02] due to a very small ratio between the coherence time and the decay time. Second, above threshold, the decay time becomes comparable with the coherence time and for pump power $2-5P_{thr}$ a constant $g^2(\tau = 0) = 1.77$ is reported. This surprisingly high bunching value shows that the polaritons are in an almost pure thermal state for pumping as high as $5P_{thr}$. The $g^2(\tau = 0)$ remains far from unity (the value predicted for the coherent state) for pumping values as high as $18P_{thr}$. Moreover, no signs of the first order coherence are present: the line narrowing is not present in the spectra shown. However, between $8-18 P_{thr}$ a slow decrease from $g^2(\tau = 0) = 1.7$ down to $g^2(\tau = 0) = 1.48$ is seen and interpreted as an improvement of the coherence.

It is interesting to confront the above experiment with our results obtained in the pulsed mode. In our case, the situation is completely different. First, thanks to the elevated number of coincidences, the bunching effect is clearly observed below threshold, giving the thermal value of the bunching during the coherence time. Second, for pumping power $1-2.5P_{thr}$ the bunching collapses down to $g^2(\tau = 0) = 1.02 - 1.1$. Finally, for pumping values bigger than $5P_{thr}$ we see opposite behavior with respect to that by [Den02]: the decoherence demonstrated by the line broadening results also in an increase of the bunching value up to $g^2(\tau = 0) = 1.35$ for pump power $10P_{thr}$. The comparison between the two sets of data is shown in figure 11.21.

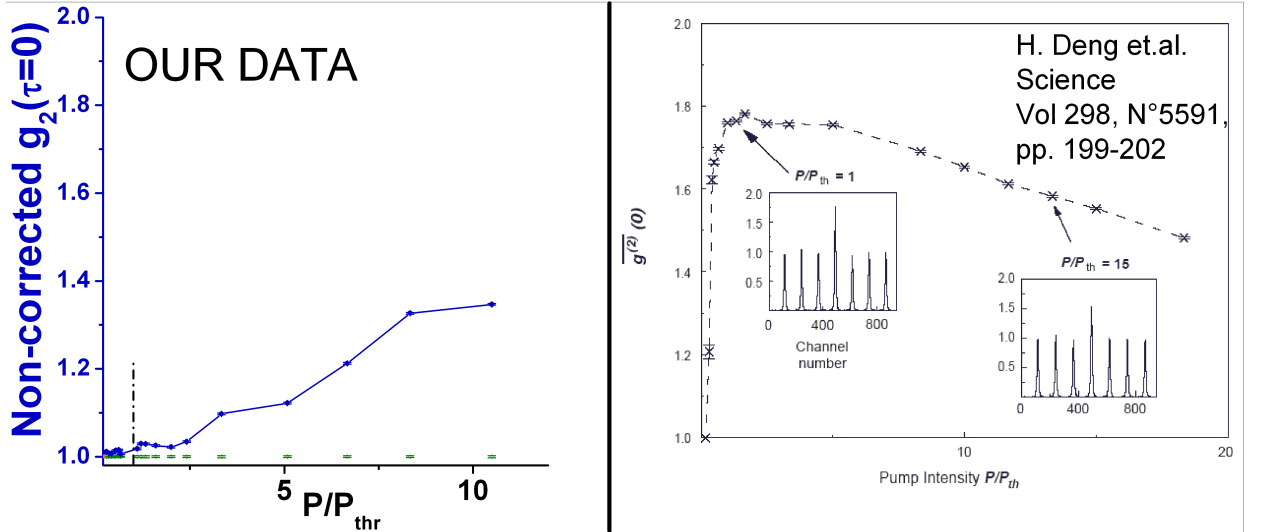


Figure 11.21: The comparison of the non-corrected $g^2(\tau = 0)(P/P_{thr})$ obtained in this work and in [Den02] (right). Left: the same data as in 11.17 on a linear scale.

Conclusions In this chapter **coherence aspects of the polariton condensation** were studied. Signs of the spontaneous coherence in CdTe microcavities have already been noticed [Max05, Mox05]. Here, the **spontaneous formation of the coherent state at the condensation point is proven** in a straightforward way, by a variety of experiments. It is confirmed that the observed line narrowing corresponds to an increase of the coherence time. Spatial coherence measurements demonstrate formation of the correlations in the whole excited zone, on the length scale of $5 \cdot \lambda_{dB}$. **For the first time in an excitonic system, formation of partial long range order is observed.** The powerful method of spatial-temporal correlations mapping will obviously be applied in the future to study such exciting aspects as the decay of the spatial correlations, the formation of vortices, condensate oscillations [Mox05], interference between separated condensates.

The intensity correlation experiments have shown **strong reduction of the thermal fluctuations in the emission from the condensed state.** In addition, the result obtained in the pulsed excitation demonstrates reappearance of thermal fluctuations far above threshold. The build-up of the second order coherence at the condensation threshold justifies the phrase "polariton laser" - coherent emission from the polariton condensate [Lau04]. At the same time, increase of bunching far above threshold reveals a fundamental difference between a "polariton laser" and a standard laser: coherence of the "polariton laser" is destroyed by polariton interactions when increasing population of the condensate, whereas coherence of the standard laser is improved with increasing number of photons in a lasing mode.

The experiment that would complete the coherence investigations is noise measurement [Baa06]. The detection of the same noise from the whole excited area would confirm formation of a single quantum state and not a "fragmented" condensate.

Chapter 12

Conclusions and outlook

Overall conclusions The work presented in this thesis was focused on the search for Bose-Einstein condensation in the solid state. To attain this goal we were guided by two features of the modern definition of the BEC:

- Massive occupation of the state
- Spontaneous phase coherence across the entire condensate

In the introduction we indicated many systems with potential for achievement of a BEC in solids. Among all of these systems, one stands out: microcavity polaritons - quasi-particles that arise from the **strong coupling** between an exciton in a quantum well and the photon mode of a Fabry-Perot like cavity. The essential advantage of the polariton is its **extremely low effective mass** ($\sim 10^{-4} - 10^{-5}m_e$) in the strong coupling zone, giving the possibility of observing **bosonic degeneracy at standard cryogenic temperatures**. Moreover, the use of **CdTe-based microcavities** allows us to work below the saturation density for excitons, ensuring bosonic character of the polariton. The second key advantage of the polariton system is its strong in-plane dispersion (inherited from the photon mode) which can be probed by angle-resolved measurements. Hence, not only is the **ground state well defined**, but also one has **direct access to the polariton statistics** $n(E)$. The strong coupling regime guarantees also that the polarization and coherence properties of the polariton are carried by its photon part leaking out of the microcavity.

The major part of this dissertation was focused on the analysis of the polariton population distribution along the dispersion curve. We have shown that, in spite of the extremely **short polariton lifetime** ($\sim 1ps$), polariton states can be efficiently filled up by an exciton-polariton scattering mechanism. With increasing exciton density, an abrupt threshold for the stimulated scattering towards the polariton ground state is seen. A **massive occupation of the ground state is reported** with a condensate fraction of around 0.4.

The BEC is a thermodynamic phase transition with a well defined critical density and temperature. Due to the short polariton lifetime, a polariton population distribution usually remains far from equilibrium. However, by optimizing the exciton fraction of the polariton, the relaxation time towards the polariton trap starts

to be comparable with the radiative lifetime. In chapter 6 it was shown that, for the case of positive photon-exciton detuning, **polaritons can reach an internal equilibrium and establish an effective temperature below the condensation threshold**. In this way the thermodynamic aspect of the BEC is approached. The estimated critical parameters for polariton condensation are: $n_{cr} \simeq 5 \times 10^8 \text{ cm}^{-2}$ and $T_{cr} \simeq 20 \text{ K}$.

The analysis of the occupancy along the dispersion curve reveals a striking bimodal distribution when condensation is reached: above the condensation threshold, the occupancy of the excited states is blocked, and any additional particle added into the system falls into the ground state (figure 6.4). Such a **saturation of the excited states** and macroscopic occupation of the ground state is a characteristic feature of the BEC.

It was also shown that polariton condensation can be induced by lowering the cryostat temperature while keeping the same excitation density. However, the interpretation of these experiments is difficult, since the temperature tuning influences not only the polariton temperature but also the polariton density.

The second main theme of this thesis was investigation of the coherence properties of the polariton condensate. In order to demonstrate a spontaneous phase transition towards the coherent state, **strictly non-resonant excitation** was used in all experiments presented. This ensures that we start with a non-coherent exciton state. All signatures of coherence are developed by the system itself and are not inherited from the excitation laser.

The central experiment here is the demonstration of the first order spatial coherence of the polariton condensate (see figure 11.5). Below the condensation threshold the coherence length corresponds to the thermal de Broglie wavelength of a polariton gas at around $T \simeq 20 \text{ K}$. At threshold a significant increase of the coherence length is seen and **spontaneous phase coherence over the entire condensate** (long range order) is found. At the same time, an increase of the coherence time from 1-1.5 ps up to 8 ps is measured. This coherence time, around six times longer than the radiative lifetime, means that the coherence is preserved by the condensate itself and its phase is imprinted on the outgoing photons.

In order to investigate the transition from the thermal state into the coherent state the second order coherence was investigated. The presence of a thermal state below the condensation threshold is evidenced by the presence of photon bunching for zero delay time. This **bunching is reduced at the condensation threshold**, demonstrating the change in the photon statistics and formation of a coherent state. Far above threshold, where the coherence properties are lost due to the inter-particle interactions, a transition back into the thermal state is seen.

Finally, it was noticed that, in agreement with the theoretical predictions, polariton condensation is accompanied by the appearance of **linear polarization in the emitted light**. Such a phenomenon was proposed as a signature of a spontaneous symmetry breaking occurring when polariton condensation is reached. Yet, in our case this interpretation is not valid, since it was found that the polarization is imposed by the slight anisotropy of the microcavity. However, the onset of linear polarization in the emission from the polariton ground state at the condensation

threshold is considered as a consequence of the polariton condensation.

Strictly speaking, **the condensation phenomenon we observe is not a standard BEC** for at least two reasons.

The first one is the presence of interactions. The genuine Einstein concept of the BEC stems exclusively from the statistical properties of a non-interacting Bose gas. As was discussed in chapter 6, a polariton gas cannot be considered as weakly interacting. Any theoretical interpretation of the observed transition should confront the role of the polaritons' interactions and internal structure. The experimental manifestation of the polariton interaction can, for instance, be found in the polariton condensate fraction. The estimated value of $\eta = 0.4$ places us between weakly interacting atomic condensates ($\eta \simeq 0.9$) and liquid helium, which is a strongly interacting Bose system ($\eta \simeq 0.08$).

The second peculiarity comes from the fact that a polariton system is not conservative. Polaritons continuously convert into photons and leak out from the microcavity. The constant CW pump is needed to sustain polariton occupancy. The question about the nature of the condensation in an open system with a pump and decay is not a trivial one and is the subject of intense theoretical studies [Szy06]; the major conclusions are that, even if the presence of a pump and of decay influences critical values of density and temperature, condensation in such a system is possible.

Other subtleties of the polariton condensation, discussed in chapter 6, come from the reduced dimensionality, the finite size effects and the disorder. All these theoretical issues are current themes of animated discussions, which are helping to understand the nature of the polariton condensation.

In spite of all these difficulties, we emphasize that proposed around ten years ago, polariton condensation and polariton lasing are achieved in this work. In a broader sense, **microcavity polaritons are becoming the third member in the family of Bose-condensed systems, next to liquid helium and the cold atomic gases.**

Outlook We trust that this thesis terminates the doubts and speculations concerning polariton condensation and opens possibilities for further investigations. In this last section we wish to sketch the outlook for such work.

In the short-term, it is necessary to continue and extend the spatial coherence studies. The spatial contrast as a function of the pump power can give an independent estimate of the condensate fraction. The limit of the coherence length in the condensed state can be investigated, either by increase of the excitation spot size or by measuring the interference between two separated condensates. Another question concerns condensation into the single quantum state in the presence of disorder. The collective polarization and a spatial interference occurring in the condensed state support the claim of condensation into a single mode. Measurements of the photon noise would finally clarify this issue. It would also be interesting to construct the phase diagram $n_{cr}(T_{eff})$ for this transition.

Further developments require improved materials. On the one hand an increase of the quality factor of the cavities would produce significantly longer polariton life-

times and favor polariton thermalization. And on the other hand, new active media are needed, with even more robust excitons (with a higher exciton binding energy). This would allow increasing the saturation densities and the bosonic character of the polariton at high densities and temperatures. It is envisaged that, in microcavities based on large gap materials like ZnSe, GaN, ZnO, or organic materials, polariton condensation could occur at higher temperatures, even at room temperature. This long-term aim is a real challenge for materials growth.

The first step towards polariton condensation at higher temperatures is a demonstration of the strong coupling regime. Up till now this has been demonstrated in the following microcavities based on large band gap materials: organic materials [Con03], GaN [Sel06] and ZnSe [Kel97, Bal02]. The strong coupling in these structures persists up to room temperature. In particular, the strong coupling regime in a ZnSe-based microcavity demonstrated in [Bal02] was confirmed during this thesis work by performing angle-resolved reflectivity measurements.

Finally, the other promising direction to favor polariton condensation is spatial trapping. This can be realized either by applying a localizing, point stress [Bal06] or by introducing a spatial 3D confinement [Obe02, Obe04, Dai06, Kai06].

Appendix A

"Polariton laser" versus photon laser

What are the physical features differing polariton condensation and commonly observed lasing from VCSEL-type⁴⁴ structures? This is one of the most frequently asked questions concerning polariton condensation. It seems to be a natural issue, since we observe a coherent emission from the optically pumped microcavity with an inserted "gain medium" - QWs. The aim of this appendix is to gather together and comment on all the observations spread over this thesis showing fundamental differences between a polariton condensation and a standard lasing. It will be shown that these two ideas are very distinct from each other.

A general scheme of a standard lasing action is the following. In the first step, population is inverted within the gain medium by external pumping. Due to the absorption, at a certain threshold power, the occupancy of excited states becomes larger than in the ground state. As a result, the spontaneous emission rate starts to be overcome by the stimulated emission. In contrast to the spontaneous emission, the stimulated emission yields twin photons with the same features concerning their energy, phase, polarization and direction of propagation. The photon occupancy in a given mode increases and is subsequently amplified, owing to the positive feedback introduced by the cavity. A part of the amplified, coherent light passes through the output coupler and is detected outside the cavity.

A standard laser operates in a weak coupling regime. On the other hand a polariton laser is founded on a strong light-matter coupling regime (see section 2.1.1). The nature of "condensing" particles in these two cases is totally different, which yields crucial distinctions between photon lasing and polariton condensation. Let us explain this statement.

In the case of standard lasing we deal with a pure electromagnetic field. Photons do not interact with each other. This means that with increasing occupancy of the given mode, the coherence properties (of all orders) of photons occupying this mode increase, in the first approximation, with no limits (see [Por03] and references therein).

On the other hand we have a polariton: a mixed state of the photon and the quantum well exciton. Thanks to the **strong coupling regime** between light and

⁴⁴Vertical Cavity Surface Emitting Laser

matter, a quasi-particle is created that shares the features of photon and exciton at the same time. Built from two bosonic particles, the polariton is also described as a boson, within the limits explained in this thesis.

Owing to the photon admixture, the polariton mass is extremely low, hence bosonic degeneracy - the origin of condensation - is revealed at unusually high temperatures and low densities.

At the same time, the excitonic part of the polariton wave function introduces interactions in the polariton gas. It is the presence of interactions that differentiates photon and polariton lasing in major ways. Moreover, the interaction strength between polaritons can be tuned by changing the exciton-photon balance. Under positive detuning, when the exciton fraction is dominant, collisions among the polaritons can be faster than their lifetime (\sim ps) (see figure 6.8), opening the possibility of reaching internal equilibrium in the polariton gas (see chapter 6). As was shown in chapter 6.3, with decreasing exciton fraction, and thus decreasing interaction strength, the polariton population remains out of equilibrium when condensation is reached.

The coherence properties of a polariton laser are also strongly influenced by polariton-polariton and polariton-exciton (from the reservoir) interactions. Here the situation is much more complicated than in a standard laser, where coherence is developed as the number of photons in a lasing mode is increased.

The impact of interactions can be studied by observing the energy renormalization and the evolution of the linewidth with increasing particle density. It was perceived that interactions cannot be neglected even in the relatively low density limit: At the condensation threshold, the energy blueshift and the decoherence (manifested in the line broadening of the polariton ground state) increase with the total density of excitons, as shown in figure A.2. This correlation shows that usually excitons from the reservoir interact with polaritons around the ground state. Only at slightly positive detuning, at the minimum of exciton density, are the line broadening and the blueshift of minor importance. In this zone an image of the polariton trap isolated from the rest of the dispersion curve can be approached. The stronger decoherence and the stronger blueshift at the condensation threshold are also observed at higher temperatures (see figure 7.8).

With crossing of the condensation threshold, spontaneous onset of the long range phase coherence is observed (figure 11.5). An increase of the coherence time (figure 11.1) is compatible with the linewidth reduction. A reduction of thermal noise is also measured (figure 11.10). However, the presence of interactions in the polariton system leads to decoherence. Under positive detuning the coherent zone is very narrow: Line broadening is observed from around twice the threshold power (figure 6.4). A characteristic asymmetric line shape predicted by theory [Por03] is observed and shown in figure A.3. The measurement of photon statistics shows degradation of the second order coherence properties far above threshold (figure 11.17). The coherent regime of a polariton laser can be enlarged by decreasing the exciton fraction, as can be followed in figures 6.5 and 6.13 - at $\delta = -1meV$, when the line remains narrow up to eight times threshold power.

All these observations show that interactions, introduced by the exciton part,

produce the major differences between a polariton and a photon laser. Another important difference can be pointed out by analyzing the physical origin of the coherent emission in these two devices.

In the case of the polariton laser, the onset of coherent emission is triggered as soon as the ground state occupancy becomes larger than unity. This is achieved when the populating rate is faster than the emission rate. Once this condition is reached, the relaxation towards the ground state becomes stimulated. Nevertheless, emission from the condensate, due to the leakage of photons from the microcavity, is still spontaneous, and is uniquely given by the polariton lifetime. Thus population inversion is not required in polariton lasing.

This statement is confirmed by measuring the threshold power as a function of the number of quantum wells embedded in a microcavity. As reported in [Boef00], the power absorbed at threshold is constant, does not depend on the number of quantum wells and is connected with the density of states at $k_{\parallel} = 0$. The condensation occurs always for the same total density of carriers in the structure, when the exciton-polariton scattering rate outgrows radiative losses.

This behavior is strong contrast with that observed in VCSELs, operating in a weak coupling regime. Here, lasing is due to the population inversion of the electron-hole plasma in the gain medium. This kind of mechanism always gives different threshold values as the number of quantum wells is varied (see [Boef00], chapter 8 in [Boe00] and references therein). The above observation also rules out lasing associated with a population inversion of localized excitons that are resonant with the lower polariton ground state. The number of these excitons depends on the number of QWs, so in order to invert their population the threshold power should vary with the number of QWs. This is not observed when measuring the threshold power for microcavities containing a different number of QWs (4, 6, 8), while maintaining the same Rabi splitting.

The final, striking difference between polariton and photon lasing is presented in chapter 8, where the transition between these two regimes is shown directly. The threshold for polariton condensation is of order $\simeq kW/cm^2$. Compared to the standard VCSEL lasing, this value is remarkably low, which is a crucial advantage of the polariton laser as a low threshold emitter of coherent light. Indeed, on increasing pump power, the exciton density finally exceeds the saturation density, where transition from a strong into a weak coupling regime occurs. The population inversion of the electron-hole plasma leads to the second threshold - a standard lasing takes place. In our case this transition is observed for pump power $\simeq 50kW/cm^2$.

We repeat that CdTe-based microcavities are well suited for condensation studies, since at helium temperature the exciton density required for attainment of condensation remains an order of magnitude lower than the saturation density. The strong coupling can be destroyed by increasing exciton density and/or by increasing temperature (which decreases the exciton saturation density). In GaAs structures up to date the transition towards a weak coupling regime has usually occurred before condensation could take place [But02]. This is due to the larger exciton Bohr radius, and thus smaller saturation density in GaAs with respect to CdTe-based structures. So far, in GaAs microcavities, only structures containing 12 QWs exhibit polariton

lasing [Den06]. The above discussion is summarized in figure A.1.

The differences between polariton and photon lasers are summarized in table A.1.

	Photon laser	Polariton laser
Condensation of...	photons, pure electromagnetic field	polaritons, strongly coupled excitons and photons
Interactions	No. No energy renormalization.	Present due to the exciton component. Can be tuned by changing the exciton-photon balance. Density dependent energy renormalization.
Thermalization	Not possible.	Possible as soon as interactions occur faster than lifetime. The polariton distribution varies with detuning.
Coherence properties...	Increase with the occupancy of lasing mode.	Spontaneous coherence at the condensation threshold: Increase of τ_C , long range phase coherence, coherent statistics. Interaction induced (density dependent) decoherence: Asymmetric line broadening, thermal statistics.
Population inversion	Yes. Threshold power increases with the number of QW in VCSELs. Stimulated emission of photons.	No. Coherent emission due to the leakage from the condensate. Stimulated relaxation towards the condensate. Threshold power 50 times smaller than in VCSELs. Threshold does not depend on the number of QWs.
		Observation of the transition towards photon lasing at the saturation density of excitons

Table A.1: The differences between "polariton lasing" and photon lasing - summary.

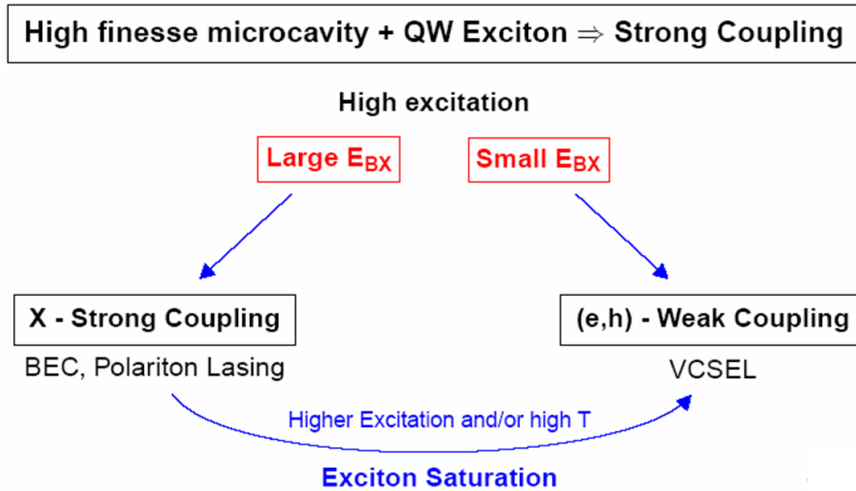


Figure A.1: Strong versus weak coupling regime in microcavities. Polariton condensation is possible in systems where a bosonic character of excitons is preserved at the density required for condensation.

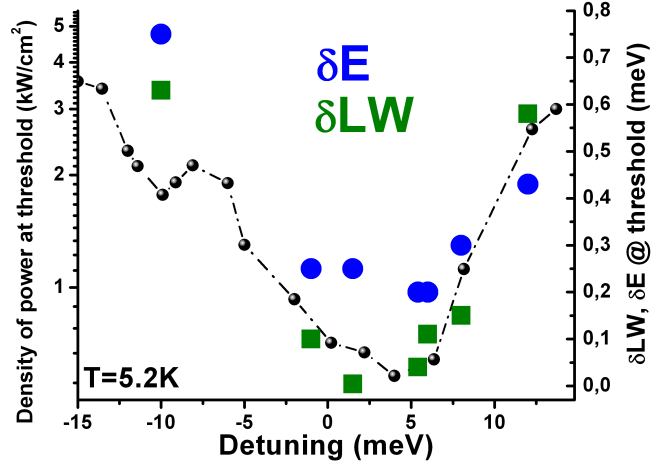


Figure A.2: *The line broadening and the blueshift as a function of detuning. The black circles are the same as in figure 6.7. The line broadening (green squares) illustrating decoherence and the blueshift (blue circles) measured at the condensation threshold are correlated with the total number of excitons (proportional to the power density). This indicates interaction between the polaritons at $k_{\parallel} \simeq 0$ and the exciton reservoir. At the slightly positive detuning, where the exciton density required for condensation is the lowest, interaction between the reservoir and the polaritons at $k_{\parallel} \simeq 0$ is of minor importance. In this region only, an image of the "polariton trap", isolated from the rest of the dispersion curve, is well adapted.*

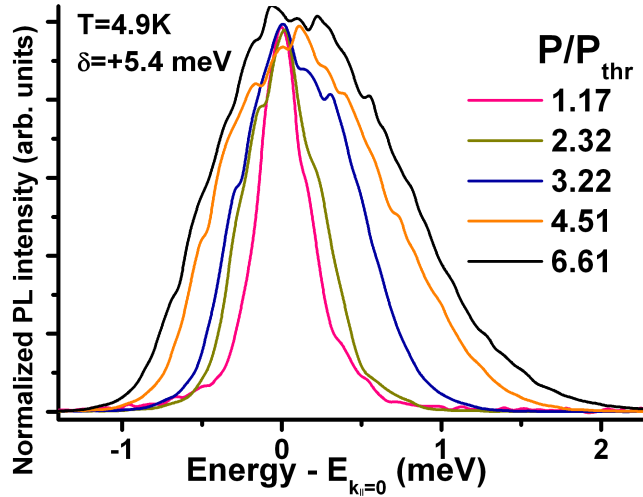


Figure A.3: *The line broadening above the condensation threshold. An asymmetric shape of the broadening is consistent with the decoherence introduced by the self-interaction within the condensate [Por03]. The spectra were normalized for clarity. The origin of energy scale for each spectrum was fixed by the energy corresponding to the maximum of intensity.*

Bibliography

- [Coh] *Coherent Mira Model 900 Laser Operator's Manual* (Coherent Inc.).
- [Bec02] *Time-Correlated Single Photon Counting Modules* (Becker-Hickl GmbH, 2002).
- [And95] M. H. ANDERSON, J. R. ENSHER, M. R. MATTHEWS, C. E. WIEMAN et E. A. CORNELL, « Observation of Bose-Einstein Condensation in a Dilute Atomic Vapor », *Science*, vol. 269, no. 5221 (1995) p. 198–201.
- [And97] R. ANDRÉ et L. S. DANG, « Low-temperature refractive indices of $CdMn_xTe$ and $CdMg_yTe$ », *Journal of Applied Physics*, vol. 82, no. 10 (1997) p. 5086–5089.
- [And98] R. ANDRÉ, D. HEGER, L. S. DANG et Y. M. D'AUBIGNÉ, « Spectroscopy of polaritons in CdTe-based microcavities », *Journal of Crystal Growth*, vol. 184/185, no. 1 (1998) p. 758–762.
- [Andr97] M. R. ANDREWS, C. G. TOWNSEND, H.-J. MIESNER, D. S. DURFEE, D. M. KURN et W. KETTERLE, « Observation of Interference Between Two Bose Condensates », *Science*, vol. 275, no. 5300 (1997) p. 637.
- [Baa06] A. BAAS, J.-P. KARR, M. ROMANELLI, A. BRAMATI et E. GIACOBINO, « Quantum Degeneracy of Microcavity Polaritons », *Physical Review Letters*, vol. 96, no. 17 (2006) p. 176401.
- [Bag91] V. BAGNATO et D. KLEPPNER, « Bose-Einstein condensation in low-dimensional traps. », *Physical Review A*, vol. 44, no. 11 (1991) p. 7439–7441.
- [Bal03] S. BALIBAR, « Looking back at superfluid helium », *Séminaire Poincaré*, vol. 1 (1996) p. 11.
- [Bal06] R. B. BALILI, D. W. SNOKE, L. PFEIFFER et K. WEST, « Actively tuned and spatially trapped polaritons », *Applied Physics Letters*, vol. 88, no. 3 (2006) p. 031110.
- [Bal02] A. BALOCCHI, *Semiconductor quantum wells in a tunable fibre-based microcavity*, Thèse de doctorat, Heriot-Watt University, Edinburgh (2002).

-
- [Bas98] G. BASTARD, *Wave mechanics applied to semiconductor heterostructures* (Les edition de minuit, Les Ulis, France, 1998).
- [Bau02] J. J. BAUMBERG, P. G. SAVVIDIS, P. G. LAGOUDAKIS, M. D. MARTIN, D. WHITTAKER, R. BUTTE, M. SKOLNICK et J. ROBERTS, « Polariton traps in semiconductor microcavities », *Physica E*, vol. 13, no. 2-4 (2002) p. 385–389.
- [Bau00] J. J. BAUMBERG, P. G. SAVVIDIS, R. M. STEVENSON, A. I. TARTAKOVSKII, M. S. SKOLNICK, D. M. WHITTAKER et J. S. ROBERTS, « Parametric oscillation in a vertical microcavity: A polariton condensate or micro-optical parametric oscillation », *Physical Review B*, vol. 62, no. 24 (2000) p. R16 247–R16 250.
- [Bla62] J. M. BLATT, K. W. BÖER et W. BRANDT, « Bose-Einstein Condensation of Excitons », *Physical Review*, vol. 126, no. 5 (1962) p. 1691.
- [Blo00] I. BLOCH, T. W. HÄNSCH et T. ESSLINGER, « Measurement of the spatial coherence of a trapped Bose gas at the phase transition », *Nature*, vol. 403, no. 6766 (2000) p. 166–170.
- [Blo97] J. BLOCH et J. Y. MARZIN, « Photoluminescence dynamics of cavity polaritons under resonant excitation in the picosecond range », *Physical Review B*, vol. 56, no. 4 (1997) p. 2103–2108.
- [Blo05] J. BLOCH, B. SERMAGE, M. PERRIN, P. SENELLART, R. ANDRÉ et L. S. DANG, « Monitoring the dynamics of a coherent cavity polariton population », *Physical Review B*, vol. 71, no. 15 (2005) p. 155 311.
- [Boe00] F. BOEUF, *Spectroscopie optique linéaire et non-linéaire dans les microcavités de semiconducteurs II-VI à base de CdTe.*, Thèse de doctorat, Université Joseph Fourier, Grenoble (2000).
- [Boef00] F. BOEUF, R. ANDRÉ, R. ROMESTAIN, L. S. DANG, E. PÉRONNE, J. F. LAMPIN, D. HULIN et A. ALEXANDROU, « Evidence of polariton stimulation in semiconductor microcavities », *Physical Review B*, vol. 62, no. 4 (2000) p. R2279.
- [Bor93] M. BORN et E. WOLF, *Principles of Optics-6th edition* (Pergamon Press, Oxford, 1998).
- [Bos24] S. N. BOSE, « », *Z. Phys.*, vol. 26 (1924) p. 178.
- [Han56] R. H. BROWN et R. TWISS, « Correlation between photons in two coherent beams of light », *Nature*, vol. 177, no. 4497 (1956) p. 27.
- [Bru06] A. BRUCHHAUSEN, A. FAINSTEIN, B. JUSSERAND et R. ANDRÉ, « Resonant Raman scattering by CdTe quantum-well-confined optical phonons in a semiconductor microcavity », *Physical Review B*, vol. 73, no. 8 (2006) p. 085 305.

- [Bru96] M. BRUNE, F. SCHMIDT-KALER, A. MAALI, J. DREYER, E. HAGLEY, J. M. RAIMOND et S. HAROCHE, « Quantum Rabi Oscillation: A Direct Test of Field Quantization in a Cavity », *Physical Review Letters*, vol. 76, no. 11 (1996) p. 1800–1803.
- [Bru05] A. BRUNETTI, M. VLADIMIROVA, D. SCALBERT et R. ANDRÉ, « Spin quantum beats in CdMnTe microcavity », *Physica Status Solidi (C)*, vol. 2, no. 11 (2005) p. 3876–3879.
- [Bur99] K. BURNET, M. EDWARDS et C. CLARK, « The theory of Bose-Einstein condensation of dilute gases », *Physics Today*, , no. December (1999) p. 37.
- [Buto02] L. V. BUTOV, A. C. GOSSARD et D. S. CHEMLA, « Macroscopically ordered state in an exciton system », *Nature*, vol. 418, no. 6899 (2002) p. 751–754.
- [But01] L. V. BUTOV, A. L. IVANOV, A. IMAMOGLU, P. B. LITTLEWOOD, A. A. SHASHKIN, V. T. DOLGOPOLOV, K. L. CAMPMAN et A. C. GOSSARD, « Stimulated Scattering of Indirect Excitons in Coupled Quantum Wells: Signature of a Degenerate Bose-Gas of Excitons », *Physical Review Letters*, vol. 86, no. 24 (2001) p. 5608.
- [Bu02] L. V. BUTOV, C. W. LAI, A. L. IVANOV, A. C. GOSSARD et D. S. CHEMLA, « Towards Bose-Einstein condensation of excitons in potential traps », *Nature*, vol. 417, no. 6864 (2002) p. 47–52.
- [But02] R. BUTTÉ, G. DELALLEAU, A. I. TARTAKOVSKII, M. S. SKOLNICK, V. N. ASTRATOV, J. J. BAUMBERG, G. MALPUECH, A. D. CARLO, A. V. KAVOKIN et J. S. ROBERTS, « Transition from strong to weak coupling and the onset of lasing in semiconductor microcavities », *Physical Review B*, vol. 65, no. 20 (2002) p. 205310.
- [Cao97] H. CAO, S. PAU, J. M. JACOBSON, G. BJÖRK, Y. YAMAMOTO et A. IMAMOGLU, « Transition from a microcavity exciton polariton to a photon laser », *Physical Review A*, vol. 55, no. 6 (1997) p. 4632–4635.
- [Ciu00] C. CIUTI, P. SCHWENDIMANN, B. DEVEAUD et A. QUATTROPANI, « Theory of the angle-resonant polariton amplifier », *Physical Review B*, vol. 62, no. 8 (2000) p. R4825–R4828.
- [Coh03] C. COHEN-TANNOUJDI, « La condensation de Bose-Einstein: Introduction », *Séminaire Poincaré*, vol. 1 (2003) p. 1–10.
- [Coh96] C. COHEN-TANNOUJDI, B. DIU et F. LALOË, *Mécanique quantique* (Hermann, Paris, 1992).

-
- [Coh88] C. COHEN-TANNOUJDI, J. DUPONT-ROC et G. GRYNBERG, *Processus d'interaction entre photons et atomes* (Savoirs Actuels, Editions du CNRS, Paris, 1988).
- [Con03] L. G. CONNOLLY, D. G. LIDZEY, R. BUTTÉ, A. M. ADAWI, D. M. WHITTAKER, M. S. SKOLNICK et R. AIREY, « Strong coupling in high-finesse organic semiconductor microcavities », *Applied Physics Letters*, vol. 83, no. 26 (2003) p. 5377–5379.
- [Cor02] E. A. CORNELL et C. E. WIEMAN, « Nobel Lecture: Bose-Einstein condensation in a dilute gas, the first 70 years and some recent experiments », *Reviews of Modern Physics*, vol. 74, no. 3 (2002) p. 875.
- [Dai06] O. E. DAÏF, A. BAAS, T. GUILLET, J.-P. BRANTUT, R. I. KAITOUNI, J. L. STAEHLI, F. MORIER-GENOUD et B. DEVEAUD, « Polariton quantum boxes in semiconductor microcavities », *Applied Physics Letters*, vol. 88, no. 6 (2006) p. 061105.
- [Dal99] F. DALFOVO, S. GIORGINI, L. P. PITAEVSKII et S. STRINGARI, « Theory of Bose-Einstein condensation in trapped gases », *Reviews of Modern Physics*, vol. 71, no. 3 (1999) p. 463.
- [Dam90] H. DAMING, J.-I. CHYI et H. MORKOÇ, « Carrier effects on the excitonic absorption in GaAs quantum-well structures: Phase-space filling », *Physical Review B*, vol. 45, no. 8 (1990) p. 5147.
- [Dan98] L. S. DANG, D. HEGER, R. ANDRÉ, F. BOEUF et R. ROMESTAIN, « Stimulation of Polariton Photoluminescence in Semiconductor Microcavity », *Physical Review Letters*, vol. 81, no. 18 (1998) p. 3920–3923.
- [Dav95] K. B. DAVIS, M. O. MEWES, M. R. ANDREWS, N. J. VAN DRUTEN, D. S. DURFEE, D. M. KURN, et W. KETTERLE, « Bose-Einstein Condensation in a Gas of Sodium Atoms », *Physical Review Letters*, vol. 75, no. 22 (1995) p. 3969.
- [Den06] H. DENG, D. PRESS, S. GOTZINGER, G. SOLOMON, R. HEY, K. PLOOG et Y. YAMAMOTO, « Quantum Degenerate Exciton-Polaritons in Thermal Equilibrium », *cond-mat/0604394*.
- [Den02] H. DENG, G. WEIHS, C. SANTORI, J. BLOCH, et Y. YAMAMOTO, « Condensation of Semiconductor Microcavity Exciton Polaritons », *Science*, vol. 298, no. 5591 (2002) p. 199.
- [Den03] H. DENG, G. WEIHS, D. SNOKE, J. BLOCH et Y. YAMAMOTO, « Polariton lasing vs. photon lasing in a semiconductor microcavity », *Proceedings of the National Academy of Sciences*, vol. 100, no. 26 (2003) p. 15318–15323.

- [Din74] R. DINGLE, W. WIEGMANN et C. H. HENRY, « Quantum States of Confined Carriers in Very Thin $Al_xGa_{1-x}As - GaAs - Al_xGa_{1-x}As$ Heterostructures », *Physical Review Letters*, vol. 33, no. 14 (1974) p. 827–830.
- [Ein25] A. EINSTEIN, « », *Sitzungsberichte, Preussische Akademie der Wissenschaften*, vol. 1 (1925) p. 3.
- [Eis04] J. P. EISENSTEIN et A. H. MACDONALD, « Bose-Einstein condensation of excitons in bilayer electron systems », *Nature*, vol. 432, no. 7018 (2004) p. 691–694.
- [Ens96] J. R. ENSHER, D. S. JIN, M. R. MATTHEWS, C. E. WIEMAN et E. A. CORNELL, « Bose-Einstein Condensation in a Dilute Gas: Measurement of Energy and Ground-State Occupation », *Physical Review Letters*, vol. 77, no. 25 (1996) p. 4984.
- [Erl01] J. ERLAND, V. MIZEIKIS, W. LANGBEIN, J. R. JENSEN et J. M. HVAM, « Stimulated Secondary Emission from Semiconductor Microcavities », *Physical Review Letters*, vol. 86, no. 25 (2001) p. 5791–5794.
- [Fan97] X. FAN, H. WANG, H. Q. HOU et B. E. HAMMONS, « Laser emission from semiconductor microcavities: Transition from nonperturbative to perturbative regimes », *Physical Review B*, vol. 56, no. 23 (1997) p. 15 256–15 260.
- [Fis95] T. A. FISHER, A. M. AFSHAR, D. M. WHITTAKER, M. S. SKOLNICK, J. S. ROBERTS, G. HILL et M. A. PATE, « Electric-field and temperature tuning of exciton-photon coupling in quantum microcavity structures », *Physical Review B*, vol. 51, no. 4 (1995) p. 2600.
- [Gab85] G. GABRIELSE et H. DEHMELT, « Observation of inhibited spontaneous emission », *Physical Review Letters*, vol. 55, no. 1 (1985) p. 67–70.
- [Ger68] V. A. GERGEL', R. F. KAZARINOV et R. A. SURIS, « Optical properties of an exciton condensate in a semiconductor », *Soviet Physics JETP*, vol. 26, no. 2 (1968) p. 354.
- [Gerg68] V. A. GERGEL', R. F. KAZARINOV et R. A. SURIS, « Superfluidity of excitons in semiconductors », *Soviet Physics JETP*, vol. 27, no. 1 (1968) p. 159.
- [Gla63] R. J. GLAUBER, « Coherent and Incoherent States of the Radiation Field », *Physical Review*, vol. 131, no. 6 (1963) p. 2766–2788.
- [Gla63] R. J. GLAUBER, « The Quantum Theory of Optical Coherence », *Physical Review*, vol. 130, no. 6 (1963) p. 2529–2539.

-
- [Goy83] P. GOY, J. M. RAIMOND, M. GROSS et S. HAROCHE, « Observation of cavity-enhanced single-atom spontaneous emission », *Physical Review Letters*, vol. 50, no. 24 (1983) p. 1903–1906.
- [Ger01] J. M. GÉRARD et B. GAYRAL, « InAs quantum dots: artificial atoms for solid-state cavity-quantum electrodynamics », *Physica E*, vol. 9, no. 1 (2001) p. 131–139.
- [Gri99] A. GRIFFIN, « A brief history of our understanding of BEC: from Bose to Beliaev », *arXiv:cond-mat/9901123 v1*.
- [Gri95] A. GRIFFIN, D. W. SNOKE et S. STRINGARI, *Bose-Einstein condensation* (Cambridge University Press, 1995).
- [Har89] S. HAROCHE et D. KLEPPNER, « Cavity quantum electrodynamics », *Physics Today*, vol. 42 (1989) p. 24–30.
- [Hen65] C. H. HENRY et J. J. HOPFIELD, « Raman Scattering by Polaritons », *Physical Review Letters*, vol. 15, no. 25 (1965) p. 964–966.
- [Hop58] J. J. HOPFIELD, « Theory of the Contribution of Excitons to the Complex Dielectric Constant of Crystals », *Physical Review*, vol. 112, no. 5 (1958) p. 1555–1567.
- [Hou05] R. HOUDRÉ, « Early stages of continuous wave experiments on cavity-polaritons », *Physica Status Solidi (B)*, vol. 242, no. 11 (2005) p. 2167–2196.
- [Hou95] R. HOUDRÉ, J. L. GIBERNON, P. PELLANDINI, R. P. STANLEY, U. OESTERLE, C. WEISBUCH, J. OGORMAN, B. ROYCROFT et M. ILEGEMS, « Saturation of the strong-coupling regime in a semiconductor microcavity: Free-carrier bleaching of cavity polaritons », *Physical Review B*, vol. 52, no. 11 (1995) p. 7810–7813.
- [Hou94] R. HOUDRÉ, C. WEISBUCH, R. P. STANLEY, U. OESTERLE, P. PELLANDINI et M. ILEGEMS, « Measurement of cavity-polariton dispersion curve from angle resolved photoluminescence experiments », *Physical Review Letters*, vol. 73, no. 15 (1994) p. 2043–2046.
- [Hua02] R. HUANG, Y. YAMAMOTO, R. ANDRÉ, J. BLEUSE, M. MULLER et H. ULMER-TUFFIGO, « Exciton-polariton lasing and amplification based on exciton-exciton scattering in CdTe microcavity quantum wells », *Physical Review B*, vol. 65, no. 16 (2002) p. 165 314.
- [Huy03] A. HUYNH, J. TIGNON, G. KELLER, P. ROUSSIGNOL, C. DELALANDE, R. ANDRÉ, R. ROMESTAIN et L. S. DANG, « Collision broadening in II-VI semiconductor microcavities », *Physical Review B*, vol. 68, no. 16 (2003) p. 165 340.

- [Ima96] A. IMAMOGLU, R. J. RAM, S. PAU et Y. YAMAMOTO, « Nonequilibrium condensates and lasers without inversion: Exciton-polariton lasers », *Physical Review A*, vol. 53, no. 6 (1996) p. 4250.
- [Shu98] S. JIANG, S. MACHIDA, Y. TAKIGUCHI, Y. YAMAMOTO et H. CAO, « Direct time-domain observation of transition from strong to weak coupling in a semiconductor microcavity », *Applied Physics Letter*, vol. 73, no. 21 (1998) p. 3031–3033.
- [Kai06] R. I. KAITOUNI, O. E. DAÏF, M. RICHARD, P. LUGAN, A. BAAS, T. GUILLET, F. MORIER-GENOUD, J.-D. GANIÈRE, J.-L. STAEHLI, V. SAVONA et B. DEVEAUD, « Engineering the spatial confinement of exciton-polaritons in semiconductors », *cond-mat/0602640*.
- [Kal83] Y. KALUZNY, P. GOY, M. GROSS, J. M. RAIMOND et S. HAROCHE, « Observation of Self-Induced Rabi Oscillations in Two-Level Atoms Excited Inside a Resonant Cavity: The Ringing Regime of Superradiance », *Physical Review Letters*, vol. 51, no. 13 (1983) p. 1175–1178.
- [Kar04] J. P. KARR, A. BAAS et E. GIACOBINO, « Twin polaritons in semiconductor microcavities », *Physical Review A*, vol. 69, no. 6 (2004) p. 063 807.
- [Karr04] J. P. KARR, A. BAAS, R. HOUDRÉ et E. GIACOBINO, « Squeezing in semiconductor microcavities in the strong coupling regime », *Physical Review A*, vol. 69, no. 3 (2004) p. 031 802.
- [Kav03] A. KAVOKIN et G. MALPUECH, *Cavity polaritons* (Elsevier Academic Press, 2003).
- [Kav04] K. KAVOKIN, I. SHELYKH, A. KAVOKIN, G. MALPUECH et P. BIGENWALD, « Quantum Theory of Spin Dynamics of Exciton-Polaritons in Microcavities », *Physical Review Letters*, vol. 92, no. 1 (2004) p. 017 401.
- [Kee04] J. KEELING, P. R. EASTHAM, M. H. SZYMAŃSKA et P. B. LITTLEWOOD, « Polariton Condensation with Localized Excitons and Propagating Photons », *Physical Review Letters*, vol. 93, no. 22 (2004) p. 226 403.
- [Kel67] L. V. KELDYSH et A. N. KOZLOV, « », *JETP Lett.*, vol. 5 (1967) p. 190.
- [Kel97] P. V. KELKAR, V. G. KOZLOV, A. V. NURMIKKO, C.-C. CHU, J. HAN et R. L. GUNSHOR, « Stimulated emission, gain, and coherent oscillations in II-VI semiconductor microcavities », *Physical Review B*, vol. 56, no. 12 (1997) p. 7564–7573.
- [Ket02] W. KETTERLE, « Nobel lecture: When atoms behave as waves: Bose-Einstein condensation and the atom laser », *Reviews of Modern Physics*, vol. 74, no. 4 (2002) p. 1131.

-
- [Ket96] W. KETTERLE et N. VAN DRUTEN, « Bose-Einstein condensation of a finite number of particles trapped in one or three dimensions », *Physical Review A*, vol. 54, no. 1 (1983) p. 656.
- [Kir97] M. KIRA, F. JAHNKE, S. W. KOCH, J. D. BERGER, D. V. WICK, T. R. J. NELSON, G. KHITROVA et H. M. GIBBS, « Quantum Theory of Nonlinear Semiconductor Microcavity Luminescence Explaining BOSER Experiments », *Physical Review Letters*, vol. 79, no. 25 (1997) p. 5170–5173.
- [Klo06] Ł. KŁOPOTOWSKI, M. D. MARTIN, A. AMO, L. VINA, I. SHELYKH, M. GLAZOV, G. MALPUECH, A. KAVOKIN et R. ANDRÉ, « Optical Anisotropy and Pinning of the Linear Polarization of Light in Semiconductor Microcavities », *Solid State Communications*, vol. 139, no. 10 (2006) p. 511–515.
- [Kun03] S. KUNDERMANN, M. SABA, C. CIUTI, T. GUILLET, U. OESTERLE, J. L. STAEHLI et B. DEVEAUD, « Coherent Control of Polariton Parametric Scattering in Semiconductor Microcavities », *Physical Review Letters*, vol. 91, no. 10 (2003) p. 107402.
- [Lag03] P. G. LAGOUDAKIS, M. D. MARTIN, J. J. BAUMBERG, A. QARRY, E. COHEN et L. N. PFEIFFER, « Electron-Polariton Scattering in Semiconductor Microcavities », *Physical Review Letters*, vol. 90, no. 20 (2003) p. 206401.
- [Lan02] W. LANGBEIN et J. M. HVAM, « Elastic Scattering Dynamics of Cavity Polaritons: Evidence for Time-Energy Uncertainty and Polariton Localization », *Physical Review Letters*, vol. 88, no. 4 (2002) p. 047401.
- [Lau90] J. P. LAURENTI, J. CAMASSEL, A. BOUHEMADOU, B. TOULOUSE, R. LEGROS et A. LUSSON, « Temperature dependence of the fundamental absorption edge of mercury cadmium telluride », *Journal of Applied Physics*, vol. 67, no. 10 (1990) p. 6454–6460.
- [Lau04] F. P. LAUSSY, G. MALPUECH, A. KAVOKIN et P. BIGENWALD, « Spontaneous Coherence Buildup in a Polariton Laser », *Physical Review Letters*, vol. 93, no. 1 (2004) p. 016402.
- [Lau06] F. P. LAUSSY, I. A. SHELYKH, G. MALPUECH et A. KAVOKIN, « Effects of Bose-Einstein condensation of exciton polaritons in microcavities on the polarization of emitted light », *Physical Review B*, vol. 73, no. 3 (2006) p. 035315.
- [Leg01] A. J. LEGGETT, « Bose-Einstein condensation in the alkali gases: Some fundamental concepts », *Reviews of Modern Physics*, vol. 73, no. 2 (2001) p. 307.

- [Lon38] F. LONDON, « On the Bose-Einstein Condensation », *Physical Review*, vol. 54, no. 11 (1938) p. 947–954.
- [Mal02] G. MALPUECH, A. KAVOKIN, A. D. CARLO et J. J. BAUMBERG, « Polariton lasing by exciton-electron scattering in semiconductor microcavities », *Physical Review B*, vol. 65, no. 15 (2002) p. 153310.
- [Man95] L. MANDEL et E. WOLF, *Optical coherence and quantum optics* (Cambridge University Press, Cambridge, 1995).
- [March06] F. M. MARCHETTI, J. KEELING, M. H. SZYMAŃSKA et P. B. LITTLEWOOD, « Absorption, Photoluminescence and Resonant Rayleigh Scattering Probes of Condensed Microcavity Polaritons », *cond-mat/0608096*.
- [Mar06] F. M. MARCHETTI, J. KEELING, M. H. SZYMAŃSKA et P. B. LITTLEWOOD, « Thermodynamics and Excitations of Condensed Polaritons in Disordered Microcavities », *Physical Review Letters*, vol. 96, no. 6 (2006) p. 066405.
- [Mar05] M. MARTIN, D. BALLARINI, A. AMO, Ł. KŁOPOTOWSKI, L. VIÑA, A. V. KAVOKIN et R. ANDRÉ, « Striking dynamics of II-VI microcavity polaritons after linearly polarized excitation », *Physica Status Solidi (C)*, vol. 2, no. 11 (2005) p. 3880.
- [Mat92] H. MATHIEU, P. LEFEBVRE et P. CHRISTOL, « Simple analytical method for calculating exciton binding energies in semiconductor quantum wells », *Physical Review B*, vol. 46, no. 7 (1992) p. 4092–4101.
- [Mie98] H.-J. MIESNER, D. M. STAMPER-KURN, M. R. ANDREWS, D. S. DURFEE, S. INOUE et W. KETTERLE, « Bosonic Stimulation in the Formation of a Bose-Einstein Condensate », *Science*, vol. 279, no. 5353 (1998) p. 1005–1007.
- [Mor66] B. L. MORGAN et L. MANDEL, « Measurement of Photon Bunching in a Thermal Light Beam », *Physical Review Letters*, vol. 16, no. 22 (1966) p. 1012–1015.
- [Mos62] S. A. MOSKALENKO, « Reversible optico-hydrodynamic phenomena in a non ideal exciton gas », *Soviet Physics Solid State*, vol. 4 (1962) p. 199.
- [Mul00] M. MÜLLER, *Étude du polariton en cavité en régime de forte excitation: dynamique et non-linéarités dans les microcavités II-VI.*, Thèse de doctorat, Université Joseph Fourier, Grenoble (2000).
- [Nel83] D. NELSON, « », *Phase transitions and critical phenomena*, vol. 7, no. 2.

-
- [Noz03] P. NOZIÈRES, « Condensation de Bose-Einstein et Cohérence Quantique: de la Superfluidité à la Localisation, des Liquides de Fermi aux Supraconducteurs », *Séminaire Poincaré*, vol. 1 (2000) p. 63–73.
- [Obe04] M. OBERT, J. RENNER, A. FORCHEL, R. ANDRÉ et L. S. DANG, « Nonlinear emission in II VI pillar microcavities: Strong versus weak coupling », *Applied Physics Letters*, vol. 84, no. 9 (2004) p. 1435.
- [Obe02] M. OBERT, B. WILD, G. BACHER, A. FORCHEL, R. ANDRÉ et L. S. DANG, « Optical confinement in CdTe-based photonic dots », *Applied Physics Letters*, vol. 80, no. 8 (2002) p. 1322.
- [Nei93] M. ONEILL, M. OESTREICH, W. W. RUHLE et D. E. ASHENFORD, « Exciton radiative decay and homogeneous broadening in $CdTe/Cd_{0.85}Mn_{0.15}Te$ multiple quantum wells », *Physical Review B*, vol. 48, no. 12 (1993) p. 8980–8985.
- [Pan99] G. PANZARINI, L. C. ANDREANI, A. ARMITAGE, D. BAXTER, M. SKOLNICK, V. ASTRATOV, J. ROBERTS, A. V. KAVOKIN, M. R. VLADIMIROVA et M. KALITEEVSKI, « Exciton-light coupling in single and coupled semiconductor microcavities: polariton dispersion and polarization splitting », *Physical Review B*, vol. 59, no. 7 (1999) p. 5082.
- [Pau96] S. PAU, H. CAO, J. JACOBSON, G. BJÖRK, Y. YAMAMOTO et A. IMAMOGLU, « Observation of a laserlike transition in a microcavity exciton polariton system », *Physical Review A*, vol. 54, no. 3 (1997) p. R1789–R1792.
- [Pel92] N. T. PELEKANOS, H. HAAS, N. MAGNEA, H. MARIETTE et A. WASIELA, « Room-temperature exciton absorption engineering in II-VI quantum wells », *Applied Physics Letters*, vol. 61, no. 26 (1992) p. 3154–3156.
- [Pen56] O. PENROSE et L. ONSAGER, « Bose-Einstein Condensation and Liquid Helium », *Physical Review*, vol. 104, no. 3 (1956) p. 576–584.
- [Per06] M. PERRIN, *Relaxation des polaritons dans une microcavité contenant un gaz d'électrons*, Thèse de doctorat, Université Paris VI (2006).
- [Per05] M. PERRIN, P. SENELLART, A. LEMAÎTRE et J. BLOCH, « Electron-Polariton Scattering in Semiconductor Microcavities », *Physical Review B*, vol. 72, no. 7 (2005) p. 075340.
- [Pet02] C. J. PETHICK et H. SMITH, *Bose-Einstein condensation in dilute gases* (Cambridge University Press, 2002).
- [Pet00] D. S. PETROV, M. HOLZMANN et G. V. SHLYAPNIKOV, « Bose-Einstein Condensation in Quasi-2D Trapped Gases », *Physical Review Letters*, vol. 84, no. 12 (2000) p. 2551.

- [Pit03] L. PITAEVSKII et S. SRTINGARI, *Bose-Einstein Condensation* (Clarendon Press, Oxford, 2003).
- [Poh92] A. POLHMANN, R. HELLMANN, E. O. GÖBEL, D. R. YAKOVLEV, W. OSSAU, A. WAAG, R. N. BICKNELL-TASSIUS et G. LANDWEHR, « Exciton lifetimes in CdTe/CdMnTe single quantum wells », *Applied Physics Letters*, vol. 61, no. 24 (1992) p. 2929–2931.
- [Por02] D. PORRAS, C. CIUTI, J. J. BAUMBERG et C. TEJEDOR, « Polariton dynamics and Bose-Einstein condensation in semiconductor microcavities », *Physical Review B*, vol. 66, no. 8 (2002) p. 085304.
- [Por03] D. PORRAS et C. TEJEDOR, « Linewidth of a polariton laser: Theoretical analysis of self-interaction effects », *Physical Review B*, vol. 67, no. 16 (2003) p. 161310(R).
- [Pur46] E. M. PURCELL, « Spontaneous emission probabilities at radio frequencies », *Physical Review*, vol. 69 (1946) p. 681.
- [Qar03] A. QARRY, G. RAMON, R. RAPAPORT, E. COHEN, A. RON, A. MANN, E. LINDER et L. N. PFEIFFER, « Nonlinear emission due to electron-polariton scattering in a semiconductor microcavity », *Physical Review B*, vol. 67, no. 11 (2003) p. 115320.
- [Rai89] M. G. RAIZEN, R. J. THOMPSON, R. J. BRECHA, H. J. KIMBLE et H. J. CARMICHAEL, « Normal-mode splitting and linewidth averaging for two-state atoms in an optical cavity », *Physical Review Letters*, vol. 63, no. 3 (1989) p. 240–243.
- [Rüe03] C. RÜEGG, N. CAVADINI, A. FURRER, H.-U. GÜDEL, K. KRÄMER, H. MUTKA, A. WILDES, K. HABICHT et P. VORDERWISCH, « Bose-Einstein condensation of the triplet states in the magnetic insulator $TlCuCl_3$ », *Nature*, vol. 423, no. 6539 (2003) p. 62–65.
- [Rei04] J. P. REITHMAIER, G. SEK, A. LÖFFLER, C. HOFMANN, S. KUHN, S. REITZENSTEIN, L. V. KELDYSH, V. D. KULAKOVSKII, T. L. REINECKE et A. FORCHEL, « Strong coupling in a single quantum dot-semiconductor microcavity system », *Nature*, vol. 432, no. 7014 (2004) p. 197–200.
- [Mox04] M. RICHARD, *Quasi-condensation de polaritons sous excitation incohérente dans les microcavités II-VI à base de CdTe.*, Thèse de doctorat, Université Joseph Fourier, Grenoble (2004).
- [Mox05] M. RICHARD, J. KASPRZAK, R. ANDRÉ, R. ROMESTAIN, L. S. DANG, G. MALPUECH et A. KAVOKIN, « Experimental evidence for nonequilibrium Bose condensation of exciton polaritons », *Physical Review B*, vol. 72, no. 20 (2005) p. 201301.

-
- [Max05] M. RICHARD, J. KASPRZAK, R. ROMESTAIN, R. ANDRÉ et L. S. DANG, « Spontaneous Coherent Phase Transition of Polaritons in CdTe Microcavities », *Physical Review Letters*, vol. 94, no. 18 (2005) p. 187401.
- [Roc00] G. ROCHAT, C. CIUTI, V. SAVONA, C. PIERMAROCCHI et A. QUATTROPANI, « Excitonic Bloch equations for a two-dimensional system of interacting excitons », *Physical Review B*, vol. 61, no. 20 (2000) p. 13856–13862.
- [Sab02] M. SABA, *Optical coherence and stimulated scattering in semiconductor microcavity*, Thèse de doctorat, Ecole Polytechnique Fédérale de Lausanne (2002).
- [Sal91] B. E. A. SALEH et M. C. TEICH, *Fundamentals of photonics* (Wiley, 1991).
- [San05] D. SANVITTO, A. DARAEI, A. TAHRAOUI, M. HOPKINSON, P. W. FRY, D. M. WHITTAKER et M. S. SKOLNICK, « Observation of ultrahigh quality factor in a semiconductor microcavity », *Applied Physics Letters*, vol. 86, no. 19 (2005) p. 191109.
- [San06] D. SANVITTO, D. N. KRIZHANOVSKII, D. M. WHITTAKER, S. CECCARELLI et M. S. SKOLNICK, « Spatial structure and stability of the macroscopically occupied polariton state in the microcavity optical parametric oscillator », *Physical Review B*, vol. 73, no. 24 (2006) p. 241308.
- [Sav05] S. SAVASTA, O. D. STEFANO, V. SAVONA et W. LANGBEIN, « Quantum Complementarity of Microcavity Polaritons », *Physical Review Letters*, vol. 94, no. 24 (2005) p. 246401.
- [Sav95] V. SAVONA, L. C. ANDREANI, P. SCHWENDIMANN et A. QUATTROPANI, « Quantum well excitons in semiconductor microcavities: Unified treatment of weak and strong coupling regimes », *Solid State Communications*, vol. 93, no. 9 (1995) p. 733–739.
- [Sav96] V. SAVONA, C. PIERMAROCCHI, A. QUATTROPANI, P. SCHWENDIMANN et F. TASSONE, *Optical properties of Microcavity Polaritons* (EPFL, 1996).
- [Sav00] P. G. SAVVIDIS, J. J. BAUMBERG, R. M. STEVENSON, M. S. SKOLNICK, D. M. WHITTAKER et J. S. ROBERTS, « Angle-Resonant Stimulated Polariton Amplifier », *Physical Review Letters*, vol. 84, no. 7 (2000) p. 1547–1550.
- [Sca66] D. B. SCARL, « Measurement of Photon Time-of-Arrival Distribution in Partially Coherent Light », *Physical Review Letters*, vol. 17, no. 12 (1966) p. 663–666.

- [Sch05] M. SCHELLEKENS, R. HOPPELER, A. PERRIN, J. V. GOMES, D. BOIRON, A. ASPECT et C. I. WESTBROOK, « Hanbury Brown Twiss Effect for Ultracold Quantum Gases », *Science*, vol. 310, no. 5748 (2005) p. 648–651.
- [Sch85] S. SCHMITT-RINK, D. S. CHEMLA et D. A. B. MILLER, « Theory of transient excitonic optical nonlinearities in semiconductor quantum-well structures », *Physical Review B*, vol. 32, no. 10 (1985) p. 6601.
- [Sch89] S. SCHMITT-RINK, D. S. CHEMLA et D. A. B. MILLER, « Linear and nonlinear optical properties of semiconductor quantum well », *Advances in Physics*, vol. 38, no. 2 (1989) p. 89–188.
- [Sel06] I. R. SELLERS, F. SEMOND, M. LEROUX, J. MASSIES, P. DISSEIX, A.-L. HENNEGHEN, J. LEYMARIE et A. VASSON, « Strong coupling of light with A and B excitons in GaN microcavities grown on silicon », *Physical Review B*, vol. 73, no. 3 (2006) p. 033 304.
- [Sen01] P. SENELLART, *Semiconductor quantum wells in a tunable fibre-based microcavity*, Thèse de doctorat, Heriot-Watt University, Edinburgh (2002).
- [Sen99] P. SENELLART et J. BLOCH, « Nonlinear Emission of Microcavity Polaritons in the Low Density Regime », *Physical Review Letters*, vol. 82, no. 6 (1999) p. 1233–1236.
- [Sen00] P. SENELLART, J. BLOCH, B. SERMAGE et J. Y. MARZIN, « Microcavity polariton depopulation as evidence for stimulated scattering », *Physical Review B*, vol. 62, no. 24 (2000) p. R16 263–R16 266.
- [Sko98] M. S. SKOLNICK, T. A. FISHER et D. M. WHITTAKER, « Strong coupling phenomena in quantum microcavity structures », *Semiconductor Science and Technology*, vol. 13, no. 7 (1998) p. 645.
- [Sko02] M. S. SKOLNICK, R. M. STEVENSON, A. I. TARTAKOVSKII, R. BUTTÉ, M. EMAM-ISMAIL, D. M. WHITTAKER, P. G. SAVVIDIS, J. J. BAUMBERG, A. LEMAÎTRE, V. N. ASTRATOV et J. S. ROBERTS, « Polariton-polariton interactions and stimulated scattering in semiconductor microcavities », *Material Science and Engineering C*, vol. 19, no. 1-2 (2002) p. 407–416.
- [Sno02] D. SNOKE, « Spontaneous Bose Coherence of Excitons and Polaritons », *Science*, vol. 298, no. 5597 (2002) p. 1368–1372.
- [Snoke02] D. SNOKE, S. DENEV, Y. LIU, L. PFEIFFER et K. WEST, « Long-range transport in excitonic dark states in coupled quantum wells », *Nature*, vol. 418, no. 6899 (2002) p. 754–757.

-
- [Spi00] I. B. SPIELMAN, J. P. EISENSTEIN, L. N. PFEIFFER et K. W. WEST, « Resonantly Enhanced Tunneling in a Double Layer Quantum Hall Ferromagnet », *Physical Review Letters*, vol. 84, no. 25 (2000) p. 5808.
- [Ste98] J. STENGER, S. INOUE, D. STAMPER-KURN, H. MIESNER, A. CHIKKATUR et W. KETTERTLE, « Spin domains in ground-state Bose-Einstein condensates », *Nature*, vol. 396, no. 6709 (1998) p. 345.
- [Szy06] M. H. SZYMAŃSKA, J. KEELING et P. B. LITTLEWOOD, « Non-equilibrium quantum condensation in an incoherently pumped dissipative system », *Physical Review Letters*, vol. 96, no. 6 (2006) p. 066 405.
- [Tar03] A. I. TARTAKOVSKII, D. N. KRIZHANOVSKII, G. MALPUECH, M. EMAM-ISMAIL, A. V. CHERNENKO, A. V. KAVOKIN, V. D. KULAKOVSKII, M. S. SKOLNICK et J. S. ROBERTS, « Giant enhancement of polariton relaxation in semiconductor microcavities by polariton-free carrier interaction: Experimental evidence and theory », *Physical Review B*, vol. 67, no. 16 (2003) p. 165 302.
- [Tas96] F. TASSONE, C. PIERMAROCCHI, V. SAVONA, A. QUATTROPANI et P. SCHWENDIMANN, « Photoluminescence decay times in strong-coupling semiconductor microcavities », *Physical Review B*, vol. 53, no. 12 (1996) p. R7642–R7645.
- [Tas97] F. TASSONE, C. PIERMAROCCHI, V. SAVONA, A. QUATTROPANI et P. SCHWENDIMANN, « Bottleneck effects in the relaxation and photoluminescence of microcavity polaritons », *Physical Review B*, vol. 56, no. 12 (1997) p. 7554–7563.
- [Tho92] R. J. THOMPSON, G. REMPE et H. J. KIMBLE, « Observation of normal-mode splitting for an atom in an optical cavity », *Physical Review Letters*, vol. 68, no. 8 (1992) p. 1132–1135.
- [Gla65] U. M. TITULAER et R. J. GLAUBER, « Correlation Functions for Coherent Fields », *Physical Review*, vol. 140, no. 3B (1965) p. B676–B682.
- [Gla66] U. M. TITULAER et R. J. GLAUBER, « Density Operators for Coherent Fields », *Physical Review*, vol. 145, no. 4 (1966) p. 1041–1050.
- [Ott05] A. ÖTTL, S. RITTER, M. KÖHL et T. ESSLINGER, « Correlations and Counting Statistics of an Atom Laser », *Physical Review Letters*, vol. 95, no. 9 (2005) p. 090 404.
- [Vah03] K. J. VAHALA, « Optical microcavities », *Nature*, vol. 424, no. 6950 (2003) p. 839–846.
- [Weh97] M. U. WEHNER, M. H. ULM et M. WEGENER, « Scanning interferometer stabilized by use of Pancharatnam’s phase », *Optics Letters*, vol. 22, no. 19 (1997) p. 1455–1457.

- [Wei92] C. WEISBUCH, M. NISHIOKA, A. ISHIKAWA et Y. ARAKAWA, « Observation of the coupled exciton-photon mode splitting in a semiconductor quantum microcavity », *Physical Review Letters*, vol. 69, no. 23 (1992) p. 3314.
- [Woo80] H. WOOLF, *Some Strangeness in the Proportion: a Centennial Symposium on Albert Einstein* (Addison-Wesley, New York, 1980).
- [Yam00] Y. YAMAMOTO, F. TASSONE et H. CAO, *Semiconductor Cavity Quantum Electrodynamics* (Springer-Verlag, 2000).
- [Yos04] T. YOSHIE, A. SCHERER, J. HENDRICKSON, G. KHITROVA, H. M. GIBBS, G. RUPPER, C. ELL, O. B. SHCHEKIN et D. G. DEPPE, « Vacuum Rabi splitting with a single quantum dot in a photonic crystal nanocavity », *Nature*, vol. 432, no. 7014 (2004) p. 200–203.
- [Zim72] J. M. ZIMAN, *Principles of the Theory of Solids* (Cambridge University Press, 1972).
-

Remerciements

My adventure with microcavity polaritons started in October 2002, when I arrived as an undergraduate student in the Equipe-Mixte NPSC. During the first days of my "stage" I met four persons, who had a crucial influence on my life and my work during the next four years, and whom I wish to thank at the very beginning. **Dang**, my guide during this PhD, for showing me day by day what it means to be a scientist: Your modesty as great as your experience; the exactness and patience, the enthusiasm and joy of discovering the truth, I hope to keep all of this in myself. Thank you for giving me the great conditions to work during this thesis. Not every student has a chance to have the entire lab for himself during almost two years and to build his own setup from the beginning. Not every student gets to travel as much as I could. **Robert**, who was a founding member of polariton studies in Grenoble. Thank you for taking care of me during my first year. I wish we could have discussed and worked together also during the second and third year. I wish we could repeat the trekking around La Salette. We are missing you a lot... **Maxime**, you were right, "La Brique" gave me several brilliant ideas! But who will take care of her now?? By the way, she is still missing you. Thank you for all the experiments that we did together. I hope to repeat "Gershwin in the dark" one day. Thank you for your hospitality in Grenoble and Lausanne. **Regis**, without your samples nothing would be possible. They are as great as your sense of humor. Thank you for helping us with an apartment.

This work was based, especially during the last year, on a strong international collaboration. I would like to acknowledge the Lausanne team (Max, Stefan, Augustin and Pierre) led by Benoit Deveaud-Plédran for taking the initiative in the decisive measurements of spatial coherence. Many thanks also for all the theoretical support from the Cambridge team (Francesca, Marzena, Jonathan) led by Peter Littlewood, and from others - Vincenzo Savona, Guillaume Malpuech, Alexey Kavokin and Wolfgang Langbein - for underlining all the difficulties and subtleties of the polariton BEC. Thank you very much for your hospitality in Cambridge and Lausanne!

I wish to express my gratitude to everyone of you in the Equipe-Mixte NPSC for all your help and discussions. In particular, to Jean-Philippe and Fabrice for your vital contribution in the intensity correlation measurements and to Lucien, David and Jean-Claude for all the advice concerning optics. I am especially thankful to Ronald Cox who always helped me with my English before oral presentations and who also corrected this manuscript to make it readable.

I wish to thank all the "thèsards" and "permanents" of LSP, whom I had great pleasure to work with. The full list of all your names would be too long here...

And finally, **Joanna**, how I can thank you for all your love and patience given to me during these years?

Résumé

La condensation de Bose-Einstein est prédite par Einstein en 1925 pour des particules indiscernables de spin entier, les bosons. Il s'agit d'une transition de phase vers un état quantique de cohérence macroscopique, dont la température critique dépend directement de la masse des particules. Ce n'est qu'en 1995 qu'un condensat a pu être formé en phase gazeuse en refroidissant des atomes alcalins à la température ultra-basse de 10^{-6} degré Kelvin, provoquant ainsi une explosion d'activités de recherche dans le monde sur le sujet.

Concernant la phase solide, les excitons dans les semi-conducteurs sont considérés comme le candidat le plus prometteur pour la condensation de Bose-Einstein. En effet leur masse est cent mille fois plus légère que celle des atomes alcalins, ce qui devrait permettre leur condensation à une température voisine du degré Kelvin. Cependant malgré de nombreuses études depuis une trentaine d'années, aucune preuve convaincante de l'existence de condensat d'excitons n'avait été apportée à ce jour. Récemment l'attention s'est portée sur les polaritons dans les microcavités semi-conductrices contenant des puits quantiques.

Une microcavité semi-conductrice à puits quantiques est une hétérostructure photonique destinée à exalter l'interaction matière-rayonnement entre les excitons confinés dans le puits quantique et les photons confinés dans la microcavité. Lorsque l'énergie de ces photons coïncide avec celle des excitons, la microcavité peut entrer dans le régime de couplage fort d'oscillations de Rabi. Les nouveaux états propres du système (microcavité-puits quantique) sont appelés polaritons qui sont des états mixtes exciton-photon. Par leur nature photonique, ces bosons possèdent une masse dix mille fois plus légère que celle des excitons, un avantage certain pour l'étude de la condensation de Bose-Einstein.

Nous avons observé l'occupation massive de l'état fondamental du polariton, qui se développe à partir d'un nuage de polaritons thermalisés à une température de (16-20) K. La formation du condensat est accompagnée par l'apparition spontanée de la cohérence temporelle et de la cohérence spatiale à longue portée, ainsi qu'une forte polarisation linéaire. La transition d'un état thermique à un état quantique est démontrée par des mesures de la fonction de corrélation d'ordre 2 en fonction de la densité des polaritons. L'ensemble de ces observations constitue la première évidence de la condensation de Bose-Einstein en phase solide.

Abstract

Because of their unique property of bringing pure quantum effects into the real world scale, phase transitions towards condensed phases - like Bose-Einstein condensation, superfluidity, and superconductivity - have always fascinated scientists. The BEC, appearing upon cooling a gas of bosons below a critical temperature, has been given a striking demonstration in dilute atomic gases of rubidium atoms at temperatures below 200nK. By confining photons in a semiconductor microcavity, and strongly coupling them to electronic excitations, one may create polaritons. These bosonic quasi-particles are 10^9 times lighter than rubidium atoms, thus theoretically allowing a BEC at standard cryogenic temperatures. Here we detail a comprehensive set of experiments giving compelling evidence for a BEC of polaritons. Above a critical density, we observe massive occupation of the ground state, developing from a thermalized and saturated distribution of the polariton population at (16-20)K. We demonstrate as well the existence of a critical temperature for this transition. The spontaneous onset of a coherent state is manifested by the increase of temporal coherence, the build-up of long-range spatial coherence and the reduction of the thermal noise observed in second order coherence experiments. The marked linear polarization of the emission from the condensate is also measured. All of these findings indicate the spontaneous onset of a macroscopic quantum phase.

Keywords: Bose-Einstein condensation, final state stimulation, long-range phase coherence, intensity correlations, exciton polaritons, semiconductor microcavity, strong coupling, CdTe